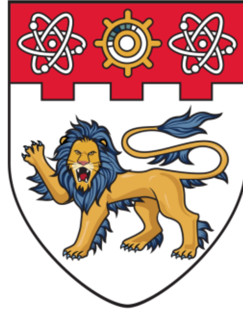

NANYANG TECHNOLOGICAL UNIVERSITY
SINGAPORE

THE PIEZOELECTRIC PROPERTIES OF 3R MOLYBDENUM DISULFIDE FLAKES

CAI WEIFAN

SCHOOL OF ELECTRICAL & ELECTRONIC ENGINEERING

2021

THE PIEZOELECTRIC PROPERTIES OF 3R MOLYBDENUM DISULFIDE FLAKES

CAI WEIFAN

School of Electrical & Electronic Engineering

A thesis submitted to the Nanyang Technological University

in partial fulfillment of the requirement for the degree of

Doctor of Philosophy

2021

Statement of Originality

I hereby certify that the work embodied in this thesis is the result of original research, is free of plagiarised materials, and has not been submitted for a higher degree to any other University or Institution.

22/01/2021

. . . .

Date

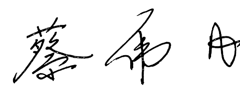

. . . .

CAI WEIFAN

Supervisor Declaration Statement

I have reviewed the content and presentation style of this thesis and declare it is free of plagiarism and of sufficient grammatical clarity to be examined. To the best of my knowledge, the research and writing are those of the candidate except as acknowledged in the Author Attribution Statement. I confirm that the investigations were conducted in accord with the ethics policies and integrity standards of Nanyang Technological University and that the research data are presented honestly and without prejudice.

22/01/2021
. . . .
Date

. . . .
Prof Zhang Qing

Authorship Attribution Statement

*(B) This thesis contains the results and discussion from 1 paper(s) published in the following peer-reviewed journal in which I am the first author.

Most of the results presented in Chapter 5 are published as **Weifan Cai**, Jingyuan Wang, Yongmin He, Sheng Liu, Qihua Xiong, Zheng Liu, Qing Zhang, Strain modulated photoelectric responses from a flexible α-In_2Se_3/3R MoS_2 heterojunction. *Nano-Micro Lett.* **13**, 65 (2021).

https://doi.org/10.1007/s40820-020-00584-1

The contributions of the co-authors are as follows:

- Prof Qing Zhang provided the initial project direction, discussed experiments results and principal mechanism, and edited the manuscript drafts.
- I prepared the manuscript drafts. The manuscript was revised by Prof Zheng Liu and Prof Qihua Xiong.
- I designed the study and performed all the laboratory work at the Schoole of Electrical and Electronics Engineering.
- All devices fabrication work, including sample preparation, characterization and testing, was conducted by me in the Nanyang Nanofabrication Centre, Nanoelectronics, and Semiconductor characterization laboratories.
- Dr Jingyuan Wang assisted in the X-ray Photoelectron Spectroscopy measurements.
- Dr Yongmin He assisted in the Scanning photocurrent microscopic image measurements.

- Dr Sheng Liu assisted in the Second Harmonic Generation measurements.

22/01/2021
. . . .
Date

蔡伟帆
. . . .
CAI WEIFAN

Acknowledgements

First and foremost, I would like to express my deepest gratitude and sincere thanks to my supervisor Prof. Zhang Qing, who has provided me this opportunity to explore the Nanoworld. It is a great pleasure to work with him as I learned a lot from him about critical thinking in scientific way, tackling problems with creativity, and preforming precise experiments with patience, etc. Without his continuous supports and generous encouragement, this journey would have never been possible.

I would like to convey my great appreciation and special thanks to Prof. Hamida Hallil Abbas (University of Bordeaux, France). I have gained invaluable experience in experiments from working with her closely. I am sincerely grateful to Prof. Liu Zheng, Prof. Xiong Qihua, Prof. Xu Shuyan for their help in my experiments implementation and valuable advises.

I would like to acknowledge to my past and current group members and cooperators, Dr. Zhang Kang, Dr. Zou Jianping, Dr. Wang Xinghui, Dr. Sun Leimeng, Dr. Xu Ran, Dr. Wang Jingyuan, Dr. Jiang Yu, Mr Tan Chee Khing, Dr. He Yongming, Dr. Liu Sheng, Dr. Qian Chen for their active cooperation, heartfelt encouragements and kind assistants in my research work and daily life.

I am thankful to all technicians, seniors, colleagues and classmates from Semiconductor Characterization, Charazterization, Nanoelectronics, Nanyang Nanofabrication Center, Nanomaterials and Photonics laboratories for their kindly help in my research work.

I would like to thank School of Electrical and Electronic Engineering, Nanyang Technological University for providing me the platform and financial support for my Ph.D. study.

Last but not least, I would like to convey my deepest gratitude to my parents Mr Cai Jun and Ms Zheng Qin for their infinite love, supports and encouragements during this journey. I would like to thank all my friends for their patient listening and supports during the past few years.

Table of Contents

Statement of Originality ....

Supervisor Declaration Statement ....

Authorship Attribution Statement ....

Acknowledgements ....

Table of Contents i

Summary iv

List of Figures vi

List of Tables xviii

Abbreviations and Symbols xix

Chapter 1 Introduction 1

1.1 Background and Motivation 1

1.2 Objectives 3

1.3 Major contributions 4

1.4 Thesis organizations 5

Chapter 2 A review on the 2D piezoelectric materials property and applications 7

2.1 Fundamental of piezoelectricity 7

2.1.1 Piezoelectric effect 7

2.1.2 Piezoresistive effect 12

2.1.3 Electronic and optoelectronic device performance modulated by strains or piezoelectric potentials 14

2.2 Piezoelectric 2D materials and their piezoelectric properties 17

2.2.1 Intrinsic piezoelectric 2D materials 18

2.2.2 Engineering modified 2D materials with piezoelectricity 23

2.2.3 Piezoelectric coefficients of 2D piezoelectric materials 25

2.2.4 Influential factors on the piezoelectric properties 26

2.3 Fabrication and characterization methods of piezoelectric 2D materials 31

2.3.1 Fabrication of 2D piezoelectric materials 31

2.3.2 Characterization methods 35

2.4 Applications of 2D piezoelectric materials 48

2.4.1 Energy harvesters 49

2.4.2 Piezotronics and piezoelectric sensors 54

2.4.3 Piezo-phototronic devices 56

Chapter 3 Piezoelectricity of 3R MoS_2 flakes 59
3.1 Introduction 59
3.2 Materials synthesis and devices fabrication 61
3.2.1 3R MoS_2 single crystal 61
3.2.2 MoS_2 devices for PFM and piezoelectric measurements 61
3.3 Methodology and experimental facilities set up 63
3.3.1 SHG measurement 63
3.3.2 Characterization of the PENG 64
3.3.3 PFM measurements 66
3.3.4 Raman and STEM Characterizations 69
3.4 Results and discussion 69
3.4.1 Structure of 3R MoS_2 69
3.4.2 Piezoelectricity of 3R MoS_2 73
3.4.3 Piezoelectric coefficients of 3R MoS_2 86
3.5 Conclusion 93
Chapter 4 Thermal transport property of 3R MoS_2 flakes under strains 95
4.1 Introduction 95
4.2 Devices fabrication and Characterization 97
4.2.1 Preparation of MoS_2 flakes 97
4.2.2 Preparation suspended 3R MoS_2 97
4.2.3 Optical and electrical characterization of 3R MoS_2 devices. 99
4.3 Results and discussion 100
4.3.1 In-plane thermal conductivity of MoS_2 flakes under strains 100
4.3.2 In-plane thermal conductivity of a metal/MoS_2 flakes/metal structure under strains 111
4.4 Conclusion 124
Chapter 5 Photoelectric responses from a flexible α-In_2Se_3/3R MoS_2 heterojunction under strain 126
5.1 Introduction 126
5.2 Experimental devices and methods 127
5.2.1 Synthesis of α-In_2Se_3/3R MoS_2 heterojunction 127
5.2.2 Materials characterizations 128
5.2.3 Electrical, optoelectronic, and mechanical characterizations 128
5.3 Results and discussion 129
5.3.1 Atomic structure and PFM measurement of α-In_2Se_3 flakes 129

5.3.2 α-In_2Se_3/3R MoS_2 heterojunction photoelectric performance without strains 131
5.3.3 α-In_2Se_3/3R MoS_2 heterojunction photoelectric performance with strain .. 141
5.4 Working Principle 147
5.5 Conclusion 150
Chapter 6 Conclusions 151
6.1 Conclusions 151
6.2 Future work 152
Author's Publications 155
Bibliography 157

Summary

Low-dimensional nanomaterials, such as Wurtzite structured materials (ZnO, GaN, etc.), and transitional metal dichalcogenides (MoS_2, WSe_2, etc.), have been widely studied for their unique physical properties which result from strong coupling effect among piezoelectric, semiconducting, and optical characteristics. In depth understanding of the physical properties could promote development of various novel functional devices, energy harvesters, etc.

The piezoelectricity in 3R (3 Rhombohedral) MoS_2 has been predicated by theoretical studies. To our best knowledge, no experimental observation has been reported so far. In this thesis, the piezoelectricity of 3R MoS_2 flakes has been studied systematically. Two kinds of flexible 3R MoS_2 based piezoelectric nanogenerator (PENG) have been fabricated. One is aligned 3R MoS_2 device, in which the zigzag direction is aligned to the electrodes direction, and another is non-aligned 3R MoS_2 device. The aligned 3R MoS_2 PENG shows superb electrical and excellent power density values. The crystal orientation dependent piezoelectric polarization generation can be clearly observed by the fact that the piezoelectric polarization depends on whether the strain is applied along the zigzag or the armchair direction. Specifically, the high piezoelectric response from 3R MoS_2 is firstly confirmed using Piezoresponse Force Microscopy (PFM) at room temperature. The out-of-plane piezoelectric coefficient d_{33} is measured around 0.7 to 1.5 pm/V for multilayer 3R MoS_2. From lateral PFM measurement, we observe a strong piezoelectric response due to the coupling of in-plane and out-of-plane piezoelectricity.

Subsequently, we find that the intrinsic thermal conductivity of 3R MoS_2 flake is slightly changed under mechanical strains. A strong modulation of heat transport is observed on 3R MoS_2 flake and its metal contact junctions under biased strains. This is the first

experimental observation which shows that heat transport of low dimensional piezoelectric material can be modulated through a mechanical strain. In addition, a flexible α-In_2Se_3/3R MoS_2 van der Waals (vdWs) p-n heterojunction is fabricated for photodetection from the visible to near infrared region. It exhibits an ultrahigh photoresponsivity of 2.9×10^3 A/W and a substantial specific detectivity of 6.2×10^{10} Jones under a compressive strain of -0.26%. The transport of photon generated carriers is clearly modulated by mechanical stimuli through the piezoelectric effect at the heterojunction interface.

List of Figures

Figure 1-1 Global market for piezoelectric devices and smart materials — a forecast for 2027..........2

Figure 2-1(a) Piezoelectricity-An interaction of electric field, polarization, mechanical stress and strain. (b) Directions of Tensors in the constitutive equations [1]..........12

Figure 2-2 The relationship of three effects between piezoelectricity, semi-conductivity, and photo-excitability [49]..........15

Figure 2-3 Schematic of piezotronic effect on a Schottky junction at a metal-semiconductor interface under (a) compressive strain and (b) tensile strain [51]..........16

Figure 2-4 Schematic illustration of the piezo-phototronic effect on a p-n junction. The presence of (a) positive and (b) negative piezoelectric polarization charges at the interface [51]..........17

Figure 2-5 (a) Schematic of an atomic structure of monolayer MoS_2. (b) Optical image of monolayer MoS_2 with lattice orientation confirmed from the SHG. (c) Optical image of a flexible MoS_2 PENG [19]. (d) Schematic of the experiment setup for probing the piezoelectric property of a MoS_2 flake. (e) Measured piezoelectric stress vs increasing driving voltage and (f) Calculated piezoelectric coefficient e_{11} of one layer, two layers and three layers of MoS_2 [54]..........21

Figure 2-6 Atomic structure of (a) group III monochalcogenides GaS [66] (b) C_{2v} orthorhombic group IV monochalcogenides [67] (c) group III-V buckled honeycomb monolayers in top and side views. Reproduced from [71]..........22

Figure 2-7 (a) Pristine graphene and graphene sheet with triangular hole [81] (b) Various chemical doped graphene [82] (c) atomic layer of tri-s-triazine [83] (d) Graphene supported on trenched SiO_2 substrate [89]..........24

Figure 2-8 Periodic trends for d_{11} in (a) metal dichalcogenides, (b) Hexagonal group III-V, (c) Group IV monochalcogenides [62]. Proportional trend between the piezoelectric coefficient d_{11} (d) of TMDC and (e) group II-VI SC monolayers [67]. 27

Figure 2-9 (a) Electric field induced deformation of h-BN nanosheet and nanotube [92]. (b) Measured piezoelectric coupling strength of m-MoS_2 as a function of crystal orientation [54]..29

Figure 2-10 (a) Piezoelectric coefficient of h-BN and h-ZnO vs their diameter [93, 94]. (b) Piezoelectric coefficient of h-BN nanosheets as a function of the layer number *N*. (c) The output piezoelectric current of m-MoS_2 PENG device [19]. 30

Figure 2-11 Schematic illustration of (a) liquid exfoliation of quasi-2D materials using acoustic waves [98], (b) CVD method for the synthesis of MoS_2 thin layers [100], (c) PVD process of In_2Se_3 synthesis, the crystal structure and optical image of In_2Se_3 monolayer or flakes [102], (d) liquid metal assisted synthesis of monolayer SnS and its application on a nanogenerator transducer [69]. 34

Figure 2-12 Schematic of (a) single frequency PFM set up, and working principles of (b) vertical PFM (c) lateral PFM. Reproduced from [109]. 37

Figure 2-13 Topography, PFM amplitude images of (a) monolayer MoS_2 [114], (b) monolayer Janus MoSSe [115], (c) Multilayers α-In_2Se_3 [77], (d) Vertical PFM amplitudes images with tip voltages from 1 to 6V [117]..40

Figure 2-14 (a) Schematics of the SHG mechanism. (b) Topography and SHG intensity mapping of mono, two and three layers MoS_2 [119]. (c) SHG polar plot of h-BN and MoS_2 and SHG intensity vs layer number from one to 5 layers [60]. (d) SHG intensity polar plots of monolayer, bilayers, triple layers and bulk 3R MoS_2, integrated polarization contrast of the SHG signal in the parallel for various thickness 3R MoS_2 and its lattice structure [120]. (e) SHG spectral insensitivity reflected from exfoliated α-

In_2Se_3, PVD growth α-In_2Se_3 and bulk GaAs and SHG polar plots of PVD growth α-In_2Se_3 and exfoliated α-In_2Se_3 [79]. 42

Figure 2-15 (a) Schematic of a direct strain testing setup, (b) Output voltages and currents of an m-MoS_2 device [19]. (c) Output currents of a multilayer α-In_2Se_3 device [77]. (d) *I-V* curves of the CVD MoS_2 device at different forces under compressive and tensile strain [121]..45

Figure 2-16 Schematic illustration for different thermal conductivity measurement (a) Optothermal raman method [122], (b) Suspended pad method [123, 131], (c) Time-domain thermoreflectance (TDTR) method [124], (d) Scanning thermal microscopy (SThM) method [134]. 48

Figure 2-17 (a) The optical image of the array, and voltage and current outputs of integrated m-MoS_2 devices [19]. (b) The optical images of CVD m-MoS_2 devices and current outputs along armchair and zigzag direction, respectively [140]. (c) Schematic and current outputs of pristine MoS_2 with intrinsic S vacancy and passivated MoS_2 after treatment [141]. (d) Schematic and current outputs of SC-MoS_2 and GB-MoS_2 [142]. (e) Schematic of a PENG based on monolayer WSe_2, piezoelectric coefficient d_{11}, piezoelectric voltage outputs, durability tests of monolayer WSe_2 and bilayer WSe_2 devices [20]. 51

Figure 2-18 (a) Atomic structures, layer dependence of simulated piezoelectric coefficient d_{22}, piezoelectric outputs with different layers of α-In_2Se_3 and γ-InSe [143]. (b) Optical image, piezoelectric voltage output under various excitation frequency from [69]. (c) Atomic structure of monolayer and multilayer PbI_2, piezoelectric outputs of PbI_2 devices [144]. 53

Figure 2-19 (a) The *I-V* characteristics and band diagrams for explaining the piezotronic effect of m-MoS_2 and bilayer MoS_2 devices under a tensile or compressive strain [19].

(b) Optical image and the performance of an m-MoS_2 humidity sensor [151]. (c) Self-powered α-In_2Se_3 piezoelectric sensor [143]. (d) Schematic and piezopoetntial modulation on the performance of a pressure sensor based on ZnO nanorod arrays and 2D indium selenide (InSe) field-effect transistor (FET) [152]. 56

Figure 2-20 The strain modulated photoresponse of (a) flexible m-MoS_2 photodetector [153], (b) flexible MoS_2/WSe_2 van der Waals photodiode [154]. (c) Schematic and strain modulated relative output power as a function of voltage under various strain, open circuit voltage and maximum output power under various strain of 2D piezo-phototronic solar cells [155]. 57

Figure 3-1 Schematic illustration of the sample fabrication processes for (a) in-plane PFM measurement, (b) direct strain bending measurement and (c) out-of-plane PFM measurement. 63

Figure 3-2 Second Harmonic Generation Experimental setup [120] 64

Figure 3-3 (a) Schematic of the circuit connection and (b) the experiment setup for PENG devices under different strains. 65

Figure 3-4 Illustration of a mechanical strain applied onto the MoS_2 flakes 66

Figure 3-5 Schematic of DART experiment setup and the working principle of the dual-frequency excitation based resonant-amplitude tracking. 68

Figure 3-6 Illustration of the lateral excitation PFM measurement. 69

Figure 3-7 Atomic structure of (a) 2H MoS_2, (b) 3R MoS_2 in top and side views. (c) STEM images of monolayer, bilayer and trilayer 3R MoS_2. 71

Figure 3-8 SHG measurement of a 3R MoS_2 flake; (a) Optical image with polarization angle θ, (b) the SHG intensity at polarization angle θ = 30°, 45° and 60°, (c) Angle dependence of the SHG intensities. 72

Figure 3-9 Raman spectra for 20 nm and 80 nm thick 3R MoS_2 flakes. 73

Figure 3-10 (a) Illustration of the PENG device under a tensile strain, (b) an aligned 3R MoS_2 PENG device with the electrodes parallel to zigzag axis, (c) a non-aligned 3R MoS_2 PENG device with the electrodes neither parallel nor perpendicular to the armchair or zigzag axis. The scale bar is 5 μm. The red arrows and black arrows stand for the armchair and zigzag orientations. 74

Figure 3-11 AFM measurement of 3R MoS_2 PENG. Morphology image and Height profile of the (a-b) aligned and (c-d) non-aligned 3R MoS_2 flake (The red arrow marks the x direction). 75

Figure 3-12 Piezoelectric outputs of an aligned 3R MoS_2 flake. Piezoelectric current and voltage under various strains applied along (a, c) the x axis (zigzag) and (b, d) the y axis (armchair). The summary of the piezoelectric current and voltage outputs as a function of strain along (e) the x axis (zigzag) and (f) the y axis (armchair). 79

Figure 3-13 Piezoelectric outputs of a non-aligned 3R MoS_2 flake. The piezoelectric current and voltage under various strains applied along (a, c) the x axis (horizontal) and (b, d) the y axis (vertical). The summary of the piezoelectric current and voltage as the function of strain along (e) the x axis (horizontal) and (f) the y axis (vertical). 80

Figure 3-14 Voltage (V_{oc}) and current (I_{sc}) responses of aligned and non-aligned 3R MoS_2 flakes under a periodic strain. Top: The external strain as a function of time, Middle: corresponding several piezoelectric output cycles along the x axis (zigzag or horizontal), Bottom: corresponding several piezoelectric output cycles along the y axis (armchair or vertical) of (a) aligned and (b) non-aligned 3R MoS_2 flake, respectively. 81

Figure 3-15 Electrical measurements on a bare polyimide substrate and 2H MoS_2 flake on polyimide. The current and voltage output of (a,b) bare polyimide substrate (without

any flake) and (c,d) 2H MoS_2 flake on polyimide substrate under a strain of 0.47%, respectively. 82

Figure 3-16 Polarity switching test of the aligned MoS_2 flake under 0.47% strain with (a) forward and (b) reverse connections. 83

Figure 3-17 Mechanical durability and stability test of an aligned MoS_2 flake under a strain of 0.47% (a) The output current as a function of time. (b) The extracted output current from 1500s to 1545s. 84

Figure 3-18 (a) The piezoelectric peak output voltage and current and (b) the instantaneous power of a 3R MoS_2 based PENG. 84

Figure 3-19 3R MoS2 based PENG monitoring finger motion (a) Optical image of the 3R MoS_2 PENG attached onto a finger. (b) Piezoelectric output of current at different curvatures of the finger clenching and releasing. (c) Piezoelectric output of current at different frequencies of the finger clenching and releasing. 86

Figure 3-20 PFM images of the out-of-plane piezoresponse amplitude and phase for the PPLN at a AC drive amplitude of (a) 0V, (b) 0.5V, (c) 1.0V and (d) 1.5V. 87

Figure 3-21 PPLN piezoelectric coefficient d_{33} estimation. 89

Figure 3-22 Out-of-plane piezo response of a 18 nm thick 3R MoS_2 flake. (a) AFM topography, (b) PFM amplitude, (c) PFM phase images at a bias voltage of 0.75 V and (d) Height profile of the 3R MoS_2 flake. 90

Figure 3-23 Out-of-plane piezo response of 15 nm and 56 nm thick 2H MoS_2 flakes (a) AFM topography, (b) PFM amplitude, (c) PFM phase images at a bias voltage of 0.75 V, (d) Height profile of the 15 nm 2H MoS_2 flake and (d) Height profile of the 56 nm 2H MoS_2 flake. 90

Figure 3-24 Piezoelectric coefficient d_{eff} fitting of 18 nm thick 3R MoS_2 flake. 91

Figure 3-25 The d_{33} piezoelectric coefficients as a function of 3R MoS_2 thickness.....91

Figure 3-26 Lateral excitation PFM of a 78nm thick 3R MoS_2 flake. (a-d) AFM topography, PFM amplitude, PFM phase images and Height profile of the 3R MoS_2 flake. (e-h) AFM topography, PFM amplitude, PFM phase images and Height profile of the 2H MoS_2 flake at a bias voltage of 8 V..92

Figure 3-27 Lateral excited piezo amplitude as function of lateral drive amplitude of the 78 nm 3R MoS_2 flake..93

Figure 4-1 (a) Optical image of a 3R MoS_2 flake (35nm thickness) suspended on a 3.2 µm wide photoresist trench (The scale bar is 10µm). (b) Schematic of Raman thermal measurement experiment set up for the suspended 3R MoS_2 flake. (c) The angle-dependence SHG plotting of 3R MoS_2 flake. (d) Optical image of the 3R MoS_2 flake on the quartz substrate (three absorption spectra measurements are performed on points 1, 2 and 3. The scale bar is 5 µm). (e) AFM topography image and (f) height profile of the 3R MoS_2 flake suspended on the photoresist trench. (g) AFM topography image and (h) height profile of the 3R MoS_2 flake on the quartz substrate......................................101

Figure 4-2 (a) Weighted average absorbance spectrum for the 3R MoS_2 flake on the quartz substrate. (b) Reflectivity spectra of polyimide substrate itself and under area at the trench bottom. 103

Figure 4-3 (a) The Raman spectra of a 3R MoS2 flake measured at different temperatures. (b) Temperature-dependent and (c) power-dependent Raman peak position shift of A_{1g} under a tensile (blue square +0.26%), zero (red circle 0%) and compressive (green triangular -0.26%) strain, respectively.......................................107

Figure 4-4 The calculated temperature distribution under a 0.3mW laser power, is calculated for a suspended 3R MoS_2 flake with $k = 70.6$ W/mK and G ranging from 0.5 MW/m^2K to 100 MW/m^2K, respectively..111

Figure 4-5 (a) Schematic of our thermal conductivity measurement set up. The heat was generated using a laser beam incident onto one thermal couple electrode. (b) An optical image of 3R MoS_2 flake with a pair of thermal couple electrodes E1 and E2. (c) The polarization dependence plot of SHG intensity of the 3R MoS_2 flake in (b) The red dots are experimental data and the blue solid lines are fitting lines. (d) An optical image of 2H MoS_2 flake with two thermal couple electrodes E1 and E2. (e) AFM topography image and (f) height profile of 3R MoS_2 flake in (b). (g) AFM topography image and (h) height profile of 2H MoS_2 flake in (d). 114

Figure 4-6 Thermal measurement of thermal couple device without flake (a) Optical image of laser heating thermal couple device without flake. (b) Temperature profile and temperature variation thermal couple electrodes E1 and E2. (c) Temperature variation profiles under uniaxial strain applied. (d) Absorptance curve of Ni/Au thin film on polyimide. 116

Figure 4-7 Evaluation of the thermal conductivities of a 3R MoS_2 flake with symmetrical thermal couple electrodes (Ni/Au/ 3R MoS_2/Au/Ni) (shown in Fig 4-5b) in the uniaxial direction under tensile (positive) and compressive (negative) strains. Temperature variation as a function of the laser light power in (a) the forward direction and (b) the reverse direction. Thermal conductivity $kquasi - total$ as a function of the strains in (c) the forward direction and (d) the reverse direction. 118

Figure 4-8 Evaluation of the thermal conductivities of a 2H MoS_2 flake with symmetry thermal couple (Ni/Au/ 2H MoS_2/Au/Ni) (shown in Fig 4-5d) in the uniaxial direction under tensile (positive) and compressive (negative) strains. Temperature variation as a function of the laser light power in (a) the forward direction and (b) the reverse direction. $kquasi - total$ as a function of the strains in (c) the forward direction and (d) the reverse direction. 119

Figure 4-9 (a) Optical image, (b) AFM topography image and (c) height profile of a 3R MoS_2 flake with an asymmetric thermal couple structure (Ni/Au/3R MoS_2/Al/Ni)...120

Figure 4-10 Evaluation of the thermal conductivities of a 3R MoS_2 flake with asymmetry thermal couple (Ni/Au/ 3R MoS_2/Al/Ni) (shown in Fig 4-9a) in the uniaxial direction under tensile (positive) and compressive (negative) strains. Temperature variation as a function of the laser light power in (a) the forward direction and (b) the reverse direction. $kquasi - total$ as a function of the strains in (c) the forward direction and (d) the reverse direction. 122

Figure 4-11 *I-V* characteristics curves of (a) a 3R MoS_2 flake with symmetry thermal couple (Ni/Au/3R MoS_2/Au/Ni, Figure 4-5), (b) 2H MoS_2 flake with symmetry thermal couple (Ni/Au/2H MoS_2/Au/Ni, Figure 4-5), and (c) 3R MoS_2 with asymmetric thermal couple structure (Ni/Au/3R MoS_2/Al/Ni, Figure 4-9). 124

Figure 5-1 Atomic structures (the side and top views) of (a) 3R phase MoS_2 and (b) Hexagonal α-In_2Se_3. 130

Figure 5-2 Out-of-plane piezo response of a 50 nm thick α-In_2Se_3 flake. (a) AFM topography, (b) PFM amplitude, (c) PFM phase images a bias voltage of 1 V and (d) Height profile of the α-In_2Se_3 flake. (e) Piezoelectric coefficient d_{33} estimation of 50 nm thick α-In_2Se_3 flake. 131

Figure 5-3 (a) Optical image, (b) Electrical measurement setup and (c) AFM image of the α-In_2Se_3/3R MoS_2 heterojunction. (d) Height profile of the α-In_2Se_3 flake. (e) Height profile of the 3R MoS_2 flake. 132

Figure 5-4 (a) The Raman spectrum of the α-In_2Se_3 flake. (b, c) The XPS spectra of In *3d* and Se *3d* core orbital peaks from the α-In_2Se_3 flake. (d) The Raman spectrum of the 3R MoS_2 flake. (e) Mo *3d* core orbital peaks from the 3R MoS_2 flake before and after

CHF_3 plasma treatment. (f) Polarization dependence plot of SHG intensity of 3R MoS_2 flake in the heterojunction (Figure 5-3a). 133

Figure 5-5 Optical images and *I-V* characteristics of α-In_2Se_3 and 3R MoS_2 flakes. (a) One pair of Cr/Au (10/150nm) electrodes were deposited on an α-In_2Se_3 flake. (b) One pair of Pd/Au (10/150nm) electrodes were deposited on a 3R MoS_2 flake. (c) *I-V* characteristics of the α-In_2Se_3 sample shown in (a) with no strain, a tensile strain of +0.26% and a compressive strain of -0.26%. (d) *I-V* characteristics of the 3R MoS_2 sample shown in (b) with no strain, a tensile strain of +0.26% and a compressive strain of -0.26% 134

Figure 5-6 Electrical characterization and photoresponse from the α-In_2Se_3/3R MoS_2 heterojunction under zero strain. (a) *I-V* characteristic in the dark with the logarithmic and linear scale. (b, c) *I-V* characteristics in the dark and under illumination of 532 nm wavelength under different light intensities from -0.5 V to 0.5 V and -0.1 V to 0.1 V with the logarithmic and linear scale, respectively. (d) Responsivity and detectivity at a bias voltage of 0.5 V as a function of illumination intensities. (e) Current vs time under 532 nm illumination with several intensities and zero bias voltage. (f) Current vs time extracted from (e) under the illumination intensity of 0.27 mW/cm^2. 137

Figure 5-7 Photoresponse from the α-In_2Se_3/3R MoS_2 heterojunction under several different light intensities under zero strain. (a) *I-V* characteristic under illumination intensity of 0.47 mW/cm^2 with different wavelengths. (b) Current vs time under the 532 nm illumination intensity of 0.47 mW/cm^2, and (c) Current vs time under 800nm illumination intensity of 0.47 mW/cm^2 with zero bias voltage. 140

Figure 5-8 The optical scanning photocurrent images of the α-In_2Se_3/3R MoS_2 heterojunction. (a) The optical image. (b-d) Photocurrent mapping of the heterojunction

under zero bias, reverse bias of -0.25 V and forward bias of 0.25 V at 532 nm with a laser power of 0.1mW and a spot waist radius of 400 nm. 141

Figure 5-9 *I-V* characteristic of the α-In_2Se_3/3R MoS_2 heterojunction under several strains in dark. 142

Figure 5-10 (a-d) *I-V* characteristics of the α-In_2Se_3/3R MoS_2 heterojunction (Fig 1c) from -0.5 V to 0.5 V under the dark and various 532 nm light illumination intensities with the strain of +0.13%, +0.26%, -0.13% and -0.26%. (e-f) Responsivity, detectivity, relative change of the responsivity and relative change of detectivity with respect to that under zero strain as a function of the light intensities and strains under +0.5 V bias. 143

Figure 5-11 (a-d) *I-V* characteristics of the α-In_2Se_3/3R MoS_2 heterojunction (Fig 1c) from -0.1 V to 0.1 V under the dark and various 532 nm light illumination intensities with the strain of +0.13%, +0.26%, -0.13% and -0.26%. (e-f) Responsivity, detectivity, relative change of the responsivity and relative change of detectivity with respect to that under zero strain as a function of the light intensities and strains under -0.1 V bias. 144

Figure 5-12 (a) Open circuit voltage V_{oc} and (b) Short circuit current I_{sc} under various light intensities and strains (The data were extracted from Figure 5-11). 145

Figure 5-13 (a, b) *I-t* of the heterojunction under zero bias and several strains at the 532 nm light intensity of 0.27 mW/cm^2 and 1.08 mW/cm^2. (c) Average photocurrent as a function of strains under zero bias at the illumination intensities of 0.27 mW/cm^2 and 1.08mW/cm^2, respectively. 147

Figure 5-14 The energy band diagrams for the α-In_2Se_3/3R MoS_2 heterojunction with\without the strains and light illumination. The energy band diagram (a) in thermal equilibrium with zero light illumination and no external strain (b) under zero light illumination and a tensile strain (c) under zero light illumination and a compressive

strain (d) under light illumination, and no strain applied (e) under light illumination and a tensile strain (f) under light illumination and a compressive strain. 150

List of Tables

Table 2-1 Compressed matrix notation. 11

Table 3-1 Calculated strains in the MoS_2 flakes and the related parameters. 66

Table 3-2 Comparison of 3R MoS_2 piezoelectric response with 2D material based PENG devices. 85

Table 4-1 Parameters for calculating the applied strains. 99

Table 4-2 First-order Temperature coefficient χT, and Power coefficient χP extracted from the A_{1g} Raman peak shifts with the strains applied. 106

Table 5-1 Parameters for calculating the applied strains. 129

Table 5-2 Comparison of the characteristic parameters of our present heterojunction devices with other 2D materials-based photo devices. 139

Abbreviations and Symbols

2D/3D	Two/Three dimensional
ADF	Anaular dark-field
AFM	Atomic Force Microscopy
BP	Black phosphorous
C_3N_4	Graphene nitride
CNTs	Carbon nanotubes
CVD	Chemical vapor deposition
DART	Dual AC Resonance-Tracking
DFT	Density functional theory
E-beam	Electron Beam Evaporator
GaN	Gallium nitride
GO	Graphene oxide
h-BN	Hexagonal boron nitride
InN	Indium nitride
In_2Se_3	Indium(III) selenide
InSe	Indium selenide
MEMS	Micro-electromechanical system
MoS_2	Molybdenum disulfide
MPSM	Metal-piezoelectric semiconductor-metal
MS	Metal-semiconductor
MSM	Metal-semiconductor-metal
NLO	Non-linear optics
OPO	Optical parametric oscillator
PbI_2	Lead iodide

PENG	Piezoelectric nanogenerator
PFM	Piezoresponse Force Microscopy
PL	Photoluminescence Spectroscopy
PMs	Piezoelectric materials
PPLN	Periodically poled lithium niobate
PVD	Physical vapor deposition
PVDF	Polyvinylidene fluoride
PZT	Lead zirconate titanate
SAW	Surface acoustic wave
SB	Schottky barrier
SBH	Schottky barrier height
SHG	Second harmonic generation
SnS	Tin(II) sulfide
SiN_x	Silicon nitride
SThM	Scanning thermal microscopy
SPCM	Scanning photocurrent microscopic image
SPM	Scanning probe microscopy
STEM	Scanning transmission electron microscopy
TMDCs	Transition metal dichalcogenides
TMDOs	Transition metal dioxides
vdWs	Van der Waals
WS_2	Tungsten disulfide
WSe_2	Tungsten diselenide
XPS	X-ray Photoelectron Spectroscopy
ZnO	Zinc oxide
d_{eff}	Effective piezoelectric coefficient

D	Electrical displacement
D (superscript)	At constant electric displacement
D_i	Electrical displacement component
E	Electric field
E (superscript)	At constant electric field
E_i	Electric field component
P	Polarization
P_i,P_{pe}	Polarization component
S	Strain
S (superscript)	At constant strain
$S_{ij}, S_p, S_{pe},$	Strain component
T	Stress
T (superscript)	At constant stress
T_i	Traction vector component
t	Thickness
T_{ij}, T_p, T_{pe}	Stress component
u_i, u_j	Mechanical displacement
ε_0	Vacuum permittivity
ε	Dielectric permittivity
χ_{semi}	Electron affinity of semiocnudctor
ϕ_{metal}	Work function of metal
e_{ijk}	e-piezoelectric coefficient tensor
d_{ijk}	d-piezoelectric coefficient tensor
C_{ijkl}	Elastic stiffness tensor
V_{tip}	AFM tip voltage
V_{dc}, V_{ac}	Amplitude of the dc and ac voltage

PR_w	Piezoresponse at a specific frequency of AFM
ω	Frequency
Q	Quality Factor

Chapter 1 Introduction

1.1 Background and Motivation

Nowadays, the demand for piezoelectric devices has been growing very fast since it enables a vast range of applications from energy harvesters to self-powered sensors. In the recently released market research reports, i.e., “Piezoelectric Devices-Global Market Trajectory & Analytics” and “Piezoelectric Smart Materials-Global Market Trajectory & Analytics”, piezoelectric devices and materials are expected to a continuous increase in the future [1, 2], as shown in Figure 1-1. The global market for piezoelectric smart materials, which is currently estimated at around USD 36.5 Billion in 2020, is expected to be double in a market size of USD 83.3 Billion by 2027 to cover, piezoelectric materials, devices and applications. Piezoelectric materials include piezoelectric crystals, ceramics, polymers and composites [3]. Among the markets for piezoelectric devices like sensors, actuators, motors, transducers and generators [4], the market for piezoelectric generators is expected to grow at the highest annual growth rate. On basis of the applications, piezoelectric devices are widely utilized in healthcare, consumer electronics, industrial and manufacturing, automotive, aerospace and defense, and so on [5-7].

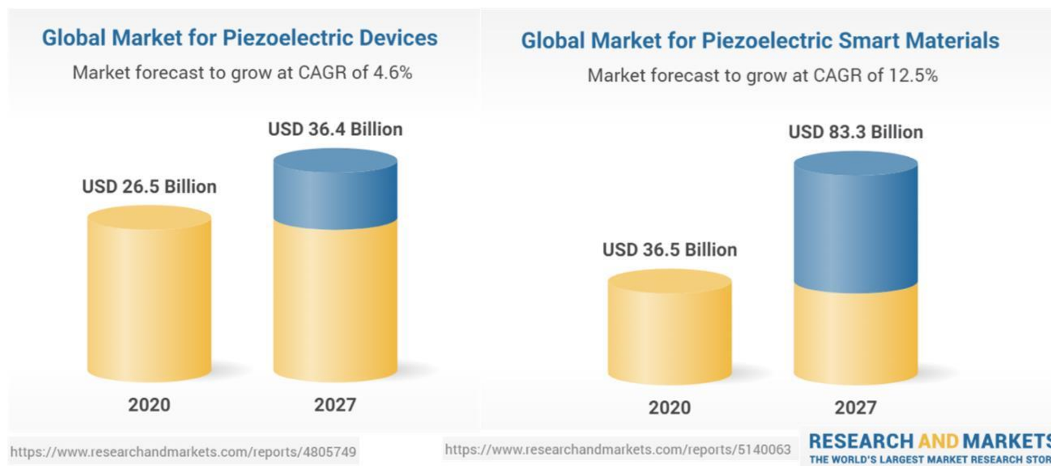

Figure 1-1 Global market for piezoelectric devices and smart materials — a forecast for 2027.

Although conventional piezoelectric materials have already found a broad spectrum of applications, only a few piezoelectric materials are appropriate for specific purpose applications. For instance, flexible and wearable electronics have attracted numerous interests including e-skin, sensors, healthcare monitors and epidermal electronics over the past few years [8-10]. The frontier flexible electronics should endure large strains or stresses with excellent mechanical properties and self-power capabilities to extract energy from the surrounding environment, including human body, like irregular motions, vibrations, etc. [11, 12]. Obviously, piezoelectric materials selection and device design are crucial for flexible and wearable electronics. Recently merging two dimensional (2D) piezoelectric materials (PMs) could satisfy the above high demands of next generation flexible electronics, owing to their large surface ratio, high flexibility, incredible mechanical robustness, and excellent intrinsic electromechanical coupling [13, 14].

Since graphene was discovered in 2004 [15], 2D materials have gained explosive popularity due to their unique electronic, optical and mechanical properties. The 2D materials with piezoelectricity are promising candidates for a vast of applications stated

above. Compared with conventional piezoelectric materials, like quartz, ceramics, PZT, wurtzite materials ZnO and GaN, etc., 2D PMs are of significant advantages in multifunctionality, miniaturization, low power consumption and easily integrated into complex flexible electronics, etc [16, 17]. Recently theoretical studies reveal that 325 potential 2D monolayers with the noncentrosymmetry structure and non-metallic properties are piezoelectric [18]. However, the experimental studies of intrinsic 2D piezoelectric materials at present are limited to several materials, like monolayer 2H-MoS_2, bilayer WSe_2 and α-In_2Se_3, due to the difficulties in the synthesis and piezoelectricity characterizations of 2D PMs [19-21]. The piezoelectricity of 2H MoS_2 is restricted to odd and few atomic layers. In sharp contrast, 3R (3 Rhombohedral) MoS_2, another phase of MoS_2, has been theoretically predicted to be of higher in-plane and out-of-plane piezoelectricity at any thickness. Unfortunately, no experimental studies of the piezoelectricity of 3R MoS_2 flakes, have ever been reported to our best knowledge [22]. No attention has been focused on the coupling effects of the thermal, semiconducting and piezoelectric properties of 2D PMs.

Hence, this Ph.D. project is motivated to explore 2D PMs, especially 3R MoS_2, and the novel devices design for the in-depth understanding of their piezoelectric properties and development of novel piezoelectric devices.

1.2 Objectives

The main objective of this thesis is to study the piezoelectric, semiconducting, thermal and optical properties of several 2D PMs. The research attention is focused on:

- characterizing novel and multifunctional 2D piezoelectric materials, like 3R MoS_2 and α-In_2Se_3, using electrical and optical characterization methods and advanced Piezoresponse Force Microscopy (PFM) technique, etc.
- investigating the thermal conductivity modulation and coupling effect between the heat transport and piezoelectric properties in the metal-piezoelectric semiconductor-metal (MPSM) structure under mechanical stimuli.
- exploring optoelectronic applications of the van der Waals heterojunction built from 2D PMs.

1.3 Major contributions

The contributions of this thesis are mainly on the systematic studies of the piezoelectric properties of 3R MoS_2 flakes and In_2Se_3 flakes, the heat transport through metal/3R MoS_2 flakes/metal under strains and the flexible α-In_2Se_3/3R MoS_2 vdWs p-n heterojunction for photodetection. They are summarized as follows:

- The vertical piezoelectric coefficient d_{33} of multilayer 3R MoS_2 flakes was measured to be around ~ 0.7-1.5 pm/V by a vertical PFM for the first time. The coupling of the in-plane and out-of-plane piezoelectricity was proved using the lateral PFM technique. Two kinds of piezoelectric nanogenerators (PENGs) based on 3R MoS_2 flakes were fabricated and demonstrated larger atomic orientation dependent electrical outputs than previously reported so far. The above results have provided an in-depth physics understanding of the piezoelectric properties of 3R MoS_2 flakes and expanded PMs selection for piezoelectric devices.

- The first experimental observation of strain modulated heat transport through an Au/3R MoS_2 flakes/Au structure, i.e., metal-piezoelectric material-metal (MPSM) structure, was obtained. The heat transport through the MPSM was also systematically studied under various strains and crystalline orientation. These results suggest that heat transport could be significantly modulated through the interface of the MPSM structure, rather than in the intrinsic 3R MoS_2 flakes themselves. This finding may provide a viable heat management strategy for flexible and miniaturized devices.
- The piezoelectricity properties of α-In_2Se_3 flakes were studied using the PFM technique. A high-performance flexible α-In_2Se_3/3R MoS_2 vdWs p-n heterojunction was fabricated for photodetection from the visible to near infrared region. The transport of photon generated carriers is clearly modulated by mechanical strains through the piezoelectric potential at the heterojunction interface. The heterojunction exhibited an ultrahigh photoresponsivity in the near IR and visible range with a much higher sensitivity than most of the other reported 2D heterojunctions so far.

1.4 Thesis organizations

This thesis consists of 6 chapters and it is organized in the following way:

- Chapter 1 presents a brief introduction to the increasing demands for novel PMs and the device designs, especially 2D PMs. The motivations, objectives, and major contributions are stated in the chapter.

- Chapter 2 briefs the fundamental knowledge of piezoelectricity, piezoelectric 2D materials and their fabrication and piezoelectric characterization methods. The state-of-art research of 2D PMs is extensively reviewed.
- Chapter 3 shows the piezoelectricity characterizations of 3R MoS_2 flakes, including the synthesis and devices fabrication of 3R MoS_2 flakes, the methodology and experimental setups. The piezoelectric output and PFM measurement results are analyzed and discussed.
- Chapter 4 discusses the thermal conductivity measurements of intrinsic piezoelectric 3R MoS_2 flakes and the MPSM structure, with detailed device fabrication processes and experimental conditions.
- Chapter 5 demonstrates an α-In_2Se_3/3R MoS_2 heterojunction, which shows a strong photoresponse to the visible and near infrared light. The mechanism of the photocurrent modulation by the strains is proposed.
- Chapter 6 concludes the main findings in this Ph.D. project and recommends some advisory opinions for future research work.

Chapter 2 A review on the 2D piezoelectric materials property and applications

2.1 Fundamental of piezoelectricity

2.1.1 Piezoelectric effect

Piezoelectricity was firstly discovered by brothers Pierre Curie and Jacques Curie, in 1880, who observed electric surface charge in certain materials, especially quartz and Rochelle salt under a stress [23]. This phenomenon is defined as the direct piezoelectric effect of a piezoelectric material, in which electric charges or potential could be generated in response to applied mechanical stress. In the next year, Lippmann predicated, from thermodynamics calculation, that reverse piezoelectric effect should also exist [24], which was experimentally confirmed by the Curie brothers in the following year. That is, when an electric field is applied on piezoelectric materials (PMs), a mechanical deformation or strain is induced [25, 26]. This is known as the reverse piezoelectric effect. Both direct and reverse piezoelectric effects could be observed from piezoelectric materials with noncentrosymmetric crystal structures in corresponding to the applied electrical field or mechanical stress. Currently, the commercial piezoelectric materials are in the form of ceramics, polymers, and crystalline materials, for example lead zirconate titanate (PZT), barium titanate, polyvinylidene fluoride (PVDF), crystalline quartz, $BaTiO_3$, $LiNbO_3$, etc [27, 28]. The piezoelectric materials could be further divided into two groups, the polar (where a net dipole moment depends on the poling direction) and non polar materials (in which a non-total electric dipole moment is determined by the crystal orientations). The above ferroelectric ceramic or polymers are polar piezoelectric materials. On the contrary, several non-ferroelectric semiconductors, like zinc oxide (ZnO) or gallium nitride (GaN) wurtzite-structured

materials, etc., belong to non-polar piezoelectric materials [29]. The direct piezoelectric effect is widely utilized in sensing, energy harvesting and modulating electrical and optical performance of integrated materials and devices, etc. The reverse piezoelectric effect is accountable for fabricating actuators using piezoelectric materials.

In summary, the relationship of the polarization, electric field, stress and strain is illustrated in Figure 2-1a [30]. Piezoelectricity is related to the electrical and elastic behaviors of PMs.

2.1.1.1 Variables related to the mechanical properties:

The variables related to the elastic behavior are introduced here in Einstein notation [31]:

The $\boldsymbol{u_i}$ is the Cartesian components of the infinitesimal mechanical displacement at a point in the material. Strain tensor $\boldsymbol{S_{ij}}$ is determined by the symmetric portion of the spatial gradient of the mechanical displacement and written as:

$$\boldsymbol{S_{ij}} = \frac{1}{2}(\boldsymbol{u_{i,j}}+\boldsymbol{u_{j,i}}) \tag{2.1}$$

where $\boldsymbol{u_{i,j}} = \partial \boldsymbol{u_i}/\partial \boldsymbol{u_j}$, a comma followed by an index denotes partial differentiation with respect to a space coordinate. The traction vector $\boldsymbol{T_i}$ is defined as the force per unit area acting on a surface. The stress tensor $\boldsymbol{T_{ij}}$ is related to traction vector $\boldsymbol{T_i}$ as:

$$\boldsymbol{T_j} = \boldsymbol{n_i}\boldsymbol{T_{ij}} \tag{2.2}$$

where $\boldsymbol{n_i}$ denotes the components of the outwardly directed unit normal to the surface across which the traction vector plays. Evidently, $\boldsymbol{T_{ij}}$ is a second rank Tensor [32].

2.1.1.2 Variables related to electrical field and polarization:

Assuming that the magnetic effects could be negligible compared to electrical effects, the electric field $\boldsymbol{E}$ and electric displacement $\boldsymbol{D}$ are related as:

$$\boldsymbol{D} = \varepsilon_0 \boldsymbol{E} + \boldsymbol{P} \tag{2.3}$$

where $\boldsymbol{P}$ is the polarization vector, and the permittivity of free space ε_0 is 8.854×10^{-12} F/m. The polarization vector is expressed as:

$$\boldsymbol{P} = \varepsilon_0 \chi \boldsymbol{E} \tag{2.4}$$

where χ is the dielectric susceptibility of material and a second rank tensor. Combining equations (2.3) and (2.4),

$$\boldsymbol{D} = \varepsilon_0 \boldsymbol{E} + \varepsilon_0 \chi \boldsymbol{E} = \varepsilon_0\,(1+\chi)\boldsymbol{E} = \varepsilon \boldsymbol{E} \tag{2.5}$$

where ε is the dielectric permittivity of the materials, the relative dielectric permittivity $\frac{\varepsilon}{\varepsilon_0} = 1 - \chi$ is also named the dielectric constant of the material.

2.1.1.3 The basic mathematical formulation for piezoelectric effect:

Based on the linear theory of piezoelectricity [31], the piezoelectric materials exhibit a linear behavior, under a low electric field and mechanical stress levels [33]. When a piezoelectric material is mechanically strained, the generated polarization charges is proportional to external stress can be formulated as:

$$\boldsymbol{P_{pe}} = d \times \boldsymbol{T} \tag{2.6}$$

where $\boldsymbol{P_{pe}}$ is the piezoelectric polarization vector, d is the piezoelectric strain coefficient and $\boldsymbol{T}$ is the stress applied to the piezoelectric materials. For simplifying discussion, the subscript ‘*pe*’ represents the polarization, stress and strain generated by piezoelectric effect. The reverse piezoelectric could be formulated in a similar way as:

$$\boldsymbol{S_{pe}} = d \times \boldsymbol{E} \tag{2.7}$$

where $\boldsymbol{S_{pe}}$ is the mechanical strain raised from reverse piezoelectric effect, $\boldsymbol{E}$ is the applied electric field. Considering the elastic properties of the materials, the direct and reverse piezoelectric effects could be in other forms as:

$$\boldsymbol{P_{pe}} = d \times \boldsymbol{T} = d \times c \times \boldsymbol{S} = e \times \boldsymbol{S} \quad (2.8)$$

$$\boldsymbol{T_{pe}} = c \times \boldsymbol{S_{pe}} = c \times d \times \boldsymbol{E} = e \times \boldsymbol{E} \quad (2.9)$$

where c is the elastic constant connecting the generated stress and the applied strain ($\boldsymbol{T} = c \times \boldsymbol{S}$), s is the compliance coefficient relating the generated strain and the applied stress ($\boldsymbol{S} = s \times \boldsymbol{T}$), and e is the piezoelectric stress constant.

2.1.1.4 Linear piezoelectric constitutive equations and its compressed notation formats:

According to the linear theory of piezoelectricity and conservation of energy [31, 32], the piezoelectric constitutive relations in the extended tensor notation are formulated as:

$$\boldsymbol{T_{ij}} = \boldsymbol{c^{E}_{ijkl}} \times \boldsymbol{S_{kl}} - \boldsymbol{e_{kij}} \boldsymbol{E_{k}} \quad (2.10)$$

$$\boldsymbol{D_{i}} = \boldsymbol{e_{ikl}} \times \boldsymbol{S_{kl}} + \boldsymbol{\varepsilon^{S}_{ik}} \boldsymbol{E_{k}} \quad (2.11)$$

all superscripts represent the quantity under constant electric field, stress or strain. When the material symmetry is considered, the compressed matric notation is adopted, by replacing ij or kl by p or q, where $i, j, k\ and\ l$ take the values 1,2,3, and p or q take the values 1,2,3,4,5,and 6, as shown in Table 2-1.

ij or kl	p or q
11	1
22	2
33	3
23 or 32	4

31 or 13	5
12 or 21	6

Table 2-1 Compressed matrix notation.

Therefore, $\boldsymbol{c_{ijkl}} = \boldsymbol{c_{pq}}$, $\boldsymbol{e_{ikl}} = \boldsymbol{e_{ip}}$, $\boldsymbol{T_{ij}} = \boldsymbol{T_p}$.

By employing the compressed matrix notation, also called as Voigt notation [34], the constitutive equations are written as:

$$\boldsymbol{T_p = c_{pq}^E \times S_q - e_{kp} E_k} \tag{2.11}$$

$$\boldsymbol{D_i = e_{iq} \times S_q + \varepsilon_{ik}^S E_k} \tag{2.12}$$

where $\boldsymbol{T_p}$ is the mechanical stress in *p* direction, $\boldsymbol{c_{pq}^E}$ is the elastic constant tensor at a constant electric field, $\boldsymbol{S_q}$ is the mechanical strain in *q* direction, $\boldsymbol{e_{kp}}$ and $\boldsymbol{e_{iq}}$ piezoelectric stress coefficient constant tensor, $\boldsymbol{E_k}$ is the electric field in *k* direction, $\boldsymbol{D_i}$ is the electric displacement in *i* direction, and $\boldsymbol{\varepsilon_{ik}^S}$ is dielectric constant tensor under constant strain. The constitutive relations defined tensor directions are shown in Figure 2-1b.

Since the stress and strain are related, the constitutive equations could also in the format as:

$$\boldsymbol{S_p = s_{pq}^E \times T_q + d_{kp} E_k} \tag{2.13}$$

$$\boldsymbol{D_i = d_{iq} \times T_q + \varepsilon_{ik}^T E_k} \tag{2.14}$$

where $\boldsymbol{S_p}$ is the mechanical strain in *p* direction, $\boldsymbol{s_{pq}^E}$ is the elastic compliance tensor at constant electric field, $\boldsymbol{T_q}$ is the mechanical stress in *q* direction, $\boldsymbol{d_{kp}}$ and $\boldsymbol{d_{iq}}$ piezoelectric strain coefficient constant tensor, $\boldsymbol{E_k}$ is the electric field in *k* direction, $\boldsymbol{D_i}$

is the electric displacement in i direction, and $\boldsymbol{\varepsilon}_{ik}^{T}$ is dielectric constant tensor under constant stress.

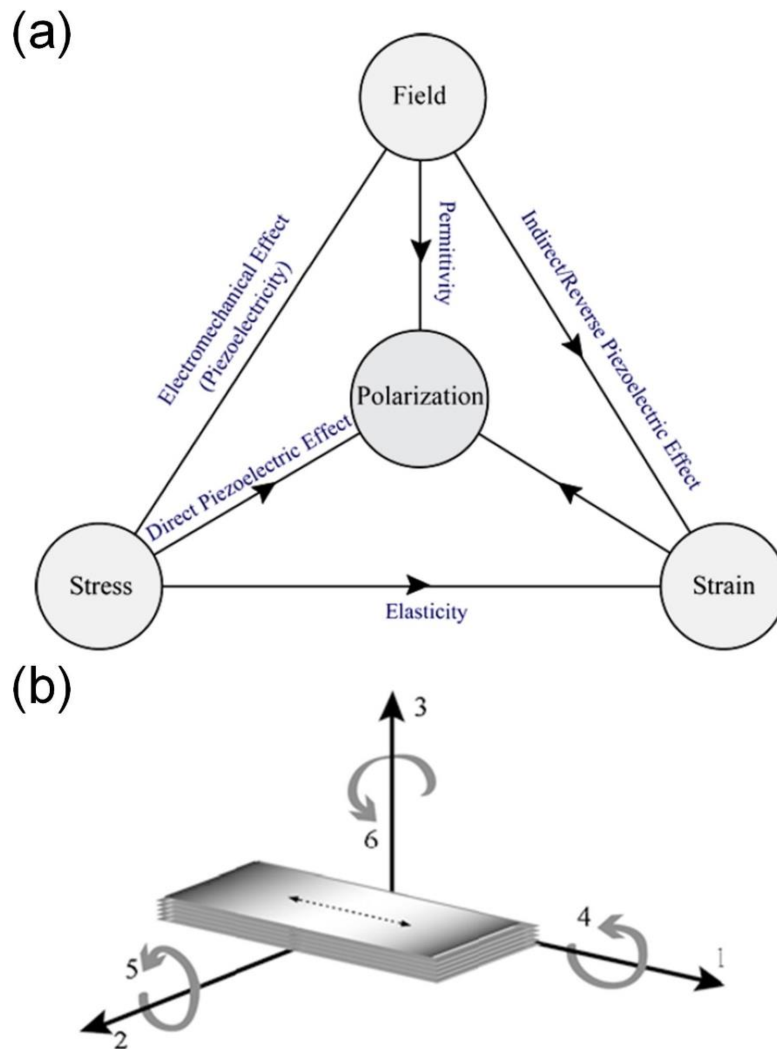

Figure 2-1(a) Piezoelectricity-An interaction of electric field, polarization, mechanical stress and strain. (b) Directions of Tensors in the constitutive equations [1].

2.1.2 Piezoresistive effect

Besides piezoelectric effect, electro-mechanical interactions in certain materials could be accomplished through piezoresistive effect, which was first applied by Cookson in 1935. Piezoresistive effect refers to electrical resistivity change, not electric potential

change, in a metal or semiconductor under an applied mechanical strain [35]. When the piezoresistive materials are applied with a voltage and mechanical strain, the induced current changes as a consequence of the change in the resistance, in accordance to Ohm's law: $R = \rho l/A$, where ρ is the material resistivity, l is the material length and A is the cross sectional area [36]. The change in resistance, which is relative to the strain and resistivity, is described by Gauge factor:

$$GF = \frac{\Delta R/R}{\varepsilon} = 1 + 2v + \frac{\Delta\rho}{\rho} \tag{2.15}$$

where ε is the strain, v is Poisson's ratio, $\Delta R/R$ is relative resistance change. The relative change in resistance is related to the geometric effects 1+2v and the relative resistivity change $\Delta\rho/\rho$. It was found that the strain Gauge factor of germanium and silicon is two orders of magnitude larger than that of metals, showing several semiconductors are of stronger piezoresistivity [37, 38]. Due to larger piezoresistive effect, piezoresistive semiconductors have been widely used, especially in the application of mechanical sensors. This kind of piezoresistive effect based sensors is defined as "active sensors" and are different from "passive sensors", in which spontaneous electric signal is generated under exerted forces without applying a voltage [39].

To explain the large semiconductor piezoresistive effect, the prevailing theories are based on the description of carrier transport change in strained crystalline structures. When the strain is applied, the crystal symmetry is reduced and lattice constants are modified, resulting in a change in the energy bands (shifting, warping or bending). These factors, including non-uniform density of states, changes in electrons mass and energy band, contribute to the carrier mobility changes [40, 41].

2.1.3 Electronic and optoelectronic device performance modulated by strains or piezoelectric potentials

Strains induce piezoelectric potentials which in turn could significantly affect the performance of electronic and optoelectronic devices based on piezoelectric materials. These phenomena were later called the piezotronic and piezo-phototronic effects by Wang in 2007 [42] and 2010 [43]. As illustrated in Figure 2-2, the three-way couplings of piezoelectric, semiconducting and optoelectrical give rise to the piezotronics, optoelectronics and piezo-phototronics. The piezotronic effect utilizes the inter piezoelectric potential as a "gate" to tune or control the charge carrier transport at the interfaces of metal/semiconductor or semiconductor/semiconductor contacts. The wurtzite structure materials, like ZnO, InN and GaN, have been widely used in the piezotronic devices, representing a wide range of potential applications in active electronics, micro-electromechanical system (MEMS) and sensors, etc. [44, 45]. The piezo-phototronic effect utilizes the piezo polarization charges to modulate the generation, transport, separation and/or recombination of photoexcited carriers at a p-n junction or Schottky contact, which successfully improves the performance of optoelectronic devices, like photodetectors, LEDs and solar cells [46-48].

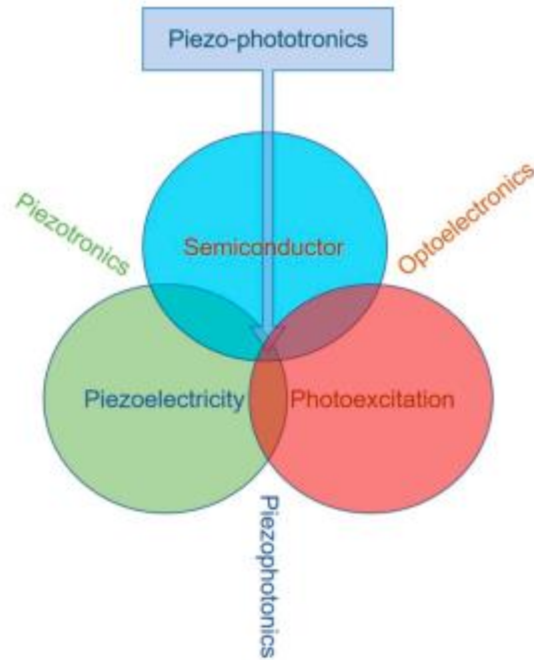

Figure 2-2 The relationship of three effects between piezoelectricity, semi-conductivity, and photo-excitability [49].

In Figure 2-3, the energy band diagram of the metal-semiconductor Schottky contact is plotted under strains, for better understanding of the mechanism of piezotronic effect. Here, the n-type piezoelectric semiconductor with a much smaller electron affinity is in contact with the metal with a higher work function ($\chi_{semi} < \phi_{metal}$). A depletion range is formed in the semiconductor near the interface and the Schottky barrier (SB) results in an abrupt discontinuity at the interface. If an external voltage applied on the two terminals of metal and semiconductor is larger than a critical value, electrons could pass through the barrier and flow from the metal into the semiconductor. Assuming that negative piezoelectric polarization charges are generated near the metal-semiconductor (MS) interface under a compressive strain, the negative piezoelectric polarization charges could repel electrons away from interface, causing an increase in the height of the SB (SBH) and a broaden depletion range. On the contrary, the positive piezoelectric

polarization charges are formed near the interface under a tensile strain, resulting in a lower SBH and a reduced depletion range. Consequently, the charge carriers transport through the MS interface and contact characteristics are effectively modulated by the piezoelectric polarization charges, or more specifically, the applied strains [50, 51].

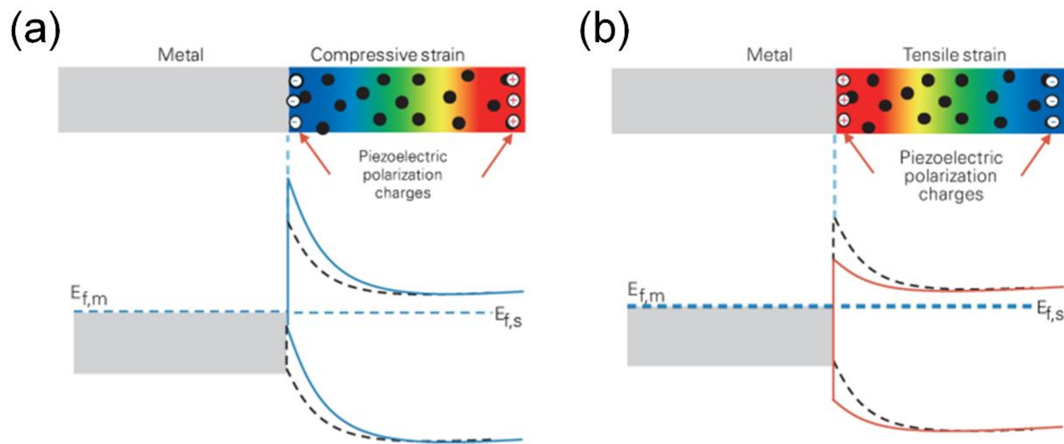

Figure 2-3 Schematic of piezotronic effect on a Schottky junction at a metal-semiconductor interface under (a) compressive strain and (b) tensile strain [51].

In Figure 2-4, when an n-type piezoelectric semiconductor is contacted with a p-type semiconductor, electrons in the n-type side and holes in the p-type side diffuse into the opposite side, creating charge depletion range near to the junction and formation of a p-n junction. The ionized donors and acceptors are then left behind after the diffusion process to induce a built-in electric field. The electric field drives charged carriers moving in the opposite of the diffusion, till the diffusion current is balanced with the drift current and a thermal equilibrium is reached. Considering that the positive piezoelectric polarization charges are generated near the junction interface under a strain, the positive piezoelectric polarization charges attract electron from the p-type side, causing the trapping or accumulation of electrons. The energy band is lowered down at the junction interface, which might promote the electron-hole recombination.

Oppositely, under a reverse strain, negative piezoelectric polarization charges are generated near the junction interface and they repel electrons from the n-type into p-type, causing a steeper energy band profile at the interface so that electron-hole recombination is suppressed.

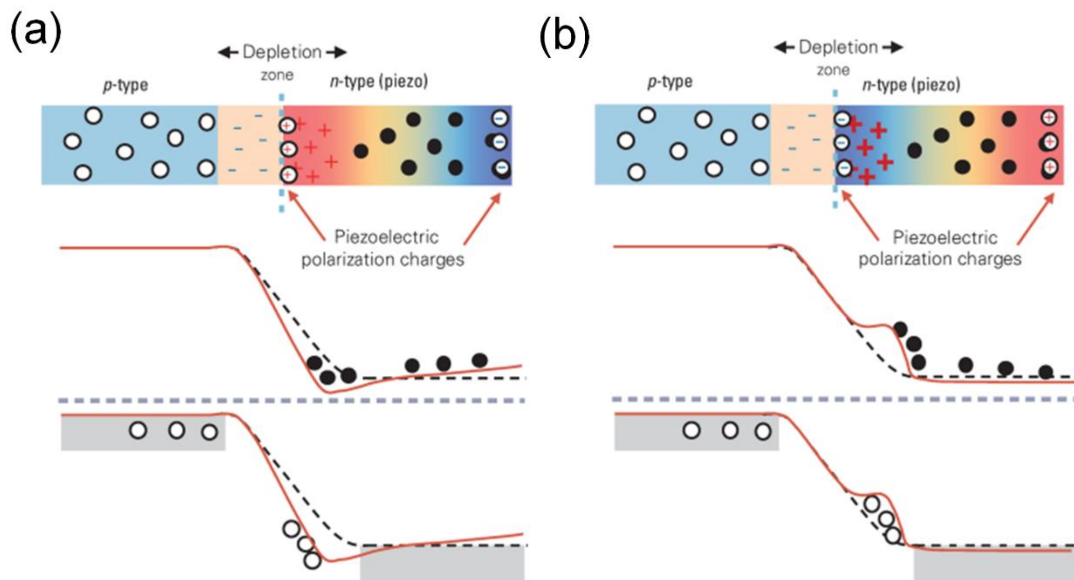

Figure 2-4 Schematic illustration of the piezo-phototronic effect on a p-n junction. The presence of (a) positive and (b) negative piezoelectric polarization charges at the interface [51].

2.2 Piezoelectric 2D materials and their piezoelectric properties

The first reported piezoelectric nanogenerator (PENG) was fabricated using nanoscale wurtzite material, ZnO nanowires in 2006 [52]. Motivated by this innovative work, research on piezoelectricity has been focused on nanoscale configurations of piezoelectric three dimensional (3D) materials with wurtzite structure. However, it is difficult to implement 3D wurtzite materials into integrated applications due to their inhomogeneous behaviors, when these materials are scaled down into nanoscale [53].

In 2014, the piezoelectricity of single layer MoS_2 were observed by *Wu et al* [19] and *Zhu et al* [54] separately and independently using different characterization methods. After that, the searching for 2D PMs and their applications attract much attention. Several 2D PMs, including hexagonal boron nitride (h-BN), transition metal dichalcogenides (TMDCs), groups III and IV monochalcogenides, group III-IV chalcogenide material, and chemically modified graphene, are indeed of unique piezoelectric properties as evidenced by theoretical simulations and experimental approaches [14, 17, 35, 55, 56].

2.2.1 Intrinsic piezoelectric 2D materials

The simplest crystal of 2D PMs is h-BN, which has been predicated with planar piezoelectric polarizations in stable planar hexagonal nanostructure [57, 58]. The theoretical piezoelectric coefficient e_{11} of h-BN is estimated around 120 pC/m [59]. The second harmonic generation (SHG) was applied on atomically few layers h-BN. Strong SHG intensity from monolayer to few odd layers was observed, while no SHG signal from even layers could be detected [60]. The SHG results suggest a non-centrosymmetric structure of h-BN flakes and the existence of piezoelectricity indirectly. [61].

The most promising 2D piezoelectric material is hexagonal transition metal dichalcogenides (2H-TMDCs), where 2H represents the Ramsdell notification for the AB stacking sequence, including MoS_2, WS_2 and WSe_2 et al [62]. For the bulk 2H-TMDCs, they are not piezoelectric in multilayers, because symmetry structure of stacking sequence in a top-to-tail configuration [63]. When the 2H-TMDCs are thinned down few atomic layers and monolayer, they reveal piezoelectric property, owing to the

non-centrosymmetric structure and loss of the inversion center. Here, we adopt monolayer MoS_2 (m-MoS_2) as an example to describe the piezoelectricity of 2H-TMDCs. The m-MoS_2 crystal is of the structure of D_{3h} symmetry, where one layer of Mo is sandwiched between two layers of S, formed into a hexagonal lattice. When an external electric field is applied from S atom to Mo atom, in asymmetrical rhombic prismatic unit cell, the Mo-S bonds are stretched and accumulated to generate internal piezoelectric polarization charges shown in Figure 2-5a. The m-MoS_2 thus has an in-plane piezoelectricity and no out-of-plane piezoelectricity due to its symmetry structure along the z-axis perpendicular to in-plane. The superimposed lattice orientation of CVD growth m-MoS_2 was confirmed from SHG measurement and plotted, shown in Figure 2-5b. To detect the piezoelectricity of m-MoS_2, an m-MoS_2 flake on a flexible substrate was fabricated for direct strain testing, shown in Figure 2-5c [19]. Another device of a free-standing m-MoS_2 was fabricated for exploring piezoelectricity by applying horizontal electric field at the two terminals of m-MoS_2 flake. The resulted vertical piezoelectric vibration $\Delta\sigma_p = -e_{11}E_1$ was monitored by an atomic force microscope (AFM) tip, as illustrated in Figure 2-5d [54]. This measurement excludes the substrate effects like doping and parasitic charges. The piezoelectric stress $\Delta\sigma_p$ should be in linear relationship with applied driving voltage, and the piezoelectric coefficient of e_{11} was measured around 2.9×10^{-10} C m^{-1}. The piezoelectric coefficients were measurable for the monolayer and three layers, but not for the double layers, as shown in Figure 2-5e, f. From the theoretical simulations and calculations, piezoelectric coefficients of TMDCs should be larger than that of h-BN and 3D wurtzite structure materials [59, 64].

Similar to TMDCs, the piezoelectricity properties of transition metal dioxides (TMDOs) with chemical formula MX_2 have been theoretically investigated using first principles calculation based on density functional theory (DFT). Besides Mo-based or W-based

materials, the other materials with M= Cr, Ti and Zr (X= O, S, Se, Te) also exhibit strong piezoelectricity, especially $CrTe_2$ with the largest in-plane piezoelectric coefficients and TiO_2 with comparable e_{11} values with Mo-based TMDCs [65].

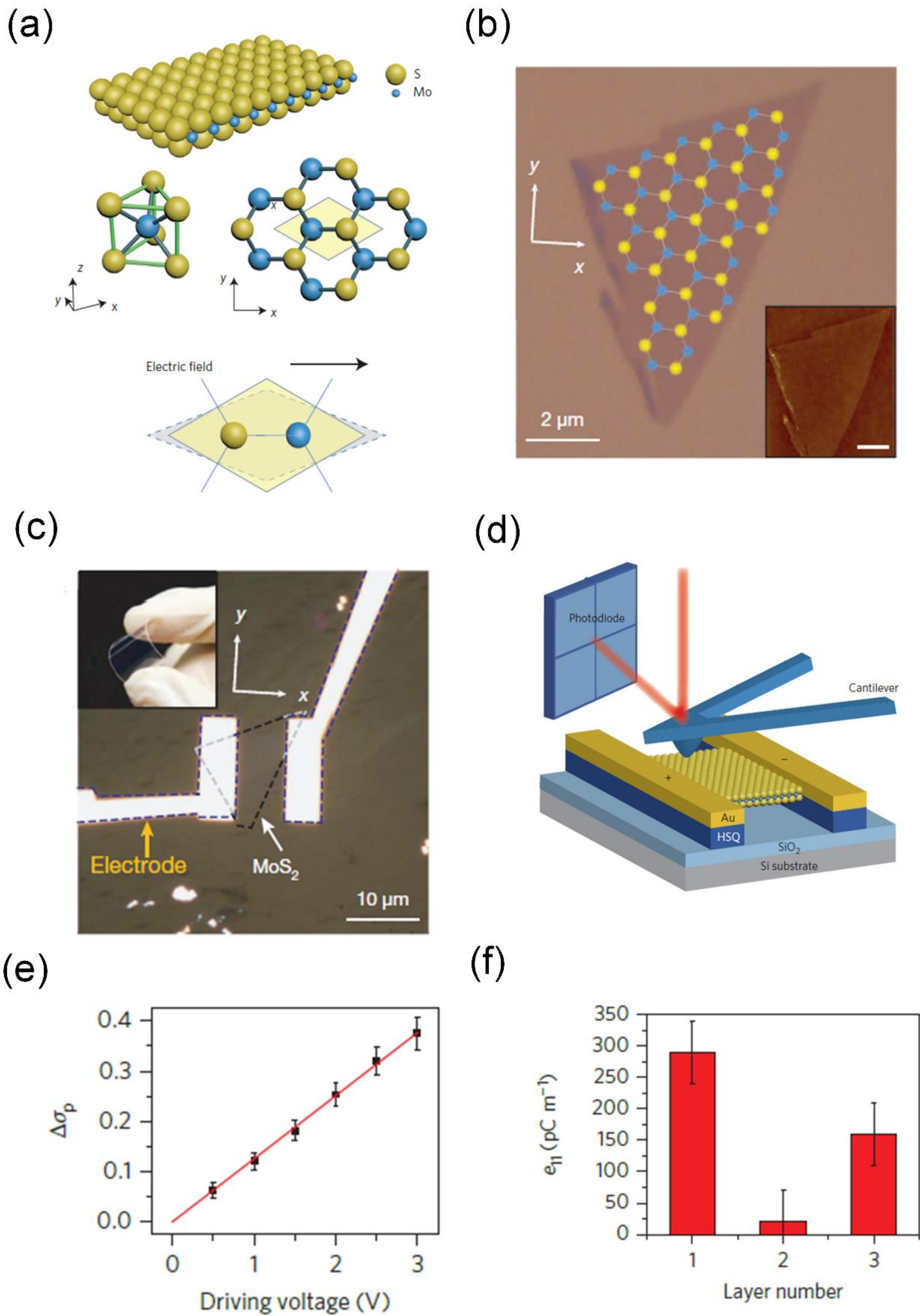

Figure 2-5 (a) Schematic of an atomic structure of monolayer MoS_2. (b) Optical image of monolayer MoS_2 with lattice orientation confirmed from the SHG. (c) Optical image of a flexible MoS_2 PENG [19]. (d) Schematic of the experiment setup for probing the piezoelectric property of a MoS_2 flake. (e) Measured piezoelectric stress vs increasing driving voltage and (f) Calculated piezoelectric coefficient e_{11} of one layer, two layers and three layers of MoS_2 [54].

Another group of 2D PMs is group III monochalcogenides, such as GaS, GaSe and InSe. As depicted in Figure 2-6a, the structure of group III monochalcogenides GaS is similar to that of 2H-TMDCs and both groups are D_{3h} point group symmetry. The two metal layers are sandwiched between two chalcogen layers. The group III monochalcogenides therefore are piezoelectric due to non-centrosymmetric structures and possess same order of magnitude of piezoelectricity with h-BN and MoS_2 monolayers. The theoretical piezoelectric coefficients of monolayer GaS, GaSe and InSe are 2.06, 2.30 and 1.46 pm/V [66], respectively.

Although h-BN and MoS_2 are promising piezoelectric materials, their piezoelectric coefficients are relatively small and the mechanical to electrical conversion rate is only about 5% [19]. One group of 2D materials, group IV monochalcogenides (M= Sn or Ge, X= Se or S), was verified with anisotropic and enhanced giant piezoelectricity property by *Fei et al* [67]. Based on the theoretical DFT calculations, the piezoelectric coefficients d_{11} of group IV monochalcogenides (e.g. GeS, GeSe, SnS and SnSe are 75.43, 212.13, 144.76 and 250.58 pm/V, respectively) are about two orders larger than that of 2D PMs, like h-BN and 2H-TMDCs. The C_{2v} symmetry puckered structure, shown in Figure 2-6b, contributes to giant piezoelectricity by softening themselves along armchair direction. In addition, there is zero piezoelectric coefficient along zigzag direction, owing to the mirror symmetry. The piezoelectric effect in group IV

monochalcogenides was also confirmed in another work, in which the electronic structures were studied [68]. Recently, large area monolayer SnS, fabricated using a liquid metal-based technique, has been measured out a large piezoelectric coefficient of 26 pm/V through a piezoresponse force microscope (PFM). The PENG based on the SnS showed a maximum output voltage of 150mV at 0.7% strain [69].

The 2D group III-V honeycomb monolayers are non-centrosymmetric in the D_{3m} point group, with the polar axis perpendicular to the in-plane monolayer [70], shown Figure 2-6c. This unique bucked structures results in non-zero e_{11}, e_{31}, d_{11} and d_{31} piezoelectric coefficients, and these theoretical values are slightly smaller than that of m-MoS_2 [71].

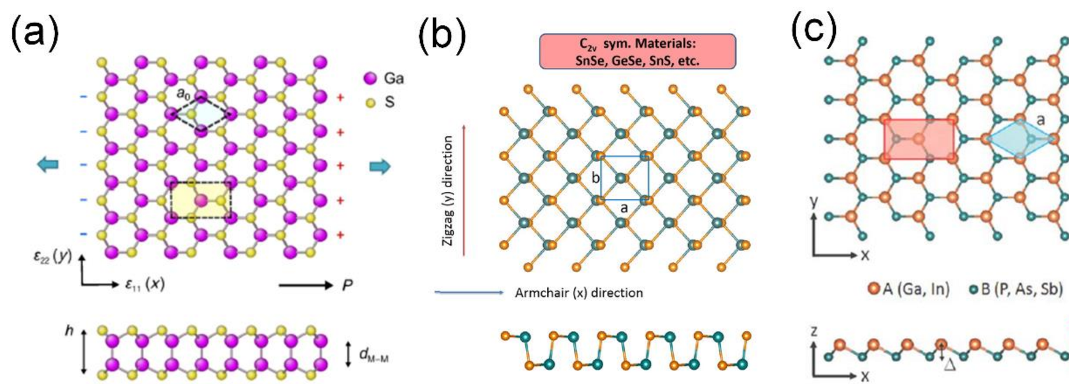

Figure 2-6 Atomic structure of (a) group III monochalcogenides GaS [66] (b) C_{2v} orthorhombic group IV monochalcogenides [67] (c) group III-V buckled honeycomb monolayers in top and side views. Reproduced from [71].

Black phosphorous (BP) is 2D materials with strong in-plane anisotropy in the optical, electrical, thermal and mechanical properties [72, 73]. The piezoelectricity coefficient d_{11} of BP is estimated around -9.48 pm/V, resulted from the linked and non-centrosymmetric structure [74].

Another theoretical reported 2D family materials, Janus MXY (M= Mo or W, X/Y = S, Se or Te) monolayer with in-plane or multilayer with out-of-plane piezoelectricity using *ab initio* calculations [75].

In addition to the materials discussed above, an attractive material In_2Se_3 of the group III-VI chalcogenide material has been widely theoretical and experimental proved with in-plane and out-of-plane piezoelectricity and ferroelectricity in α and β phases, due to its unique atomic structure [76-79].

2.2.2 Engineering modified 2D materials with piezoelectricity

Graphene is the first mechanical exfoliated 2D materials, with a planar sheet of sp^2 bonded carbon atoms in a honeycomb structure, and thus non-piezoelectric material intrinsically [80]. To make graphene into piezoelectric materials, several engineering methods are implemented, including coaxing, chemical doping or alternative graphene based materials [81-83].

One of the methods is to create holes in the dielectric graphene nanoribbons, shown in Figure 2-7a. When a strain is applied on graphene with triangular shaped holes, a non-zero piezoelectric polarization charges should be induced due to the symmetry broken holes [81]. Chemical doping is the most common method to functionalized graphene into a piezoelectric material [82, 84-86]. The famous flexoelectric response of graphene is realized by doping its surface with various atoms, shown in Figure 2-7b. Besides, several alternative graphene based materials, like graphene nitride (C_3N_4) and graphene oxide (GO), also behave piezoelectric response under strain [83, 87, 88]. In Figure 2-7c, the graphene nitride nanosheet shows a non-centrosymmetric pores structure and its piezoelectric coefficient e_{11} is estimated around 0.758 C/m^2.

A fascinating study of doped piezoelectric graphene was accomplished by placing single layer graphene on a trenched SiO_2 substrate [89]. An apparent vertical piezoelectricity was probed by AFM tip and the piezoelectric coefficient was measured around 1.4 nm/V, which is much larger than values of other reported 2D PMs. The strong piezoelectric response is originated from the interactions between carbon atoms in graphene and oxygen atoms in SiO_2, which induces dipolar surfaced states.

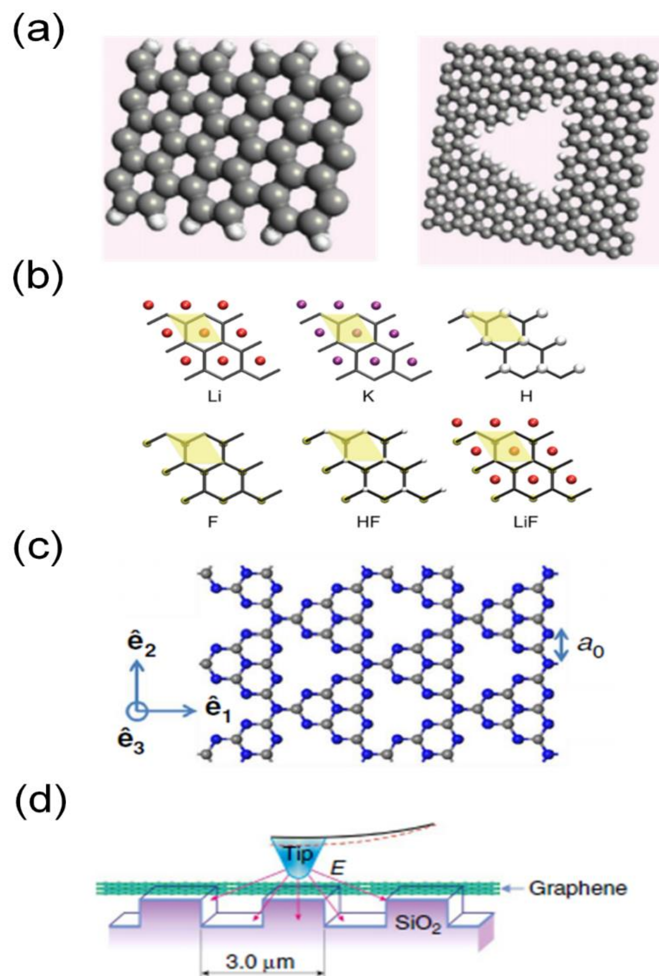

Figure 2-7 (a) Pristine graphene and graphene sheet with triangular hole [81] (b) Various chemical doped graphene [82] (c) atomic layer of tri-s-triazine [83] (d) Graphene supported on trenched SiO_2 substrate [89].

2.2.3 Piezoelectric coefficients of 2D piezoelectric materials

To describe 2D PMs piezoelectric effect, the basic mathematic formulas of piezoelectric coefficient are deduced according to their atomic symmetry structure and linear piezoelectricity theory. Here, the derivation of piezoelectric coefficients of 2H-TMDC of D_{3h} point group is introduced here as an example [90, 91]. The linear piezoelectric effect could be considered as a first order relations between polarization $\boldsymbol{P_i}$, the stress $\boldsymbol{T_{jk}}$ or strain $\boldsymbol{S_{jk}}$ tensor in the following relationship:

$$\boldsymbol{d_{ijk}} = \frac{d\boldsymbol{P}_i}{d\boldsymbol{T_{jk}}} \tag{2.16}$$

$$\boldsymbol{e_{ijk}} = \frac{d\boldsymbol{P_i}}{d\boldsymbol{S_{jk}}} \tag{2.17}$$

The third rank piezoelectric tensors $\boldsymbol{e_{ijk}}$ and $\boldsymbol{d_{ijk}}$ are related:

$$\boldsymbol{e_{ijk}} = \boldsymbol{d_{ijk}C_{jjkl}} \tag{2.18}$$

Where $\boldsymbol{C_{ijkl}}$ is the elastic stiffness tensor, i, j, k and l take the values 1,2,3. For the D_{3h} point group materials, like h-BN and 2H-TMDCs, only one d- and one e-coefficient need to be considered due to the uniqueness raised from the symmetry structure. By adopting the Voigt notation to reduce the number of the indices, the allowed non-zero piezoelectric d-coefficient and e coefficients are [34, 59]:

$$\begin{gathered} d_{111} = d_{11} \\ d_{122} = d_{12} = -d_{11} \\ d_{212} = d_{221} = \frac{1}{2}d_{26} = -d_{11} \\ e_{111} = e_{11} \\ e = e_{12} = -e_{11} \\ e_{212} = e_{221} = e_{26} = -e_{11} \end{gathered} \tag{2.19}$$

For the monolayer 2H-TMDC, the d_{11} and e_{11} are related as:

$$d_{11} = \frac{e_{11}}{C_{11} - C_{12}} \tag{2.20}$$

2.2.4 Influential factors on the piezoelectric properties

Through extensive investigations of 2D PMs have been conducted for several years, several factors that influence the piezoelectric properties, including the periodic trends, crystal orientation direction and diameter/layer number, are discussed here. This discussion provides an in-depth understanding of 2D PMs and a principal guide in choice of piezoelectric materials and design of novel piezoelectric devices.

2.2.4.1 Periodic trend dependence:

The major periodic trend is a well-known phenomenon for materials, in aspects of ionization energy, electron affinity and ionic radius *et al*. Based on theoretical simulation, the piezoelectric properties of compound 2D PMs also follow the periodic trend [62, 67], as illustrated in Figure 2-8. It is observed that piezoelectric coefficients for the 15 kinds of 2H-TMDCs become larger, when the TM elements move upward or the dichalcogenides elements move from left to right, until the piezoelectric coefficient d_{11} of $CrTe_2$ reaches to 13.5 pm/V in Figure 2-8a. It also highlights that a good linear proportionality between the piezoelectric coefficient d_{11} and the ratio of the anion and cation polarizabilities α. The higher piezoelectric coefficient d_{11} is achieved for larger anion and smaller cation combination, which might be attributed to the amplification of e_{11} due to smaller difference of elastic stiffness coefficients C_{11} and C_{12}, shown in Equation 2.12 [59]. The hexagonal group III-V and group IV monochalcogenides also obey this periodic trend, shown in Figure 2-8b, c [62, 67]. In addition, the group II-VI SC monolayers d_{11} follow a similar trend proportional not only to the anion and cation,

but also to the product of the Bader charge and the lattice parameters, see Figure 2-8d,e [62].

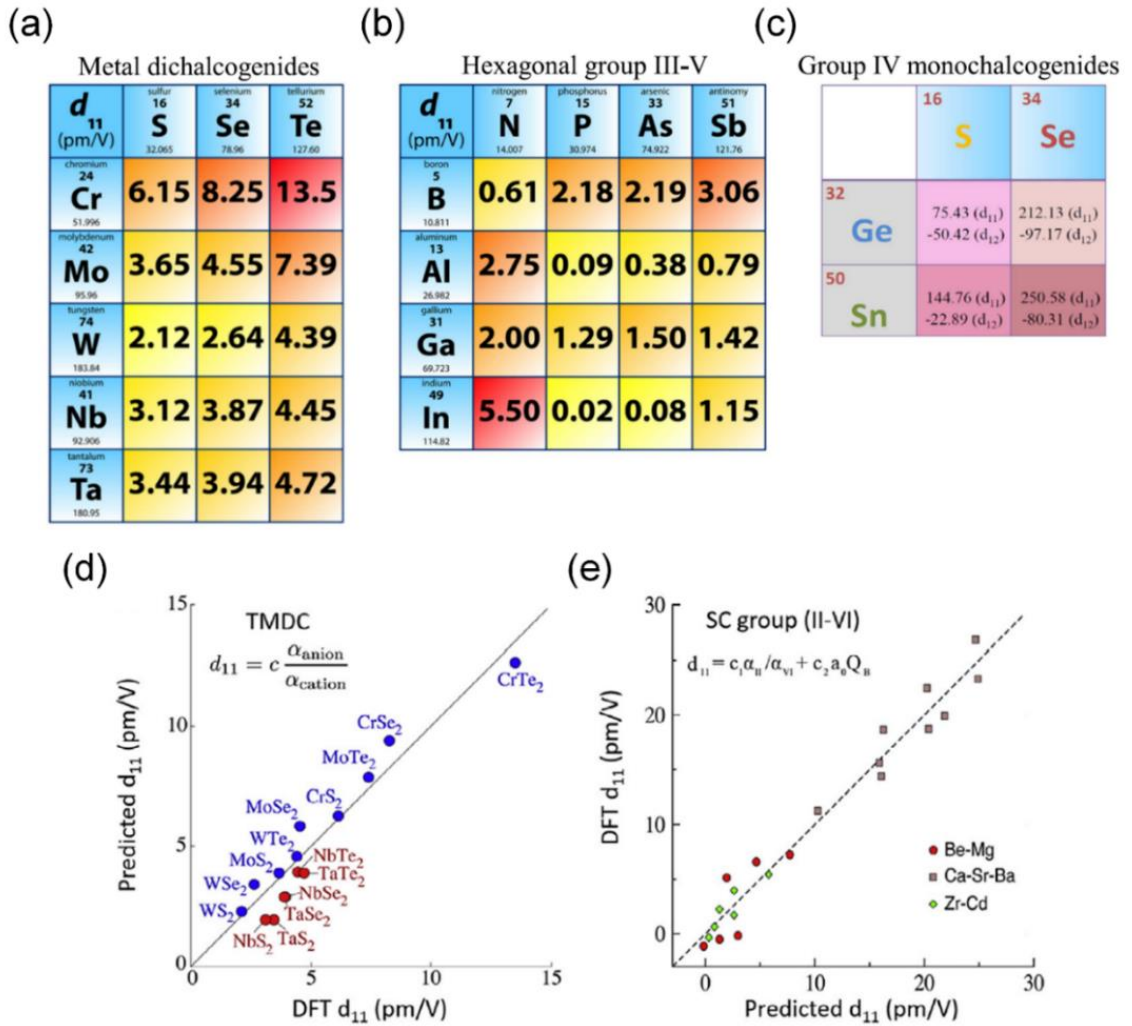

Figure 2-8 Periodic trends for d_{11} in (a) metal dichalcogenides, (b) Hexagonal group III-V, (c) Group IV monochalcogenides [62]. Proportional trend between the piezoelectric coefficient d_{11} (d) of TMDC and (e) group II-VI SC monolayers [67].

2.2.4.2 Polarization direction and crystal orientation dependence:

Polarization charges are generated at piezoelectric materials by application of an electric field or a mechanical strain. The polarization direction could be coupled with the electric field and mechanical strain direction, and described with axes number 1,2 and 3,

corresponding to the x, y and z directions. The piezoelectric 2D materials could be categorized with the polarization directions as in-plane, out-of-plane or both. Besides, crystal orientation and atomic structure of materials also play role in the polarization charges generation, and render the materials with in-plane anisotropy piezoelectric properties.

The h-BN could be either in the form of nanosheets or nanotubes, in which the tube chirality is described by the chiral angle θ, as displayed in Figure 2-9a. When the electric field is applied along the zigzag direction, only the axial polarization will be generated with an axial piezoelectric coefficient e_{xx}. While, the electric field applied on the armchair direction gives rise to a shearing polarization and a shearing (or torsional) piezoelectric coefficient e_{xy} for h-BN nanosheets and nanotubes [92]. From theoretical simulation, the h-BN nanostructure with chirality $0° < \theta < 30°$ will have both axial and shearing piezoelectricity, and the axial piezoelectric coefficient e_{11} and shearing piezoelectric coefficient e_{14} fit the following relations [92]:

$$\begin{aligned} e_{11} &= e_{xx} \sin(3\theta) \\ e_{14} &= e_{xy} \cos(3\theta) \end{aligned} \tag{2.21}$$

From the experiments, the crystal orientation dependent piezoelectricity has also been found on the monolayer MoS_2, which show reverse signs of output piezoelectricity under different strains applied along armchair and zigzag directions [19]. Another experiments showed that piezoelectric coupling strength of m-MoS_2 is angular-dependence, from $0° < \theta < 60°$, shown in Figure 2-9b [54]. This similar crystal orientation dependence is also observed on the Group IV monochalcogenides [67]. As introduced above, some modified 2D materials exhibit out-of-plane piezoelectricity, like graphene on a SiO_2 substrate [89]. The material α-In_2Se_3 shows both in-plane and out-of-plane piezoelectricity, owing to its atomic structure [77].

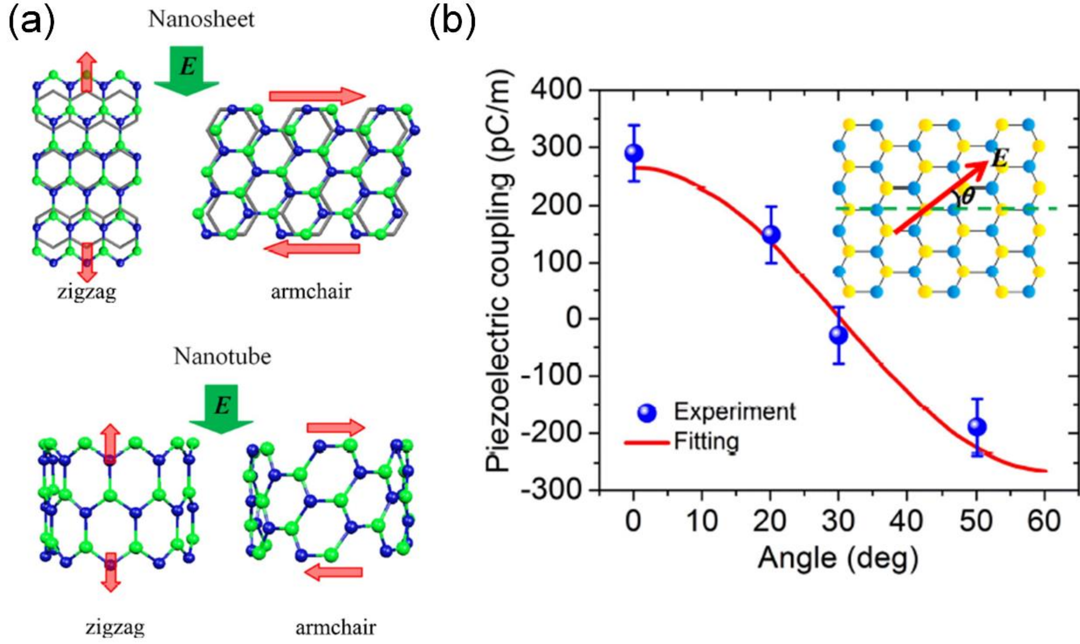

Figure 2-9 (a) Electric field induced deformation of h-BN nanosheet and nanotube [92]. (b) Measured piezoelectric coupling strength of m-MoS_2 as a function of crystal orientation [54].

2.2.4.3 The nanotube diameter and layer number dependence:

The h-BN and h-ZnO nanotubes are piezoelectric materials, which could be considered as a result of rolling up nanosheets. It is found that the piezoelectric coefficients of h-ZnO and h-BN nanotubes build a linear and inverse relationship with the diameter and square of the diameter, respectively [93, 94], as shown in Figure 2-10a.

Based on theoretical studies, the multilayer h-BN have piezoelectricity in odd layers and non-piezoelectricity in even layer, due to its AA' stacking symmetry. The piezoelectric coefficient e_{11} of odd layers h-BN decrease with increased layers, shown in Figure 2-10b, and fit the equation as [95]:

$$e_{11} = \frac{e_{11}^{1}}{N} \tag{2.22}$$

where e_{11}^{1} is the piezoelectric coefficient of monolayer h-BN nanosheet with a value of 1.38×10^{-10} C m^{-1} [59].

Multilayer 2H-TMDCs materials are centrosymmetric without piezoelectricity at even layer number and non-centrosymmetric with piezoelectricity at odd layer number. The m-MoS_2 PENG devices proved this layer number dependence well shown in Figure 2-10c, where piezoelectric currents were generated at odd-layered samples. Overall, the piezoelectricity or piezoelectric coefficients are decreased with increasing layer numbers.

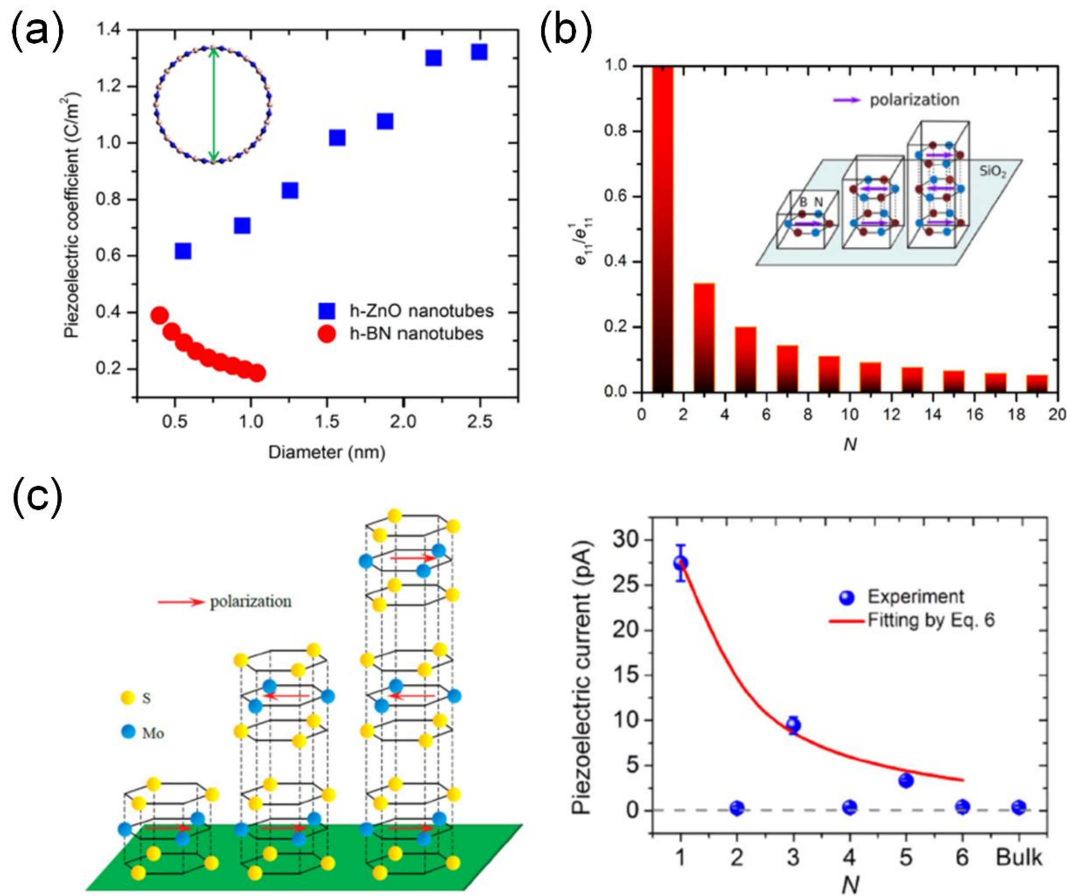

Figure 2-10 (a) Piezoelectric coefficient of h-BN and h-ZnO vs their diameter [93, 94]. (b) Piezoelectric coefficient of h-BN nanosheets as a function of the layer number *N*. (c) The output piezoelectric current of m-MoS_2 PENG device [19].

2.3 Fabrication and characterization methods of piezoelectric 2D materials

2.3.1 Fabrication of 2D piezoelectric materials

Up to now, fabrication of 2D materials could be categorized into two major approaches, i.e., “top-down” and “bottom-up” [96]. Much attention and effort are put into the fabrication of large-area, high-quality 2D materials. In this section, the fabrication of 2D PMs is discussed.

2.3.1.1 Mechanical exfoliation

The mechanical exfoliation, in which an adhesive tape is adopted to split the bulk layered materials into mono or few layers, is a general “top-down” method. It was first applied to obtain graphene in 2004. Since then, this method has been widely used in fabricating 2D materials, like h-BN, TMDCs, etc. to achieve high quality crystalline and clean surfaces of the materials. To overcome the disadvantages of low production efficiency and small yields, several derivative methods are developed like mechanical cleavage, mechanical force/ion intercalation or exchange-assisted liquid phase exfoliation, etc. [96]. The liquid shear-exfoliation of MoS_2 nanosheets in an aqueous surfactant solution was demonstrated using a blender [97]. Inspired by and taking advantage of the piezoelectric property of bulk TMDCs, microfluidic nebulization with high frequency acoustic waves placed the layered TMDCs under a combination of a larger mechanical stress and electric field and exfoliated them into high yield mono and few layer nanosheets shown in Figure 2-11a [98]. This method was further improved by using surface acoustic wave (SAW) device, and an extraordinary monolayer yield of 58% was achieved [99].

2.3.1.2 Vapor phase deposition

Vapor phase deposition belongs to the "bottom-up" approach, in which the desired compounds in vapor gaseous form are deposited onto a specified substrate to form a good coverage and uniformity atomically thin layer or flake. Chemical vapor deposition (CVD) and physical vapor deposition (PVD) are the two main techniques to be employed in this approach. Due to precise control of thickness and convenient for the integration of van der Waal heterostructures (vdWs), CVD has been extensively used to fabricate 2D PMs, like MoS_2, WS_2 and WSe_2 [96]. In 2002, the CVD growth of large area few layer MoS_2 was firstly achieved on a variety of insulating substrates by *Li et al*, shown in Figure 2-11b [100]. An insulating layer was immersed into the $(NH_4)_2MoS_2$ solution, following by a two-step annealing process in a homemade furnace system. Various 2D PMs could also be prepared through PVD process, and here the synthesis of 2D In_2Se_3 is taken as an example. The first controlled growth of mono and few layers In_2Se_3 was reported by *Lin et al* [101]. They successfully deposited atomically thick In_2Se_3 on various substrates, like graphene and mica, by using PVD technique. After controlling the cooling rate and improving growth condition, *Zhou et al* achieved high-quality growth of monolayer In_2Se_3 for the first time, as shown in Figure 2-11c. The Raman and PL signals suggested that 2D In_2Se_3 is not only a good candidate for the piezoelectric application but also a suitable choice for the optoelectronics [102].

2.3.1.3 Liquid metal-based synthesis

For some 2D PMs including $GaPO_4$, In_2Se_3 and SnS, it is difficult to fabricate using conventional synthesis method, like mechanical exfoliation, etc. Especially for the monolayer SnS, the exfoliation process is hindered by strong interlayer forces caused by the long-pair electrons of S, which are much stronger than vdWs forces [103]. A novel liquid metal-based technique was reported to synthesis larger area and

homogenous monolayer SnS by *Khan et al*, as shown in Figure 2-11d [69]. A molten droplet of Sn is exposed to an atmosphere containing a Sulphur source at 350°C. According to the self-limiting Cabrera-Mott reaction, a sulphide skin is formed at the Sn droplet surface. Then, the ultrathin SnS nanosheets are exfoliated onto a specific substrate from the ultra-smooth liquid metal surface. Similar to the monolayer SnS synthesis process, piezoelectric $GaPO_4$ was also synthesized using the liquid metal-based technique and subsequently phosphatized process. First, thin layer Ga_2O_3 skin that forms on the surface of liquid gallium, is transferred onto desired substrates. The Ga_2O_3 nanosheets are then phosphatized by a chemical vapor reaction using phosphoric acid. The vertical piezoelectricity d_{33} of 2D $GaPO_4$ was measured to be around 7.5 pm/V using PFM, in consistent with the theoretical DFT calculations [104].

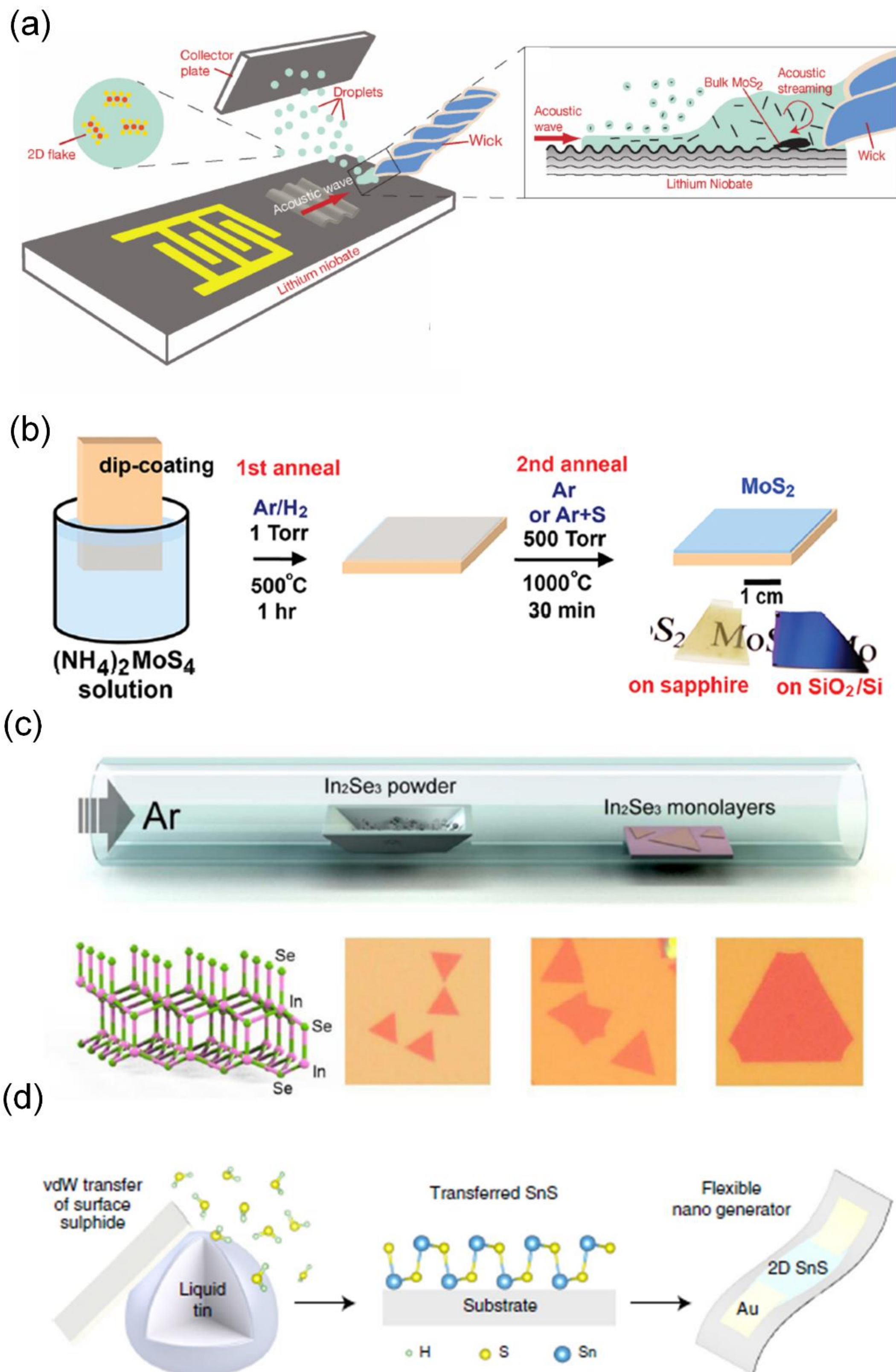

Figure 2-11 Schematic illustration of (a) liquid exfoliation of quasi-2D materials using acoustic waves [98], (b) CVD method for the synthesis of MoS_2 thin layers [100], (c)

PVD process of In_2Se_3 synthesis, the crystal structure and optical image of In_2Se_3 monolayer or flakes [102], (d) liquid metal assisted synthesis of monolayer SnS and its application on a nanogenerator transducer [69].

2.3.2 Characterization methods

Generally, a variety of methods have been employed to study the piezoelectric properties of 2D materials from macroscale to nanoscale. The experimental techniques, including PFM, SHG and direct strain testing, are reviewed and discussed here. By utilizing various methods, it is possible to build a full and comprehensive picture of piezoelectric 2D materials, which could enhance our understanding of piezoelectric properties in nanoscale and provide insights into new applications.

2.3.2.1 Piezoresponse force microscope (PFM)

Piezoresponse force microscope (PFM) is a powerful and direct technique for observing piezoelectric and ferroelectric response from piezoelectric or ferroelectric material, for its advantages such as simple sample preparation and scanning operation, fast scanning, high resolution and non-destructive to the samples [105]. The basic physical principles of PFM mapping and several examples of PFM mapping on 2D materials are discussed as follows.

In conventional PFM, the conductive AFM tip is in contact with the sample surface and monitors the mechanical deformation i.e. surface volume change generated by an applied ac bias voltage on the tip. This working mechanism is based on the reverse piezoelectric effect mentioned before. The conductive AFM tip here plays two important roles: one as an actuator to allow electric field interacted with the sample surface in nanoscale, another as a sensor to measure the piezoelectric response by monitoring the

cantilever mechanical vibration, as displayed in Figure 2-12a. The voltage on the tip is described as [106]:

$$V_{tip} = V_{dc} + V_{ac}\sin(\omega t) \quad (2.23)$$

Where ω and t are the frequency of the ac voltage and time, V_{dc}, V_{ac} are the amplitudes of the dc and ac components. The cantilever displacement resulted from piezoelectric response is:

$$z = z_{dc} + A(\omega, V_{dc}, V_{ac})V_{ac}\sin(\omega t) \quad (2.24)$$

When tip voltage is driven at a frequency below that of the contact resonance of the cantilever, it is further expressed as:

$$z = d_{33}V_{dc} + d_{33}V_{ac}\sin(\omega t) \quad (2.25)$$

where d_{33} is the typical vertical component of the piezoelectric tensor, a direct coupling among the vertical piezoelectric response, applied electric field and vertical motion of the cantilever [107]. Not only the vertical component information provided by tip vibrations, the cantilever could also detect the lateral mechanical deformation, like torsion or bending shown in Figure 2-12b,c. Both vertical and lateral piezoelectric response therefore could be mapped by PFM, with a proper calibration process of vertical and lateral PFM signals. This approach is termed as vector PFM, allowing construction of 2D polarization with the in-plane and out-of-plane components [108]. The measured piezoresponse could be generally written as:

$$PR_w = d_{eff}V_{ac}\sin(\omega t) \quad (2.26)$$

where PR_w and d_{eff} are the piezoresponse at a specific frequency and effective piezoelectric coefficient, respectively.

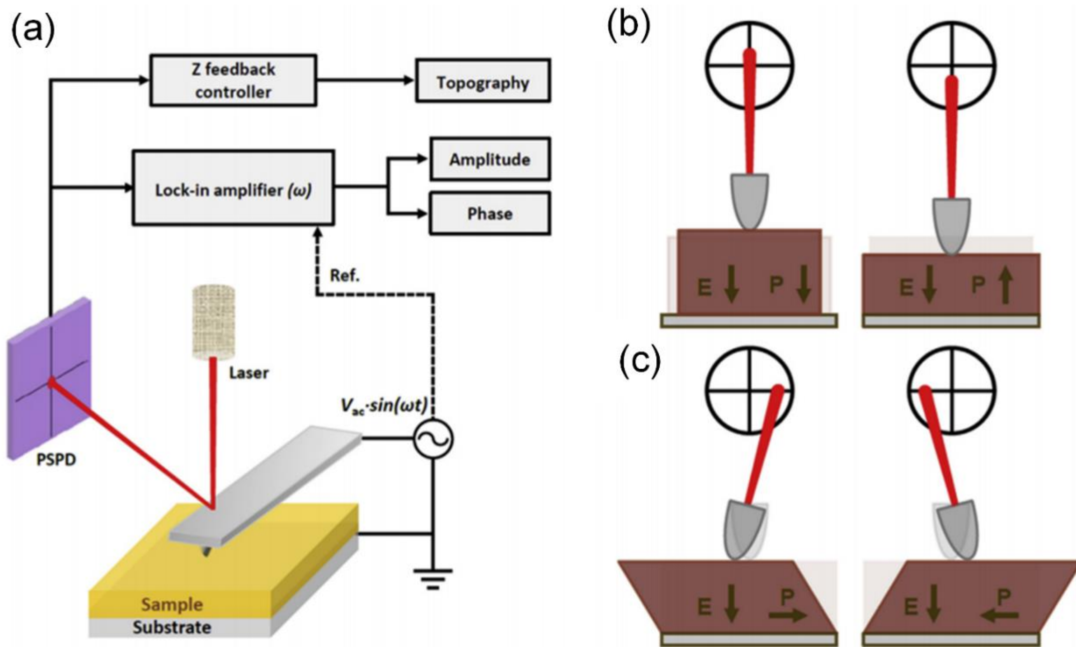

Figure 2-12 Schematic of (a) single frequency PFM set up, and working principles of (b) vertical PFM (c) lateral PFM. Reproduced from [109].

The conventional PFM still faces various challenges and issues, like surface parasitic charges, image construction and difficulty in precise data interpretation. To distinguish real piezoresponse from artifacts and get comprehensive information from the PFM mapping, several advanced modes of PFM, like vector PFM, resonance-enhanced PFM, switching spectroscopy PFM and Band-excitation PFM, have been developed [108, 110-112]. One important resonance-enhanced PFM, Dual AC Resonance-Tracking (DART) PFM mode, is frequently used in characterizing the materials with intrinsically weak piezoelectric properties, i.e. 2D PMs, for its superior sensitivity by improving several orders of magnitude of piezoresponse [77, 113].

Bulk MoS_2 shows no response to any strain or electric field applied vertical on its surface, owing to symmetry structure. However, there exists flexoelectricity that arises from strain gradient in contrary to uniform strain in m-MoS_2. In Figure 2-13a, the vertical

PFM was used to measure the out-of-plane piezoresponse of m-MoS_2 using a vectorial background subtraction technique [114]. The measured effective out-of-plane piezoelectric coefficient, d_{33}^{eff}, was estimated around 1.03 pm/V on an Au/Si substrate and 1.35 pm/V on Al_2O_3/Si. The out-of-plane PFM measurement was also performed on monolayer Janus MoSSe in Figure 2-13b, from which the out-of-plane piezoelectric coefficient was estimated around 0.1pm/V [115]. In Figure 2-13c, vertical and lateral PFM images of a multilayer α-In_2Se_3 flake were displayed, which proves the coexistence of out-of-plane and in-plane piezoelectricity in α-In_2Se_3 from monolayer to multilayer. Another enhanced and advanced PFM technique adopted a lateral excitation scanning probe microscopy (SPM) to directly measure the piezoelectric response of atomically thin WSe_2 on a substrate [116]. A pair electrodes deposited on the two terminals of the WSe_2 provides in-plane stimuli and result in out-of-plane piezoelectric response due to Poisson's effect, which could be probed by the SPM tip. The vertical PFM amplitude images of ultrathin CdS films, were abstained using single and DART PFM in Figure 2-13d. The out-of-plane effective piezoelectric was estimated as high as 33 pm/V [117].

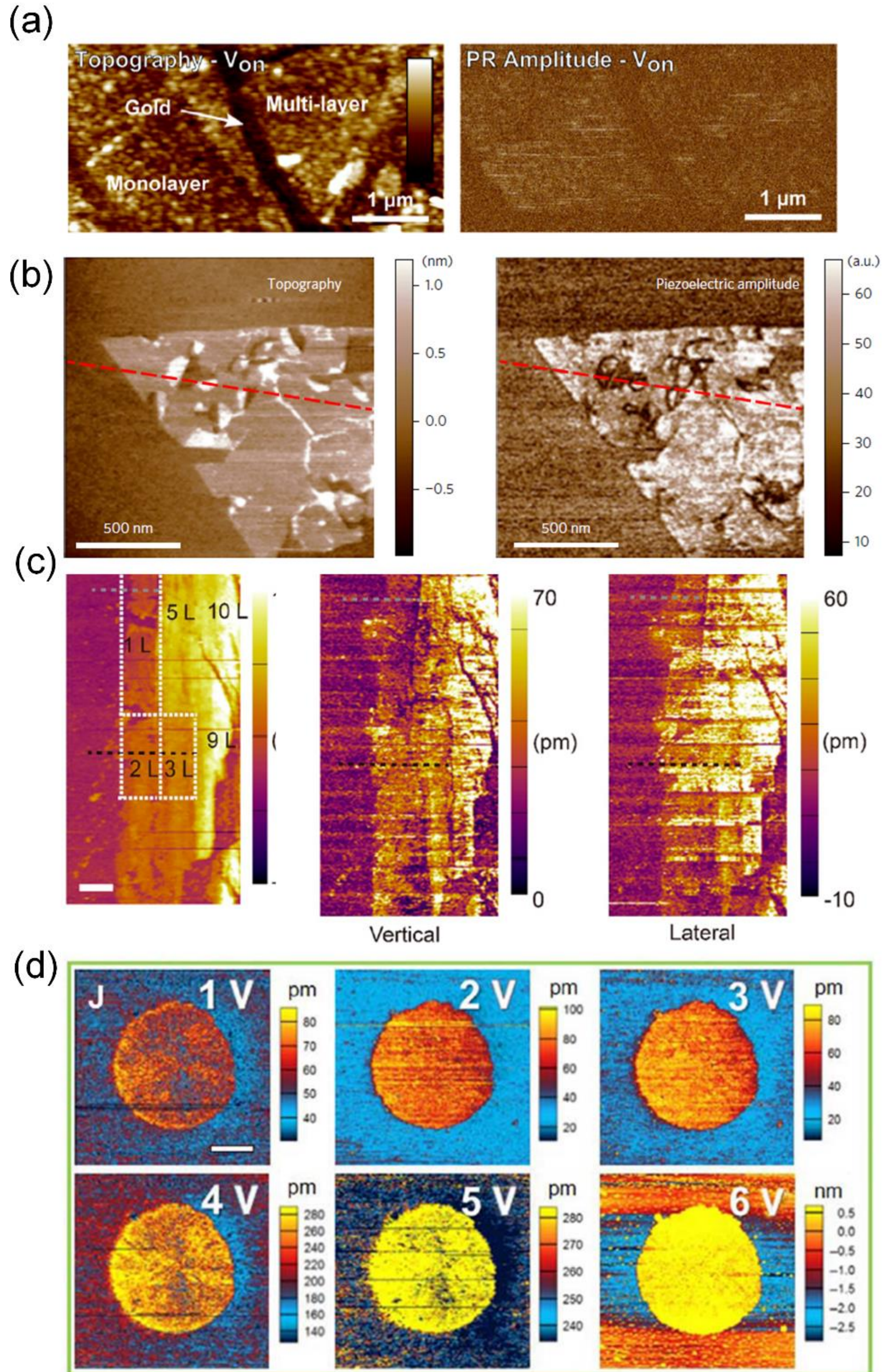
(a)
Topography - Von
Gold
Multi-layer
Monolayer
1 µm
PR Amplitude - Von
1 µm
(b)
Topography
(nm)
1.0
0.5
0.0
−0.5
500 nm
Piezoelectric amplitude
(a.u.)
60
50
40
30
20
10
500 nm
(c)
5 L
10 L
1 L
9 L
2 L
3 L
70
(pm)
0
60
(pm)
-10
Vertical
Lateral
(d)
J
1 V
2 V
3 V
4 V
5 V
6 V
pm
nm

Figure 2-13 Topography, PFM amplitude images of (a) monolayer MoS_2 [114], (b) monolayer Janus MoSSe [115], (c) Multilayers α-In_2Se_3 [77], (d) Vertical PFM amplitudes images with tip voltages from 1 to 6V [117].

2.3.2.2 Second harmonic generation (SHG)

Second harmonic generation (SHG) is the most fundamental non-linear optics (NLO) process, in which one photon with certain frequency (ω) is interacted with nonlinear materials, resulting in a generation of output photon with double frequency and half the wavelength of the incident photons, as illustrated in Figure 2-14a [118]. The SHG occurs in the materials with non-symmetry crystalline structures and nonzero nonlinear susceptibility tensors. The SHG therefore is a powerful and sensitive tool for the characterization of piezoelectric and ferroelectric materials, especially in the field of layered 2D materials with broken inversion symmetry [55]. It could provide the crystalline orientation of the 2D materials.

In 2013, *Malard et al* reported an observation of highly efficient SHG from odd layers 2H MoS_2 flakes and presented a method for imaging the underlying crystalline structure, which revealed the broken symmetry atomic structure [119], displayed in Figure 2-14b. This SHG results from layered 2D PMs were confirmed on h-BN and MoS_2 with one to five layers. In Figure 2-14c, the six-fold polarization dependence patterns were characterized for both h-BN and MoS_2 [60]. Different from 2H MoS_2, 3R (3 Rhombohedral) MoS_2 possesses broken inversion symmetry from monolayer to bulk, regardless of the thickness. The SHG polar plots and lattice pattern are displayed in Figure 2-14d, demonstrating that 2D 3R MoS_2 is a promising nonlinear optical and piezoelectric material [120]. Inspired by the excellent SHG results and due to lack of systematical and comprehensive study, we put our efforts into the piezoelectric

properties and related application study of 3R MoS_2. In addition, the α-In_2Se_3 also showed six-fold SHG pattern from the exfoliated and PVD growth flakes [79].

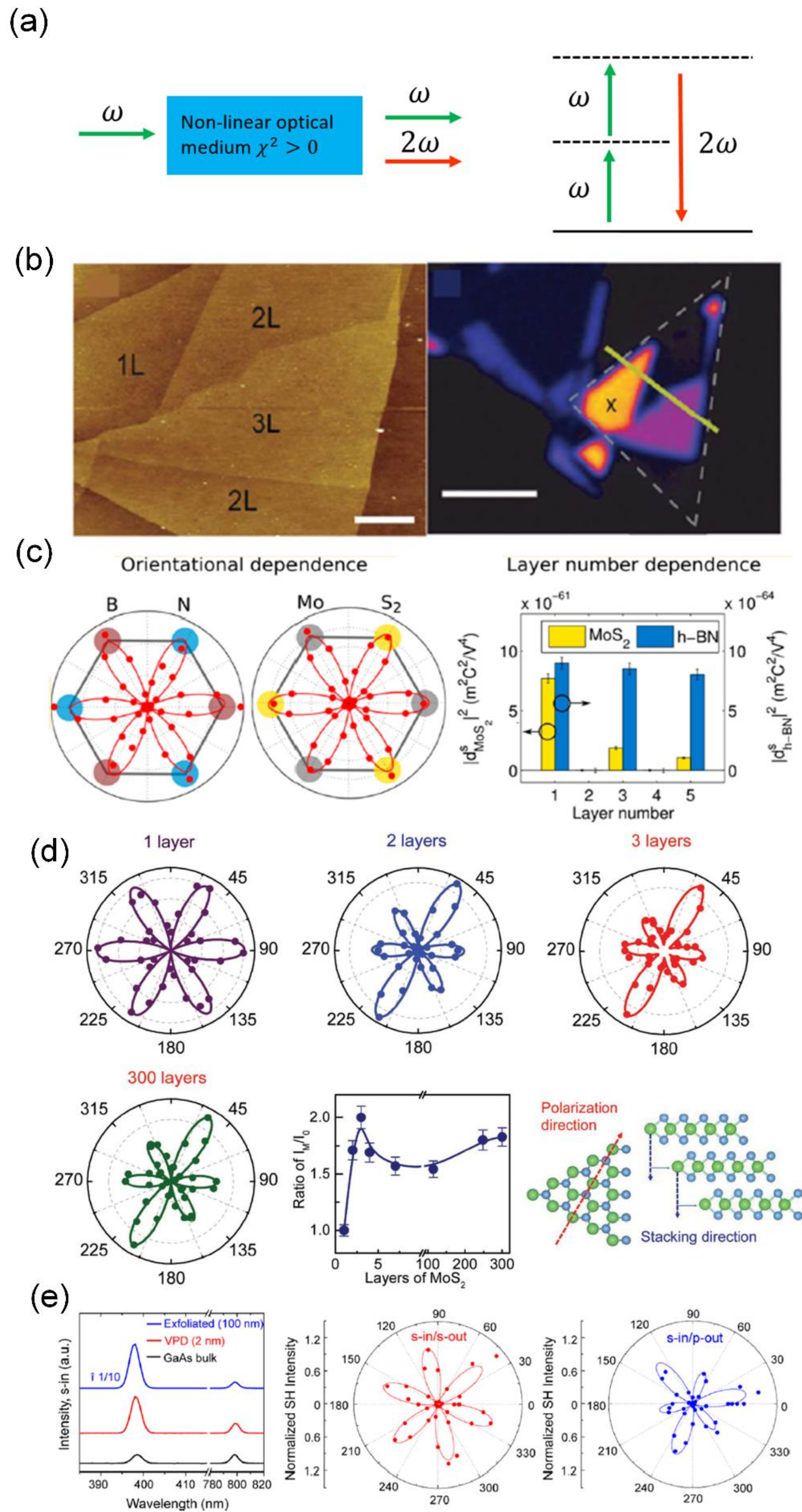

Figure 2-14 (a) Schematics of the SHG mechanism. (b) Topography and SHG intensity mapping of mono, two and three layers MoS_2 [119]. (c) SHG polar plot of h-BN and MoS_2 and SHG intensity vs layer number from one to 5 layers [60]. (d) SHG intensity polar plots of monolayer, bilayers, triple layers and bulk 3R MoS_2, integrated polarization contrast of the SHG signal in the parallel for various thickness 3R MoS_2 and its lattice structure [120]. (e) SHG spectral insensitivity reflected from exfoliated α-In_2Se_3, PVD growth α-In_2Se_3 and bulk GaAs and SHG polar plots of PVD growth α-In_2Se_3 and exfoliated α-In_2Se_3 [79].

2.3.2.3 Direct strain testing

Direct strain testing, or called lateral bending testing, is the most straightforward way to observe piezoelectricity by measuring generated electric potential or charge under a tensile or compressive strain on 2D nanostructures. It requires an ultrasensitive low current/voltage measurement setup, due to the low amplitudes of output voltages or currents.

In the direct strain testing, a 2D material nanostructure is generally laid on a flexible substrate, while two electrical contacts are fabricated at the two terminals of the material, connected to a current preamplifier for current acquisition. The piezo polarization charges could be induced by the strain owing to the piezoelectric effect and therefore determined from the acquired current. The fabricated devices can also function as mechanical to electrical energy harvesters or/and self-power sensors. From *Wu et al's* experiments shown in Figure 2-15a and b, the m-MoS_2 devices were applied strains through stretching and releasing, which induced an oscillating current and voltage. Both the current and voltage presented positive outputs when a tensile strain was applied along the x direction (armchair), and negative outputs when a tensile strain was applied along the y direction (zigzag) [19]. Due to the symmetry of the D_{3h} point group of

monolayer MoS_2, the piezoelectric polarization charges P_1 along the x axis could be written as:

$$P_1 = e_{11}(\varepsilon_{11} - \varepsilon_{22}) \quad (2.27)$$

where ε_{11} and ε_{22} are strain along x and y axis. This equation well interprets the dependency of the strains on the piezoelectric polarization direction. In contrary to the strain direction testing for m-MoS_2, the positive current occurred at multilayer α-In_2Se_3 when a stretching strain was applied along both x or y direction as shown in Figure 2-15c [77]. No evident dependency between the strain and piezoelectric polarization direction is observed in multilayer α-In_2Se_3, most likely due to the coupling of in-plane and out-of-plane piezoelectricity [77]. Another form of strain testing was done on CVD growth triangular m-MoS_2 device, and the strain was provided by placing AFM tip on the m-MoS_2. The strain was provided by placing an AFM tip on the m-MoS_2. The current was observed an increasing trend and decreasing trend under a compressive and tensile strain, respectively, as shown in Figure 2-15d. These opposite trends were probably caused by the locally strain-induced piezoelectric polarization charges, which may alter the interfaces barrier height [121].

(a)

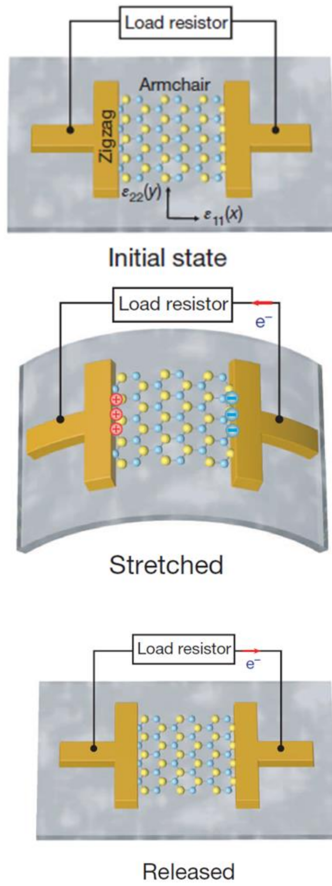

(b)

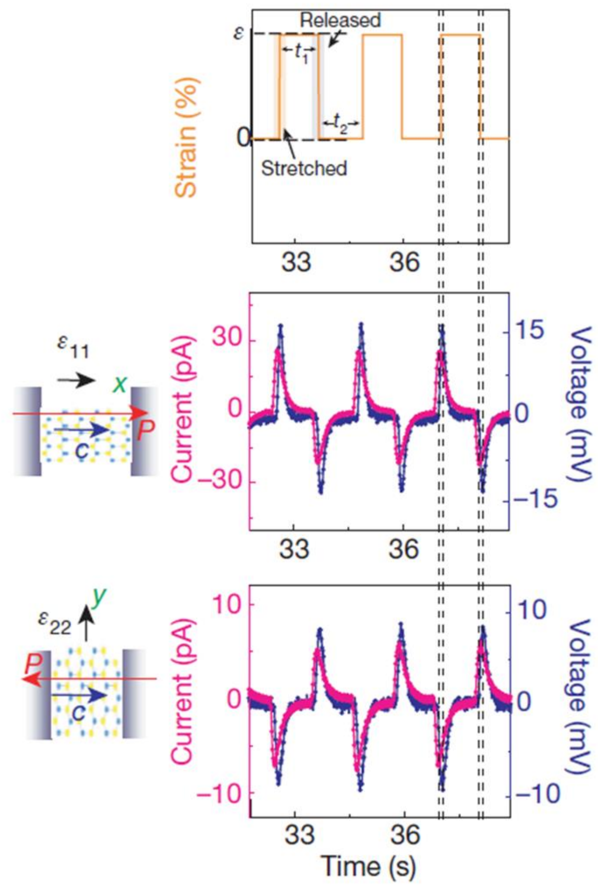

(c)

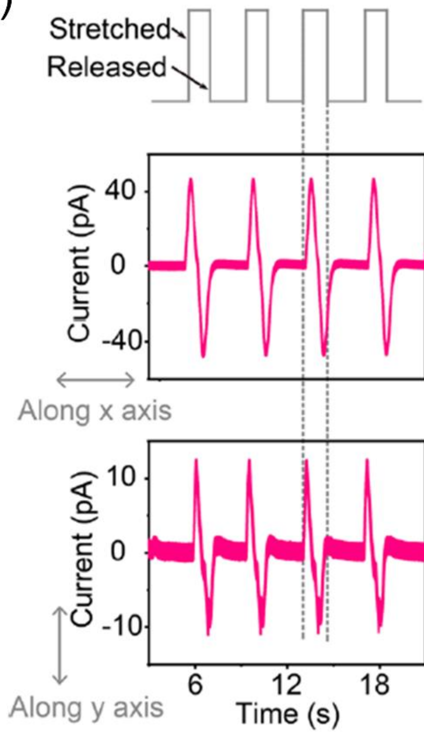

(d)

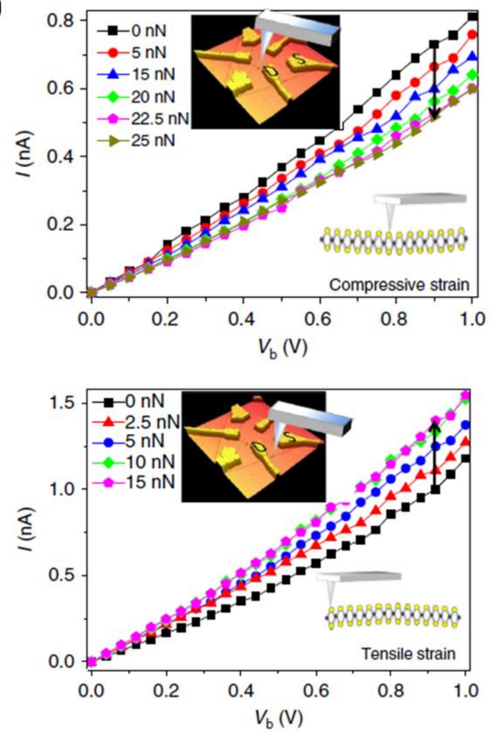

Figure 2-15 (a) Schematic of a direct strain testing setup, (b) Output voltages and currents of an m-MoS_2 device [19]. (c) Output currents of a multilayer α-In_2Se_3 device [77]. (d) *I-V* curves of the CVD MoS_2 device at different forces under compressive and tensile strain [121].

2.3.2.4 Characterization of thermal conductivity

Till now, the coupling effects among piezoelectricity, semi-conductivity, and photo-excitability have been studied extensively. Few theoretical and experimental studies pay attention to the coupling effect between heat transport and piezoelectric properties. Thermal conductivity measurement at nanoscale of 2D materials is important and useful for thermal management yet challenging. The challenges are from handling tiny samples, poor accuracy of temperature measurement at nanoscale and complex experimental set ups and devices fabrication processes. Several methods have been reported till now, including optothermal Raman method, suspended pad method, time-domain thermoreflectance (TDTR), scanning thermal microscopy (SThM), etc [122-125].

Optothermal Raman method utilizes a laser light beam as a heat source. When the light beam is focused on a 2D material flake, a radial temperature gradient in the basal plane of the flake is generated, as shown in Figure 3-17a. *Balandin et al.* firstly used this method to characterize the in-plane thermal conductivity of a single layer graphene flake [126]. The temperature rise of the flake can be extracted from the Raman characteristic peak shifts. The thermal conductivity can be assessed through the temperature variation prolife away from the beam location on the 2D materials, especially MoS_2 [127, 128]. However, optothermal Raman method faces relatively high experimental errors, which might be incorporated from inaccurate estimation laser light power absorption by the 2D materials and thermal conductance of the supported area. Suspended pad method, which was first developed to measure carbon nanotubes (CNTs) thermal conductivity

in 2001 [129], has a relatively high accuracy for low dimensional materials. A 2D material flake is usually suspended on two silicon nitride (SiN_x), on which metal lines are patterned. The metal lines function as micro-heaters and micro-thermometers, providing joule heating and monitoring the temperature variation. Due to reliable calibration on temperature variation with high resolution, the suspended pad method has been utilized to measure the in-plane thermal conductivity of 2D materials, like MoS_2, SnS_2 and BP, shown in Figure 3-17b [130-132]. The above methods are designed for measuring intrinsic and in-plane thermal conductivity. For the cross-plane thermal conductivity of 2D materials and interface thermal transport, time-domain thermoreflectance (TDTR) is a powerful and straightforward method. As illustrated in Figure 3-17c, TDTR is a 'pump-probe' optical method, in which a mode-locked laser is splited into a 'pump' beam and a 'probe' beam. The 'pump' beam causes a temperature rise of ~3K near the transducer metallic surface and the 'probe' beam monitors temperature from the change of the optical reflectivity. *Pop et al.* adopted TDTR to study the cross-plane thermal conductivity and thermal interface resistance of MoS_2 thin layers [133]. Scanning thermal microscopy (SThM) is a method to provide spatial resolution of temperature profile on the assessed material surface at the nanoscale. The method utilizes the topography function of atomic force microscopy (AFM) with the temperature mapping by using a specially designed AFM probe, which is equipped with a temperature sensor near the apex [125, 134], as shown in Figure 2-16d. The SThM method was used to study the interface thermal resistance between MoS_2 and WSe_2 [135].

(a)

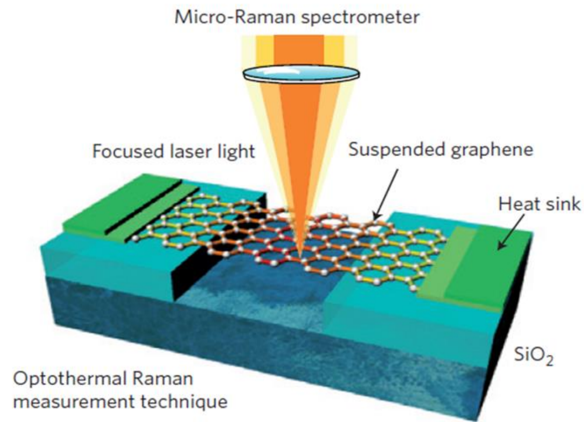

(b)

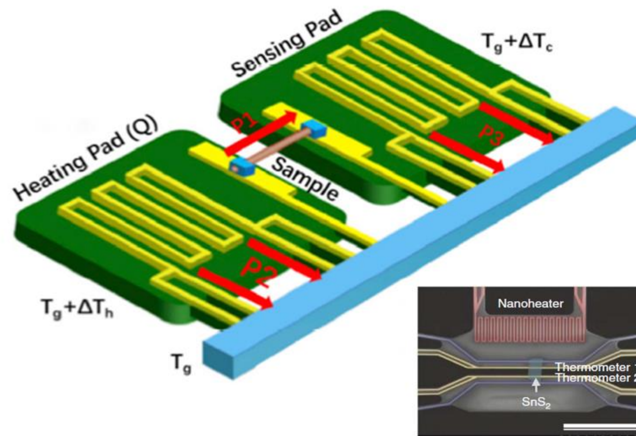

(c)

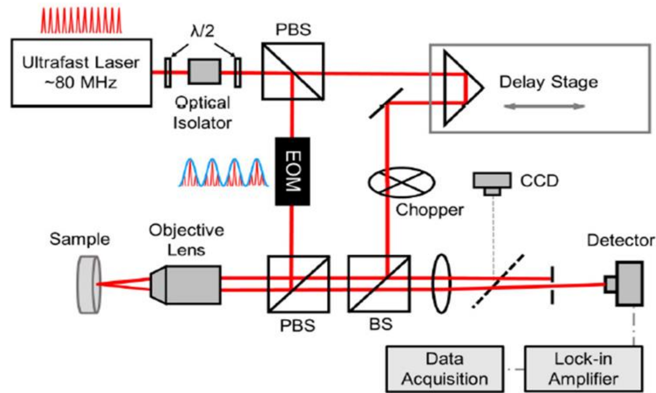

(d)

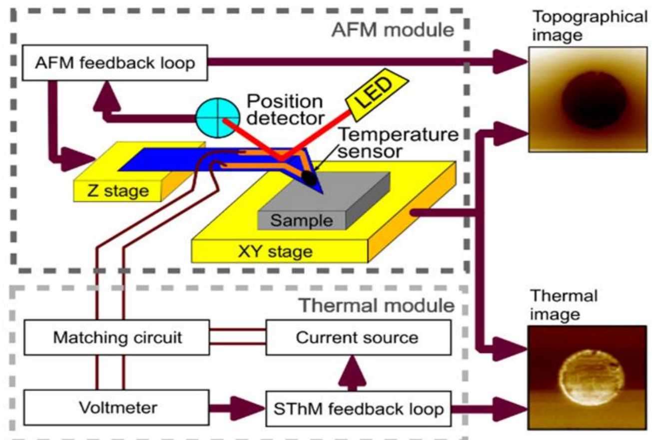

Figure 2-16 Schematic illustration for different thermal conductivity measurement (a) Optothermal raman method [122], (b) Suspended pad method [123, 131], (c) Time-domain thermoreflectance (TDTR) method [124], (d) Scanning thermal microscopy (SThM) method [134].

2.3.2.5 Other characterization methods

To better characterize piezoelectric materials and fabricate piezoelectric devices, several conventional characterization methods are frequently used.

The optical microscopy is the simplest and efficient method to locate the 2D PMs and collect information about the shapes and rough thickness [96]. The accurate thickness could be confirmed by AFM and Raman spectroscopy. Because piezoelectric materials lose the inversion symmetry, Raman and photoluminescence (PL) spectroscopy, X-ray Photoelectron Spectroscopy (XPS) and scanning transmission electron microscopy (STEM), are widely used. Raman spectroscopy could fast provide information about the material structures and electronic information noninvasively [136]. XPS is used to characterize the material elemental composition [137]. To characterize atomically structural information of 2D materials, like grain sizes and boundary, interfaces, phase and chemical composition information at the nanoscale, STEM is the most efficient technique [138].

2.4 Applications of 2D piezoelectric materials

Numerous 2D materials have been theoretically predicated with piezoelectric property. In fact, it is just few years since the piezoelectricity of 2D MoS_2 has been proved experimentally. After that, a series of 2D PMs and 2D piezoelectric applications have been demonstrated, owing to the unique piezoelectric polarization charges and superior

material characteristics, like extraordinary semiconductor properties, outstanding mechanical durability, good flexibility, high crystallinity and excellent optical properties. Here, we will discuss the foremost 2D PMs applications, like energy harvesters, piezotronics and piezoelectric sensors, piezo-phototronic devices [16, 56, 139].

2.4.1 Energy harvesters

The piezoelectric polarization charges play a crucial role in energy harvesters based on 2D materials, which is also usually named as piezoelectric nanogenerator (PENG). TMDCs is one the most important family group of 2D materials, and great efforts are put into the researches of TMDCs based PENG. In Figure 2-17a and b, the CVD MoS_2 flakes are used to fabricate PENG with a triangular shape. To boost the piezoelectric output, four m-MoS_2 devices were fabricated and connected either in parallel or series to enhance output voltages and currents [19]. In addition, the m-MoS_2 device, in which the electrodes are located along the armchair direction, generate larger piezoelectric output voltages than that of devices with electrodes located along the zigzag direction [140]. For CVD monolayer MoS_2, there exists a large density of point defects, especially sulfur (S) vacancies, and those defects could play a role in screening piezoelectric charges and hence degrade PENG performance. After sulfur treatment on the pristine MoS_2 surface, the S vacancies were effectively passivated and the output current and voltage were found to increase 2 and 3 times, respectively, as shown in Figure 2-17c [141]. For CVD monolayer MoS_2, it could grow into large-scale area with many grains and grain boundaries (GBs) with different crystalline orientations, not only in the shape of triangles. The butterfly-shaped m-MoS_2 PENG showed a 50% improvement on the output currents and voltages, because the deformable GBs promotes the generation of piezoelectric polarization charges along various directions in Figure 2-17d [142].

Mechanical exfoliated even layers TMDCs do not show any piezoelectric due to their stable stacking structures with opposite orientation between neighboring layers. *Lee et al* manipulated bilayer WSe_2 stacking order with enhanced polarization in one direction (called turbostratic stacking) by transferring synthesized monolayer WSe_2 onto another monolayer. The piezoelectric coefficients d_{11} for various stacking orders are stimulated with zero coefficients for alternating bilayer stacking and non-zero for same orientation stacking, in Figure 2-17e. The bilayer WSe_2 PENG generated a maximum output voltage of 85 mV and exhibited an excellent mechanical reliability up to a strain of 0.95%, in contrast the monolayer WSe_2 output voltage and current started to decrease upon the strain of 0.65% [20]. This approach has provided a feasible and artificial way to build reliable and high output PENG devices.

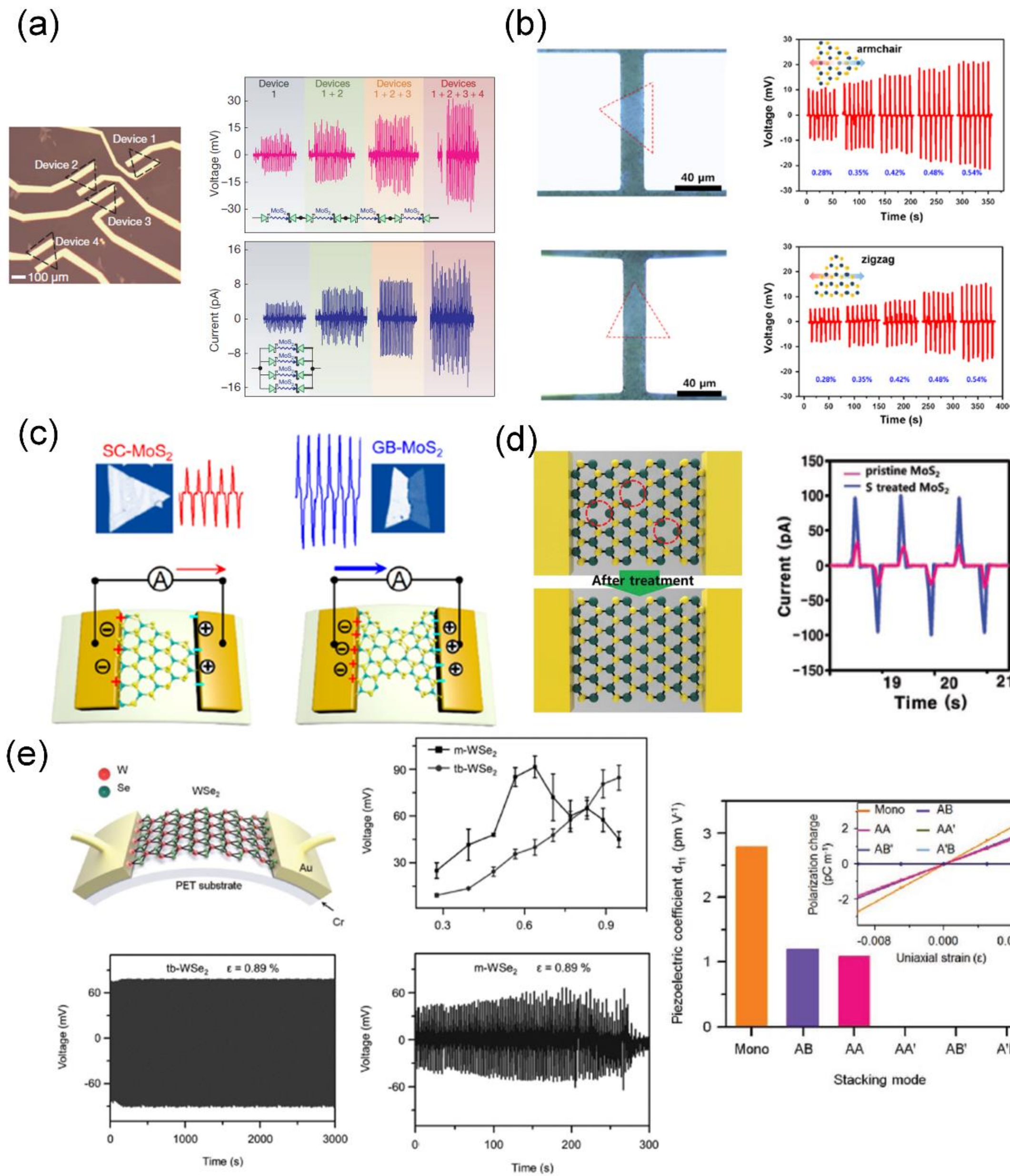

Figure 2-17 (a) The optical image of the array, and voltage and current outputs of integrated m-MoS_2 devices [19]. (b) The optical images of CVD m-MoS_2 devices and current outputs along armchair and zigzag direction, respectively [140]. (c) Schematic and current outputs of pristine MoS_2 with intrinsic S vacancy and passivated MoS_2 after treatment [141]. (d) Schematic and current outputs of SC-MoS_2 and GB-MoS_2 [142]. (e) Schematic of a PENG based on monolayer WSe_2, piezoelectric coefficient d_{11},

piezoelectric voltage outputs, durability tests of monolayer WSe_2 and bilayer WSe_2 devices [20].

In addition to TMDCs, excellent piezoelectric outputs are achieved from several other 2D layered materials. α-In_2Se_3 and γ-InSe, belonging to the group of indium selenides, are thermodynamically stable in ambient with non-centrosymmetric structures (AA stacking) from monolayer to multilayers. The simulated in-plane piezoelectric coefficients e_{22} are increased with layer numbers. The highest piezoelectric output voltage of 0.363 V for a 7-layer α-In_2Se_3 device, with the highest output current of 598.1 pA under 1% strain, was one order of the magnitude higher than that of other reported PENG [143], as displayed in Figure 2-18a. Recently, Group IV layered material SnS, that is predicated with high intrinsic piezoelectric coefficient, has been experimentally synthesized in monolayer with a measured piezoelectric coefficient of 26 pm/V, as shown in Figure 2-18b. The PENG fabricated with the SnS monolayer achieved the highest output voltage of 150 mV at 0.7% strain [69]. In Figure 2-18c, a novel material lead iodide, PbI_2, of the 2D structures was found to possess piezoelectricity from 2, 3 and 5 layers. The peak output voltage and current were 29.4 mV and 20 pA with a 1Gohm load resistor [144], respectively.

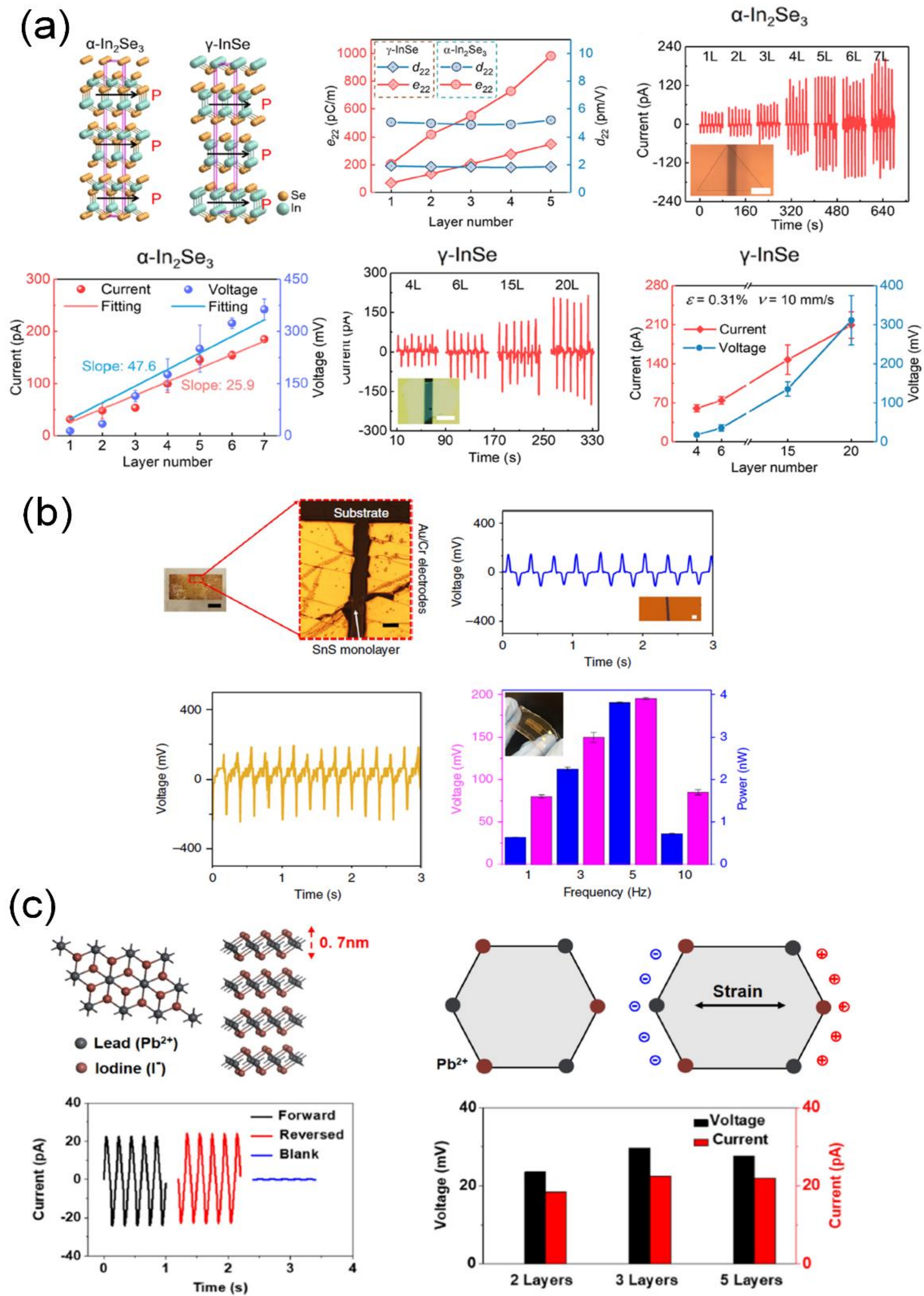

Figure 2-18 (a) Atomic structures, layer dependence of simulated piezoelectric coefficient d_{22}, piezoelectric outputs with different layers of α-In_2Se_3 and γ-InSe [143]. (b) Optical image, piezoelectric voltage output under various excitation frequency from [69]. (c) Atomic structure of monolayer and multilayer PbI_2, piezoelectric outputs of PbI_2 devices [144].

2.4.2 Piezotronics and piezoelectric sensors

As discussed in Section 2.1.3, piezoelectric potential can be utilized to gate the electrons or holes in the channels of transistors, i.e. piezotronics devices. Hence, piezoelectric semiconductors can have numerous applications in sensing, like force/pressure/strain sensors, gas sensors, humidity sensor, chemical and biological sensors [44, 145-150]. 2D PMs, such as MoS_2 and indium selenide group materials, are suitable candidates for piezotronics and piezoelectric sensors owing to the excellent piezoelectric and semiconducting properties. In Figure 2-19a, The first piezo potential modulated MoS_2 device was implemented by constructing two back-to-back Schottky barriers on monolayer MoS_2 in the metal-semiconductor-metal (MSM) structure. The m-MoS_2 device exhibited asymmetry changes in the output *I-V* characteristic curves in the presence of piezotronic effect, sharply different from a bilayer device with the same metal/semiconductor structures, in which only piezoresistive effect existed [19]. Subsequently, a piezotronic effect enhanced humidity sensor, which was also based on the back-to-back Schottky barrier m-MoS_2, was reported in Figure 2-19b [151]. To date, flexible and long term sensors can find many applications for healthcare monitoring. A piezoelectric sensor, fabricated by multilayer α-In_2Se_3 on PDMS with back-to-back electrodes, was used to monitor pulse and breath, as shown in Figure 2-19c. This self-powered sensor achieved a good sensitivity on pulse counting like a commercial pulse sensor and recognition of various breath states, including normal, ragged and deep breaths [143]. In Figure 2-19d, a pressure sensor, integrated of a ZnO nanorod array with a 2D indium selenide (InSe) based field effect transistor (FET), could sense a minimum weight of 0.1g equivalent to a piezoelectric potential of 0.2 mV [152].

(a)

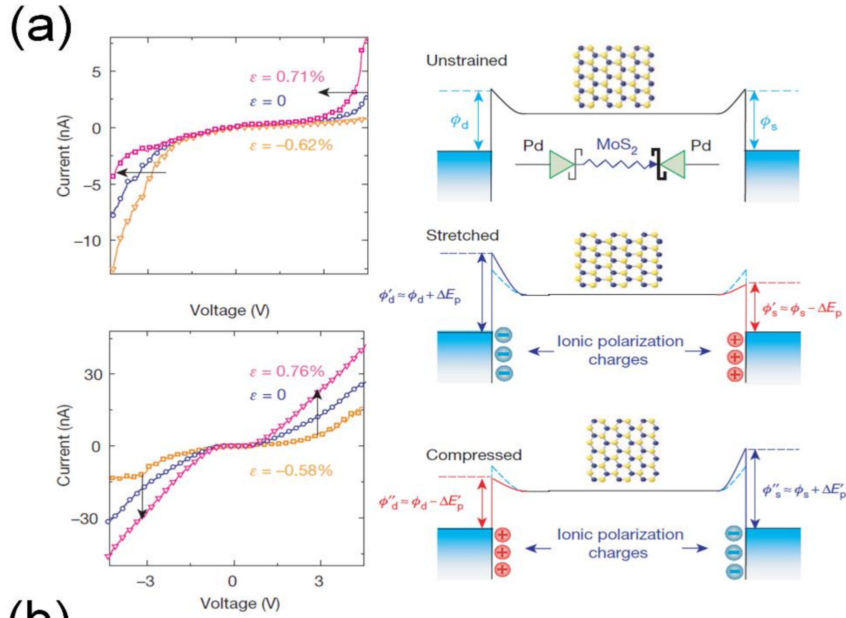

(b)

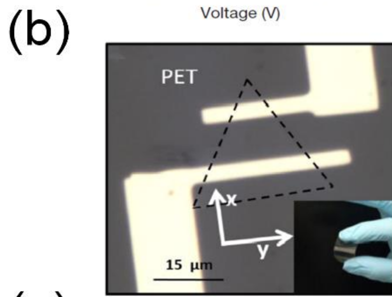

Current(pA)
Strain(%)
Relative humidity(%)

(c)

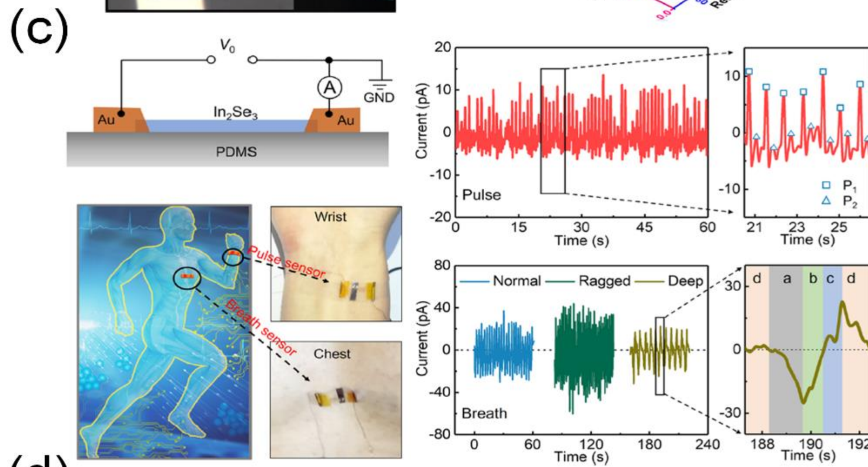

(d)

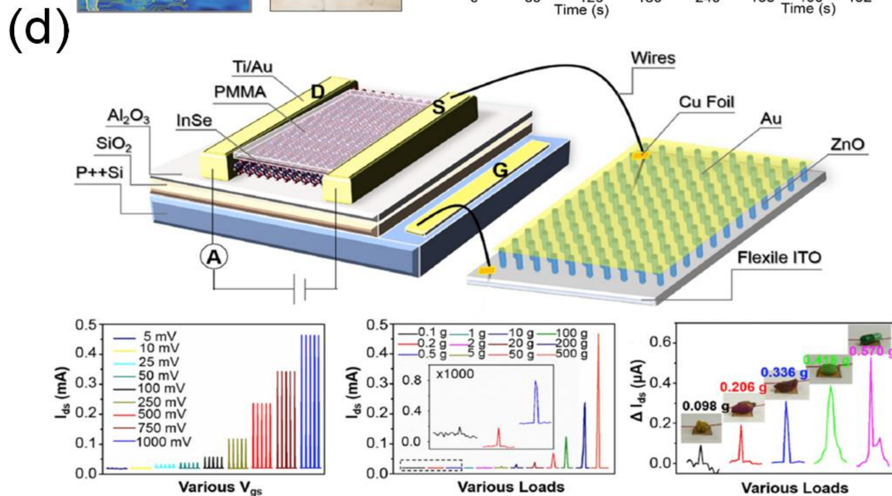

Figure 2-19 (a) The *I-V* characteristics and band diagrams for explaining the piezotronic effect of m-MoS_2 and bilayer MoS_2 devices under a tensile or compressive strain [19]. (b) Optical image and the performance of an m-MoS_2 humidity sensor [151]. (c) Self-powered α-In_2Se_3 piezoelectric sensor [143]. (d) Schematic and piezopoetntial modulation on the performance of a pressure sensor based on ZnO nanorod arrays and 2D indium selenide (InSe) field-effect transistor (FET) [152].

2.4.3 Piezo-phototronic devices

In addition to the piezoelectric properties, 2D piezoelectric materials also show superb optical properties. Thus, a certain number of innovative optoelectronics have been reported using 2D PMs, and piezoelectric potential modulated 2D optoelectronic and photonic properties have been observed. These devices are called piezo-phototronic devices. The first 2D piezo-phototronic device was fabricated by transferring mechanically exfoliated MoS_2 flake onto a flexible substrate in 2016, as depicted in Figure 2-20a . Before transferring, the MoS_2 flake orientation was confirmed through SHG and then Pd/Au electrodes were deposited along the armchair direction. Then, the piezopotential modulated photoresponse was systematically characterized under various strain and illumination intensities. When a -0.38% compressive strain at low illumination light, a maximum photoresponsivity of 2.3×10^4 A/W was measured, a 26-fold enhancement over the previously reported highest photoresponsivity from m-MoS_2 device [153]. For piezo-phototronic devices, the interfaces play crucial roles in the modulation. In Figure 2-20b, a flexible van der Waals photodiode, fabricated by stacking monolayer n-MoS_2 and few layers p-WSe_2, achieved an increased 86% photoresponsivity under a -0.62% compressive strain along MoS_2 armchair direction [154]. Solar cells are another important category of optoelectronic devices. A 2D piezo-

phototronic solar cell model, based on a monolayer MoS_2 with Schottky and Ohmic contact, was theoretically studied. The open circuit voltage could be increased by 5.8% at strain of 1%, caused by piezo-phototronic effect, shown in Figure 2-20c [155]. Furthermore, a recent study proved that the piezo-phototronic effect could also improve multijunction solar cells [156].

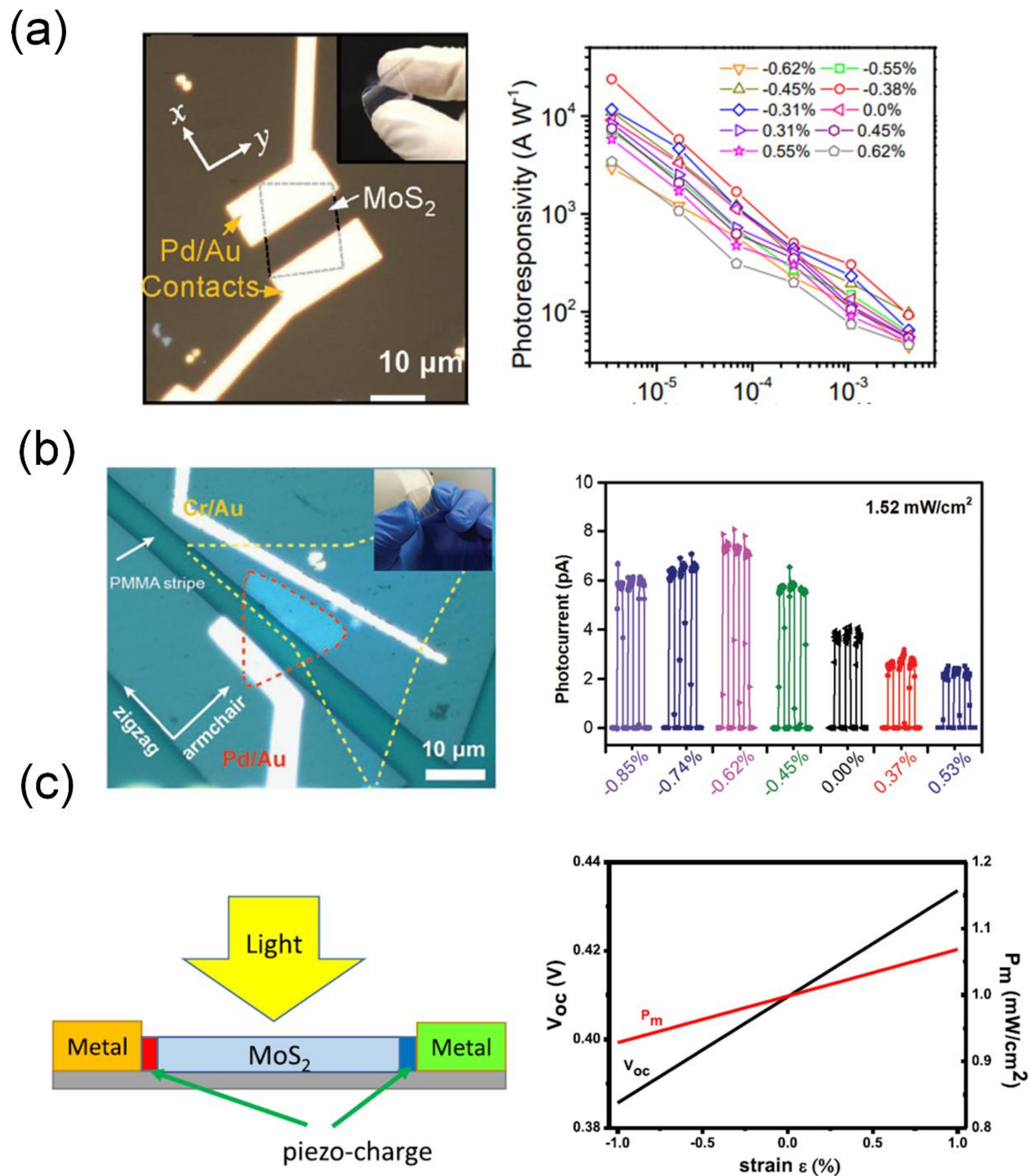

Figure 2-20 The strain modulated photoresponse of (a) flexible m-MoS_2 photodetector [153], (b) flexible MoS_2/WSe_2 van der Waals photodiode [154]. (c) Schematic and strain

modulated relative output power as a function of voltage under various strain, open circuit voltage and maximum output power under various strain of 2D piezo-phototronic solar cells [155].

Chapter 3 Piezoelectricity of 3R MoS_2 flakes

3.1 Introduction

For decades, conventional piezoelectric materials, like ceramics, PZT, wurtzite materials ZnO and GaN, etc. have been widely used in actuators, sensors, energy harvesters, etc [157-160]. When the devices are scaled down to nano/macro sizes, the conventional piezoelectric materials are in general very brittle and difficult to miniaturize, and thus it is challenging to fabricate flexible and high integrated electronics [161]. To overcome these obstacles and meet the new application requirements, novel piezoelectric materials with several advantages over the conventional materials, like ultrathin, flexible and chemically stable, are demanded with comprehensive and systematic studies of their piezoelectric properties and geometries of structures.

Very recently, atomic layered materials, like h-BN and monolayer TMDCs with flexibility and ultrathin properties, which have been theoretically and experimentally proved with piezoelectric properties due to their broken inversion symmetry, could solve the obstacles and satisfy the new demands [19, 59, 140]. The piezoelectricity of monolayer MoS_2 was firstly experimentally proved by *We et al* in 2014, in which the piezoelectric nanogenerator (PENG) was developed [19]. In the following year, the in-plane piezoelectricity coefficient of $e_{11} = 2.9 \times 10^{-10}$ C m^{-1} was estimated by AMF probing of a free-standing MoS_2 on a membrane [54]. After that, several monolayer TMDCs devices have been fabricated and tested [20, 140-142]. However, there are still several bottlenecks to drive monolayer TMDCs into practical applications: (i) their piezoelectricity output is small due to its small effective volume, (ii) the piezoelectricity only exists in odd layers and it decreases significantly as layer numbers increase. For

example, the piezoelectricity is not observable when the number of layers of MoS_2 is more than 5 layers [19], (iii) Poor mechanical stability of monolayer TMDCs cannot guarantee their performance under large elastic strains and long-term durability. To solve these issues, a turbo-static approach was used in fabricating bilayer WSe_2 [20] piezoelectric devices manually for enhanced piezoelectric performance and long-term usage. However, the uncontrollable performance and complicated fabrication process hinder this artificial device in more applications.

Herein, another stacking structure of MoS_2, 3R (3 Rhombohedral) MoS_2 have been theoretically predicated with large in-plane piezoelectric coefficients $d_{22} = 3.6$ pm/V ($e_{22} = 0.64$ C m^{-2} for five layers), $d_{31} = -0.21$ pm/V and out-of-plane piezoelectric coefficient of $d_{33} = 0.27$ pm/V [22, 162]. This material therefore possesses a large piezoelectricity and excellent mechanical properties and could be affordable for long-term usage in multilayer structures. To our understanding, direct observation of the piezoelectricity of 3R-MoS2 flakes has not been reported yet. Here, we present the first proof of a strong piezoelectricity of exfoliated 3R-MoS_2 flakes.

In this chapter, 3R MoS_2 flakes were fabricated by mechanical exfoliation and their non-centrosymmetry atomic structure was characterized and evidenced. The 3R-MoS_2 flakes based piezoelectric nanogenerators (PENG) were developed for the first time with enhanced piezoelectric outputs and high mechanical energy to electricity conversion efficiency. The piezoelectric coefficients d_{33} and lateral excited in-plane and out-of-plane piezoelectricity were obtained using piezoresponse force microscopy (PFM). These findings reveal a promising performance of the piezoelectricity of 3R-MoS_2 flakes and pave the way to develop novel ultra-high frequency piezoelectric devices for various promising applications.

3.2 Materials synthesis and devices fabrication

3.2.1 3R MoS_2 single crystal

3R-MoS_2 single crystal was synthesized in an argon-filled glove box with low oxygen and moisture levels below 0.1 ppm. 3R MoS_2 single crystals were grown using chemical vapor transport (CVT) method. The materials Mo (powder, 99.99%), S (powder, 99.99%), and $MoCl_5$ (powder, 99.99%) were purchased from Sigma Aldrich. The stoichiometric amounts of Mo: S: $MoCl_5$ at 9:20:1, with a total weight of 450 mg, were sealed in an evacuated 20 cm long quartz tube under vacuum of 10^{-6} Torr. The sealed tube was placed in a three-zone furnace and pretreated at 850 °C for 30 hours, while the grown zone was maintained at 920 °C to prevent the diffusion of samples. The temperature in the reaction zone was then increased to 1080 °C, while the growth zone was maintained at 920 °C for 6 days to generate a temperature gradient at the place, where the growth of single crystals took place. At last, 3R MoS_2 single crystals were collected in the growth zone after the furnace and tube were cooled downed to room temperature [120].

The 2H MoS_2 single crystal was purchased from 2D SEMICONDUCTORS.

3.2.2 MoS_2 devices for PFM and piezoelectric measurements

3.2.2.1 Devices for lateral excitation PFM and piezoelectric measurements

In Figure 3-1a and b, a silicon oxide (280 nm) coated silicon wafer (500 μm) and a polyimide (PI) thin film (125 μm) substrates were firstly cleaned by acetone, isopropyl, and deionized water. 3R MoS_2 and 2H MoS_2 flakes were mechanically exfoliated onto the SiO_2/Si wafer or polyimide thin film using the CVD growth 3R MoS_2 crystal or commercial 2H MoS_2 single crystal, respectively. A Ti/Au thin film (20/150 nm) was deposited using an electron beam evaporator (Edwards Auto 360) on the MoS_2/SiO_2/Si

samples, followed by a lift-off process to define a pair of electrodes on the two terminals of the MoS_2 flakes. Then, the samples for lateral excitation PFM characterization were annealed in argon gas at 180°C for 1.5 hours. For the PENG devices, an Au thin film (150nm) was deposited on the MoS_2/polyimide samples. Then, a pair of electrodes at the two terminals of the MoS_2 flakes were fabricated with the standard photolithography etch-down process using gold etchant through a photoresist (AZ5214E) as a protecting layer.

3.2.2.1 Devices for piezoelectric coefficient D_{33} PFM measurement

In order to measure d_{33}, MoS_2 flakes were firstly mechanically exfoliated onto a SiO_2/Si substrate. A layer of PMMA was spin-coated on the samples at 3000 rpm for 45 s, and then pre-baked at 105 °C for 5 minutes. The KOH solution was adopted as the etchant to remove SiO_2 layer. The PMMA/3R-MoS_2 flakes was transferred on a Ti/Au (20/150 nm) coated silicon wafer. Then, the PMMA was cleaned with acetone solution. The sample was also annealed in argon gas at 180 °C for 1.5 hours, as shown in Figure 3-1c..

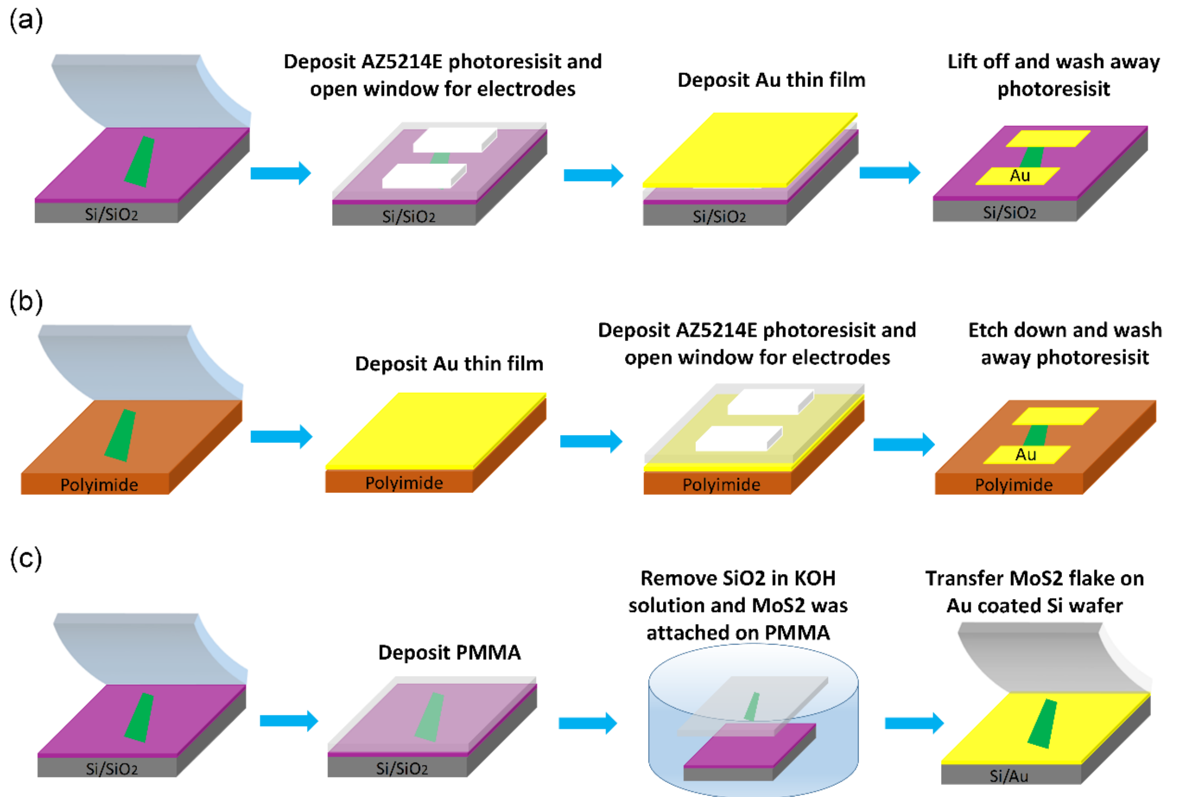

Figure 3-1 Schematic illustration of the sample fabrication processes for (a) in-plane PFM measurement, (b) direct strain bending measurement and (c) out-of-plane PFM measurement.

3.3 Methodology and experimental facilities set up

3.3.1 SHG measurement

The SHG measurement utilizes a mode-locked Ti:sapphire laser (output wavelength: 800nm and repetition rate: 76MHz) to generate tunable wavelength light ranging from 500 to 1600 nm filtered through optical parametric oscillator (OPO), then circularly polarized by a quarter-wave plate, attenuated and focused on a sample by a microscope objective lens (100×, NA = 0.95). The SHG signal can be collected by the same lens using a dichroic mirror and filtered by a short pass filter before entering a spectrometer (PI-Acton 2500i with a liquid nitrogen cooled charge coupled device-CCD camera), as shown in Figure 3-2.

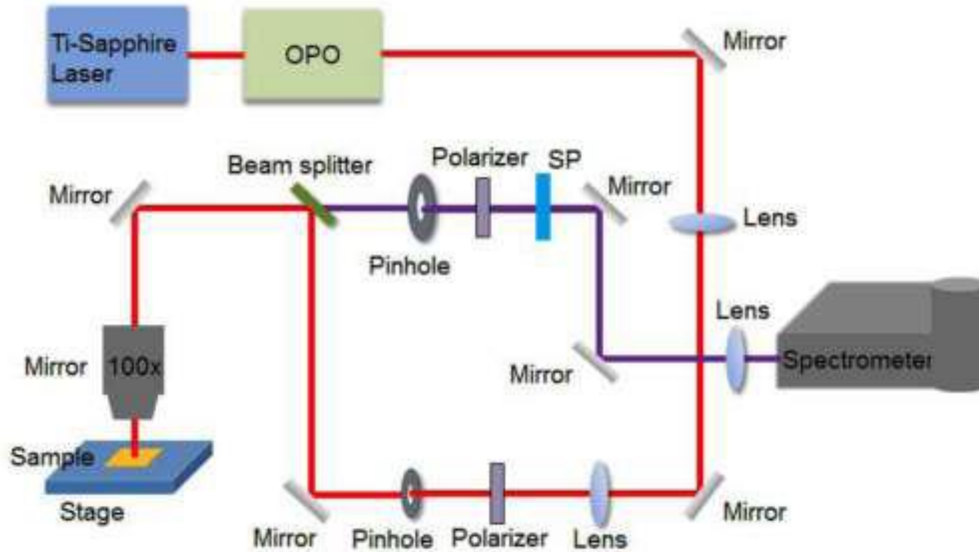

Figure 3-2 Second Harmonic Generation Experimental setup [120].

3.3.2 Characterization of the PENG

For MoS_2 based PENG, the dimension of MoS_2 flakes was significantly smaller than that of the polyimide substrate. Hence the mechanical strain was induced by bending the substrate. One end of the MoS_2 PENG was clamped on a movable holder that was driven by a linear motor (LinMot E1100-GP) controlled translation stage, and the other end was fixed onto a stationary stage. The strain applied to the MoS_2 flake was realized by compressing the flexible substrate and releasing it through the movable holder. The relative motion distance was acquired by a commercial software and used for calculating the bending angle of the substrate, from which the strain applied to the MoS_2 flake was determined. A Low-Noise Current Preamplifier (SR570, Stanford Research Systems), up to a sensitivity of 10^{-12} with a 1MΩ impedance, and a Low-Noise Voltage Preamplifier (SR560, Stanford Research Systems) were employed. The circuit connection for the voltage and current measurements and setup are displayed in Figure 3-3. The output signals were collected by a Multifunction DAQ and home-built software

programmed by LabVIEW, and a 3 Hz low-pass filter was engaged in the current and voltage measurements to reduce the noises.

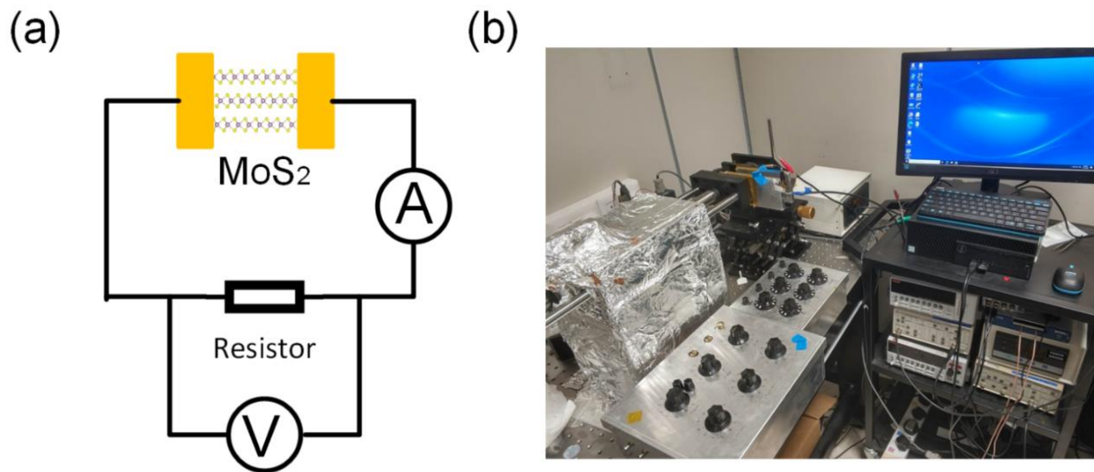

Figure 3-3 (a) Schematic of the circuit connection and (b) the experiment setup for PENG devices under different strains.

Since the dimensions of the MoS_2 flakes (~20 μm long and a few tens of nanometer thick) are much smaller than the polyimide substrate (50 mm × 50 mm × 125 μm), the tensile and compressive strains exerted onto the flakes deposited onto the PI substrate could be given by $\varepsilon = h/2r$, where h is the thickness of the PI substrate, and r is the bending radius. Figure 3-4 and Table 3-1 present the strain calculation in details, where the L is the bended length of the substrate. The bended length L and rending r fit the relation as: $L=2r\sin(\theta)$, where θ is the bending angle.

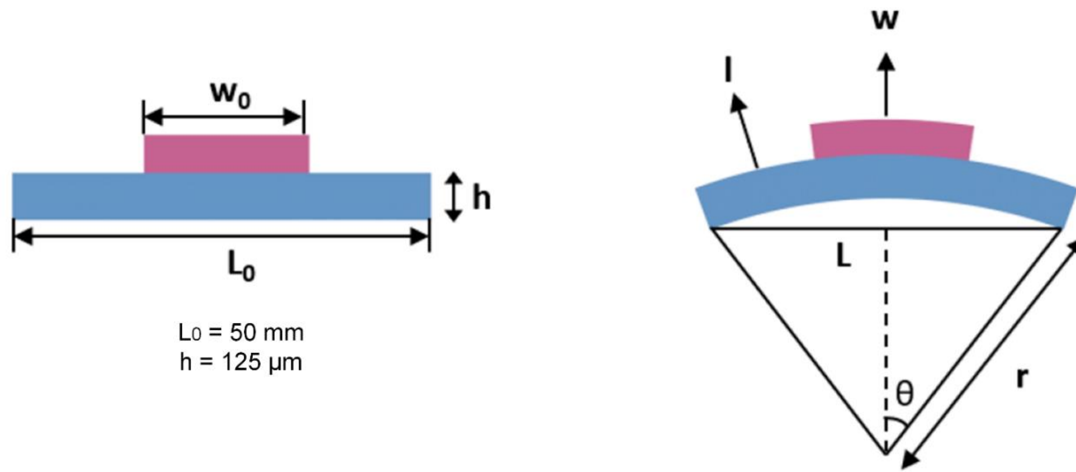

Figure 3-4 Illustration of a mechanical strain applied onto the MoS_2 flakes.

H (μm)	L (mm)	r (mm)	ε
125	45	31.78	0.20%
125	40	22.10	0.28 %
125	35	17.73	0.35 %
125	30	15.06	0.42 %
125	25	13.19	0.47 %

Table 3-1 Calculated strains in the MoS_2 flakes and the related parameters.

3.3.3 PFM measurements

3.3.3.1 Calibration of PFM

The Asylum Research Periodically Poled Lithium Niobate (PPLN) was employed to calibrate our Asylum Research PFM. The reference sample has strip domains permanently polarized for easy identification and optimization of PFM parameters. It consists of a 3mm x 3 mm x 0.5 mm $LiNbO_3$ transparent die. Alternating patterns of oppositely poled strip domains were in parallel to the one axis of the die and covered the entire die surface. The pitch of the domains was 10 μm.

3.3.3.3. Out-of-plane piezoelectric coefficient d_{33} measurement methodology

The out-of-plane piezoelectric coefficient measurements were performed using the same Asylum AFM with a dual AC resonance tracking PFM mode (DART-PFM). A Pt/Ir coated conductive tip with a force constant of 2.8 N/m was used to apply an electric field to the MoS_2 flakes. By applying a V_{AC} sweep from 0V to a certain voltage like 1.5V at a step of 0.25V between the tip and the back electrode, the deflection of the conductive tip caused by the expansion and contraction of the flakes could reveal the different amplitude and phase of the piezo generated vertical displacement. The amplitude images were analyzed with selected area to calculate d_{33} [117, 163].

Here, the working mechanism of DART-PFM is illustrated in Figure 3-5. Different from single frequency PFM using the phase lock loop (PLL) as the input to frequency feedback [164], DART adopts the amplitude difference (A_2-A_1) as the input feedback. The two amplitude A_1 and A_2 are generated from two individual lock-in amplifiers, which receive cantilever deflection and two separate frequencies f_1 and f_2. The AFM tip is driven by the f1 and f2 frequencies, which are close to the resonance frequencies. When the tip is scanned over the surface, the resonant frequency would shift to a low frequency or high frequency. The amplitude difference is no longer be zero, as the A_1 and A_2 move into opposite direction. The drive frequencies therefore will shift as a response until the amplitude difference become zero again, where the differential of drive frequencies (f_2-f_1) is constant around 10kHz [117]. By taking DART-PFM, the crosstalk, which is usually raised from larger AC voltage in conventional PFM for boosting small piezoresponse, could be highly reduced [113].

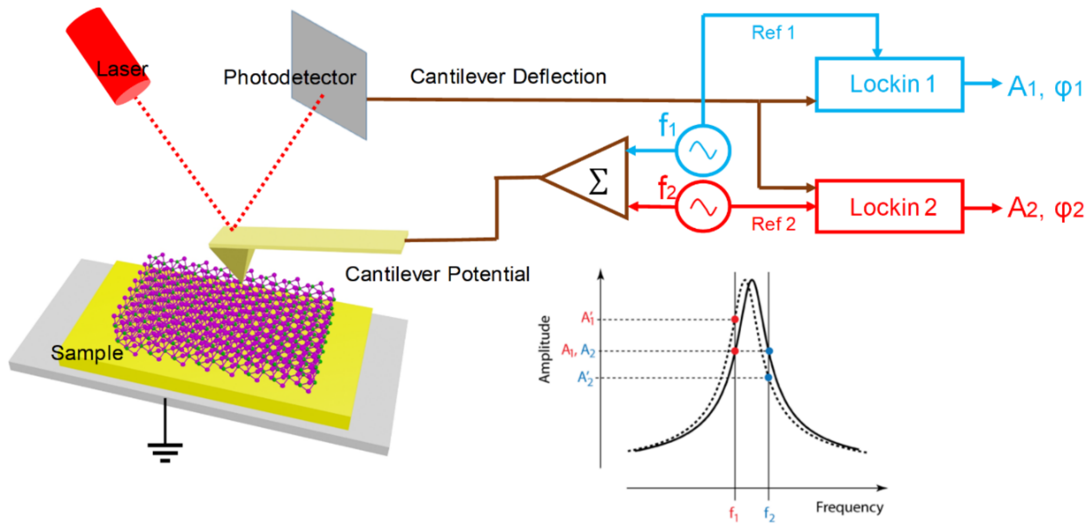

Figure 3-5 Schematic of DART experiment setup and the working principle of the dual-frequency excitation based resonant-amplitude tracking.

3.3.3.2 Lateral excitation PFM measurement

The lateral piezoelectric measurements were performed using a single frequency PFM mode using a non-conductive tip with a very low force constant of 0.02 to 0.77 N/m. Here, the non-conductive tip was used to measure only the deformation of 3R MoS_2 flakes by applying a AC voltage sweep of up to several volts through the electrodes covered the ends of the MoS_2 flakes on SiO_2 substrates, as depicted in Figure 3-6. Then, the surface of the 3R MoS_2 flake was scanned with the tip to obtain a distribution of vertical displacement in amplitude images and phase image as a function of the applied voltage. The average of piezoresponse amplitude was calculated from the vertical displacement [116].

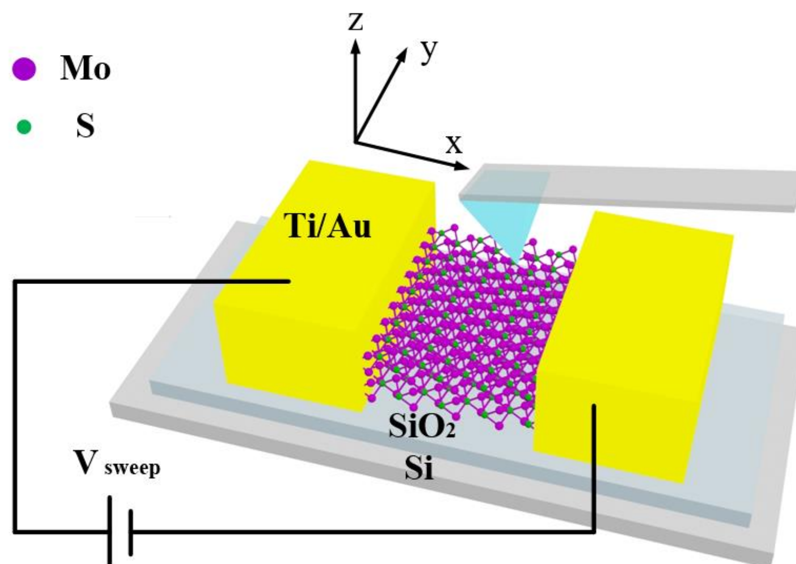

Figure 3-6 Illustration of the lateral excitation PFM measurement.

3.3.4 Raman and STEM Characterizations

The Raman scattering measurements (WITec alpha 300 confocal Raman microscopy) were carried out under a laser light of 532 nm, laser power of 0.1 mW and beam diameter of 400nm with a 100X objective lens.

The MoS_2 samples for TEM were mechanically exfolited from the 2D crystals by using toluene (99.85%, Acros Organics) and then transferred onto the TEM grids (Quantifoil Mo grids). The high-resolution transmission electron microscopy (HRTEM) and the SAED pattern were performed with a FEI Tecnai F20 operated with an acceleration voltage of 200 kV.

3.4 Results and discussion

3.4.1 Structure of 3R MoS_2

The layered MoS_2 could be in three stacking configurations (phases), 2H, 3R and 1T, where 2H and 3R MoS_2 phases are naturally semiconducting, while octahedral 1T phase is metastable metallic [165, 166]. The conventional 2H phase MoS_2, displayed in Figure

3-7a in AB-AB stacking configuration (in reverse direction), shows a centrosymmetry of the hexagonal structure with the space group of 6mm (D_{3h} point group) [167]. When the strain is applied on multilayer 2H MoS_2, the generated dipoles have reverse directions in neighboring layers such that the polarization charges are neutralized between alternating layers. As a result, the significant piezoelectricity only exists in few and odd layers, and disappears in even layers [19]. Such a characteristic greatly hampers MoS_2 based piezoelectric application [168, 169].

On the contrary to 2H MoS_2, 3R MoS_2 has been theoretically predicted with piezoelectricity from monolayer to bulk, because of its non-centrosymmetric structure (C_{3v} point group) [22, 162]. In Figure 3-7b, 3R MoS_2 possesses a ABC-ABC stacking layers, in which the strain-induced dipoles are in the same direction, contributing to the strong piezoelectricity. A strong in-plane piezoelectric coefficient d_{22} of 3.6 pm/V and out-of-plane piezoelectric coefficients d_{31} and d_{33}, -0.21 pm/V and 0.27 pm/V, respectively, have been predicted [22]. As 2D layered materials is highly flexible, 3R MoS_2 based piezoelectric devices could thus be easily integrated with other flexible electronic devices. As shown in Figure 3-7c, the atomic lattice structures of the monolayer, bilayer and trilayer were confirmed their ABC-ABC stacking configuration in the unit cells of S-Mo-S, adopting scanning transmission electron microscopy (STEM) annular dark-field (ADF) images. The simulated structure (to the right of the STEM image) agrees well with the structure illustration of 3R-MoS2 flake. The inset in Figure 3-7c shows the selected area electron diffraction (SAED) patterns. The atomic arrangement in the form of hexagonal symmetry manifests that the MoS_2 sheets are in the single crystal domain.

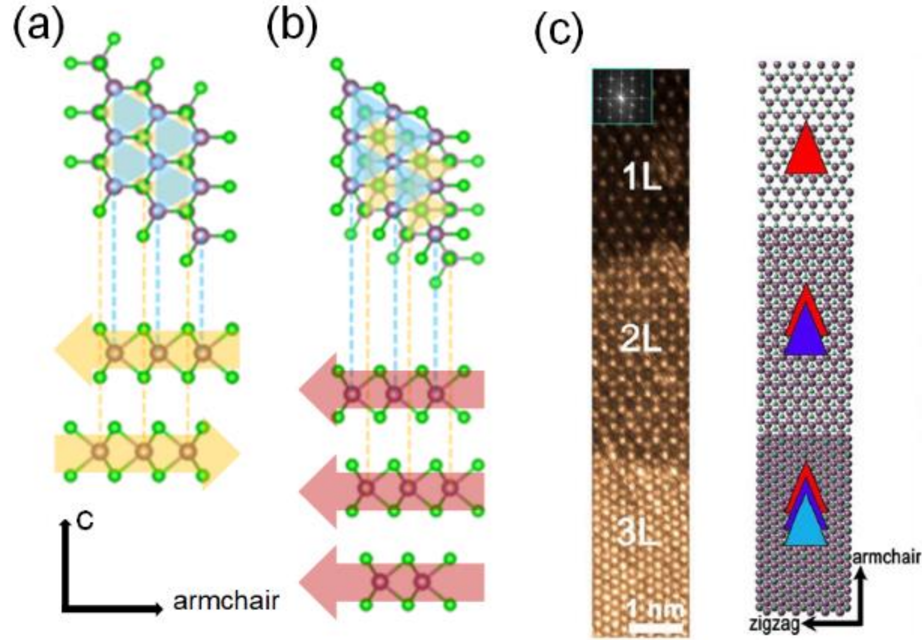

Figure 3-7 Atomic structure of (a) 2H MoS_2, (b) 3R MoS_2 in top and side views. (c) STEM images of monolayer, bilayer and trilayer 3R MoS_2.

The broken lattice symmetry of 3R MoS_2 was confirmed by SHG using a femtosecond optical parametric oscillation (OPO) laser as the excitation source, with a wavelength of λ_{ex} = 800nm and normal incident on the sample, shown in Figure 3-8a. It has been well-accepted that natural 2H MoS_2 flakes have no SHG due to their central symmetry, while 3R MoS_2 flakes break the inversion symmetry, and thus should in principle have SHG [60, 170]. As shown in Figure 3-8b and c, the 3R MoS_2 with a thickness around 30 nm shown obvious SHG signals, in consistency with the previous study [120]. Since angle-resolved SHG is crystal-orientation dependent, the SHG intensity versus the sample rotation angle should be able to unveil the underlying crystalline symmetry of 3R MoS_2 flakes. The angle between the incident laser polarization and the sample orientation (perpendicular to upper edge) was defined as θ, and the SHG peaks at 400 nm were observed and any incident laser angle, which is half of wavelength and double frequency of incident polarization light. The minimum SHG intensity at θ = 30° represents the

zigzag direction, while θ = 60° corresponds to the armchair direction of the 3R MoS_2 flake. The polarization-resolved SHG in 360° clearly shows a six-fold rotational symmetry, consistent with previous reports [60]. For the 3R MoS_2 flakes used in this work, their lattice orientations were determined by fitting their angle-dependent SHG intensity with I_0 = sin2h, where h represents the angle between the light polarization direction and the armchair edge of the flakes, and I_0 is the peak intensity of the polarization.

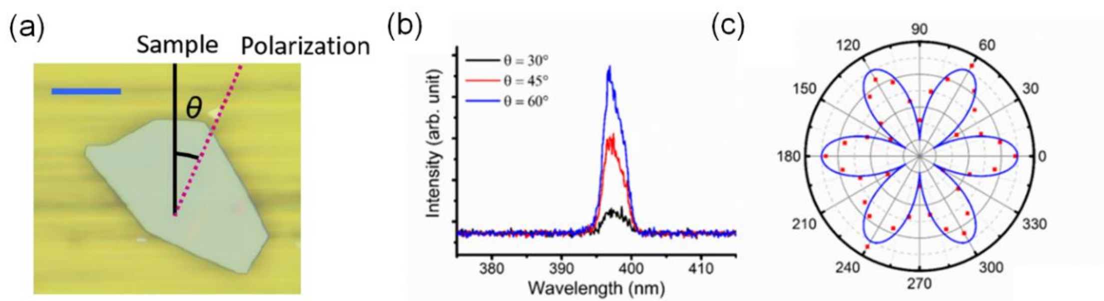

Figure 3-8 SHG measurement of a 3R MoS_2 flake; (a) Optical image with polarization angle θ, (b) the SHG intensity at polarization angle θ = 30°, 45° and 60°, (c) Angle dependence of the SHG intensities.

The Raman spectra of 3R MoS_2 flakes were characterized using a confocal Raman spectroscopy. In Figure 3-9, the Raman spectra for a 20 nm and 80 nm thick 3R MoS_2 flakes, show E_{2g}^1 peaks are at ~ 383 cm^{-1} and the A_{1g} peaks are at ~ 408m^{-1}. These are the typical Raman spectra of thick 3R MoS_2 flakes as reported [120, 171].

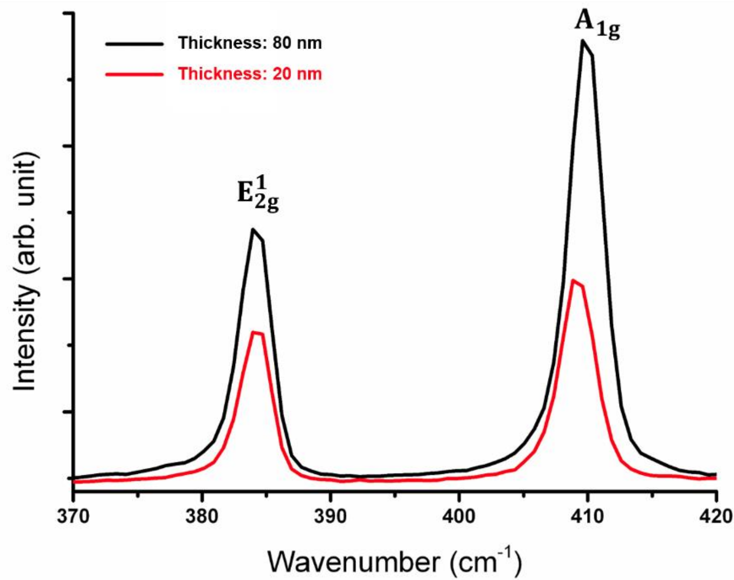

Figure 3-9 Raman spectra for 20 nm and 80 nm thick 3R MoS_2 flakes.

3.4.2 Piezoelectricity of 3R MoS_2

3.4.2.1 3R MoS_2 PENG devices with distinguishing crystal orientations.

The piezoelectricity of 3R MoS_2 flakes was characterized by applying mechanical uniaxial strains to the 3R MoS_2 PENG devices, in which the two terminals of the 3R MoS_2 flakes on a polyimide substrate were buried underneath a pair of Au (150 nm) electrodes, as shown in Figure 3-10. The x and y axis correspond to the direction parallel and perpendicular to the electrodes, respectively. 3R MoS_2 devices were fabricated with same channel width of ~ 6.5 µm and length of 50 µm, but different atomic orientation and thickness. Some of 3R MoS_2 PENG devices, in which zigzag axis of the flakes was lied along to the electrodes direction, are simply named as the aligned 3R MoS_2 PENG devices. The rest are named as non-aligned 3R MoS_2 PENG devices, as their flakes were neither perpendicular to the armchair nor zigzag axis. The atomic orientations of the two devices were measured and confirmed using SHG.

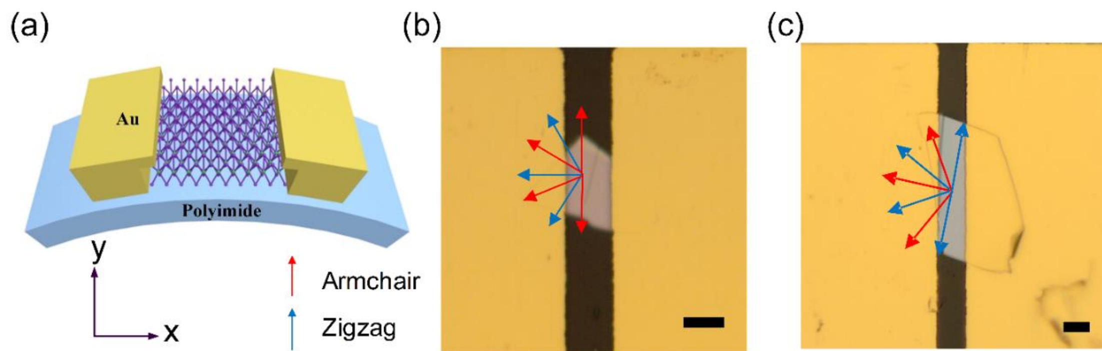

Figure 3-10 (a) Illustration of the PENG device under a tensile strain, (b) an aligned 3R MoS_2 PENG device with the electrodes parallel to zigzag axis, (c) a non-aligned 3R MoS_2 PENG device with the electrodes neither parallel nor perpendicular to the armchair or zigzag axis. The scale bar is 5 μm. The red arrows and black arrows stand for the armchair and zigzag orientations.

In Figure 3-11, the morphologies of aligned and non-aligned 3R MoS_2 PENG devices were characterized by AFM. The thicknesses for aligned and non-aligned devices, are around 48 nm and 110 nm, respectively.

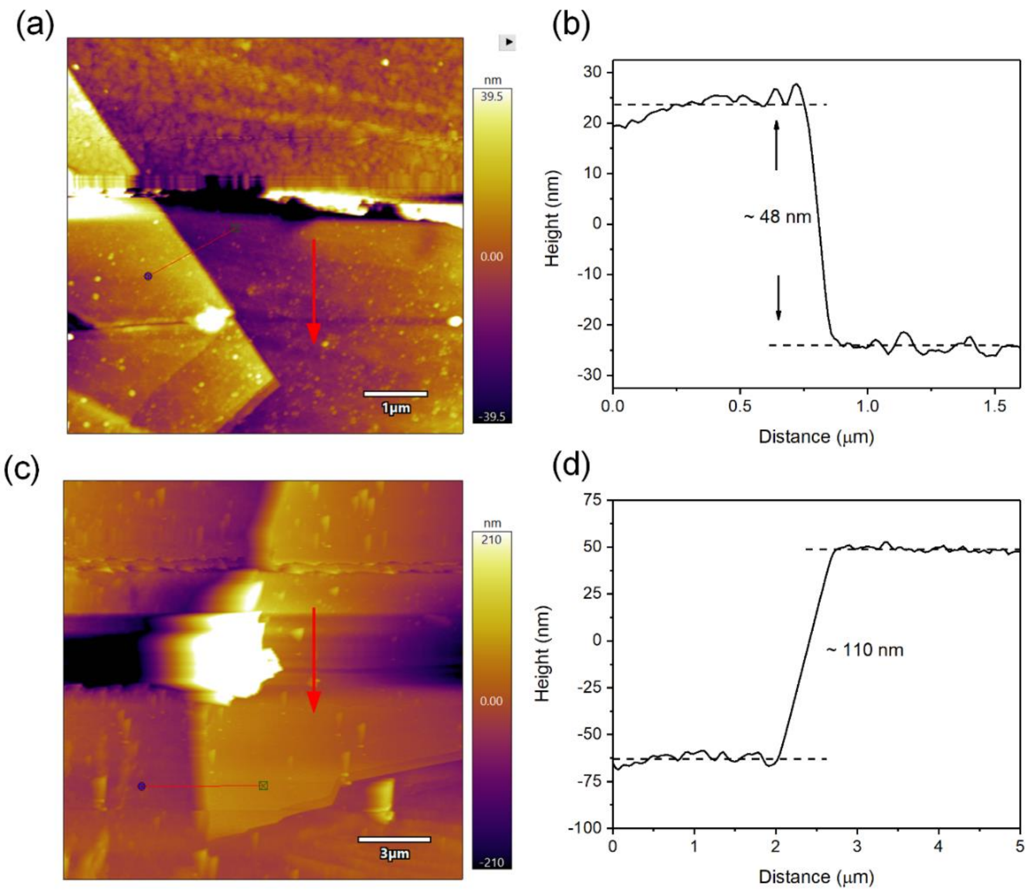

Figure 3-11 AFM measurement of 3R MoS_2 PENG. Morphology image and Height profile of the (a-b) aligned and (c-d) non-aligned 3R MoS_2 flake (The red arrow marks the x direction).

3.4.2.2 Piezoelectric outputs of aligned and non-aligned 3R MoS_2 flakes

When 3R MoS_2 flakes are subjected to a mechanical strain, effective polarization charges could be induced at the edges and surfaces. The positive and negative polarization charges could accumulate at the two interfaces separately, forming an electric field in the flake, attracting electrons to the positive polarization charges and giving rise to a transient current through the external circuit that is in contact with the two electrodes. When the strain is released, the piezoelectric polarization charges vanish immediately and the attracted electrons flow back, leading to an opposite direction transient current. Besides, the Schottky contacts between n type semiconducting MoS_2

and the Au electrodes could fully block the electron injection from the metal electrodes to the MoS_2 flakes. The above phenomenon was also observed from monolayer 2H MoS_2 and other 2D piezoelectric materials [19, 69, 77]. When the substrate was bended along x axis or y axis, one tensile strain is applied to the MoS_2 flakes and the strain is constrained to a maximum magnitude of 0.48%, in order to avoid sample slippage [172].

The piezoelectric response of an aligned 3R MoS_2 PENG device was comprehensively studied and displayed in Figure 3-12. When the 48 nm thick aligned 3R MoS_2 flake was subjected to a tensile strain of the magnitude from 0.2% to 0.48% along the x axis (the zigzag orientation), the average peak output voltage and current increased from ~ 25 mV to ~ 102 mV and ~ 60 pA to 210 pA, respectively. Meanwhile, the 3R MoS_2 flake gave a peak output voltage and current from ~ 20 mV to ~ 90 mV and ~ 25 pA to 120 pA, respectively, under a uniaxial strain along the y axis (armchair orientation). It is observed that the piezoelectric output voltage and current increased almost linearly with the strain in a step of ~0.07%, from the chart plotting in Figure 3-12e, f.

For a non-aligned 3R MoS_2 flake with a thickness of 110 nm, the strain was also performed along from the x-axis and y axis. The angle between armchair and x axis is 10°. The peak piezoelectric output voltage and current only increased from ~ 11 mV to ~ 39 mV and ~ 42 pA to 116 pA along the x-axis, and from ~ 10 mV to ~ 45 mV and ~ 33 pA to 97 pA along the y-axis for a tensile strain from 0.2% to 0.48%. It is seen clearly that the piezoelectric outputs of non-aligned 3R MoS_2 were also proportional to the strains, but weaker than those from the aligned devices, as shown in Figure 3-13.

Our aligned 3R MoS_2 device achieved a significant improvement of nearly two times larger than the output voltage and current from the reported MoS_2 and WSe_2 flakes. [19, 20, 141]. The large piezoelectricity of the 3R MoS_2 flakes might be attributed to the

larger in-plane piezoelectricity and non-zero out-of-plane piezoelectricity [22, 162]. More importantly, as depicted in Figure 3-14a, when an aligned 3R-MoS_2 flake was stretched along x direction for 1 s and released for 1.5 s, the polarities of the generated current and voltage were clearly opposite to those caused by stretching along its y direction. This is because a tension strain applied along its zigzag direction would cause an effective compression strain in the armchair direction, leading to induction of opposite piezo-charges to the two electrodes and, in turn, opposite voltage and current polarities. For a non-aligned 3R MoS_2 in Figure 3-14b in contrast, the polarities of the generated current and voltage were consistent under a strain along the x or y axis, which might be attributed to the unique coupling function of the in-plane and out-of-plane piezoelectricity in 3R MoS_2. This is also observed in the previous studies of α-In_2Se_3 flakes, which also owns in-plane and out-of-plane piezoelectricity properties [77, 79].

To illustrate this phenomenon, the third-order relation of the induced polarization charges and stress tensor is expressed as:

$$P_i = e_{ijk}\varepsilon_{jk} \quad (3.1)$$

where P_i is the polarization charges along *i* direction, e_{ijk} is the third-order piezoelectric coefficient and ε_{jk} is the strain tensor. The i, j, k and l take the values 1,2,3.

Since the stress tensor ε_{jk} is symmetry, the two-index natation (*j,k* in the stress tensor) is replaced by a single index ranging from 1 to 6 as:

$$11 \rightarrow 1; 22 \rightarrow 2; 33 \rightarrow 3; 23 \rightarrow 4; 31 \rightarrow 5; 12 \rightarrow 6$$

Therefore, the tensor multiplication in equation 3.1 is rewritten as [173]:

$$\begin{pmatrix} P_1 \\ P_2 \\ P_3 \end{pmatrix} = \begin{pmatrix} e_{11} & e_{12} & e_{13} & e_{14} & e_{15} & e_{16} \\ e_{21} & e_{22} & e_{23} & e_{24} & e_{25} & e_{26} \\ e_{11} & e_{11} & e_{11} & e_{11} & e_{11} & e_{11} \end{pmatrix} \begin{pmatrix} \varepsilon_1 \\ \varepsilon_2 \\ \varepsilon_3 \\ 2\varepsilon_4 \\ 2\varepsilon_5 \\ 2\varepsilon_6 \end{pmatrix} \quad (3.2)$$

The e-piezoelectric coefficient tensor for the C_{3v} point group 3R MoS_2 is expressed as [22]:

$$\begin{pmatrix} 0 & 0 & 0 & 0 & e_{15} & -e_{22} \\ -e_{22} & e_{22} & 0 & e_{15} & 0 & 0 \\ e_{31} & e_{31} & e_{33} & 0 & 0 & 0 \end{pmatrix} \quad (3.3)$$

The P_i polarization charges becomes:

$$\begin{pmatrix} P_1 \\ P_2 \\ P_3 \end{pmatrix} = \begin{pmatrix} 0 & 2e_{15}\varepsilon_5 & -2e_{22}\varepsilon_6 \\ 2e_{15}\varepsilon_4 & -e_{22}\varepsilon_1 & e_{22}\varepsilon_2 \\ e_{31}\varepsilon_1 & e_{31}\varepsilon_2 & e_{33}\varepsilon_3 \end{pmatrix} \quad (3.4)$$

According to theoretical calculation, the e_{22}, e_{31}, e_{33} and e_{15} are 0.64, -0.045, 0.14 and -0.079 C/m^2. Due to e_{15} is much smaller than e_{22}, the P_2 could be expressed as:

$$P_2 = e_{22}(\varepsilon_2 - \varepsilon_1) \quad (3.5)$$

where $\varepsilon_1$and ε_2 are strain along x, y axis. The polarization P_2 output signs could be reserved when strain is rotated 90 degrees, which is inconsistent with our experimental results. The crystal orientation-dependent polarization generation of multilayer 3R MoS_2 is different from monolayer 2H MoS_2, in which the experimental study showed that polarization could reverse signs along armchair direction when strain is rotated 90°[19]. While, for multilayer 3R MoS_2, the polarization revere signs along zigzag direction under the same condition. Besides, the 3R MoS_2 is able to generate polarization charges under applied strain at any directions.

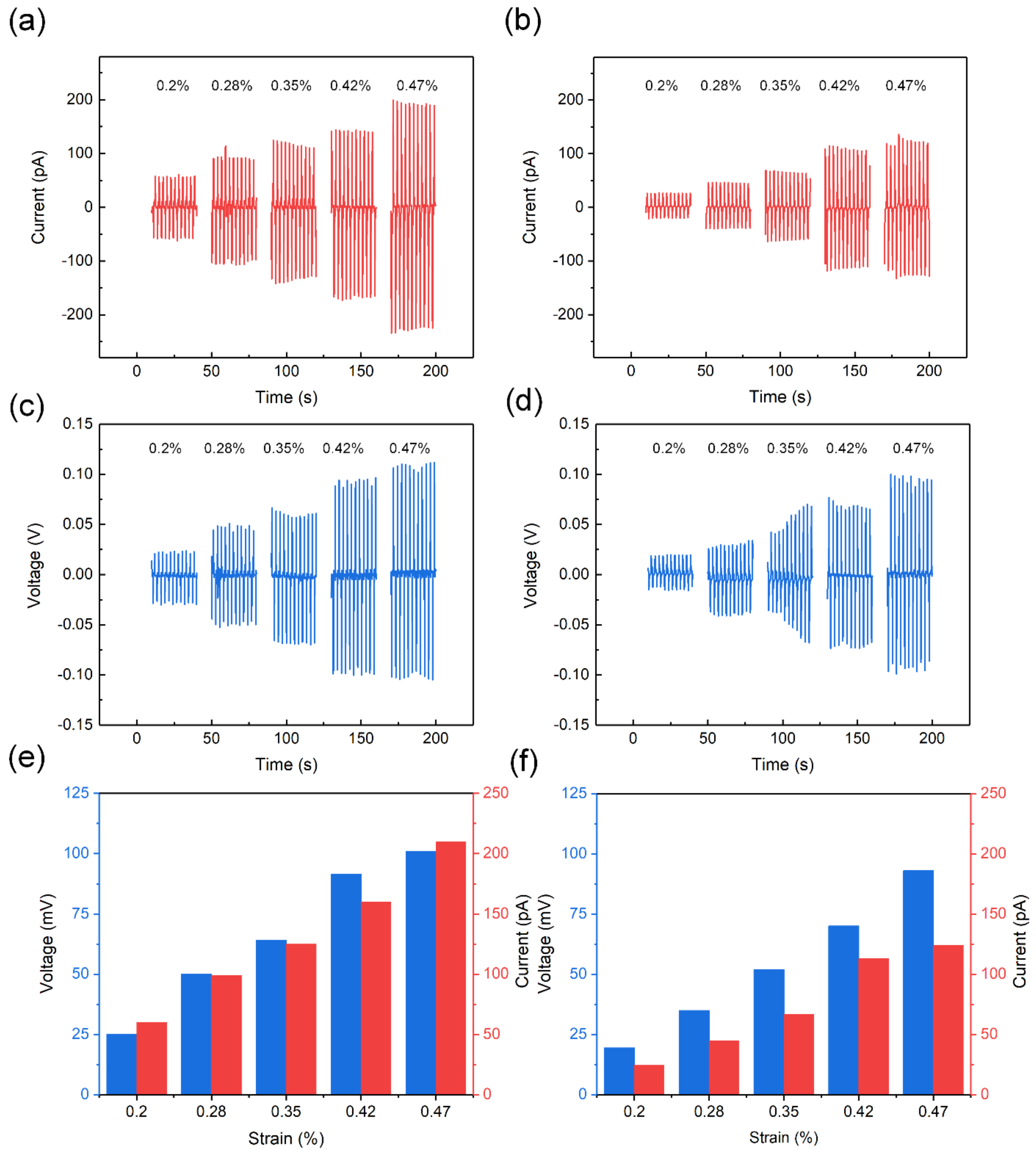

Figure 3-12 Piezoelectric outputs of an aligned 3R MoS_2 flake. Piezoelectric current and voltage under various strains applied along (a, c) the x axis (zigzag) and (b, d) the y axis (armchair). The summary of the piezoelectric current and voltage outputs as a function of strain along (e) the x axis (zigzag) and (f) the y axis (armchair).

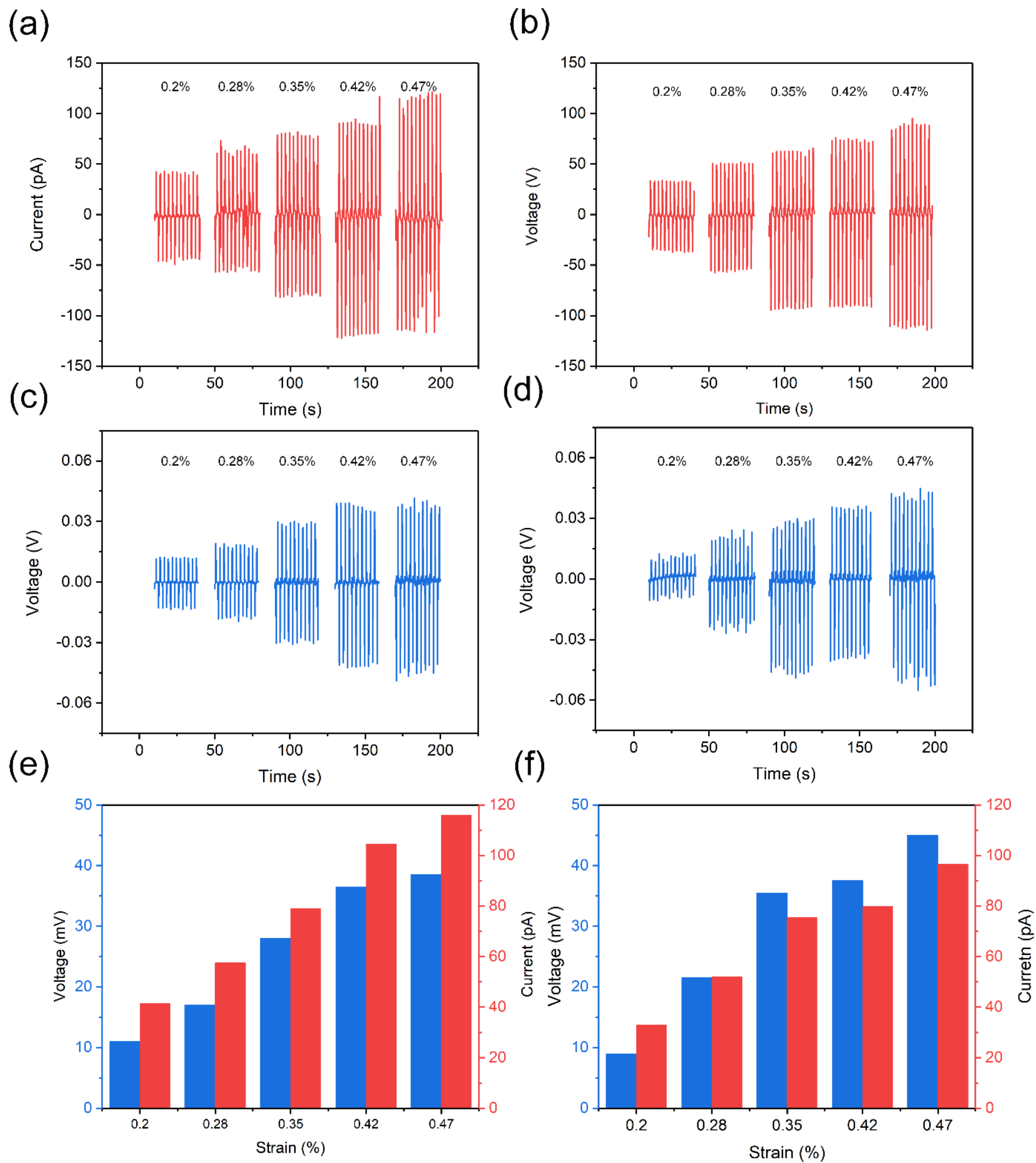

Figure 3-13 Piezoelectric outputs of a non-aligned 3R MoS_2 flake. The piezoelectric current and voltage under various strains applied along (a, c) the x axis (horizontal) and (b, d) the y axis (vertical). The summary of the piezoelectric current and voltage as the function of strain along (e) the x axis (horizontal) and (f) the y axis (vertical).

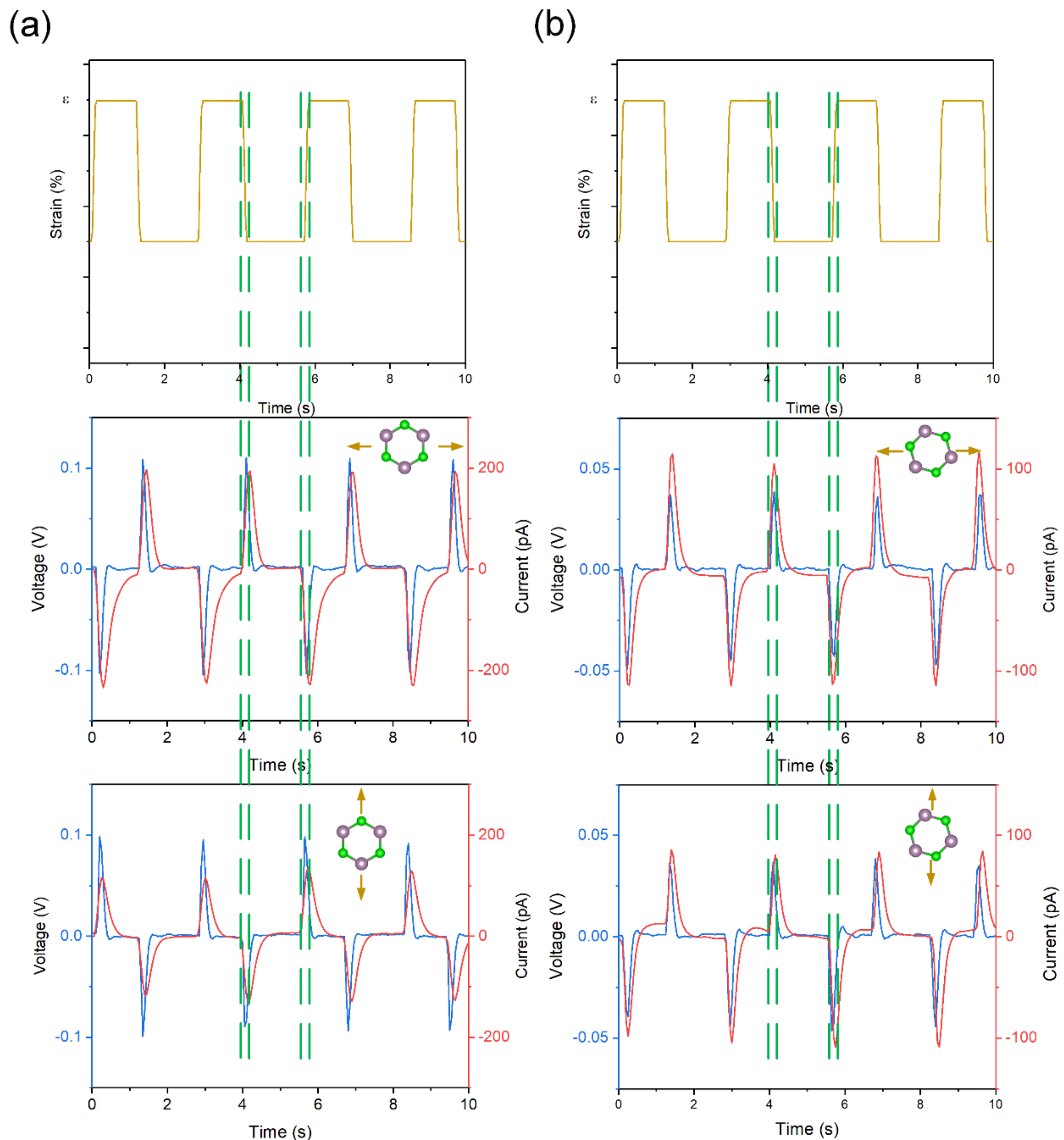

Figure 3-14 Voltage (V_{oc}) and current (I_{sc}) responses of aligned and non-aligned 3R MoS_2 flakes under a periodic strain. Top: The external strain as a function of time, Middle: corresponding several piezoelectric output cycles along the x axis (zigzag or horizontal), Bottom: corresponding several piezoelectric output cycles along the y axis (armchair or vertical) of (a) aligned and (b) non-aligned 3R MoS_2 flake, respectively.

To exclude the electrical influence from the substrate, a bare polyimide substrate and a 2H MoS_2 flake on polyimide were characterized under 0.47% tensile strain, respectively, and no obvious output voltage and current were detected, as shown in Figure 3-15.

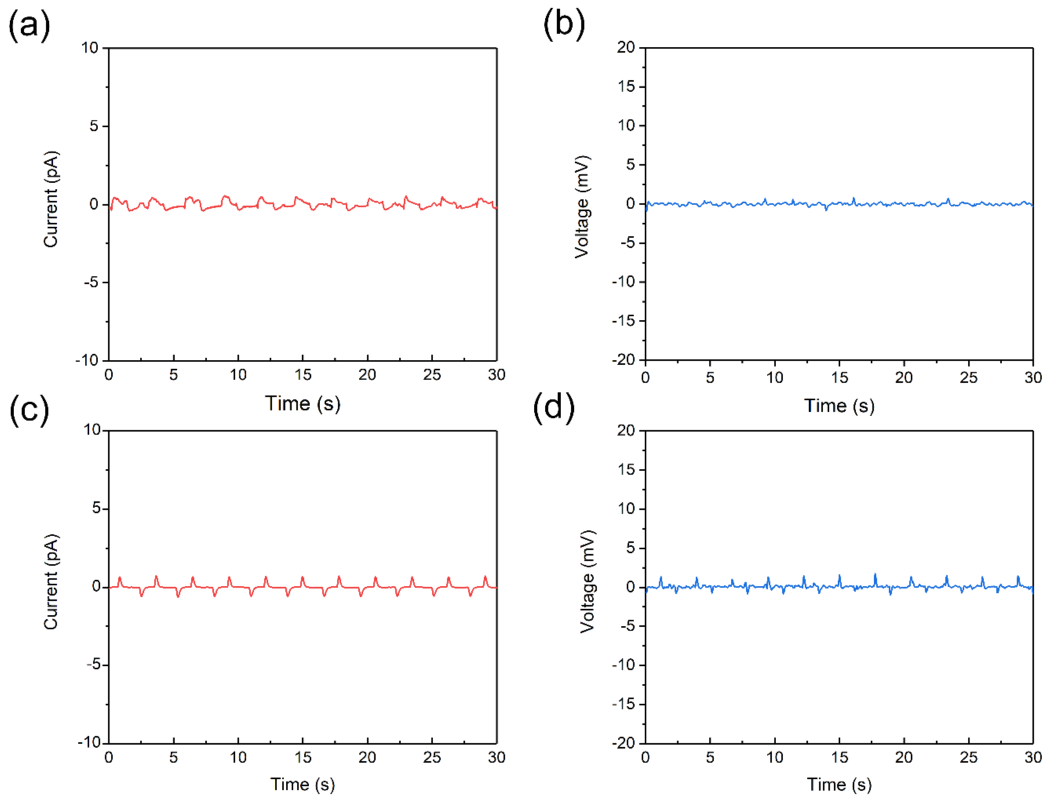

Figure 3-15 Electrical measurements on a bare polyimide substrate and 2H MoS_2 flake on polyimide. The current and voltage output of (a,b) bare polyimide substrate (without any flake) and (c,d) 2H MoS_2 flake on polyimide substrate under a strain of 0.47%, respectively.

In addition, a probe connection switching test was conducted on the aligned MoS_2 flake under 0.47% strain. A reverse output current occurred when the connection polarity was switched, proving that the electrical output from 3R MoS_2 flakes, in Figure 3-16.

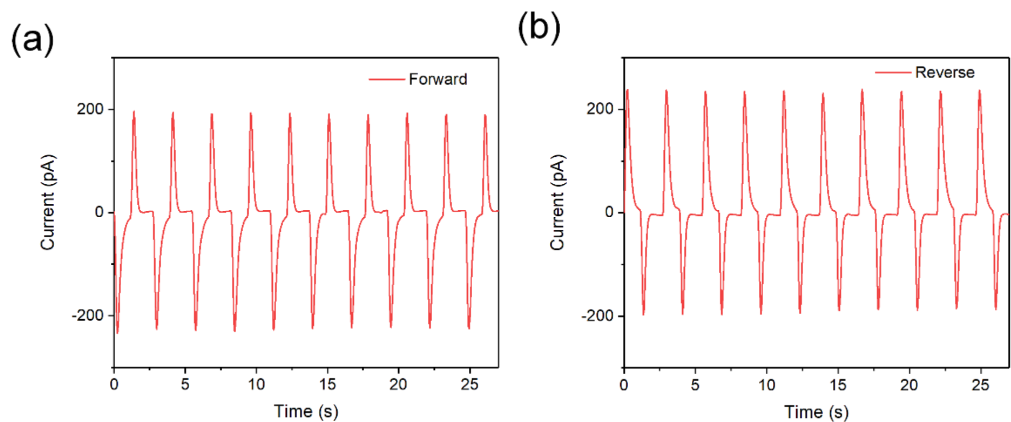

Figure 3-16 Polarity switching test of the aligned MoS_2 flake under 0.47% strain with (a) forward and (b) reverse connections.

In a comparison of monolayer PMs, multilayer MoS_2 flakes have a high Young's modulus and are promising for energy harvesting applications [13, 174]. A mechanical durability test was performed on an 3R MoS_2 flake with a frequency of 0.25Hz cycling bending test, as shown in Figure 3-17. After 720 cycles, the output current decreased from ~210 pA to ~180 pA, about 85.7% of the initial values, suggesting that multilayer MoS_2 flakes are of a high mechanical durability, a very good material for flexible sensors, etc.

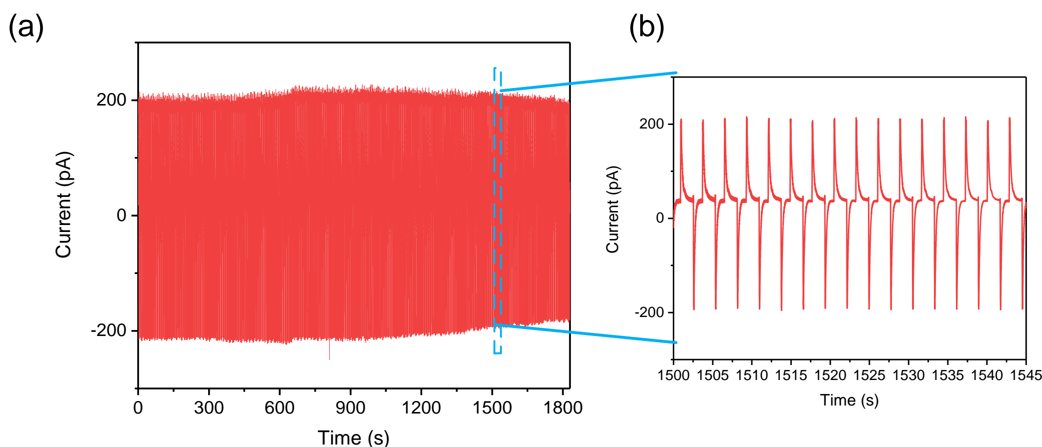

Figure 3-17 Mechanical durability and stability test of an aligned MoS_2 flake under a strain of 0.47% (a) The output current as a function of time. (b) The extracted output current from 1500s to 1545s.

To better evaluate the mechanical to electric power conversion performance, the peak piezoelectric output voltage and current were measured as a function of external resistance at a tensile strain of 0.47% in Figure 3-18a. The maximum instantaneous power was around 11.8 pW at a load resistance of 200 MΩ, as displayed in Figure 3-18b. The whole size of the aligned 3R MoS_2 flake was estimated around 182 μm^2, and the power density was calculated around 65 mW/m^2. To our best knowledge, this power density was at least one order larger than any other m-MoS_2 based PENG devices reported so far, as listed in Table 3-2 Comparison of 3R MoS_2 piezoelectric response with 2D material based PENG devices. To further improve the power density, doping of the MoS_2 flakes might be adopted [141].

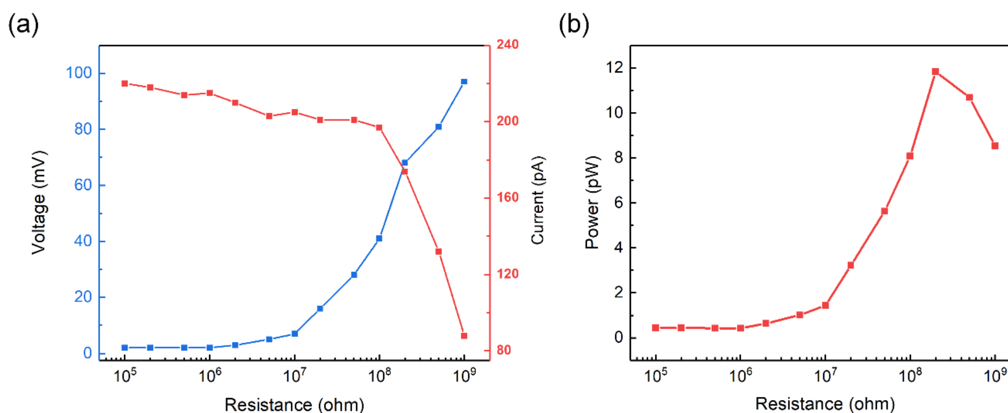

Figure 3-18 (a) The piezoelectric peak output voltage and current and (b) the instantaneous power of a 3R MoS_2 based PENG.

2D materials	V (mV)	I (pA)	Maximum instantaneous power (Load resistance)	Strain (%)	Power density (mW/m^2)	Reference
m-MoS_2	18 (V_{oc})	27 (I_{sc})		0.64		[19]
	3.5 (calc)	12.5 (calc)	55.3fW (220 MΩ)	0.53	2	
m-MoS_2 (armchair)	20 (1GΩ)		0.4 (1GΩ)		0.5	[140]
m-MoS_2 (zigzag)	10 (1GΩ)		0.2 (1 GΩ)		0.25	
Bilayer-WSe_2	57	71	4.05 (0.1 GΩ)	0.89	0.8	[20]
S-treated MoS_2	20 (1GΩ)	100 (1GΩ)	0.73 (500 MΩ)	0.7	0.073	[141]
7L-In_2Se_3	363	185	67.2	0.31	224	[143]
4L-InSe	22	63	1.39	0.31	4.6	
m-SnS	150(1 GΩ)	160 (1 GΩ)	24 (1GΩ)	0.7	24	[69]
3R MoS_2	97(V_{oc})	210 (I_{sc})	11.8 (200 MΩ)	0.47	65	This work

Table 3-2 Comparison of 3R MoS_2 piezoelectric response with 2D material based PENG devices.

3.4.2.3 3R MoS_2 based PENG monitoring finger motion

Due to superior flexibility and easy integration, 2D piezoelectric materials have a great potential in wearable electronics, biosensing and bio-energy harvester [175-177]. Here, finger motion monitor can be achieved by attaching a 3R MoS_2 based PENG on a finger,

see Figure 3-19a. Once the finger clenched and released, the device could immediately give positive and negative voltage/current pulses. The amplitudes of the voltage/current pulses were proportional to the degree of bending, as despicted in Figure 3-19b. The device could immediately and constantly provide outputs as the finger bended at different frequencies, as shown in Figure3-19c.

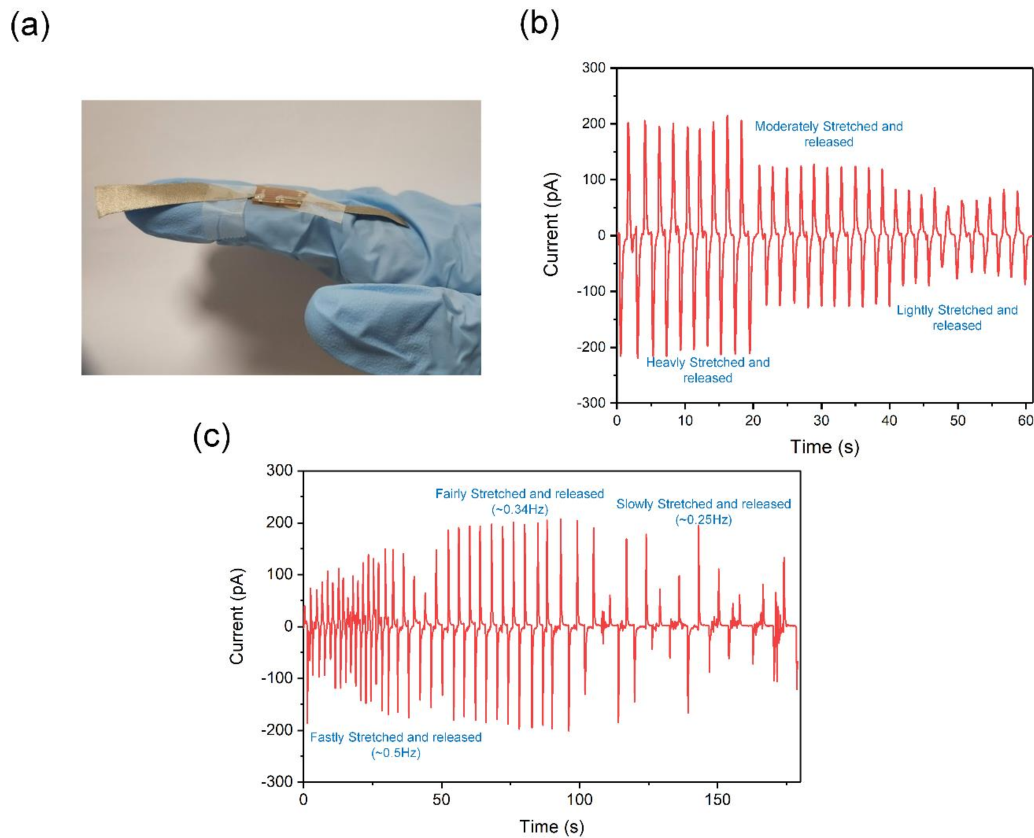

Figure 3-19 3R MoS2 based PENG monitoring finger motion (a) Optical image of the 3R MoS_2 PENG attached onto a finger. (b) Piezoelectric output of current at different curvatures of the finger clenching and releasing. (c) Piezoelectric output of current at different frequencies of the finger clenching and releasing.

3.4.3 Piezoelectric coefficients of 3R MoS_2

When an electric field is applied to a piezoelectric material, mechanical stress/strain must be induced (reverse piezoelectric effect). Here, the out-of-plane piezoelectric

coefficient d_{33} and excited lateral piezoresponse were measured and observed through PFM. In fact, for thin piezoelectric film applications in nanoelectronic devices, piezoelectric coefficients are the most important piezoelectric parameters. The d_{33} here is the induced strain in direction 3 (z) while the flakes are polarized per unit electric field applied in direction 3 [105].

3.4.3.1 Out-of-plane piezoelectric coefficient d_{33} of 3R MoS_2

Prior to the DART PFM measurements of 2D materials, our PFM was calibrated using a piece of periodically poled lithium niobate (PPLN), one of the conventional inorganic piezoelectric materials, provided by our AFM/PFM manufacturer specially for the calibration purpose. As illustrated in Figure 3-20, the PPLN was implemented with a sweep of AC drive amplitude from 0V to 1.5V at a step of 0.25V [178]. The results showed a good out-of-plane piezo response of PPLN and clear 180° phase change between the adjacent and opposite orientation polarization charge.

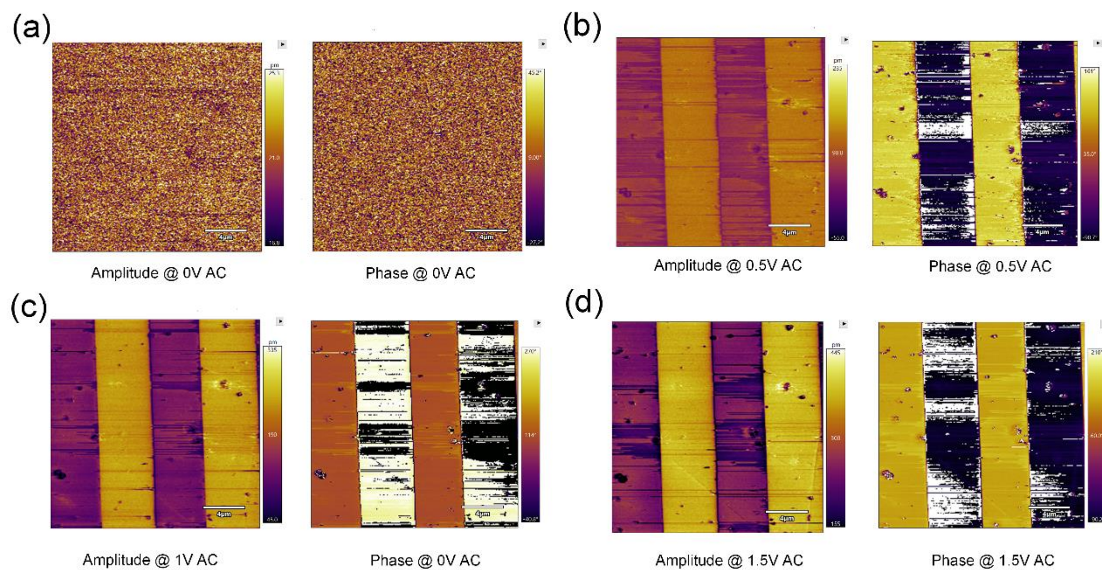

Figure 3-20 PFM images of the out-of-plane piezoresponse amplitude and phase for the PPLN at a AC drive amplitude of (a) 0V, (b) 0.5V, (c) 1.0V and (d) 1.5V.

Several areas were selected from the PFM amplitude image to quantitatively evaluate d_{33}. The inverse optical lever sensitivity (InvOLS), a necessary parameter for the cantilever spring constant calculation, was calibrated. The tip moving distance could be derived by multiplying the InvOLS with the deflection signals. Due to the AFM sharp tip, the electric field is not uniform between the tip and conductive substrate. As a result, the relationship between the piezoelectric amplitude and effective piezoelectric coefficient d_{eff} is given by the equation:

$$Amplitude = V_f \times \sigma = Q \times d_{eff} \times V_{ac} \tag{3.6}$$

where V_f is the vertical deflection signal, σ is the calibration constant of InvOLS, Q is the quality factor and V_{ac} is the applied AC bias voltage. The AFM tip was in weak indentation with the flakes, and therefore, the d_{33} and d_{eff} follow the relationship of $d_{33} = 2 \times d_{eff}$ [117, 179]. The d_{eff} was estimated around 3.52 ± 0.11 pm/V and 2.09 ± 0.13 pm/V for the PPLN 'up' and 'down' domains, respectively, as shown in Figure 3-21. The 'up' and 'down' domains represent opposite piezoelectric polarization directions of PPLN. The higher piezoelectric amplitude domain was considered as 'up' domain and the lower piezoelectric amplitude domain was considered as 'down' domain.

The measured piezoelectric coefficient d_{33} of PPLN was 7.04 ± 0.22 pm/V and 4.2 ± 0.26 pm/V for 'up' and 'down' domains, which were in consistent with previously reported value [180, 181], as shown in Figure 3-21. This calibration suggested that our DART-PFM measurement system was in a good condition and it was employed to determine d_{33} of the 2D materials studied in this work.

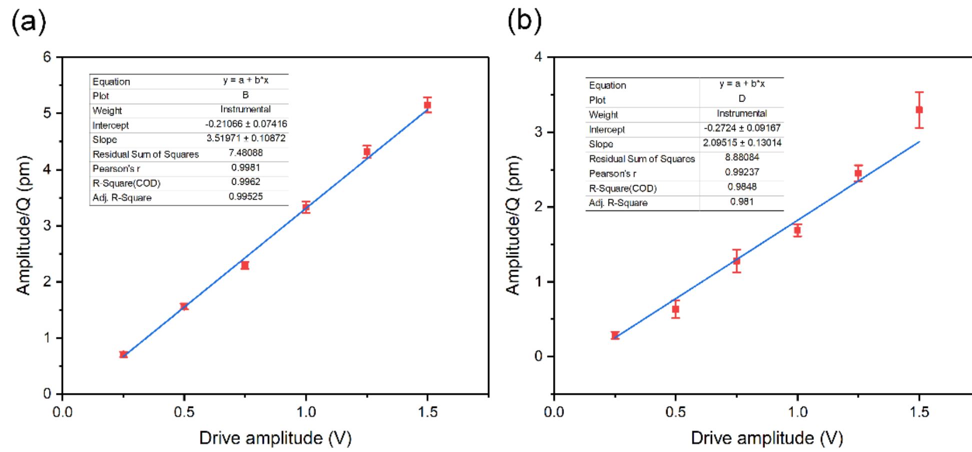

Figure 3-21 PPLN piezoelectric coefficient d_{33} estimation.

The out-of-plane piezoresponse of an 18 nm thick 3R MoS_2 flake was conducted using the DART-PFM technique, as displayed in Figure 3-22. The PFM images show a strong piezoelectric response, proving the existence of out-of-plane piezoelectricity in the thick multilayer 3R MoS_2 flake for the first time. For comparison, the 2H MoS_2 flakes were also mechanically exfoliated and transferred on the Au surface for DART-PFM measurement. The 2H MoS_2 flakes of 15 nm and 56 nm thickness did not show any out-of-plane piezoelectric response, as shown in Figure 3-23.

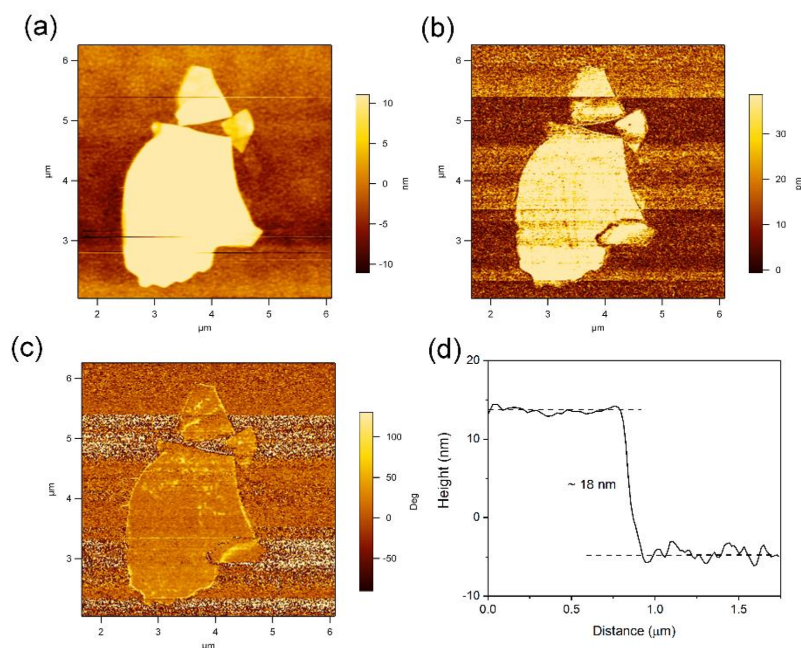

Figure 3-22 Out-of-plane piezo response of a 18 nm thick 3R MoS_2 flake. (a) AFM topography, (b) PFM amplitude, (c) PFM phase images at a bias voltage of 0.75 V and (d) Height profile of the 3R MoS_2 flake.

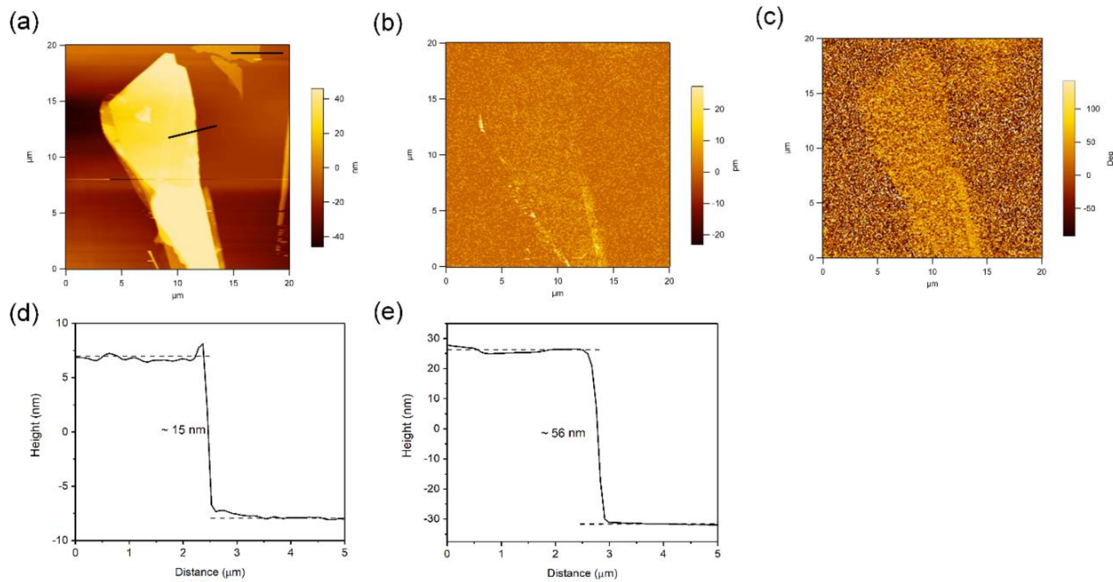

Figure 3-23 Out-of-plane piezo response of 15 nm and 56 nm thick 2H MoS_2 flakes (a) AFM topography, (b) PFM amplitude, (c) PFM phase images at a bias voltage of 0.75 V, (d) Height profile of the 15 nm 2H MoS_2 flake and (d) Height profile of the 56 nm 2H MoS_2 flake.

To determine d_{33} of 18 nm thick 3R MoS_2 flake, the AC voltage sweeping from 0 V to 1.5 V at a step of 0.25V were applied on the flake. The calculation method is the same used in the PPLN d_{33} calibration. In the experiments with the 18 nm thick 3R MoS_2 flake, the d_{eff} was estimated around 0.44 ± 0.02 pm/V as illustrated in Figure 3-24. The d_{33} hence was around 0.88 ± 0.04 pm/V for 18 nm 3R MoS_2 flakes.

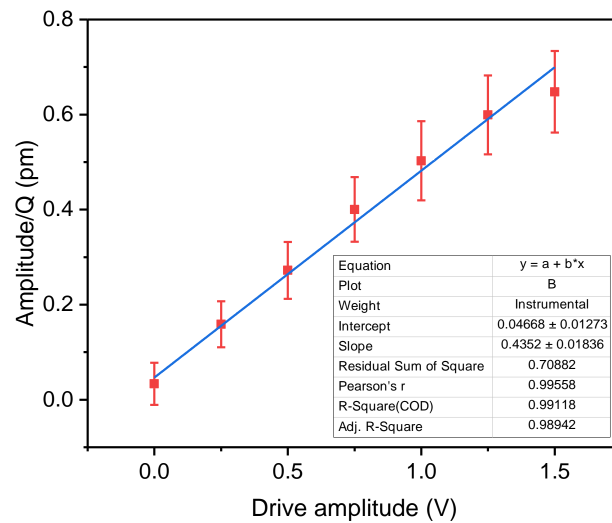

Figure 3-24 Piezoelectric coefficient d_{eff} fitting of 18 nm thick 3R MoS_2 flake.

Furthermore, the values of d_{33} of 3R MoS_2 as the function of the flakes thickness plotted in the Figure 3-25. There was no an apparent dependence relation between d_{33} and the thickness. But the d_{33} increase and saturate around 1.0 pm/V when the thickness increase more than 20 nm. It should be pointed out that our results are three to five times larger than the theoretical value of 0.27 pm/V [22].

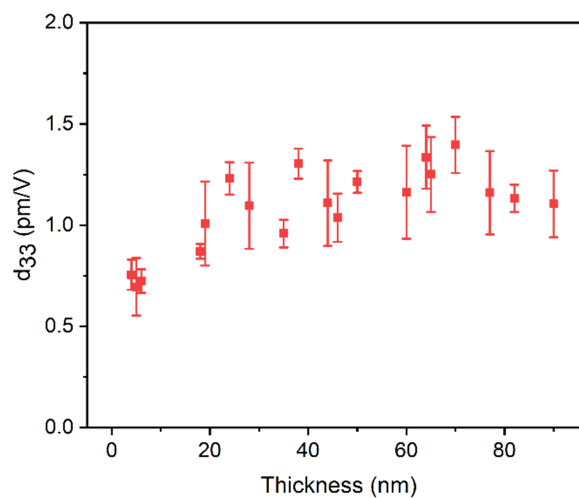

Figure 3-25 The d_{33} piezoelectric coefficients as a function of 3R MoS_2 thickness.

3.4.3.2 Lateral excitation PFM of 3R MoS_2

As illustrated in Figure 3-25a-d, the lateral field excitation on a 78 nm thick 3R MoS_2 flake could transform the in-plane strain into out-of-plane detectable mechanical deformation, which was probed by the non-conductive tip. In comparison, no piezo response was observed from 150 nm thick 2H MoS_2 when it was subject to a lateral electric field, owing to its centrosymmetry structure in Figure 3-26e-h. These experimental results proved again the 3R MoS_2 flakes are of the in-plane and out-of-plane piezoelectricity, irrespective of the thickness.

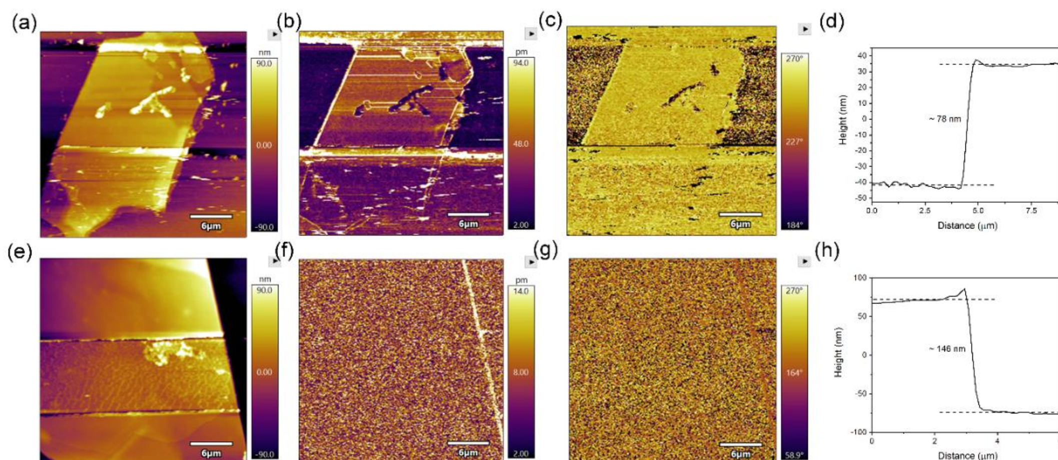

Figure 3-26 Lateral excitation PFM of a 78nm thick 3R MoS_2 flake. (a-d) AFM topography, PFM amplitude, PFM phase images and Height profile of the 3R MoS_2 flake. (e-h) AFM topography, PFM amplitude, PFM phase images and Height profile of the 2H MoS_2 flake at a bias voltage of 8 V.

The lateral excited piezo amplitude as function of the applied voltage is shown in Figure 3-27. It was found that the across the lateral excited piezo amplitude was hyperbolically, rather than linearly increased with the voltage. This might be attributed to stronger coupling of enhanced in-plane strain at high field and out-of-plane deformation.

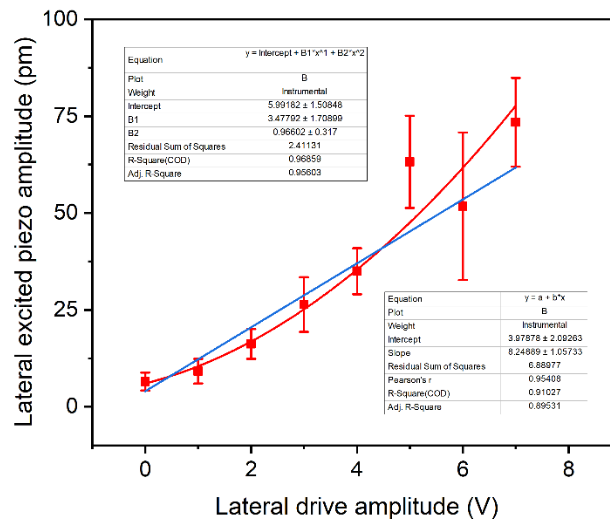

Figure 3-27 Lateral excited piezo amplitude as function of lateral drive amplitude of the 78 nm 3R MoS_2 flake.

The limitation here is hard to quantify precisely the piezoelectric coefficients d_{22} and d_{13}, which requires improved device structure and novel methods. The findings from PFM experiments provide us with an in-depth understanding of the piezoelectric properties of this new 2D material, with which a new generation of advanced piezo devices could be developed.

3.5 Conclusion

In this chapter, the strong piezoelectricity of 3R MoS_2 flakes is clearly observed for the first time with several thicknesses. The broken inversion symmetry structure of 3R MoS_2 was evidenced and characterized using SHG, STEM and Raman spectroscopy. The 3R MoS_2 piezoelectric nanogenerators have been successfully fabricated and produced oscillating piezoelectric voltage and currents under tensile strain and compressive strain. For an aligned 3R MoS_2 device, a peak output open circuit voltage

Voc of ~102 mV and a short circuit current of ~ 210 pA were achieved at a uniaxial strain of 0.47% along x-axis (zigzag direction), whereas the output revised its sign when the strain direction is rotated to y-axis (armchair direction). The crystal orientation-dependent polarization generation of 3R MoS_2 is along the zigzag direction, which is unique and different from a monolayer MoS_2 flake. The highest power density was measured around 65 mW/m^2 with 200 MΩ load resistance, which achieves the highest mechanical to electric energy conversion efficiency among piezoelectric TMDCS so far. This device also exhibited an excellent mechanical stability. In general, the 3R MoS_2 PENGs demonstrate the large piezoelectricity in 3R MoS_2 flakes and suitability in the low frequencies. The amplitude and phase images obtained from PFM measurements suggest an apparent piezoelectric response from 3R MoS_2 flakes, in a sharp contrast to 2H MoS_2 without vertical piezoelectric response. The piezoelectric coefficient d_{33} were measured around from 0.7 pm/V to 1.5 pm/V for multilayer 3R MoS_2, and the lateral excited piezoelectric images confirm that a coupling of a strong in-plane and out-of-plane piezoelectricity.

Chapter 4 Thermal transport property of 3R MoS_2 flakes under strains

4.1 Introduction

As introduced in Chapter 2, low-dimensional piezoelectric nanomaterials, such as Wurtzite structured materials (ZnO, GaN and CdS), and transition metal dichalcogenides (TMDCs) (like MoS_2, WS_2 and WSe_2), have been extensively studied for their strong coupling among piezoelectric, semiconducting and optical properties and provide paths for novel and functional flexible devices [19, 20, 54, 182].

Alongside the electronic and optical properties, thermal transport properties of low dimensional materials, like h-BN, graphene and MoS_2, have attracted much attention. They are not only good candidates for future flexible electronics but also suitable for thermal control and management for miniaturized and integrated devices [123, 183, 184]. Especially for atomically thin MoS_2, extensive studies have been focused onto the influences of grain boundaries and layer-thickness and isotopes on the thermal transport [185-189]. Several theoretical studies showed that the intrinsic thermal conductivities of MoS_2 flakes could be enhanced or weaken by uniaxial strains [190-192]. In addition, it has been suggested that the heat transport property of the monolayer GaN could be modulated by the electric field owing to its piezoelectric characteristics [193].

For the devices based on low dimensional materials, the electrical contacts are usually made of metals in contact with the materials on supporting substrates. Thus, interfacial thermal conductance (ITC) between metals-2D materials and 2D materials-substrate deserves in-depth study. Several theoretical and experimental kinds of research have been focused on ITC measurements of vertical MoS_2 on various substrates or their 2D materials heterostructure [133, 194-197]. For metal/MoS_2 contacts, the ITC is

dominated by the interface interactions from van der Waals (vdWs) bonding at the side contact and\or covalent bonds at the edge contact [198, 199]. The theoretical calculation found that the ITC also depends on the interface orientation at the MoS_2/Au contact. Especially for both MoS_2/Au (111) and MoS_2/Au (110) contacts, the ITC decreases significantly when θ increased from 0° to 30°, where θ is the angle between the Au (011) direction and the contact line of MoS_2/Au [200]. However, to our knowledge, no experimental studies about strain modulated thermal transport across piezoelectric MoS_2 devices until now. In this chapter, we present our results of the intrinsic thermal conductivity and ITC of metal/3R MoS_2 contacts under uniaxial strains.

In this chapter, we present the study of intrinsic thermal conductivity of 3R MoS_2 flakes measured under uniaxial strains. The intrinsic thermal conductivity is slightly changed around 3% to 4% under a uniaxial strain of ±0.26%. The thermal conductivity of metal-piezoelectric semiconductor-metal (MSPM), which is influenced by the intrinsic thermal conductivity and ITC, was measured using a novel laser heating method. The thermal conductance of metal/3R MoS_2 flake contacts displayed a significant change under a uniaxial strain, in comparison with metal/2H MoS_2 flake contacts. These findings are the first time experimental observation of strain-modulation heat transport in the metal-piezoelectric semiconductor-metal structures, which would help us to better understand the underlying physics of low-dimensional piezoelectric materials heat transfer and offer a thermal management strategy for piezoelectric nanomaterials-based devices.

4.2 Devices fabrication and Characterization

4.2.1 Preparation of MoS_2 flakes

Before being mechanically exfoliated, the flexible polyimide substrate was fabricated by spinning coating Poly (pyromellitic dianhydride-co-4,4′-oxydianiline), amic acid solution (Purchased from Sigma Aldrich) on a piece of flexible polished stainless steel at 3000rpm for 45 seconds, and then was annealed in argon gas at 250 °C for 2 h. All mechanically exfoliated crystal 2H or 3R MoS_2 flakes were successively identified by optical microscopy. The morphology and orientation of the flakes were determined by AFM imaging and SHG.

4.2.2 Preparation suspended 3R MoS_2

The suspended 3R MoS_2 samples were fabricated by conventional photolithography process as follows: One layer of thermal stable negative resist around 3.5μm thick (AZ® nLOF 2035, Microchemicals GmbH) was firstly spin coated on a polyimide substrate at 4000rpm for 45 seconds, and then soft baked at 110 °C for 60s. Then, a series of straight trenches with the width of 3 μm were transferred to the photoresist and developed. Subsequently, the 3R MoS_2 flakes were mechanically exfoliated on a SiO_2/Si substrate and transferred from the SiO_2/Si surface using PMMA to the prepared flexible polyimide surface with photoresist trenches. The PMMA was removed by acetone. The 3R MoS_2 flakes suspended on the trenches were located using optical microscopy. A pair of Au (150 nm) electrodes were deposited on the two terminals of the flake using a conventional lift-off process.

Next, the 3R MoS_2 flakes were mounted at a stage in a sealed chamber, in which the sample temperature could be modulated by liquid nitrogen and a heater. The

temperature-dependent Raman spectra were measured from 220 K to 460 K with a step of 20 K using WITec alpha 300 confocal Raman microscopy. The laser power was controlled to be less than 0.05 mW to avoid flake self-heating effect. After the temperature-dependent Raman measurements, the samples were brought out and bent to achieve a certain degree of tensile strains. They were then put back into the sealed chamber and performed laser power-dependent Raman measurements, in which the power was tuned from 0.05 mW to 0.36 mW with a step around 0.05 mW.

The thermal conductivity of the 3R MoS2 samples were also studied using a laser heating thermal couple technique The samples for this technique were fabricated by conventional photolithography process as follows: Firstly, a flexible polyimide substrate was cleaned by acetone, isopropyl alcohol, and deionized water. Then, the polyimide substrate was dried by nitrogen gas and baking at 105°C for 10min. The multilayer 3R MoS_2 flakes with typical thicknesses of 30-100nm and side lengths of 10-30 µm were mechanically exfoliated on polyimide substrate were selected. Then, a layer of 150nm Au thin film was deposited with an electron beam evaporator system (Edwards Auto 360). Au microelectrodes were fabricated by etching through photoresist (AZ5214w, photoresist image reversal, Microchemicals GmbH) patterns. The samples were then annealed in argon gas at 180 °C for 2 hours. After that, a 200 nm Ni film was deposited by a sputtering system (Elite sputter) at a DC power of 300W with 100 sccm Argon gas on top of the bottom Au microelectrodes to form a microthermal couple. In addition, Ni, Pd and Ag were deposited onto the bottom Au microelectrodes to microthermal couples.

For the thermal conductivity measurements, two Keithley 197A Autoraning Microvolt Digital Multimeters (DMMs) were used to measure thermal induced voltages on two thermal couple electrodes, respectively. The exaction laser of 532nm (WITec alpha 300 confocal Raman microscopy) on the Raman measurement system was used as a heating

source on one thermal couple electrode. The laser power was measured by a digital optical power and energy meter (Thorlabs'C-series Power Meter PM100D).

As 3R MoS_2 flakes (~20 μm long and a few tens of nanometer thick) were much smaller than the PI substrates deposited on the stainless steel (15 mm × 15mm × 30 μm), the tensile and compressive strains exerted onto the flakes deposited onto the PI substrate could be given by $\varepsilon = h/2r$, where h is the thickness of the PI substrate, and r is the bending radius. The strain ε was calculated and shown in Table 4-1.

Table 4-1 Parameters for calculating the applied strains.

h (μm)	r (mm)	ε
30	11.74	0.13%
30	5.68	0.26%

4.2.3 Optical and electrical characterization of 3R MoS_2 devices.

All Raman, AFM and SHG measurements were conducted with the same processes as those stated in section 3.3. The laser light absorbance, transmittance and reflectance spectra of the metal thin films and polyimide substrate were measured by UV-Vis spectroscopy (SHIMADZU UV-2450). The *I-V* characterizations were measured by Agilent B1500a semiconductor analyzer.

4.3 Results and discussion

4.3.1 In-plane thermal conductivity of MoS_2 flakes under strains

4.3.1.1 Sample structure and calibration of 3R MoS_2 flake light power absorption

To investigate the influences of strains on the in-plane thermal conductivities of 3R MoS_2 flakes, the Raman spectroscopy-based thermal conductivity measurement was performed on the suspended 3R MoS_2 flakes. This optothermal Raman method has been widely used to determine the thermal conductivities of 2D materials, recently for monolayer, bilayer and multilayer 2H MoS_2 [186, 201]. Figure 4-1a shows the optical image of a 3R MoS_2 flake suspended on a photoresist trench which was 3.2 μm wide and 3.5 μm deep on a flexible polyimide/stainless steel substrate. The length and width of uncovered flake are around 25 μm and 5 μm, respectively. In Figure 4-1b, a focused laser was incident on the center of the 3R MoS_2, which was suspended on trench. The Raman measurements were carried out using WITec alpha 300 confocal Raman microscopy with an excitation wavelength of 532 nm. The SHG plotting confirms that the armchair orientation of 3R MoS_2 was perpendicular to the electrodes in Figure 4-1c. To precisely determine the laser light power absorbed by the 3R MoS_2 flake, a similar thickness 3R MoS_2 flake was mechanically exfoliated on a quartz substrate, as shown in Figure 4-1d. As illustrated in Figure 4-1e-h, the 3R MoS_2 flake suspended on the trench and quartz substrate were measured using AFM, and the height profiles showed that both two flakes were around 35 nm thick.

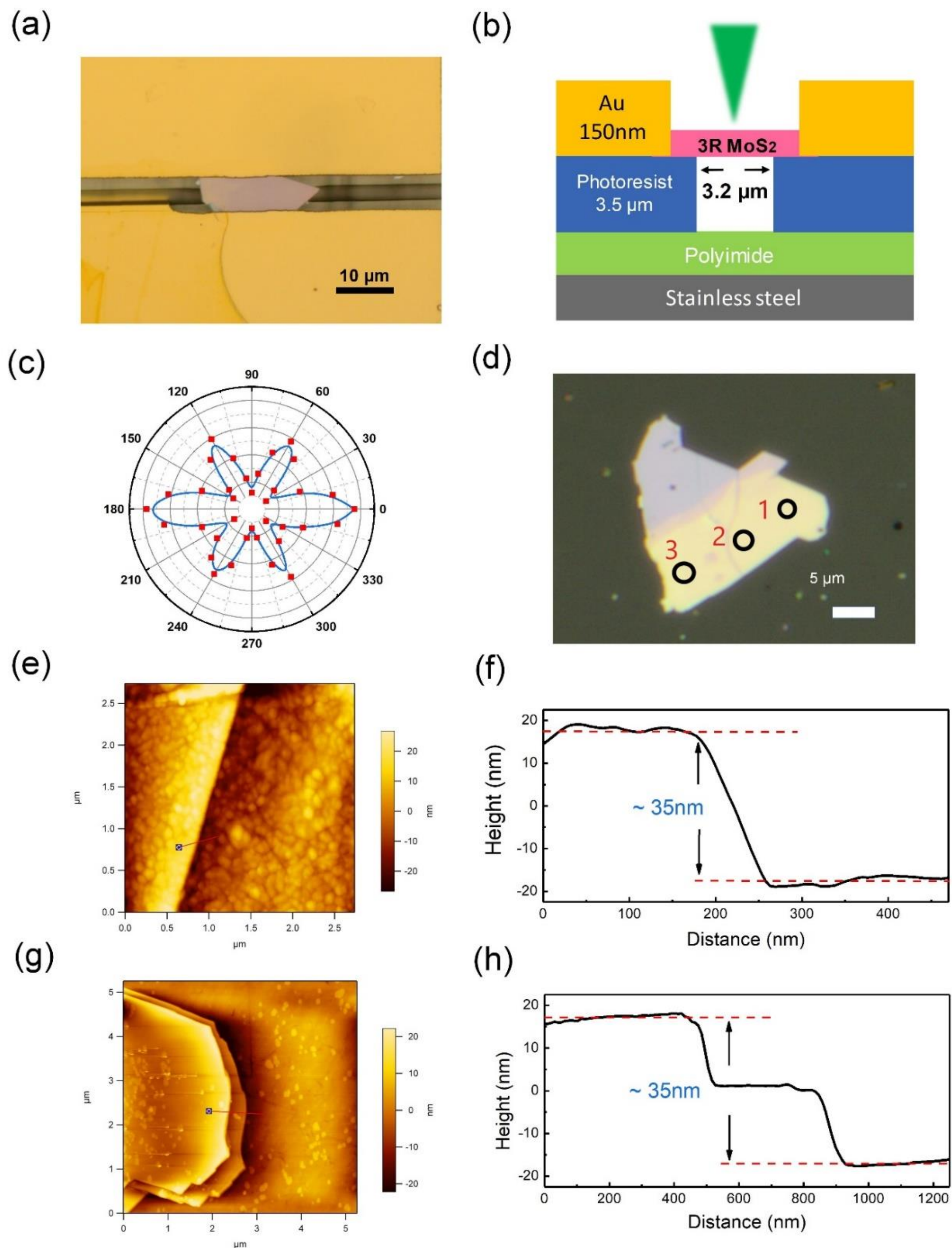

Figure 4-1 (a) Optical image of a 3R MoS_2 flake (35nm thickness) suspended on a 3.2 μm wide photoresist trench (The scale bar is 10μm). (b) Schematic of Raman thermal measurement experiment set up for the suspended 3R MoS_2 flake. (c) The angle-dependence SHG plotting of 3R MoS_2 flake. (d) Optical image of the 3R MoS_2 flake on the quartz substrate (three absorption spectra measurements are performed on points 1,

2 and 3. The scale bar is 5 μm). (e) AFM topography image and (f) height profile of the 3R MoS_2 flake suspended on the photoresist trench. (g) AFM topography image and (h) height profile of the 3R MoS_2 flake on the quartz substrate.

The laser light absorbance spectra were obtained from the transmittance measurement of the 3R MoS_2 flake by using WITec alpha 300 confocal Raman microscopy at a wavelength of 532 nm. The small reflectance was neglected here [202]. Light incident from bottom to top, and was collected by Raman system after passing through MoS_2. The transmittance (T) values throughout the flake, was obtained from dividing the transmitted power through the flake and the quartz by that through quartz substrate near to the flake. The weighted average absorbance spectrum was acquired (from points 1,2 and 3) and calculated from the transmitted optical power, and the absorbance at 532nm around is 0.47 ± 0.01, as shown in Figure 4-2a. Absorbance is the logarithm of incident to transmitted optical power through a material (absorbance = $2 - \log_{10\%}T$). Here, the reflection light from MoS_2 is neglected and the absorbance is dimensionless [203]. From the absorbance spectra, two prominent peaks at wavelengths ~620 nm (B excitonic transition peak) and ~665 (A excitonic transition peak) nm is related to the absorption due to the direct transitions at the K point of the Brillouin zone, were suspected [204]. Another C excitonic transition peak is at ~440 nm and its origin is still a subject of debate [205, 206]. The absorption peaks reflect that 3R MoS_2 flakes have high absorption of violet, orange and red light [207]. To estimate total incident laser power exposed on the 3R MoS_2 flake, the laser light reflectivity of bare polyimide substrate and polyimide with trenches were measured by using the same Raman system. The light incident from top to bottom and was collected by Raman system after reflecting from polyimide surface. The light transmission through polyimide was neglected. The total incident laser power was calculated using the following equation 4.1, with a reflection

coefficient R_{bot} at the wavelength 532nm from trench bottom and transmission coefficient T_{mos2} = 34% measured on same thickness 3R MoS_2 flake on the quartz substrate [208]:

$$I_{total} = I_0(1 + R_{bot} \times T_{mos2}) \tag{4.1}$$

where I_{total}, standing for the total incident laser power, is $1.054I_0$ and I_0 is the source laser power read from power meter. For the reflectivity spectra, the reflectivity is steadily increased from a wavelength of 450 nm and saturated ~ 600 nm [209]. The reflectivity of trenched polyimide area is decreased, which might be caused by the surrounding photoresist absorption.

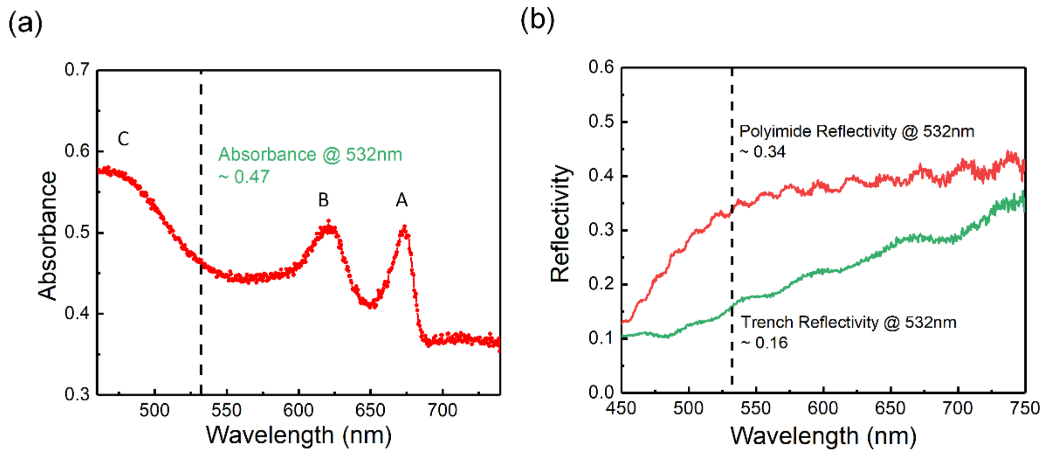

Figure 4-2 (a) Weighted average absorbance spectrum for the 3R MoS_2 flake on the quartz substrate. (b) Reflectivity spectra of polyimide substrate itself and under area at the trench bottom.

4.3.1.2 Calculation of intrinsic in-plane thermal conductivity under strains

Two kinds of measurements, i.e., the temperature-dependent Raman measurement and the power-dependent Raman measurement, were carried out to determine the intrinsic thermal conductivity of a 35nm thick 3R MoS_2 flake. The laser beam was focused on the center of the flake using a 100×objective lens (numerical aperture NA=0.95), with

Gaussian beam width of $2\lambda_0/(\pi NA) \approx 357$ nm for both measurements. Compared with the dimensions of the flake, it could result in a quasi-radial steady and uniform heat conduction in the flake laterally [126]. For a temperature-dependent measurement, a first-order temperature coefficient was obtained from the substrate temperature modulation induced Raman shift, where the substrate temperature was controlled by a heat stage [128]. For the laser power-dependent measurement, a first-order power coefficient was acquired from the laser power induced Raman shift, where the flake was heated up by the laser.

The Raman peak shifts of the MoS_2 frequency modes result mainly from thermal expansion or volume contribution and the temperature contribution caused by anharmonicity. The following equation describes the phonon frequency as a function of volume and temperature:

$$\left(\frac{\partial \ln \omega}{\partial T}\right)_p = \left(\frac{\partial \ln V}{\partial T}\right)_p \left(\frac{\partial \ln \omega}{\partial V}\right)_T + \left(\frac{\partial \ln \omega}{\partial T}\right)_V = -\frac{\gamma}{k}\left(\frac{\partial \ln \omega}{\partial P}\right)_T + (\frac{\partial \ln \omega}{\partial T})_V \tag{4.2}$$

where $\gamma \approx (\partial \ln V/\partial T)_p$ and $k \approx -(\partial \ln V/\partial P)_T$ are the volume thermal coefficient and isothermal volume compressibility [210]. In addition, MoS_2 phonon frequency modes shift to lower frequency ω as the lattice expands with a rate which is given by the Grüneisen parameter γ_m for a phonon mode m (which could be E_{2g} or A_{1g}):

$$\gamma_m = -\frac{1}{\omega_m}\frac{\partial \omega_m}{\partial \epsilon} \tag{4.3}$$

where the strain $\epsilon = \epsilon_x + \epsilon_y$ [211].

In Figure 4-3a, the Raman spectra were measured from a 3R MoS_2 sample whose temperature was increased from 220 K to 460 K. Two prominent peaks at about 383 and

480 cm^{-1} could be attributed to the in-plane E_{2g}^1 mode (in-plane opposing motions of sulfur and molybdenum) and out-of-plane A_{1g} mode (out-of-plane relative motions of sulfur atoms). Apparent linear red shift of the peaks with the temperature could be observed, as shown in Figs 4-3b,c [127, 201]. Since the A_{1g} mode is much stronger than that of the E_{2g}^1 mode and less sensitive to in-plane strains, the A_{1g} peak shifts were chosen to calculate temperature coefficient [212]. The Raman peak position ω (cm^{-1}) of A_{1g} mode follows a linear function of temperature:

$$\omega\,(T) = \omega_{T0} + \chi_T \Delta \mathrm{T} \qquad (4.4)$$

where ω_{T0} is the frequency of the A_{1g} at absolute zero temperature and χ_T, the slope of temperature dependence for A_{1g} mode, is the first-order temperature coefficient. Higher order temperature coefficients are only significant at high temperatures and these terms are not considered here [127]. The A_{1g} peak values, extracted from Lorentzian fitted Raman Spectra from 200 K to 460 K with each step of 20 K with fixed laser power, showed a reasonably good linear relation under different strains in Figure 4-3b. χ_T was found to be weakly dependent on the strains applied to the 3R MoS_2 flake and its values are listed in Table 4-2.

Similar to temperature-dependent Raman spectra measurement, the Raman spectra were collected with increasing laser power at room temperature of 300 K. A linear relation of A_{1g} phonon peak with the laser beam power could be described as:

$$\omega\,(P) = \omega_{P0} + \chi_P \Delta \mathrm{P} \qquad (4.5)$$

where ω_{P0}, is the frequency of the A_{1g} at zero power and χ_P, the slope of the power dependence for A_{1g} mode, is the first-order power coefficient. As seen in Figure 4-3c, χ_P under different strains was extracted from linear fittings. The values of χ_T and χ_P are summarized in Table 4-2.

Strain-biased 3R MoS_2 (%)	Temperature coefficient χ_T(cm^{-1}/K)	Power coefficient χ_P(cm^{-1}/mW)
+ 0.26	-0.01167±0.00012	-1.70749 ± 0.06947
0	-0.01145±0.00026	-1.66466 ± 0.06604
- 0.26	-0.01073±0.00032	-1.51399 ± 0.07312

Table 4-2 First-order Temperature coefficient χ_T, and Power coefficient χ_P extracted from the A_{1g} Raman peak shifts with the strains applied.

Based on χ_T and χ_P, the intrinsic in-plane thermal conductivity k can be estimated using two models. Considering radial heat flow, *Balandin et al* derived an simple expression for calculating *k* for a single layer graphene, i.e., $k = (1/2\pi h)(\Delta P/\Delta T)$, where *h* is the thickness of graphene [126]. This expression could be further modified for MoS_2 flakes as:

$$k = x_T\ (\frac{1}{2\pi t})\frac{1}{x_P} \tag{4.6}$$

where *t* is the thickness of the MoS_2 flake. The k therefore was estimated around 31.1 ± 1.5, 31.3 ± 1.9 and 32.2 ± 2.4 W/mK for the 3R MoS_2 with a strain of +0.26%, 0% and -0.26%, respectively. Since the contact interfacial thermal resistance and power absorption are not involved in this expression, the value of calculated *k* may have a large error.

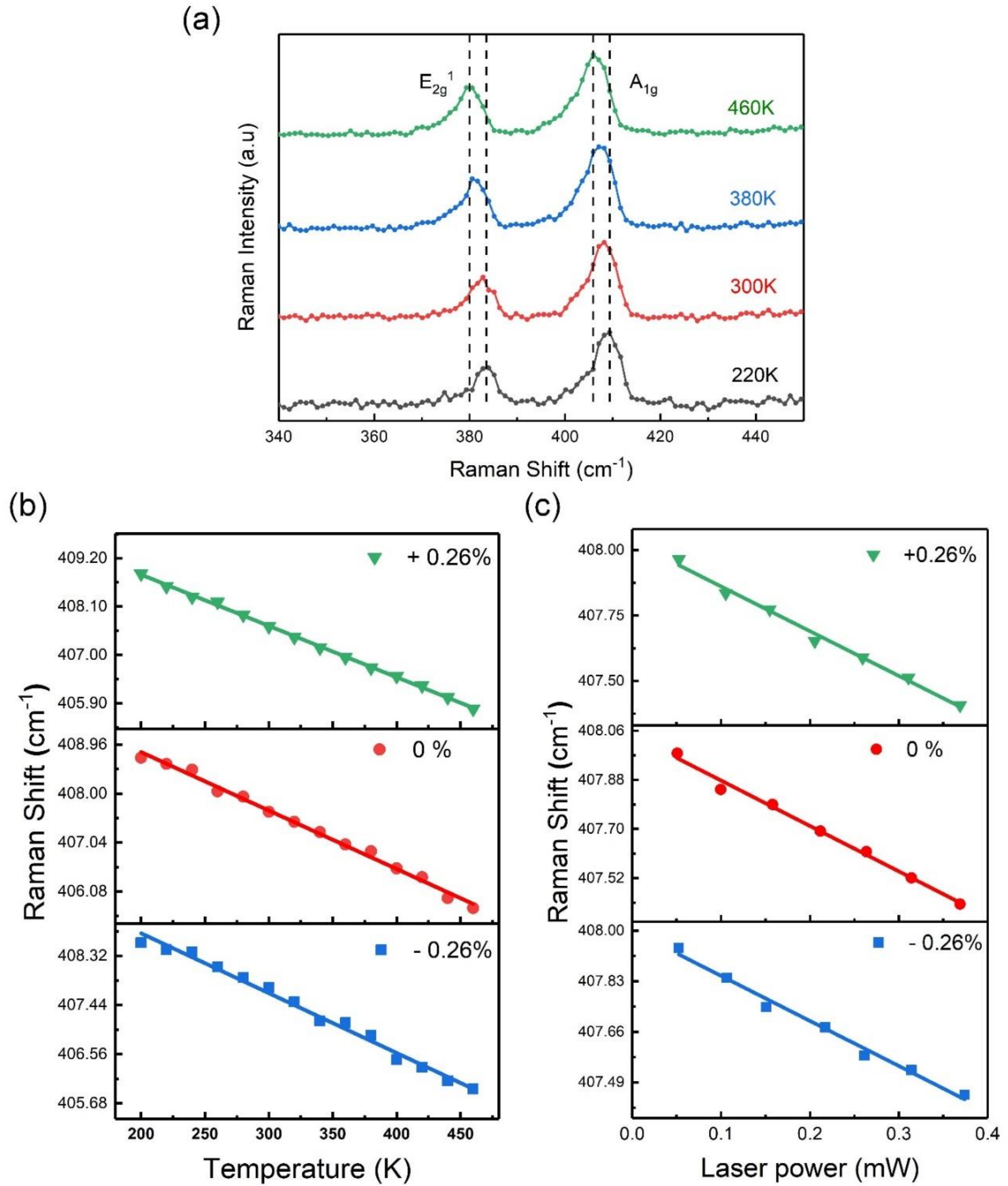

Figure 4-3 (a) The Raman spectra of a 3R MoS2 flake measured at different temperatures. (b) Temperature-dependent and (c) power-dependent Raman peak position shift of A_{1g} under a tensile (blue square +0.26%), zero (red circle 0%) and compressive (green triangular -0.26%) strain, respectively.

In the following, we use another model to calculate the thermal conductivity, in which the light absorbance in the flake and heat transport in the suspended and supported flake are taken into account Note that from the absorption spectrum discussed above, the value of the absorption was around 0.47 ± 0.01 at the wavelength 532 nm. The heat convection to the air could be ignored here as it only accounts the maximum up to 0.1 % of the total heat conduction [128]. Three specific assumptions are introduced in the modeling in order to simplify the analysis process: (i) the heat transfers radially from the center to edge of the flake, (ii) the heat deposited at the center of the flake under the laser light illumination is equal to the heat absorbed in a steady state and (iii) the temperature of the 3R MoS_2 flake under an Au thin film is considered to be the same as the ambient temperature far away from the center of the flake. Therefore, the heat dissipation equations of cylindrical coordinates in the suspended and supported area are [128, 201, 213]:

$$\frac{1}{r}\left[r\frac{dT_1(r)}{dr}\right]+q(r)=0 \qquad for\, r<R \qquad (4.7)$$

$$k'\frac{1}{r}\frac{d}{dr}\left[r\frac{dT_2(r)}{dr}\right]-\frac{G}{t}[T_2(r)-T_a]=0 \qquad for\, r>R \qquad (4.8)$$

where $T_1(r)$, k and $T_2(r)$, k' are the temperature distributions and corresponding thermal conductivities of the suspended and supported flake, respectively, R = 1.6 μm is pseudo-radius obtained from our trench structure, r is the radial distance from the flake center, T_a = 300 K is the ambient temperature, G is the ITC between the flake and supported AZ2025 photoresist, and t is the thickness of 3R MoS_2 flake. The heat absorbed $q(r)$ in the above equations is the volumetric Gaussian beam heating and given as [214]:

$$q(r) = \frac{I\alpha}{t}\exp(-\frac{r^2}{r_0^2}) \tag{4.9}$$

where α = 0.47 represents the flake absorbance at the wavelength 532 nm, r_0 = 0.18 μm is the radius of Gaussian laser beam radius. I = P/ (π r_0^2) is the laser power per unit at the center of the laser beam spot, with P is the incident laser power. The general solutions to Equation (4.7) and (4.8) are written as:

$$T_1(r) = c1 + c2\ln(r) + c3Ei(-\frac{r^2}{r_0^2}) \qquad for\, r < R \tag{4.10}$$

$$T_2(\gamma) = c4I_0(\gamma) + c5k_0(\gamma) + T_a \qquad for\, r > R \tag{4.11}$$

where $Ei(x)$ is the exponential integral and $\gamma = r \times (G/k't)^{1/2}$, $I_0(\gamma)$ and $k_0(\gamma)$ are the zero-order modified Bessel exponential function of the first and second kind, respectively, and c_i (*i*= 1-5) are the constants which can be determined with the following boundary conditions:

$$T_1(R) = T_2(\gamma)|_{\,r=R} \tag{4.12}$$

$$T_2(r \to \infty) = T_a \tag{4.13}$$

$$-k\frac{dT_1(r)}{dr}\bigg|_{r=R} = -k'\frac{dT_2(\gamma)}{dr}\bigg|_{r=R} \tag{4.14}$$

$$-2\pi Rtk'\frac{dT_2(\gamma)}{dr}\bigg|_{r=R} = \alpha P \tag{4.15}$$

the constants are solved by programmed python codes, and the weighted average temperature in the beam spot T_m can be approximated by using the calculated $T_1(r)$ and $q(r)$:

$$T_m \approx \frac{\int_0^{r_0} T_1(r)q(r)rdr}{\int_0^{r_0} q(r)dr} \tag{4.16}$$

T_m could be used to extract the thermal conductivity k from different thick 3R MoS_2 flakes by fitting T_m with P obtained from Raman measurements.

The thermal conductivities of the suspended and supported flake, are considered equal ($k = k'$), and we assumed G = 2 MW/m^2K, Ta = 300 K, t = 35 nm, and α = 0.47 for the flake to achieve the thermal conductivity under zero strain about 70.6 W/mk. In Figure 4-4, the calculated temperature distribution is shown for $k = 4$ W/mK and G ranging from 0.5 MW/m^2K to 50 MW/m^2K, respectively. The intrinsic thermal conductivities were 70.2 ± 4 W/mK ,70.6 ± 4 W/mK and 72.9 ± 4 W/mK for 0.26%,0% and -0.26% strain, respectively, by fitting ΔT_m with ΔP using this method. If the absorption coefficient was also considered in equation 4.6, the intrinsic thermal conductivities for the 3R MoS_2 with a strain of +0.26%, 0% and -0.26% were 66.1 ± 3, 66.6 ± 4 and 68.6 ± 5 W/mK, respectively. Both of the results calculated using above two modes were consistent with reported thermal conductivity of multilayer 2H MoS_2 thermal conductivities [186, 213]. More importantly, we emphasize here that the intrinsic thermal conductivity of piezoelectric 3R MoS_2 flakes under different external strains did not show a significant change.

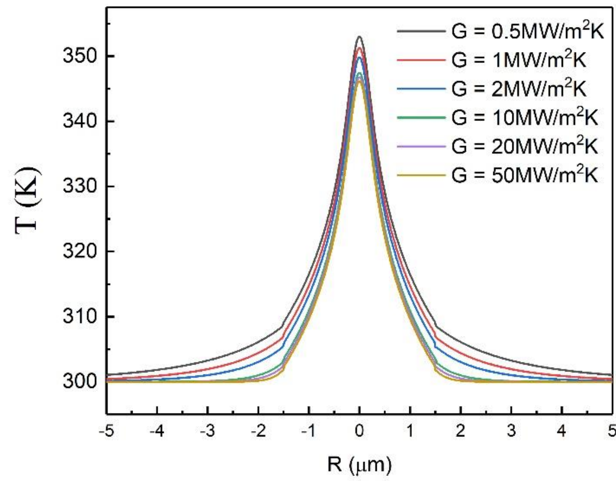

Figure 4-4 The calculated temperature distribution under a 0.3mW laser power, is calculated for a suspended 3R MoS_2 flake with $k = 70.6$ W/mK and G ranging from 0.5 MW/m^2K to 100 MW/m^2K, respectively.

The slightly intrinsic thermal conductivity modulation of 3R MoS_2 might be raised from modified phonon dispersions and interlayer interactions under strain, or change of the phonon group velocity as reported based theoretical studies [190-193, 215]. It should be pointed out that the actual strains applied on the MoS_2 flakes in our experiments were much smaller than those used in these theoretical studies. This could be the reason why the observed intrinsic thermal conductivity modulation was much weaker in our experiments.

.

4.3.2 In-plane thermal conductivity of a metal/MoS_2 flakes/metal structure under strains

4.3.2.1 The sample structure and calibration

In addition to the Optothermal Raman method for determining the thermal conductivity of 2D materials under different strains, another novel method can be applied. For this

purpose, a focused laser beam is engaged to generate a local heat spot on one side of the MoS_2 flake, creating a temperature gradient across it. As illustrated in Figure 4-5a, a pair micro-thermal couple electrodes (150 nm Au/150 nm Ni) on the two ends of the MoS_2 flake were fabricated using the standard photolithography and metallization process. A laser beam with a wavelength of 532 nm and a spot size of 380 nm was focused on the one thermal couple electrode. The temperature increase of the two electrodes was monitored by measuring the voltage difference between the Au and Ni layer, as shown in Figure 4-5b. The channel length L, between the two thermal couple electrodes E1 and E2, was 5 μm and the width W of the 3R MoS_2 flake was 19.6 μm. Since the piezoelectric property of a 3R MoS_2 flake is related to its crystal orientation. The angle resolved SHG of the 3R MoS_2 flake in the sample shown in Fig 4-5b exhibited a six-fold symmetric anisotropy SH response in consistent with previous study, which reveals that the 3R MoS_2 flake belongs to the C_{3v} point group with the broken inversion symmetry, as shown in Figure 4-5c. The armchair axis of the 3R MoS_2 flake was confirmed to be perpendicular to the thermal couple electrodes. To compare 3R MoS_2 with 2H MoS_2, the 2H MoS_2 samples with the same suspended sample structure of 3R MoS_2 were also fabricated, as shown in Figure 4-5d. From the AFM image of the 3R MoS_2 flake (Fig 4-5e) and the 2H MoS_2 flake (Fig 4-5g), the flake thicknesses were found to be 75nm (Fig 4-5f) and 78 nm (Fig 4-5h), respectively.

The heat dissipation process through the sample can be described by the following equation:

$$\Delta T = \frac{Q}{k} \times \frac{L}{A} \tag{4.17}$$

where Q is the rate of the heat flow analogous to the electric current in Ohm's law, k is the total thermal conductivity analogous to the electric conductivity, A is the cross-

sectional area of the sample normal to the direction of the heat flow, L is the sample length and ΔT is the temperature difference analogous to electric voltage. In the measurement, the heat could flow from one thermal couple electrode exposed to the laser beam to the other electrode. Hence, k is contributed from two factors, i.e., the intrinsic thermal conductivity k_{int} (W/mK) of the flakes and the interfacial thermal conductance (ITC) $G_{interface}$ (K/m^{2}W) of the two metal-semiconductor interfaces.

$$\Delta T = \Delta T_1 + \Delta T_2 \quad (4.18)$$

$$\Delta T = \frac{Q}{k_{int}} \times \frac{L_{mos_2}}{A_{mos_2}} + \frac{Q}{G_{interface}} \times \frac{2}{A_{interface}} \quad (4.19)$$

where ΔT, ΔT_1 and ΔT_2 are temperature difference between two thermal couples, two terminals of flakes and two metal-semiconductor interfaces. A_{mos_2} is the cross-sectional area of the flakes normal to the direction of the heat flow, L_{mos_2} is the flakes channel length and $A_{interface}$ is the contact area of the thermal couple electrode with the MoS_2 flake. To simplify discussion, the $A_{interface}$ is considered the same at the two interfaces.

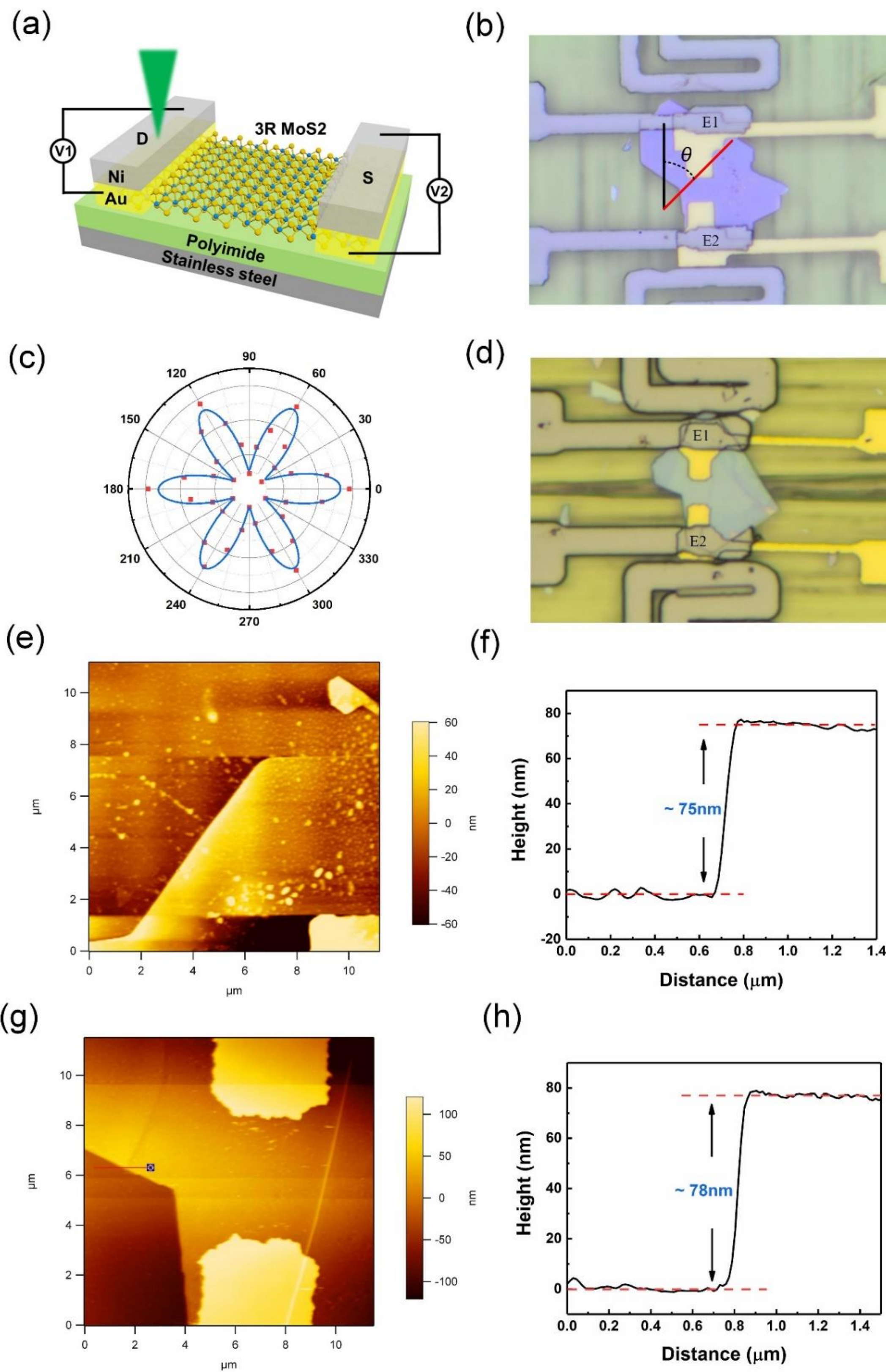

Figure 4-5 (a) Schematic of our thermal conductivity measurement set up. The heat was generated using a laser beam incident onto one thermal couple electrode. (b) An optical

image of 3R MoS_2 flake with a pair of thermal couple electrodes E1 and E2. (c) The polarization dependence plot of SHG intensity of the 3R MoS_2 flake in (b) The red dots are experimental data and the blue solid lines are fitting lines. (d) An optical image of 2H MoS_2 flake with two thermal couple electrodes E1 and E2. (e) AFM topography image and (f) height profile of 3R MoS_2 flake in (b). (g) AFM topography image and (h) height profile of 2H MoS_2 flake in (d).

To understand the thermal conductivity of the polyimide substrate, a dummy sample in which a pair thermal couple electrodes E1 and E2, were fabricated on the polyimide substrate without any MoS_2 flakes, as shown in Figure 4-6a, was prepared. With the laser beam was incident onto one of the electrodes E1, the temperature of the electrode with the laser beam was found to be increased linearly with the laser power. In contrast, the temperature of the other electrode maintained unchanged within the experimental error, as described in Figure 4-6b. These findings were not affected by any strains introduced by bending the substrates. These results suggest, the polyimide substrate was a thermal insulator no matter it was under strain-free and strained bias situations (see Figure 4-6c). The slope of $\frac{Q}{\Delta T_{plain}}$ is around 26.7 μw/K for the plain thermal couple device. Thus, in the following discussion, heat is regarded to transport only through the MoS_2 flakes, while heat conductance through the substrate is ignored. The laser power through objective lens was measured using a power meter. The absorption spectra of thermal couple was obtained by measuring continuous Ni/Au metal thin film on polyimide substrate with UV-Vis spectrophotometer. The absorbance of Ni/Au surface at the wavelength of 532 nm is around 0.42, see Figure 4-6d. Thus, the total power absorbed by the metal surfaces was calculated by multiplying the power read from power meter with the absorbance factor.

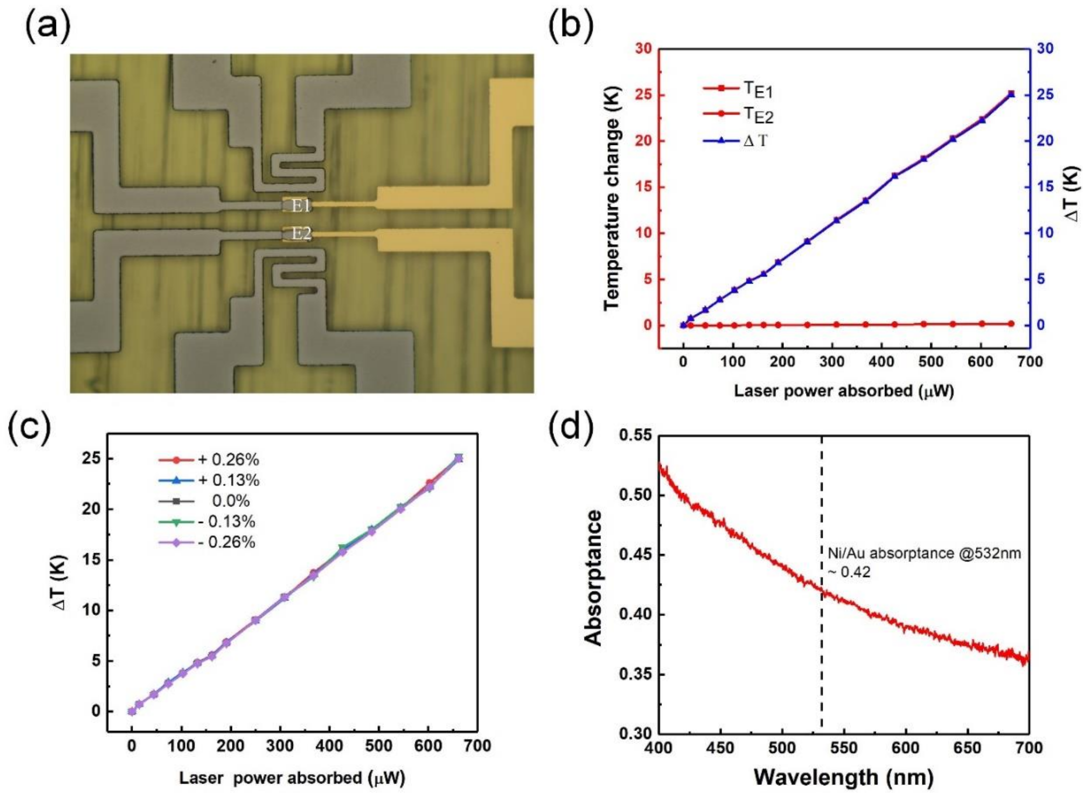

Figure 4-6 Thermal measurement of thermal couple device without flake (a) Optical image of laser heating thermal couple device without flake. (b) Temperature profile and temperature variation thermal couple electrodes E1 and E2. (c) Temperature variation profiles under uniaxial strain applied. (d) Absorptance curve of Ni/Au thin film on polyimide.

4.3.2.2 Thermal conductivity calculation of metal-MoS_2 flakes-metal structure under strains

Prior to calculation of thermal conductivities, we define that the forward direction is along the heat flow direction from thermal couple electrode E1 to E2. On the contrary, the reverse direction is from E2 to E1, opposite to the heat flow direction. To simplify calculation, the equation for the effective thermal conductivity of this structure is modified as:

$$k_{quasi-total} = \frac{Q}{\Delta T} \times \frac{L_{mos_2}}{A_{mos_2}} \qquad (4.20)$$

where $k_{quasi-total}$ the effective thermal conductance of metal-semiconductor-metal structure, with the contribution from intrinsic thermal conductivity of MoS_2 flakes here and the MoS_2/metal ITC. The $k_{quasi-total}$ was characterized in the forward and reverse directions. The ratio of $\frac{Q}{\Delta T}$ stands for the heat transfer through the MoS_2 flake on the substrate by $\frac{Q}{\Delta T_{MoS2+plain}}$ minus through the substrate only, $\frac{Q}{\Delta T_{plain}}$. The temperature difference ΔT between the two thermal couple electrodes increased linearly with the laser light power, and it was maintained at a constant value under the laser heating. When a strain was applied on the structure, ΔT was monitored in the two uniaxial directions, where heat transfer from E1 to E2 or vice versa, as shown in Figure 4-7a and b. It was observed that ΔT in the forward direction increased (decreased) under a tensile (compressive) strain and the ratio of $\frac{Q}{\Delta T}$ decreased (increased) by a maximum around 8.9% (6%) at a tensile (compressive) strain of +0.26% (-0.26%). In contrast, the temperature variation ΔT showed an opposite change in the reverse direction with a decrease (increase) under a tensile (compressive) strain. These findings suggest the uniaxial strain could affect heat transport and modulate $k_{quasi-total}$, as summarized in Figure 4-7c and d. $k_{quasi-total}$ was changed from 52.7 ± 2 W/mK at zero strain to 39.6 ± 1 W/mK under under a tensile strain of 0.26%, decreased by around 24.7%. Note that the value of $k_{quasi-total}$ is contributed from k_{int} of the flake and the ITC $G_{interface}$. As k_{int} of the MoS_2 flakes is not change evidently under strains applied, the modulation of $k_{quasi-total}$ may be dominated by the ITC $G_{interface}$.

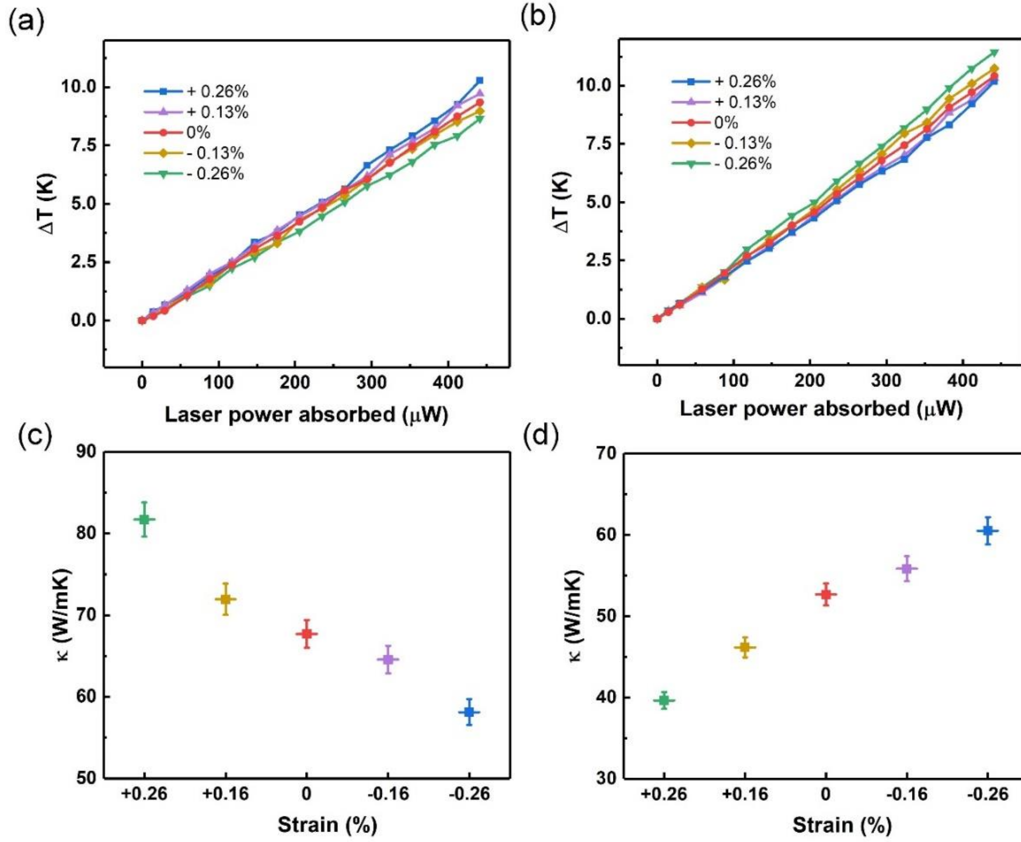

Figure 4-7 Evaluation of the thermal conductivities of a 3R MoS_2 flake with symmetrical thermal couple electrodes (Ni/Au/ 3R MoS_2/Au/Ni) (shown in Fig 4-5b) in the uniaxial direction under tensile (positive) and compressive (negative) strains. Temperature variation as a function of the laser light power in (a) the forward direction and (b) the reverse direction. Thermal conductivity $k_{quasi-total}$ as a function of the strains in (c) the forward direction and (d) the reverse direction.

For the purpose of comparison, $k_{quasi-total}$ of a 2H MoS_2 flake were also characterized in the forward and the reverse directions under different uniaxial strains, as shown in Figure 4-8. The ΔT showed a slight increase in the forward direction and decrease in the reverse direction under either compressive or tensile strains. Consequently, $k_{quasi-total}$ of the 2H MoS_2 flake decreased in the forward direction and increased in the reverse direction upon applying both tensile and compressive strains. These observations

suggest that the strain modulation on $k_{quasi-total}$ of the 2H MoS_2 flake was much weaker than that for the 3R MoS_2 flake in the range of applied uniaxial strains.

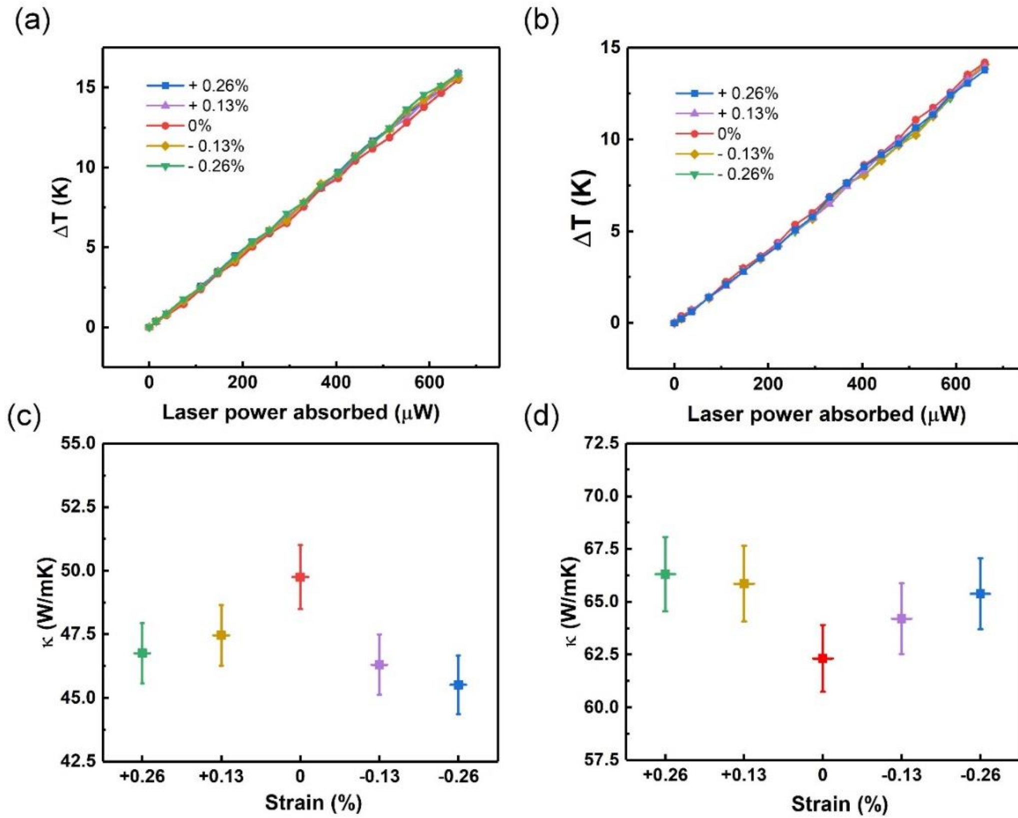

Figure 4-8 Evaluation of the thermal conductivities of a 2H MoS_2 flake with symmetry thermal couple (Ni/Au/ 2H MoS_2/Au/Ni) (shown in Fig 4-5d) in the uniaxial direction under tensile (positive) and compressive (negative) strains. Temperature variation as a function of the laser light power in (a) the forward direction and (b) the reverse direction. $k_{quasi-total}$ as a function of the strains in (c) the forward direction and (d) the reverse direction.

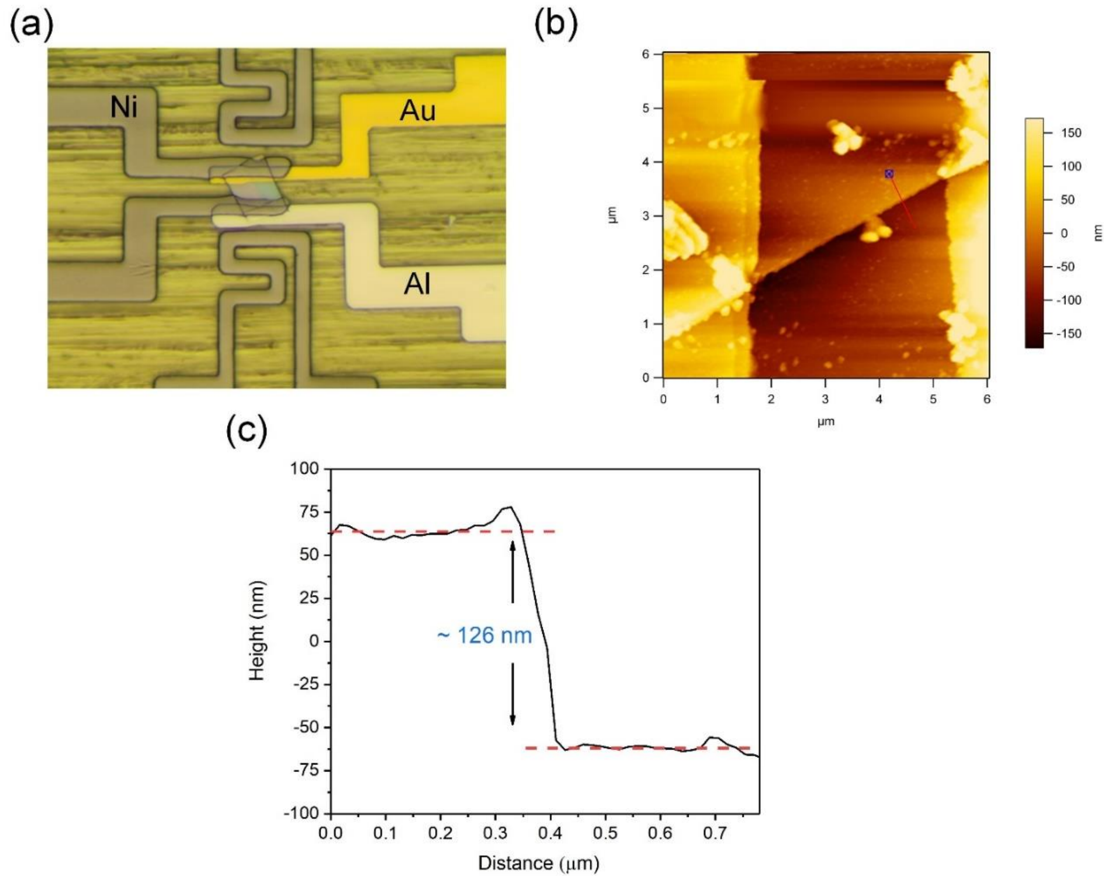

Figure 4-9 (a) Optical image, (b) AFM topography image and (c) height profile of a 3R MoS_2 flake with an asymmetric thermal couple structure (Ni/Au/3R MoS_2/Al/Ni).

To further investigate the strain effect on heat transport in the metal-semiconductor-metal structure, a pair asymmetric thermal couples, in which one is Ni/Au/3R MoS_2 and another is Ni/Al/3R MoS_2, were fabricated and examined as shown in Figure 4-9. In this structure, Au was in contact with the 3R MoS_2 flake on one side and Al was in contact with the 3R MoS_2 flake on the other side. $k_{quasi-total}$ of the asymmetric Ni/Au/3R MoS_2/Al/Ni structure was also characterized as shown in Figure 4-10. The heat transferred across the Ni/Al/3R MoS_2 contact, ~126 nm 3R MoS_2 flake and the Ni/Au/3R MoS_2 contact. Similar to the symmetry structure of the Ni/Au/ 3R MoS_2/Au/Ni, strain-modulated $k_{quasi-total}$ was observed. In Figure 4-10, a maximum

23.4% increase in $k_{quasi-total}$ was found with applying a tensile strain of 0.26% in the forward direction. The significant modulation of $k_{quasi-total}$ could be attributed to the modulation of the strains on ITC between 3R MoS_2 flakes and contacted metals, since the intrinsic thermal conductivity of 3R MoS_2 flakes does not show evident changes under external strain as studied in section 4.3.1. The interfacial thermal conductance (ITC) in the metal/ MoS_2 interfaces, also known as Kapitza resistance, was theoretical studied [199, 200, 216, 217]. It has been suggested that the ITC could be tuned by interfacial interactions, e.g., the weak van der Waals (vdW) interaction at the contacted surfaces of MoS_2 flakes and metals, or the covalent bonds formed at the contacted edges of MoS_2 flakes and metals. Generally, the phonon-phonon coupling changes, like in the mismatch of phonon density of states or phonon vibration spectra under strains may play a main role in the ITC vibrations. Besides, theoretical studies have confirmed that efficient injection of electrons may mainly occur at the contacted edges from the metal to the MoS_2 flake, and the piezoelectric polarization charges formed at the interfaces might alter the electrons injection efficiency [199, 218, 219] and, in turn the heat transport properties under strains. From the results obtained in this chapter, we thus suggest that the electron-electron coupling might also play a role in the heat transfer in addition to phonon-phonon and electron-phonon coupling.

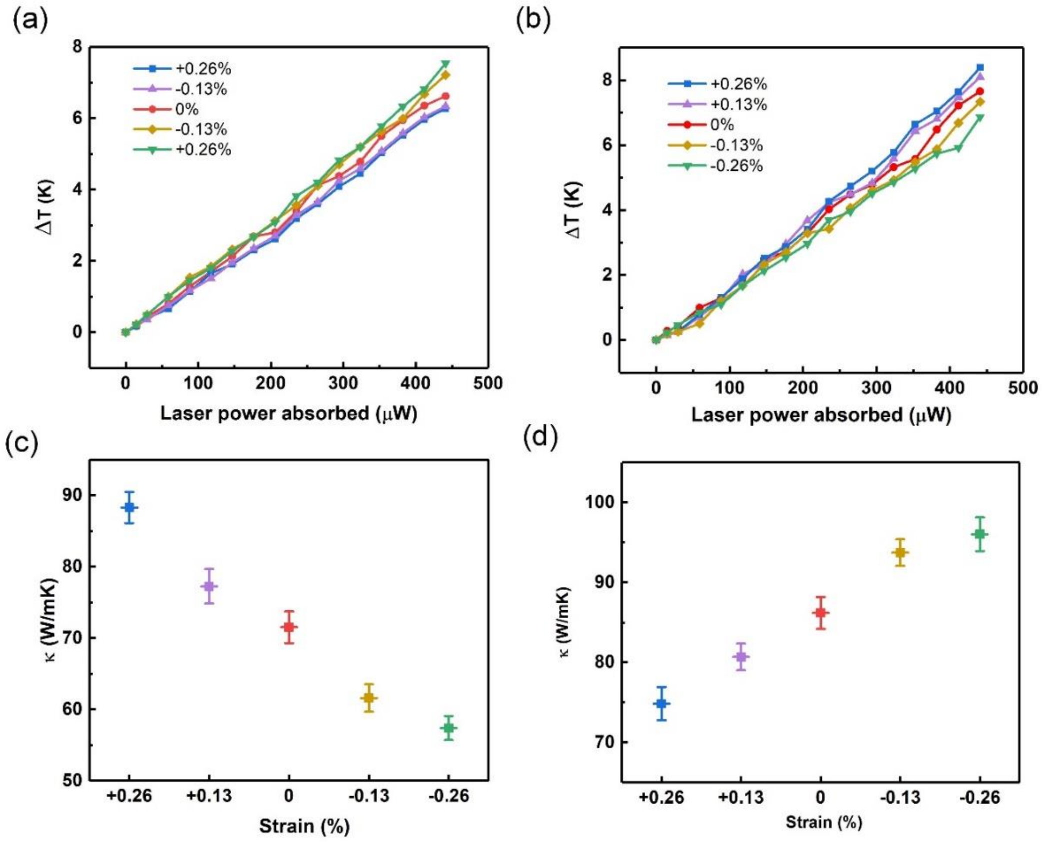

Figure 4-10 Evaluation of the thermal conductivities of a 3R MoS_2 flake with asymmetry thermal couple (Ni/Au/ 3R MoS_2/Al/Ni) (shown in Fig 4-9a) in the uniaxial direction under tensile (positive) and compressive (negative) strains. Temperature variation as a function of the laser light power in (a) the forward direction and (b) the reverse direction. $k_{quasi-total}$ as a function of the strains in (c) the forward direction and (d) the reverse direction.

The *I-V* curves of above three device configurations were also measured with strain. For the symmetric Ni/Au/3R MoS_2/Au/Ni sample (Fig 4-5b, two back-to-back Schottky barriers with a similar barrier height under zero strain were formed, and the reverse Schottky barrier limited electron transport [220, 221], so that the *I-V* curve should be symmetrical to the applied bias voltage between the two electrodes. However, these symmetrical potential barriers would not exist once a strain is applied because the

piezoelectric polarization charges would be enhanced at one contact and weakened at the other such that the *I-V* current was found to be asymmetric, as shown in Figure 4-11a, similar to the results reported in monolayer MoS_2 [19]. In the symmetric structure of Ni/Au/2H MoS_2/Au/Ni configuration, the Schottky *I-V* curves showed little change in the *I-V* curve upon strains applied, see Figure 4-9b, due to the negligible piezoelectricity of 78 nm 2H MoS_2 flake. The minor *I-V* curves is caused by the strain-induced bandgap change, known as piezoresistive effect [222]. For the asymmetric structure of Ni/Al/3R MoS_2/Au/Ni configuration, evident strain-modulated *I-V* curves were observed, as shown in Figure 4-11c, due to the piezoelectric polarization charges formed at the interface of Au/ 3R MoS_2. The above results suggest that the thermal modulation of 3R MoS_2 under applied strain might be raised from the polarization charges at the MS interface. The physics underlying this phenomenon might need further and deep investigation.

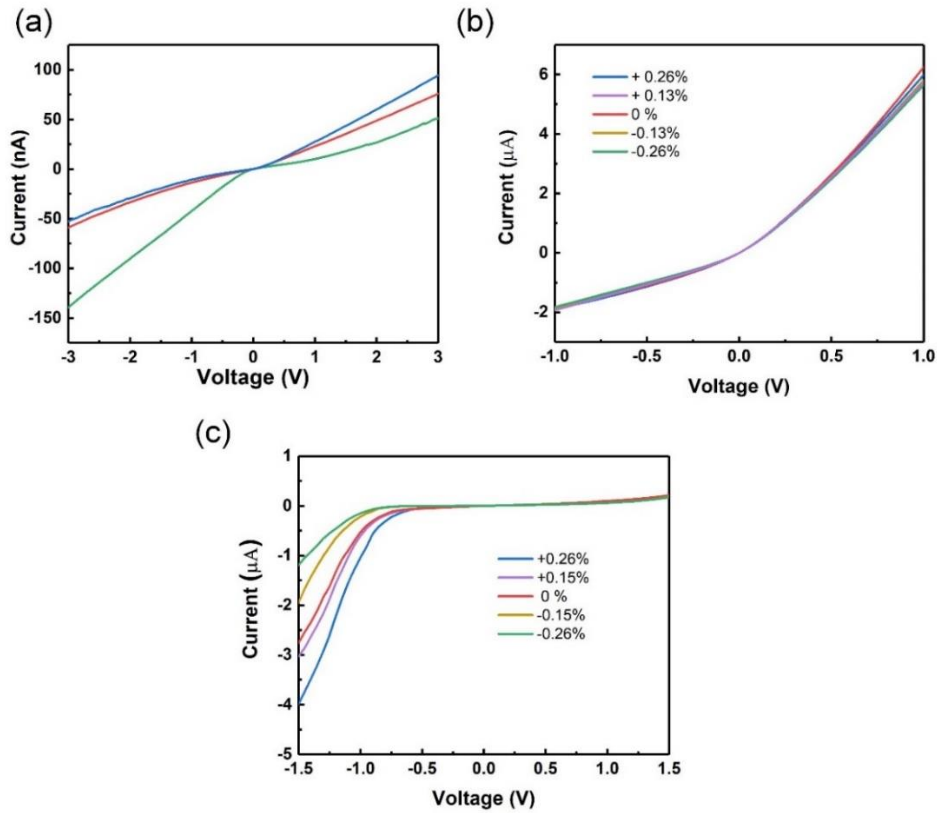

Figure 4-11 *I-V* characteristics curves of (a) a 3R MoS_2 flake with symmetry thermal couple (Ni/Au/3R MoS_2/Au/Ni, Figure 4-5), (b) 2H MoS_2 flake with symmetry thermal couple (Ni/Au/2H MoS_2/Au/Ni, Figure 4-5), and (c) 3R MoS_2 with asymmetric thermal couple structure (Ni/Au/3R MoS_2/Al/Ni, Figure 4-9).

4.4 Conclusion

In this chapter, heat transport in piezoelectric 3R MoS_2 flakes was studied using the Optothermal Raman method and laser heating thermal couple method. The thermal conductivity of intrinsic 3R MoS_2 flakes was observed to be around only 3% ~ 4% variation upon applying uniaxial strains of 0.26%. The thermal conductance of the metal/3R MoS2/metal structures was found to be changed with a maximum 24.7 % upon applying the uniaxial strains. These findings suggest that the 2D piezoelectric potentials

induced by the piezoelectric polarization changes under strains at the two contacts modulate not only electron injection into the flakes, as reported by many groups with a variety of piezoelectric material/metal contacts, but also heat transport through the modulated electrical junctions.

Chapter 5 Photoelectric responses from a flexible α-In_2Se_3/3R MoS_2 heterojunction under strain

5.1 Introduction

2D layered materials, like graphene, h-BN, and TMDCs, etc. have been successfully assembled in the vertical direction and held together through van der Waals forces, to uncover their unique physical properties and develop novel electronic, optoelectronic, ferroelectric, thermoelectric and electrochemistry devices [223-226]. In addition, these 2D materials are of excellent mechanical properties which endow them a huge advantage in flexible electronic applications over conventional crystalline semiconductors which are very brittle. With appropriate stacking of these 2D vdW materials, p-n junctions can be formed for the sake of development of flexible electronic and optoelectronic devices. Among these 2D materials, several ultrathin layers with non-centrosymmetric structures, like monolayer MoS_2, bilayer WSe_2, etc, are of piezoelectricity and they are the most promising for mechanically modulated electronic and optoelectronic applications through mechanical agitations, like wurtzite structure material ZnO [52, 227].

Monolayer MoS_2 has been employed to develop optoelectronic devices in which strain-induced piezoelectric polarization charges are utilized to modulate photoexcited carrier transport and recombination at the Schottky barrier or p-n junction interfaces [153, 154, 228, 229]. However, the piezoelectricity of 2H MoS_2 flakes is restricted in odd few layers and it is significantly weakened with increasing the thickness [19]. In contrast, due to broken inversion symmetry, 3R MoS_2 flakes exhibit piezoelectricity from bilayer to thick multilayers, having a promising potential for nonlinear optics, valley-dependent spin polarization, and advancing flexible wearable electronics [120]. In addition, indium

selenide, a direct bandgap and layered structure III-V compound, has recently attracted enormous attention, due to its superior electric, piezoelectric, thermoelectric, photoelectric and electrochemical properties [102, 230-234]. Ding et al theoretically revealed that In_2Se_3 and other III_2-V_3 van der Waals materials exhibit room-temperature ferroelectricity, originated from both spontaneous in-plane and out-of-plane electric polarization [235]. It is widely accepted that all ferroelectric materials are also piezoelectric [26, 29]. Indeed, the in-plane and out-plane ferroelectric and piezoelectric properties have been confirmed and characterized experimentally in α and β phase In_2Se_3 [77-79, 236, 237]. Theoretically speaking, controllable energy band alignment in the 3R MoS_2/In_2Se_3 heterostructure could be realized through an applied electric field, to achieve a broad spectrum of light absorption for novel tunable optoelectronic applications [238].

In this chapter, we report on the first self-powered n-type α-In_2Se_3 / p-type 3R MoS_2 heterojunction photodetector built on a flexible substrate. Our attention is focused on the mechanism study of the photocurrent modulation by the strains.

5.2 Experimental devices and methods

5.2.1 Synthesis of α-In_2Se_3/3R MoS_2 heterojunction

The device substrate was fabricated by spinning coating polyimide on a flexible polished stainless steel at 3000rpm for 45 seconds, and then annealed in argon gas at 250 °C for 2 h. 3R MoS_2 flakes were mechanically exfoliated from a chemical vapor deposition (CVD) synthesized bulk 3R MoS_2 crystal onto the polyimide thin film. The surfaces of the MoS_2 flakes were then doped with CHF_3 plasma treatment in a PlasmaThermo 790 MF Reactive ion etch (RIE) system. For the plasma doping, the RF power, gas pressure, precursor gas flow and process time were 100 W, 10 mTorr, 10 sccm and 45 s,

respectively. Bulk α-In_2Se_3 crystals were bought on the market. The α-In_2Se_3 flakes were then mechanically exfoliated onto the plasma treated 3R MoS_2 flakes/polyimide. The overlapped α-In_2Se_3/3R MoS_2 flakes were identified using optical microscopy. A Cr/Au (10/150nm) pad was deposited on the α-In_2Se_3 flake and a Pd/Au (10/150nm) pad was coated on the 3R MoS_2 flake, using an electron beam evaporator system (Edwards Auto 360) and then patterned through photolithography process.

5.2.2 Materials characterizations

The atomic force microscopy (AFM) and piezoresponse force microscopy (PFM) characterizations (Cypher S Asylum Research Oxford Instruments) were carried out using the non-contact mode and DART-PFM mode. XPS measurements were conducted on a Kratos AXIS Supra X-ray photoelectron spectrometer. The SHG measurement was described in Chapter 2. The Raman scattering measurements (WITec alpha 300 confocal Raman microscopy) were carried out under the laser light of 532 nm, laser power of 0.1 mW and beam diameter of 400nm with a 100X objective lens.

5.2.3 Electrical, optoelectronic, and mechanical characterizations

The electrical characteristic measurements were performed using a Keysight B1500A Semiconductor Device Parameter Analyzer. 532 nm and 800 nm wavelength light with tunable intensity were obtained from a Quartz Halogen light system and a monochromator for the photovoltaic and photo-sensing measurement. For the spatial photocurrent mapping, the sample was fixed on the motorized stage in WITec alpha 300 confocal Raman microscopy with a continuous 532 nm laser with a beam diameter of 400nm. The photocurrent was measured using Keithley 2450 source meter, and a Femto DLPCA-200 universal low noise current amplifier.

Since the dimensions of the α-In_2Se_3 and 3R MoS_2 flakes (~20 μm long and a few tens of nanometer thick) were much smaller than the PI substrate deposited on the stainless steel (15 mm × 15mm × 30 μm), the tensile and compressive strains exerted onto the flakes deposited onto the PI substrate could be given by $\varepsilon = h/2r$, where h is the thickness of the PI substrate, L is the bended length of the device and r is the bending radius, refer to Chapter 3.3.2 for the details. The strain ε was calculated and shown in Table 5-1 Parameters for calculating the applied strains.

L (mm)	r (mm)	ε
14	11.74	0.13%
11.5	5.68	0.26%
8.5	4.31	0.35%

Table 5-1 Parameters for calculating the applied strains.

5.3 Results and discussion

5.3.1 Atomic structure and PFM measurement of α-In_2Se_3 flakes

The atomic structure and piezoelectric characterizations of 3R MoS_2 flakes are discussed in Chapter 3. The atomic structure and PFM measurement of α-In_2Se_3 flakes are discussed here in comparison of 3R MoS_2, as shown in Figure 5-1. Hexagonal α-In_2Se_3 flakes at any thickness possess non-centrosymmetric property along the vertical direction, leading to the out-of-plane piezoelectricity (d_{33}). In a single quintuple layer, one In atom and two Se atoms are located at nonequivalent sites of the hexagonal structure, generating the in-plane (d_{11}) piezoelectricity under a planar strain. Bilayer hexagonal α-In_2Se_3 constructed by two dislocated quintuple layers results in the reservation of non-centrosymmetry, so does a multilayer hexagonal α-In_2Se_3 flake. Thus,

hexagonal α-In_2Se_3 is of in-plane and out-of-plane piezoelectricity at any thickness [21, 77, 235].

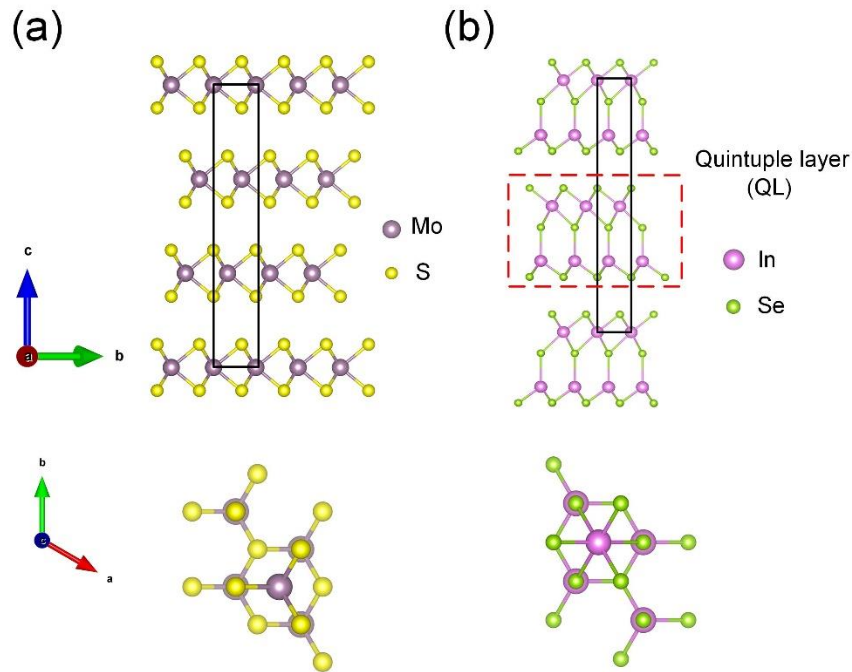

Figure 5-1 Atomic structures (the side and top views) of (a) 3R phase MoS_2 and (b) Hexagonal α-In_2Se_3.

To confirm the piezoelectricity of α-In_2Se_3, a 50nm α-In_2Se_3 flake was exfoliated on an Au coated substrate and characterized with PFM measurements, as shown in Figure 5-2. The PFM images showed an evident mechanical response under a vertical electrical field, and the piezoelectric coefficient d_{33} was estimated 1.53 ± 0.5 pm/V, similar to the theoretical results 1.23 pm/V of bulk α-In_2Se_3 and nearly half of the value of 3.6 pm/V for a 50 nm α-In_2Se_3 flake reported other groups' experimental work [77, 239].

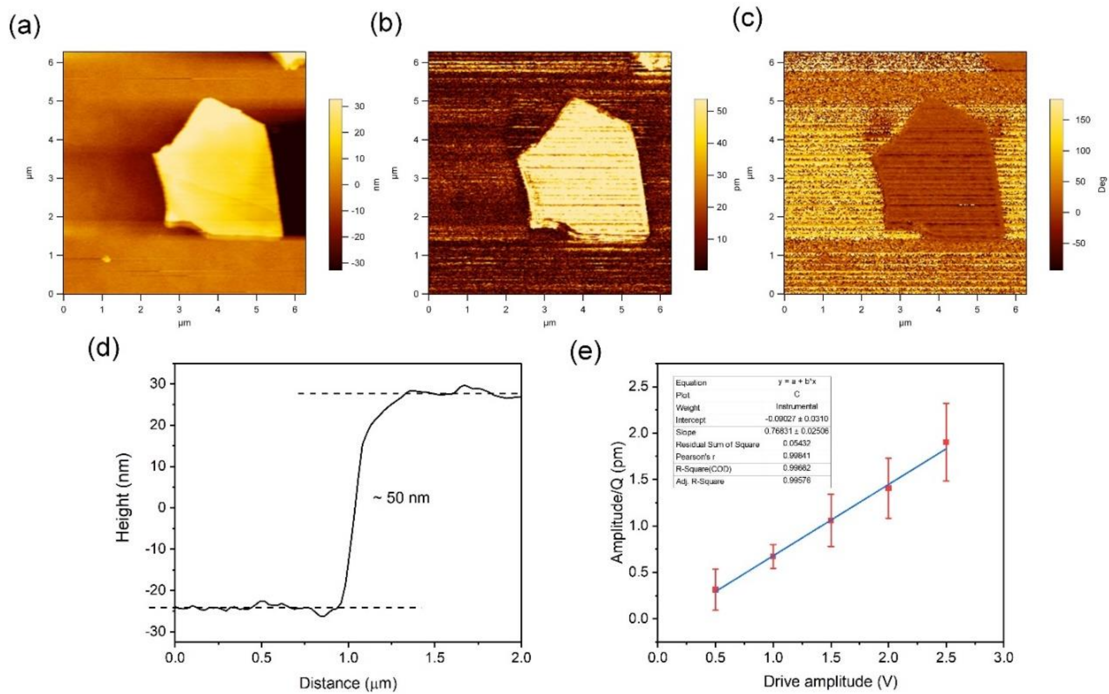

Figure 5-2 Out-of-plane piezo response of a 50 nm thick α-In_2Se_3 flake. (a) AFM topography, (b) PFM amplitude, (c) PFM phase images a bias voltage of 1 V and (d) Height profile of the α-In_2Se_3 flake. (e) Piezoelectric coefficient d_{33} estimation of 50 nm thick α-In_2Se_3 flake.

5.3.2 α-In_2Se_3/3R MoS_2 heterojunction photoelectric performance without strains

To prepare a heterojunction of 3R MoS_2 & α-In_2Se_3 flakes, the flakes were mechanically exfoliated from 3R MoS_2 and α-In_2Se_3 crystals and then deposited on a clean flexible polyimide thin film in sequence. As illustrated in Figure 5-3a, a location with a 3R MoS_2 flake overlapped with an α-In_2Se_3 flake was selected with help of an optical microscope. A Cr/Au (10/150 nm) electrode and a Pd/Au (10/150 nm) electrode were deposited on the side of the α-In_2Se and 3R MoS_2 flakes, respectively. The experimental setup for the photoelectric measurement is illustrated in Figure 5-3b The flexible heterojunction was characterized by a semiconductor parameter analyzer (Agilent B1500A) under different wavelength illumination and intensities from a Quartz Halogen light system through a

monochromator. To study the strain-modulation on the p-n heterojunction, the uniaxial compressive and tensile strains were applied through bending the flexible device downward and upward, see the insets in Figure 5-3b. The morphology and height profiles of the heterojunction showed that the thickness of the 3R MoS_2 and α-In_2Se_3 flakes were 30 nm and 206 nm, respectively, in Figure 5-3 c-e.

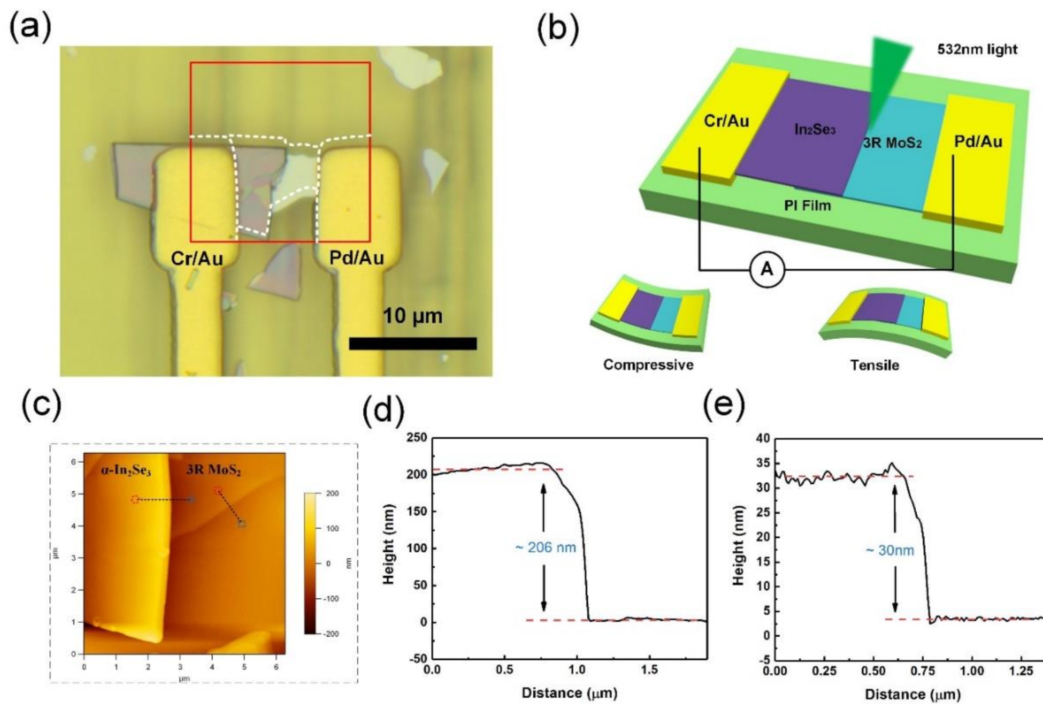

Figure 5-3 (a) Optical image, (b) Electrical measurement setup and (c) AFM image of the α-In_2Se_3/3R MoS_2 heterojunction. (d) Height profile of the α-In_2Se_3 flake. (e) Height profile of the 3R MoS_2 flake.

In Figure 5-4, four characteristic Raman peaks at 90, 104, 180 and 195 cm^{-1} and XPS spectra of In *3d* and Se *3d* core orbital peaks from the top flake (shown in Figure 5-4a-c) indicate a hexagonal structure of an α-In_2Se_3 flake. Among the four Raman peaks, the peak at 90 cm^{-1} always occurs in the Raman spectra of hexagonal structure α-In_2Se_3 and disappears for rhombohedral α-In_2Se_3 [240, 241]. Two characteristic Raman peaks shown in Figure 5-4d, attributed to in-plane mode (E_{2g}^1) and out-of-plane mode (A_{1g}),

were observed from the bottom 3R MoS_2 flake. The polarization-resolved second-harmonic generation (SHG) measurement evidenced a non-centrosymmetric structure from 6-fold pattern (see Figure 5-4f), confirming that the bottom flake was indeed a 3R MoS_2 flake. Furthermore, the bottom 3R MoS_2 flake was p-type semiconducting after CHF_3 plasma treatment and the top α-In_2Se_3 was n-type, as characterized by the XPS. The plasma doping is the common method to obtain p-type MoS_2 [242-244].

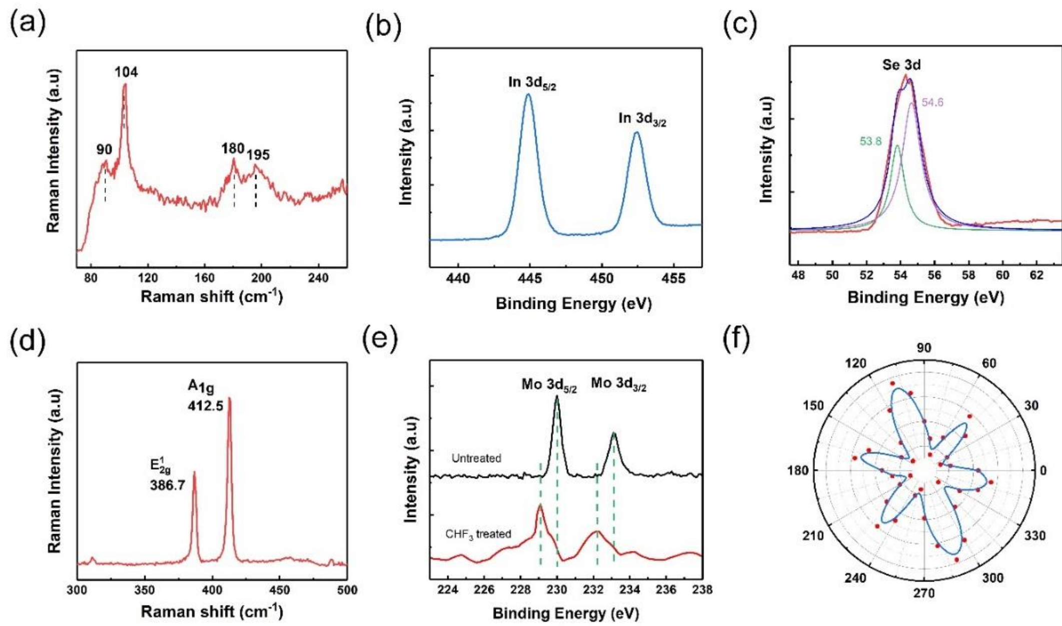

Figure 5-4 (a) The Raman spectrum of the α-In_2Se_3 flake. (b, c) The XPS spectra of In *3d* and Se *3d* core orbital peaks from the α-In_2Se_3 flake. (d) The Raman spectrum of the 3R MoS_2 flake. (e) Mo *3d* core orbital peaks from the 3R MoS_2 flake before and after CHF_3 plasma treatment. (f) Polarization dependence plot of SHG intensity of 3R MoS_2 flake in the heterojunction (Figure 5-3a).

To exclude the possible influence of the metal/semiconductor contacts on device performance, Cr and Pd were selected as the electrode metal with the n-type α-In_2Se_3 and p-type 3R MoS_2, respectively. In general, for a metal in contact with an n-type semiconductor, a rectifying Schottky contact is formed when the work function of the

metal Φ_M is larger than that of the semiconductor Φ_S, i.e, $\Phi_M > \Phi_S$, and an Ohmic contact is formed when $\Phi_M < \Phi_S$. Similarly, for a metal and an p-type semiconductor, the MS contact will be rectifying Schottky when $\Phi_M < \Phi_S$, and Ohmic contact when $\Phi_M > \Phi_S$ [245]. It was reported that the n-type In_2Se_3 formed Ohmic contacts with low work function metals, like In, Ti, Ag and Cr. The p-type MoS2 showed Ohmic contacts with high work function metals, like Au, Pd [240, 246, 247]. As illustrated in Figure 5-5a-b, we have fabricated symmetrical metal electrodes in contact with In_2Se_3 flake and MoS_2 flakes with the same annealing process, i.e, Au/Cr/n-type In_2Se_3/Cr/Au and Au/Pd/p-type MoS_2/Pd/Au as our testing structures. The *I-V* characteristics of the two testing structures showed very good linear Ohmic responses with various strains, in Figure 5-5c-d.

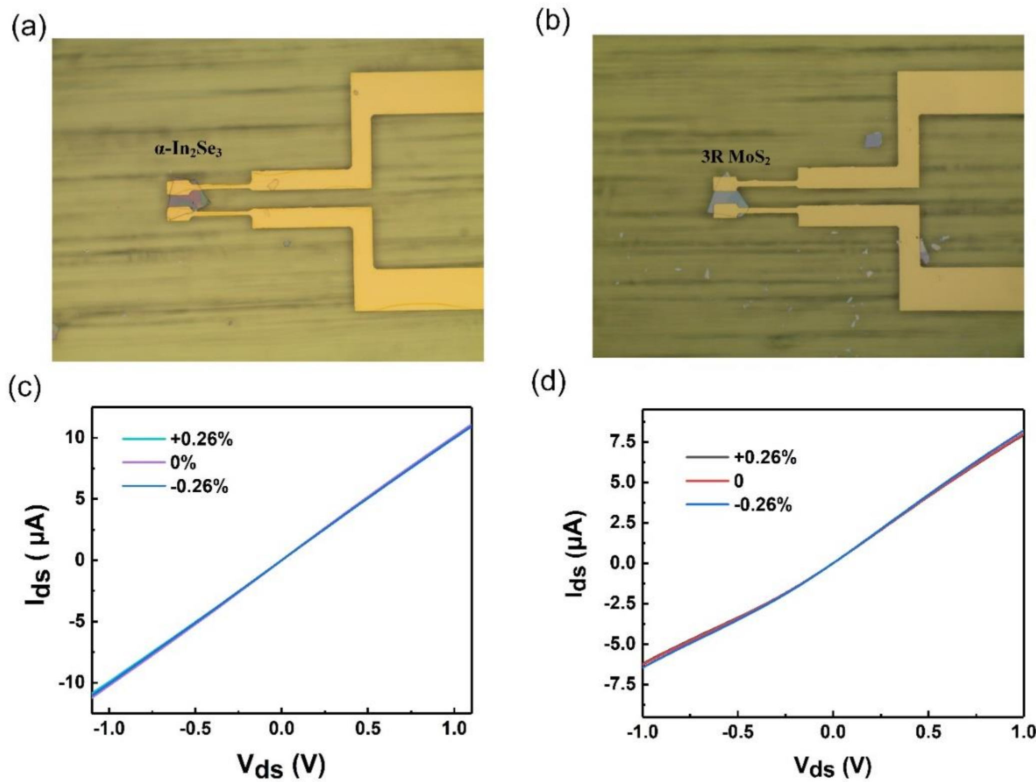

Figure 5-5 Optical images and *I-V* characteristics of α-In_2Se_3 and 3R MoS_2 flakes. (a) One pair of Cr/Au (10/150nm) electrodes were deposited on an α-In_2Se_3 flake. (b) One

pair of Pd/Au (10/150nm) electrodes were deposited on a 3R MoS_2 flake. (c) *I-V* characteristics of the α-In_2Se_3 sample shown in (a) with no strain, a tensile strain of +0.26% and a compressive strain of -0.26%. (d) *I-V* characteristics of the 3R MoS_2 sample shown in (b) with no strain, a tensile strain of +0.26% and a compressive strain of -0.26%.

The dark *I-V* characteristic from the heterojunction device (Figure 5-3a) was measured under the strain-free condition, as shown in Figure 5-6a. The ideality factor was found to be 1.72 and the rectification factor under bias voltages of ±0.5V was I(0.5)/I(-0.5) = 405. The observed excellent rectification characteristic indicates formation of a high-quality p-n junction between the α-In_2Se_3 and 3R MoS_2 flakes, rather than the contributions from the Cr/α-In_2Se_3 and the Pd/3R MoS_2 contacts. Under 532 nm light illumination with an intensity of 0.47 mW cm^{-2} and a bias voltage of +0.5 V, a 4-fold rise in the current, I_{ds}, from 123 nA in the dark to 415 nA was observed in Figure 5-6b. The *I-V* characteristics measured under the light intensity from 0.07 to 0.47 mW/cm^2 and bias voltage of ±0.1V are shown in Figure 5-6c. To evaluate the device performance, a set of photodetector performance indicators are introduced and discussed here. The photoresponsivity, the ratio of the photocurrent over the incident optical power, is given as:

$$R = \frac{I_{light} - I_{dark}}{P_t * A} \tag{5.1}$$

where P_t and A are the illumination intensity and effective area of the heterojunction I_{dark} and I_{light} are photocurrent without and with light illumination, respectively. Without strain applied, the highest value of R was around 2.1×10^3 A/W at an intensity of 0.47 mW/cm^2 and a bias voltage +0.5V. The key performance indicators of our p-n heterojunction with those reported by other groups are listed in Table 5-2 for

comparison. Our heterojunction has showed an ultrahigh photoresponsivity at very low bias voltages, owing to a higher photocurrent generation efficiency and lower power consumption [243, 248]. The specific detectivity is defined as:

$$D^* = \frac{R}{\sqrt{\frac{2qI_{dark}}{A}}} \tag{5.2}$$

where R and q are the responsivity and elementary charge. It is used to evaluate the capability of detecting the incident photons. The D^* value for our device was about 5.7×10^{10} Jones at the intensity of 0.47 mW/cm^2, showing a good sensitivity to the light. The R and D^* under a bias voltage of +0.5 V and several illumination intensities from 0.07 mW/cm^2 to 0.47 mW/cm^2 are given in Figure 5-6d. All these performance indicators suggest that this α-In_2Se_3/3R MoS_2 heterojunction could function as a self-powered photodetector.

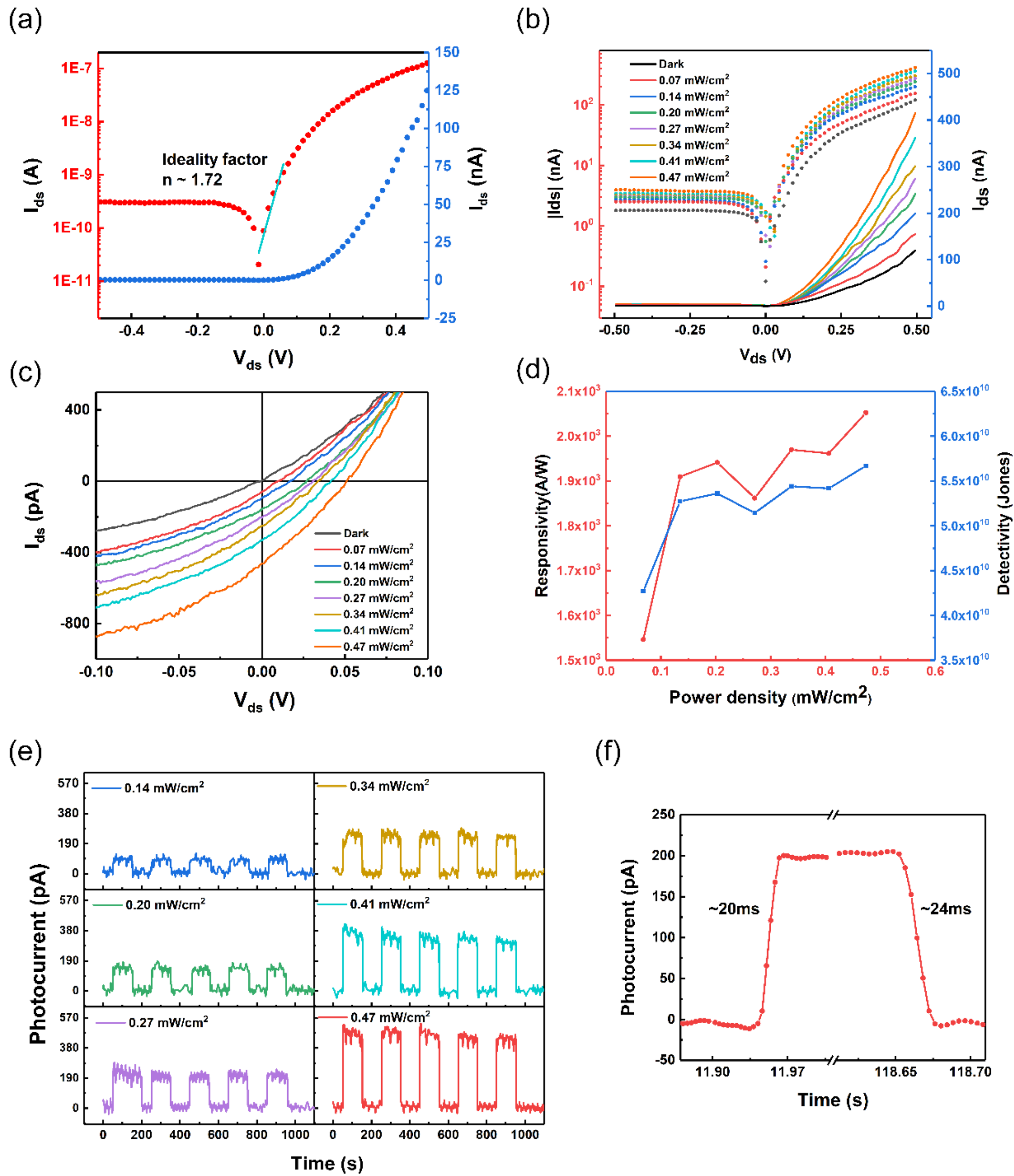

Figure 5-6 Electrical characterization and photoresponse from the α-In_2Se_3/3R MoS_2 heterojunction under zero strain. (a) *I-V* characteristic in the dark with the logarithmic and linear scale. (b, c) *I-V* characteristics in the dark and under illumination of 532 nm wavelength under different light intensities from -0.5 V to 0.5 V and -0.1 V to 0.1 V with the logarithmic and linear scale, respectively. (d) Responsivity and detectivity at a bias voltage of 0.5 V as a function of illumination intensities. (e) Current vs time under

532 nm illumination with several intensities and zero bias voltage. (f) Current vs time extracted from (e) under the illumination intensity of 0.27 mW/cm^2.

The photocurrent as a function of time under several illumination intensities and zero bias voltage is shown in Figure 5-6e. The photocurrent could stabilize from ~100 pA to ~500 pA under a series illumination light from 0.07 mW/cm^2 to 0.47 mW/cm^2. The device showed a rise and fall time of 20 and 24 ms with an illumination light of 0.27 mW/cm^2, as shown in Figure 5-6f, suggesting a faster light response than most of the In_2Se_3 based photodetectors developed by other groups [233, 249-252].

Materials	λ (nm)	V_{bias} (V)	Responsivity (A/W)	Detectivity (*D**)	Response time (ms)	Refs
α-In_2Se_3/3R MoS_2	532	0.5	2052	5.7×10^{10}	20	This work
MoS_2 Monolayer	442	2	2.3×10^4	NA	NA	[153]
MoS_2 Monolayer	532	-10	1162	1.7×10^{12}	NA	[228]
MoS_2 Multilayer	532	1.2	59	NA	0.042	[243]
α-In_2Se_3 Monolayer	532	2	340	NA	6	[102]
α-In_2Se_3 Nanosheets	300	5	395	2.3×10^{12}	18	[231]
In_2Se_3 nanosheets	532	5	20.5	6.0×10^{11}	24.6	[232]
β-In_2Se_3 flake	650	20	3.8	1×10^{10}	3870	[233]

WSe_2 / CdS	680	2	33.4	NA	NA	[248]
MoS_2 / WSe_2	532	NA	1.8×10^{-3}	NA	NA	[154]
β-In_2Se_3 / MoS_2	450	1	4.47	1.1×10^{9}	52	[249]
MoS_2 / GaN	365 /685	20	127 @ 365 33 @ 685	1.1×10^{11}	1500 @ 365 8000 @ 685	[250]
β-In_2Se_3 / GaN	365 /685	20	1.6 @ 365 0.3 @ 685	1.6×10^{9}	210 @ 365 2300 @ 685	[250]
CuO / MoS_2	432	10	NA	3.3×10^{8}	NA	[229]
WSe_2 / α-In_2Se_3	650	-1	0.026	NA	2.3	[251]
GaN / α-In_2Se_3	365 /850	3	127 @ 365 33 @ 850	3.6×10^{10} @ 850	130 @ 365 200 @ 850	[252]

Table 5-2 Comparison of the characteristic parameters of our present heterojunction devices with other 2D materials-based photo devices.

Recent theoretical calculation predicts that the photocurrent generation from a α-In_2Se_3/3R MoS_2 heterojunction could cover from visible light to near infrared region, with a higher optical absorption coefficient and current density than an isolated In_2Se_3 layer [238]. Indeed, infrared photoresponse from few layer β-In_2Se_3/monolayer MoS_2 heterojunctions showed an extended detection range from the visible to near infrared region [249], due to the relatively small bandgap of β-In_2Se_3. As illustrated in Figure 5-7, the photoresponse from our α-In_2Se_3/3R MoS_2 heterojunction did cover the visible and near infrared regions. Our device showed a superior performance with three orders

higher responsivity and detectivity than that of β-In_2Se_3/monolayer MoS_2 heterojunctions. It is easily found from Figure 5-7b, c that the photocurrent under 532 nm illumination was around four times larger than that under 800 nm illumination, very likely due to weak light absorption in the near infrared region [253].

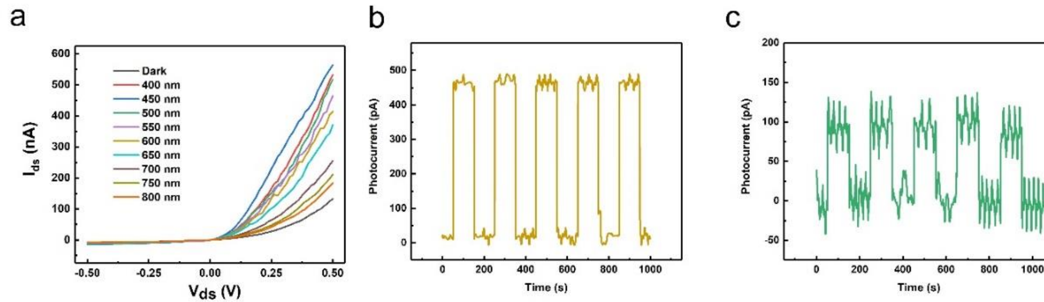

Figure 5-7 Photoresponse from the α-In_2Se_3/3R MoS_2 heterojunction under several different light intensities under zero strain. (a) *I-V* characteristic under illumination intensity of 0.47 mW/cm^2 with different wavelengths. (b) Current vs time under the 532 nm illumination intensity of 0.47 mW/cm^2, and (c) Current vs time under 800nm illumination intensity of 0.47 mW/cm^2 with zero bias voltage.

To confirm the photoresponse was dominated the heterojunction, rather than from the α-In_2Se_3 or 3R MoS_2 flake, a scanning photocurrent microscopic image (SPCM) was performed on the entire area between the two electrodes using a WITec Raman system with laser light of 532 nm at a power of 0.1 mW. The SPCM images shown in Figure 5-8 clearly displayed that it was only in the heterojunction area where the photocurrent was apparently generated when the α-In_2Se_3/3R MoS_2 heterojunction was applied with a reverse bias of -0.25V, zero bias and a forward bias of 0.25 V. The photocurrent was evidently large with forward bias.

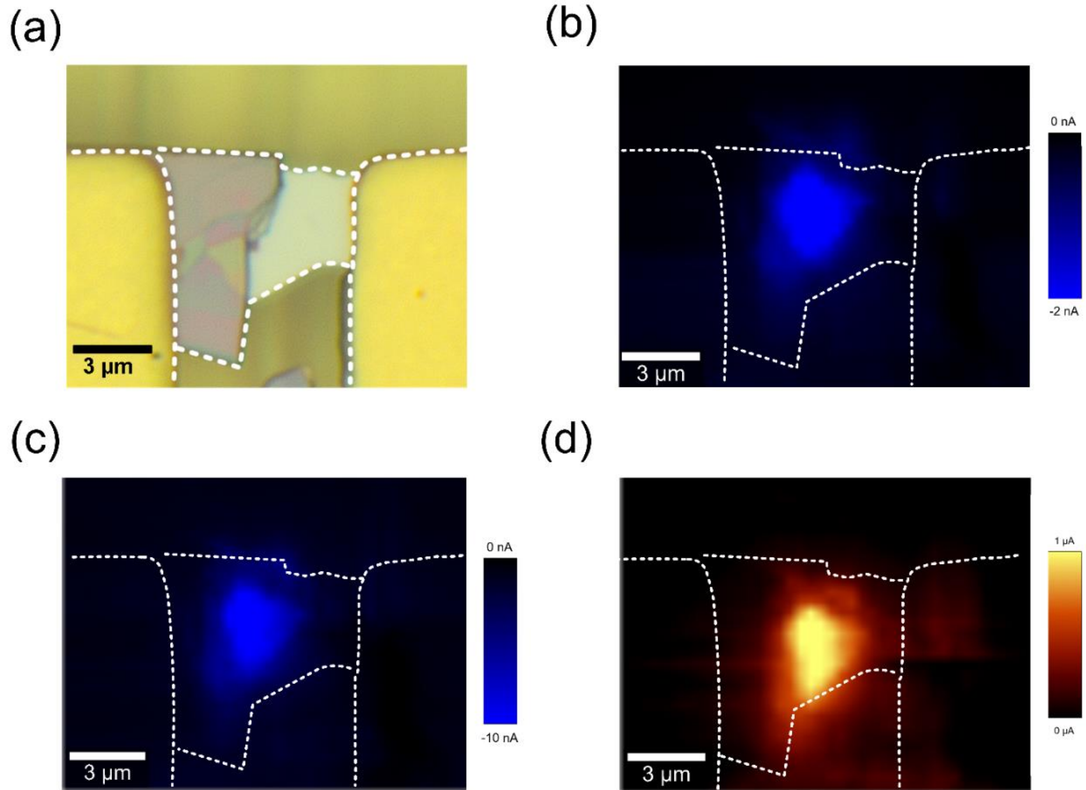

Figure 5-8 The optical scanning photocurrent images of the α-In_2Se_3/3R MoS_2 heterojunction. (a) The optical image. (b-d) Photocurrent mapping of the heterojunction under zero bias, reverse bias of -0.25 V and forward bias of 0.25 V at 532 nm with a laser power of 0.1mW and a spot waist radius of 400 nm.

5.3.3 α-In_2Se_3/3R MoS_2 heterojunction photoelectric performance with strain

The α-In_2Se_3/3R MoS_2 heterojunction was characterized under various strains in dark, to especially observe the piezoelectric modulated carrier transport as shown in Figure 5-9. Apparent strain-modulated *I-V* characteristics can be seen with enhancing (weakening) rectification characteristics under compressive (tensile) strains. The enhancing (weakening) rectification might be attributed to the energy barrier decrease (increase) at the interface due to the piezoelectric polarization charges. With a bias voltage of +0.5V, the current I_{ds} was increased from 136 pA to 200 pA under a compressive strain of -0.26% and decreased to 65 pA under a tensile strain of +0.35%.

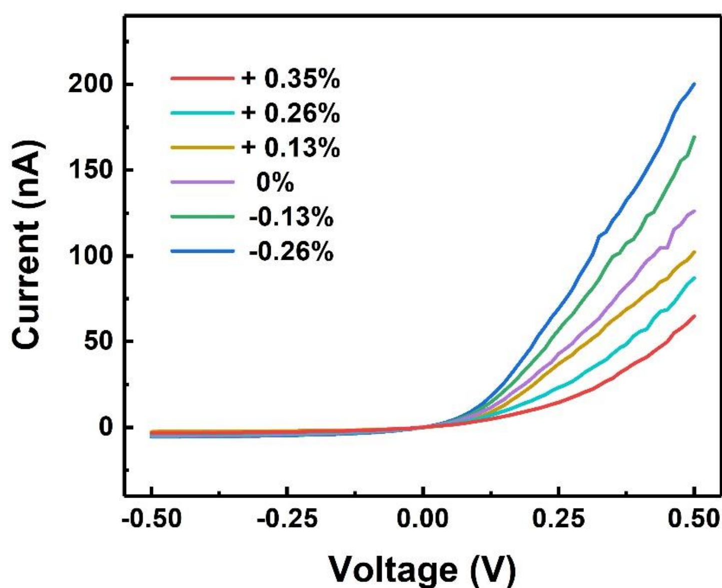

Figure 5-9 *I-V* characteristic of the α-In_2Se_3/3R MoS_2 heterojunction under several strains in dark.

Then, the α-In_2Se_3/3R MoS_2 heterojunction was measured under the dark and various 532 nm light illumination intensities with the strain of +0.13%, +0.26%, -0.13% and -0.26% from -0.5V to 0.5V, and -0.1V to 0.1, respectively, as depicted in Figure 5-10 and Figure 5-11. The corresponding responsivity, detectivity, and relative change of the responsivity or detectivity were also extracted from the *I-V* characteristic curves and plotted. Upon a compressive strain of -0.26%, the responsivity increased from 1.5×10^3 A/W to 2.9×10^3 A/W, by 88%, while the detectivity rose from 4.3×10^{10} Jones to 6.2×10^{10} Jones, by 46% with a bias voltage +0.5V. Under a bias voltage of -0.1 V, the strain-modulations of the responsivity and detectivity occurred at a low illumination intensity of 0.07 mW/cm^2 were much more significant than at a high intensity of 0.41 mW/cm^2, as shown in Figure 5-11e and f. The responsivity and detectivity decreased by 80% (from 5.9 A/W to 1.2 A/W) and 80% (3.4×10^9 Jones to 6.9×10^8 Jones), under a compressive strain of -0.26%. This power-dependent modulation was also observed in

the relative changes in the responsivity and detectivity of the heterojunction under a bias voltage of -0.5 V.

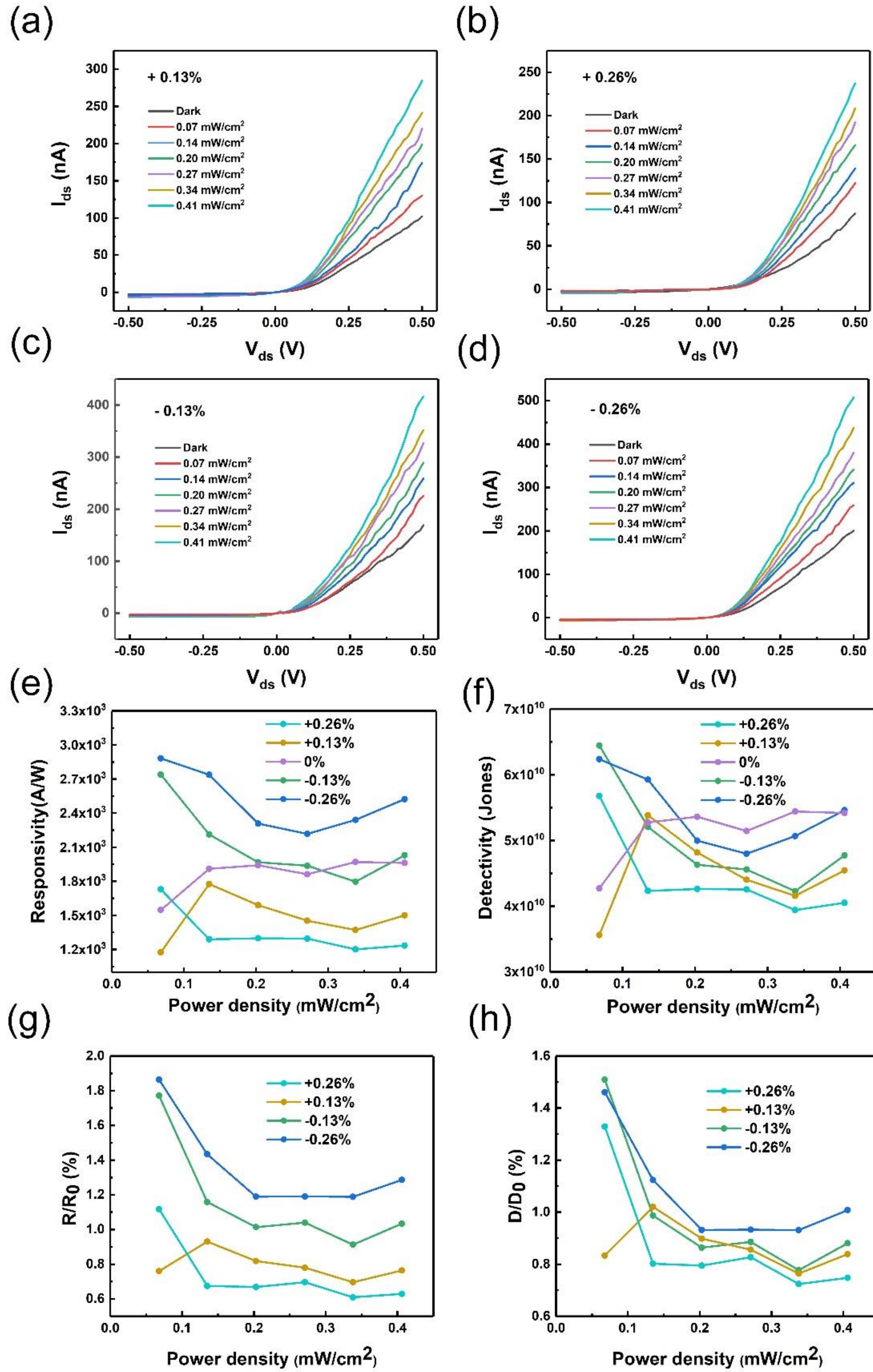

Figure 5-10 (a-d) *I-V* characteristics of the α-In_2Se_3/3R MoS_2 heterojunction (Fig 1c) from -0.5 V to 0.5 V under the dark and various 532 nm light illumination intensities

with the strain of +0.13%, +0.26%, -0.13% and -0.26%. (e-f) Responsivity, detectivity, relative change of the responsivity and relative change of detectivity with respect to that under zero strain as a function of the light intensities and strains under +0.5 V bias.

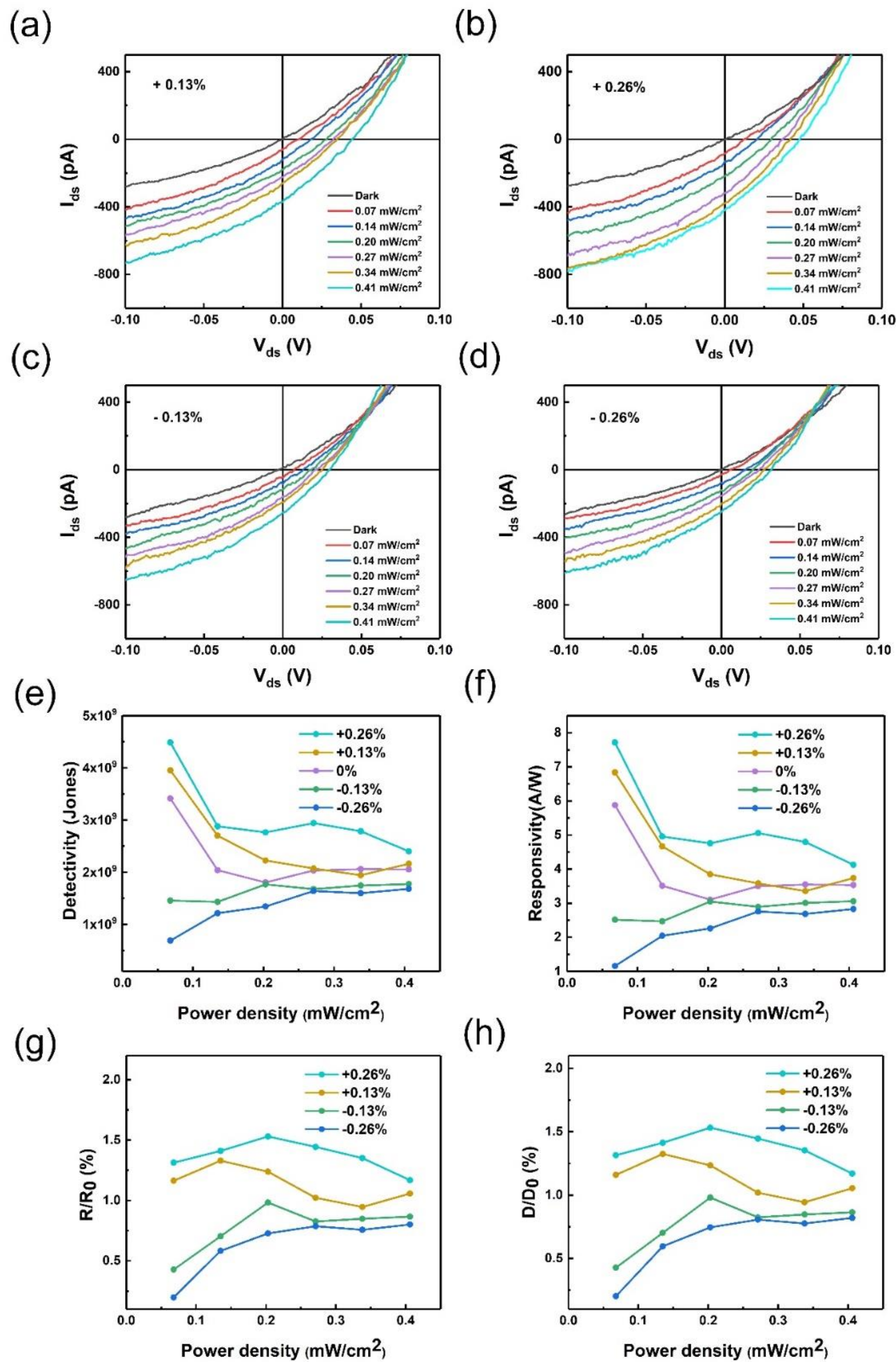

Figure 5-11 (a-d) *I-V* characteristics of the α-In_2Se_3/3R MoS_2 heterojunction (Fig 1c) from -0.1 V to 0.1 V under the dark and various 532 nm light illumination intensities

with the strain of +0.13%, +0.26%, -0.13% and -0.26%. (e-f) Responsivity, detectivity, relative change of the responsivity and relative change of detectivity with respect to that under zero strain as a function of the light intensities and strains under -0.1 V bias.

Extracted from Figure 5-11a-d, the open circuit voltage V_{oc} and short circuit current I_{sc} were increased with increasing the tensile strain but decreased with increasing the compressive strain as shown in Figure 5-12.

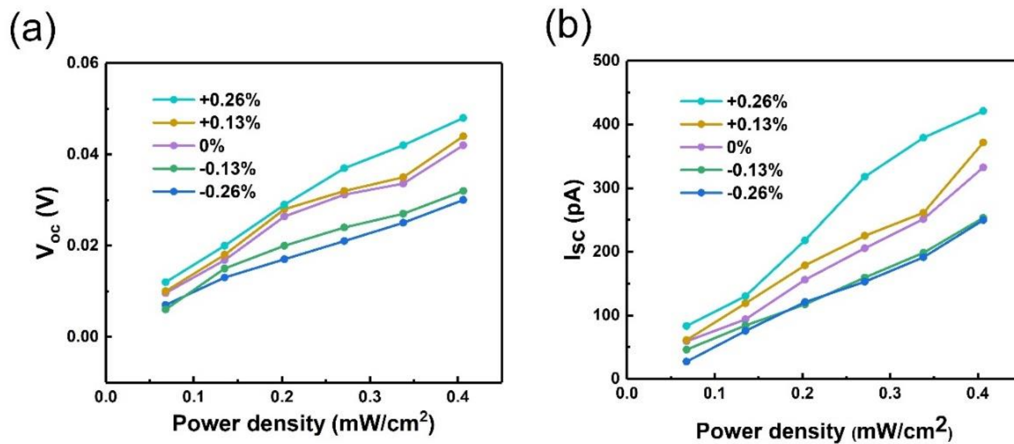

Figure 5-12 (a) Open circuit voltage V_{oc} and (b) Short circuit current I_{sc} under various light intensities and strains (The data were extracted from Figure 5-11).

The *I-t* of the heterojunction was measured under zero bias and several strains under a low illumination of 0.27 mW/cm^2 and a high illumination of 1.08 mW/cm^2, shown in Figure 5-13a and b, respectively. In Figure 5-13c, , under a low light intensity of 0.27 mW/cm^2, the photocurrent was increased from 220 pA to 360 pA (by 64%) up on a tensile strain of +0.35%, but decreased from 220 pA to 130 pA (by 41%) with a compressive strain of -0.26%. In contrast, under a high illumination intensity of 1.08 mW/cm^2, it was only increased from 710 pA to 750 pA (by 5.6%) under the tensile strain and decreased from 710 pA to 650 pA (by 8.5%) under the compressive strain. All the

above results showed that the strain-influenced photocurrent was apparent under low intensity than under high intensity.

Illumination intensity dependent strain-modulation of the photocurrent may not be accounted for by the strain induced optical light absorption coefficient change in the 2D vdWs flakes, as the theoretical calculation has indicated that only a small change in light absorption coefficient in a 2% strained In_2Se_3/MoS_2 heterojunction from ultraviolet to near-infrared light range [253]. As the strains applied in this study were much smaller than 2%, the strain induced optical light absorption coefficient change in the 2D flakes can be ignored. In Figure 5-5, the In_2Se_3 and MoS_2 devices with good Ohmic contacts did not show detectable electrical transport modulation under mechanical strains. It implies very little change in the energy bandgaps of In_2Se_3 and MoS_2 under the same magnitude of the strains. In addition, in one previous study, the Raman shift became apparent for a monolayer MoS_2 flake only when applied strain was larger than 0.6% [212]. For our devices, the maximum strain applied was 0.35%, much smaller than 0.6%. These phenomena rule out the contribution from piezoresistive effect. Instead, the findings could be well interpreted using a piezoelectric potential originated from the piezoelectric charges at the heterojunction interface.

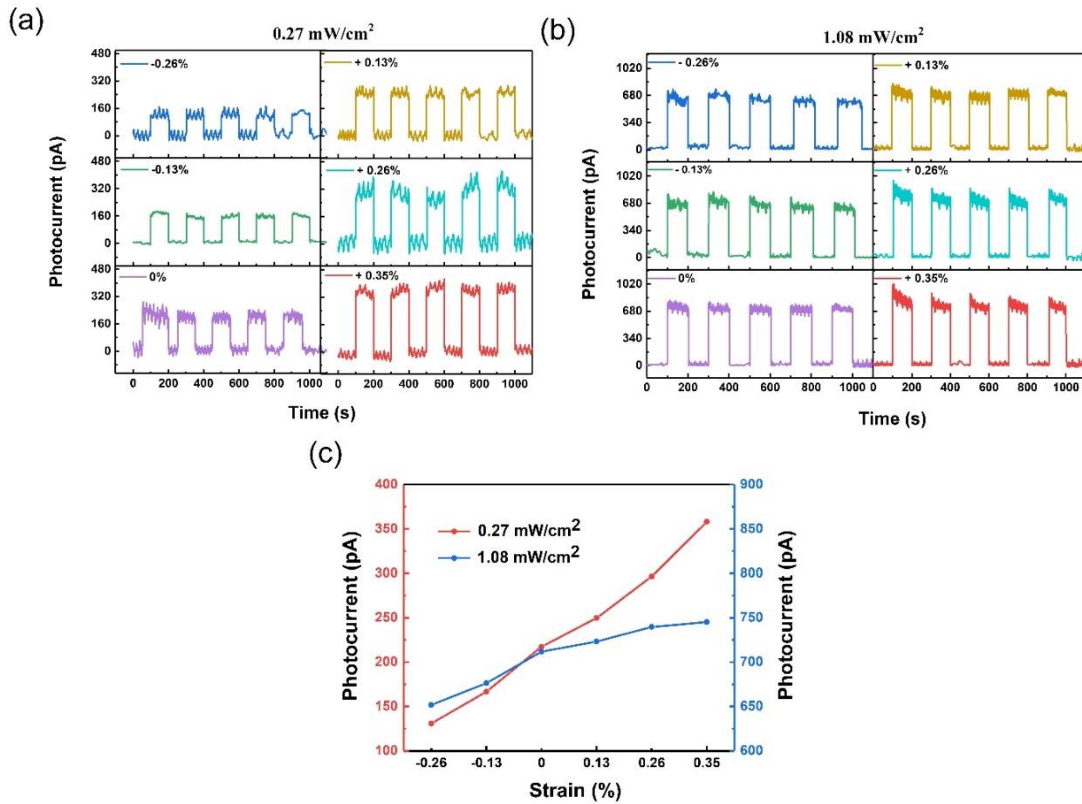

Figure 5-13 (a, b) *I-t* of the heterojunction under zero bias and several strains at the 532 nm light intensity of 0.27 mW/cm^2 and 1.08 mW/cm^2. (c) Average photocurrent as a function of strains under zero bias at the illumination intensities of 0.27 mW/cm^2 and 1.08mW/cm^2, respectively.

5.4 Working Principle

To explain the strain-modulated photoresponse, the energy band diagrams of the heterojunction are plotted in Figure 5-14. When a 3R MoS_2 flake (with an indirect band gap of 1.29 eV and a higher electron affinity of 4.0 eV) is in contact with an α-In_2Se_3 flake (having a direct band gap of 1.55 eV and a lower electron affinity of 3.6 eV) [240, 253-257], a negative (positive) space charge region in the 3R MoS_2 (α-In_2Se_3) flake is established, forming a p-n heterojunction in the thermal equilibrium under zero strain. The widths of the depletion region located in 3R MoS_2 and α-In_2Se_3 sides can be

estimated using the depletion model for a conventional p-n heterostructure, as given below:

$$x_p = \sqrt{\frac{2N_d\varepsilon_{In_2Se_3}\varepsilon_{MoS_2}V_{bi}}{qN_a\left(\varepsilon_{In_2Se_3}N_a + \varepsilon_{MoS_2}N_d\right)}} \tag{5.3}$$

$$x_n = \sqrt{\frac{2N_a\varepsilon_{In_2Se_3}\varepsilon_{MoS_2}V_{bi}}{qN_d(\varepsilon_{In_2Se_3}N_a + \varepsilon_{MoS_2}N_d)}} \tag{5.4}$$

where N_a and N_d are the doping concentrations in the 3R MoS_2 and α-In_2Se_3 flakes, respectively; V_{bi} is the built-in voltage; q is the elementary charge, ε_{MoS_2} and $\varepsilon_{In_2Se_3}$ are the permittivity of 3R MoS_2 and α-In_2Se_3 flakes, respectively [245, 258-260]. As the carrier concentration, layer thickness and permittivity for the MoS_2 (In_2Se_3) flake are $p \approx 2.3 \times 10^{12}$ $(n \approx 1.2 \times 10^{12})$ cm^{-3}, $t_{\mathrm{MoS_2}} \approx 30\ (t_{\mathrm{In_2Se_3}} \approx 206)$ nm, $\varepsilon_{MoS_2} = 6.9 \times \varepsilon_0 (\varepsilon_{In_2Se_3} = 17 \times \varepsilon_0)$ [261-264], where ε_0 is the permittivity in vacuum, the doping concentration could be estimated as $N_a = \frac{n}{t_{\mathrm{In_2Se_3}}} \approx 5.7 \times 10^{16}$ $(N_d = \frac{p}{t_{\mathrm{MoS_2}}} \approx 7.7 \times 10^{17})$ cm^{-3}. The built-in voltage $V_{bi} \approx \frac{KT}{q}\ln\left(\frac{N_aN_d}{np}\right) \approx 0.61$ V, for the type II band alignment, and the depletion width in the 3R MoS_2 (α-In_2Se_3) flake should be $x_p \approx 130$ $(x_n \approx 9.7)$ nm. As the depletion width in the MoS_2 flake exceeded the thickness of MoS_2 flake, the 3R MoS_2 could be fully depleted. Since the theoretical d_{13} magnitude of α-In_2Se_3 is 3.08 pm/V, a factor of 15 times larger than that of 3R MoS_2, we could ignore the out of plane piezoelectric polarization in the 3R MoS_2 flake for simplicity of discussion [22, 239]. Under a tensile (compressive) strain in dark, positive (negative) piezoelectric charges could emerge at the bottom surface of the α-In_2Se_3 flake [261]. The positive (negative) piezoelectric charges lower (raise) the energy band near the interface of the α-In_2Se_3 flake, as shown in Figure 5-14b, c. The total internal electric

field is enhanced (weakened) so that the potential barrier height is increased (decreased) in comparison with the condition of zero strain. As a result, the current under a forward bias would be reduced (enhanced) so that the rectification factor was found to be smaller (larger) under a tensile (compressive) strain, as shown in Figure 5-9. Upon illumination, only those electron-hole pairs created in or near the heterojunction could be separated by the built-in electric field so that the electrons (holes) could be swept into α-In_2Se_3 (3R MoS_2), giving rise to a photocurrent, see Figure 5-14d. Upon a tensile (compressive) strain applied, the total internal electric field is enhanced (weakened) and the electric potential difference is then increased (decreased) in the heterojunction as discussed above, in favor of (weakening) separation of the electron-hole pairs and injection efficiency in or near the heterojunction, as illustrated in Figure 5-14e and f, causing V_{oc} and I_{sc} increasing (decreasing) with raising tensile (compressive) strain, as shown in Figure 5-12. At a high illumination intensity, the number of electron hole pairs in or near the heterojunction is greatly increased so that the piezoelectric polarization charges could be effectively screened. This could equivalently reduce strain modulation effect [153, 154, 228], in consistence with our experimental finding of the light intensity dependence of the photocurrent modulation.

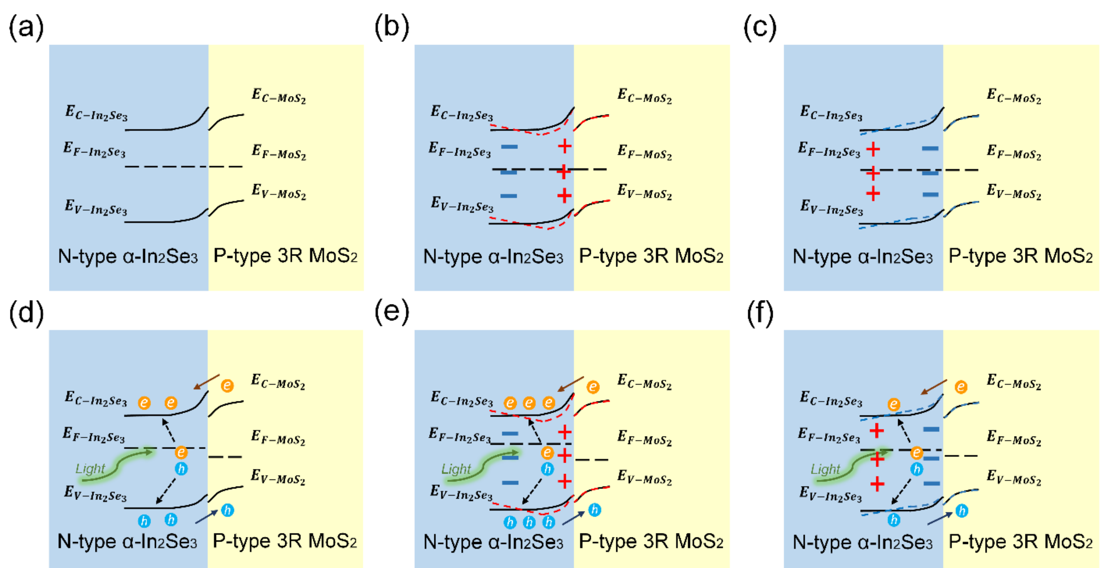

Figure 5-14 The energy band diagrams for the α-In_2Se_3/3R MoS_2 heterojunction with\without the strains and light illumination. The energy band diagram (a) in thermal equilibrium with zero light illumination and no external strain (b) under zero light illumination and a tensile strain (c) under zero light illumination and a compressive strain (d) under light illumination, and no strain applied (e) under light illumination and a tensile strain (f) under light illumination and a compressive strain.

5.5 Conclusion

In this chapter, we successfully fabricated a high performance flexible heterojunction photodetectors by stacking an α-In_2Se_3 flake with a 3R MoS_2 flake. The devices showed clear photocurrent response to visible and near infrared light. These heterojunction devices exhibit an ultrahigh photoresponsivity of 2.9×10^3 A/W and a substantial specific detectivity of 6.2×10^{10} Jones under a compressive strain of -0.26%. The photocurrent response was found to be enhanced (reduced) with a tensile (compressive) strain and the strain modulation of the photocurrent response was much more significantly under weak illumination than that under strong illumination. Under a low light intensity of 0.27 mW/cm^2, the photocurrent was increased from 220 pA to 360 pA (by 64%) up on a tensile strain of +0.35%. The strain modulation could be caused by strain-induced piezoelectric polarization charges, which alter the total internal electric field in the heterojunction, promoting (weakening) collection of the photocarriers

Chapter 6 Conclusions

6.1 Conclusions

In the thesis, a systematic study of 2D piezoelectric 3R MoS_2 flakes has been conducted to characterize their piezoelectricity; intrinsic thermal conductivity, interfacial thermal conductance and to develop 3R MoS_2 van der Waals heterojunction for near-infrared to visible range photodetection.

Firstly, the 6-fold polarization dependence observed in multilayer 3R MoS_2 flakes with the SHG technique provides a clear evidence of broken symmetry structure of the multilayer material. The polarization charges generated in the flakes are dependent on both the crystalline orientation and mechanical strain directions. The piezoelectric polarization clearly depends on whether the strain is applied along the zigzag or the armchair direction. The 3R MoS_2 piezoelectric nanogenerator exhibited excellent electrical outputs of ~102 mV and ~210 pA and an outstanding power density of 65 mW/m^2, which is at least one order larger than the previous transition metal dichalcogenides based piezoelectric nanogenerators due to the higher in-plane and out-of-plane piezoelectricity of 3R MoS_2 from monolayer to bulk. The out-of-plane piezoelectric coefficient d_{33} has been determined to be around 0.7 to 1.5 pm/V for multilayer 3R MoS_2 using the DART-PFM technique, about five time larger than the theoretical value. We suggest that a strong piezoelectric response exists due to the coupling of in-plane and out-of-plane piezoelectricity, from lateral PFM excitation measurement.

Secondly, the in-plane intrinsic thermal conductivity of 3R MoS_2 flakes exhibits a 3% to 4% change under a uniaxial strain of 0.26%, by adopting Optothermal Raman method. The thermal conductance of metal/3R MoS2/metal structures could decreased a

maximum 24.7% under a tensile strain of 0.26%, using a laser heating thermal couple method. We suggest that the interfacial thermal conductance could be modified by strains, through electron-electron coupling in addition to the phonon-phonon and electron-phonon coupling. This is the first experimental observation of strain-modulated thermal conductance from the structures of the metal/2D 3R MoS_2 contact.

Lastly, our 3R MoS_2 /α-In_2Se_3 heterojunction achieved an ultrahigh photoresponsivity of 2.9 $\times 10^3$ A/W and a substantial specific detectivity of 6.2 $\times$ 10^{10} Jones under a compressive strain of -0.26%. It yields a wide spectrum response to the visible and infrared light. This flexible heterojunction achieved a better photodetector performance than most other MoS_2 and In_2Se_3 based devices. The photocurrent response of α-In_2Se_3/3R MoS_2 shows clear strain modulation under weak illumination, compared with that under high illumination. The photocurrent was increased from 220 pA to 360 pA (by 64%) under a tensile strain of 0.35%, under a light intensity of 0.27mW/cm^2. This modulation is attributed to the potential barrier height modulation by the generated piezo polarizations at the interface.

6.2 Future work

According to the present results obtained and showed in this thesis, several aspects of 3R MoS_2 properties are still unclear, like the values of in-plane piezoelectric coefficients d_{22} and d_{13}; the dominant heat modulation mechanism at the metal-piezoelectric semiconductor structures, etc. Hence, several recommendations for future work are summarized here:

- In the lateral PFM measurement, AFM tip probes the out-of-plane deformation that results from lateral voltage-induced strain. There are several factors that

might affect and amplify the tip detection, like substrate-sample charging effect and coupling of in-plane and out-of-plane piezoelectricity, etc. To avoid the substrate effect, a suspended 3R MoS_2 could be fabricated for the measurement.

- In addition to the piezoelectric coefficients, other possible influential factors or parameters, like polarization of charges at multidirectional 2D PMs, the flakes size and shape, and surface modification, etc. should be investigated for in-depth understanding of the 2D PMs.
- To drive the 2D piezoelectric materials for practical application, the 2D piezoelectric nanogenerators can be integrated with other electronic devices, like energy storage devices, sensors and other wearable electronics, to construct advanced self-powered flexible systems.
- For the thermal conductivity measurement, apart from the two methods used in this thesis, the time-domain thermoreflectance (TDTR) is another optical method to measure thermal transport at the atomic level. Due to heat penetration at the nanoscale, TDTR is also a power technique for the interface thermal transport measurement, especially focusing on metal-semiconductor interfaces. Using TDTR, we could further investigate the interfacial thermal conductance of various metals and piezoelectric combinations under external strains.
- In addition to the experiments, theoretical study should be carried out for the heat transport at the metal-piezoelectric semiconductor interfaces using first principle calculation, Density functional theory and MD simulations, etc.
- For 2D piezo-phototronic devices, the interest is not only limited to the physics and devices performance, but also the potential in the practical applications. The stability and durability of the piezo-phototronic devices, and the metal-

semiconductor contact under strains, ambient environment influences and the passivation methods, could be further studied.

- Unique scientific merits may come from the atomic stacking structures of 2D piezoelectric materials. It is highly worthy to study the physical properties, like ferroelectricity, ferromagnetism and quantum spin, of the coupling effects relevant to the stacking.

Author's Publications

[1] **Weifan Cai**, Jingyuan Wang, Yongmin He, Sheng Liu, Qihua Xiong, Zheng Liu, Qing Zhang, Strain modulated photoelectric responses from a flexible α-In_2Se_3/3R MoS_2 heterojunction. Nano-Micro Lett. 13, 65 (2021). https://doi.org/10.1007/s40820-020-00584-1

[2] Hamida Hallil, **Weifan Cai**, Kang Zhang, Peng Yu, Sheng Liu, Ran Xu, Chao Zhu, Qihua Xiong, Zheng Liu, Qing Zhang. Observation of strong piezoelectricity in 3R MoS_2 flakes. to be submitted.

[3] Zhang, Qing, Ran Xu, and **Weifan Cai**, Pumping Electrons from Chemical Potential Difference. Nano Energy 51 (2018): 698–703. https://doi.org/10.1016/j.nanoen.2018.07.016.

[4] Zou, Jianping, Kang Zhang, **Weifan Cai**, Tupei Chen, Arokia Nathan, and Qing Zhang, Optical-Reconfigurable Carbon Nanotube and Indium-Tin-Oxide Complementary Thin-Film Transistor Logic Gates. Nanoscale 10, no. 27 (2018): 13122–29. https://doi.org/10.1039/c8nr01358f.

[5] Zhang, Kang, Jingyuan Wang, Jianping Zou, **Weifan Cai**, and Qing Zhang, Low Excitation of Raman D-Band in [2+1] Cycloaddition Functionalized Single-Walled Carbon Nanotubes. Carbon 138 (2018): 188–96. https://doi.org/10.1016/j.carbon.2018.05.073.

[6] Sun, Leimeng, Xinghui Wang, Yurong Wang, Dongyang Xiao, **Weifan Cai**, Yuan Jing, Yanrong Wang, Fangjing Hu, and Qing Zhang, In-Situ Functionalization of Metal Electrodes for Advanced Asymmetric Supercapacitors. Frontiers in Chemistry 7 (2019). https://doi.org/10.3389/fchem.2019.00512.

[7] Deng, Liying, Wangyang Li, Hongnan Li, **Weifan Cai**, Jingyuan Wang, Hong Zhang, Hongjie Jia, Xinghui Wang, and Shuying Cheng, A Hierarchical Copper Oxide–Germanium Hybrid Film for High Areal Capacity Lithium Ion Batteries. Frontiers in Chemistry 7 (2020). https://doi.org/10.3389/fchem.2019.00869.

Bibliography

1. *Piezoelectric Devices - Global Market Trajectory & Analytics*. September 2020 Available from: https://www.researchandmarkets.com/reports/4805749/piezoelectric-devices-global-market-trajectory#rela0-5140063.
2. *Piezoelectric Smart Materials - Global Market Trajectory & Analytics*. September 2020 Available from: https://www.researchandmarkets.com/reports/5140063/piezoelectric-smart-materials-global-market#rela1-5229211.
3. Uchino, K., *Chapter 1 - The Development of Piezoelectric Materials and the New Perspective*, in *Advanced Piezoelectric Materials (Second Edition)*, K. Uchino, Editor. 2017, Woodhead Publishing. p. 1-92.
4. Dagdeviren, C., et al., *Recent progress in flexible and stretchable piezoelectric devices for mechanical energy harvesting, sensing and actuation.* Extreme Mechanics Letters, 2016. **9**: p. 269-281.
5. Duan, W.H., Q. Wang, and S.T. Quek, *Applications of Piezoelectric Materials in Structural Health Monitoring and Repair: Selected Research Examples.* Materials (Basel), 2010. **3**(12): p. 5169-5194.
6. Elahi, H., et al., *A Review on Applications of Piezoelectric Materials in Aerospace Industry.* Integrated Ferroelectrics, 2020. **211**(1): p. 25-44.
7. Kulkarni, H., et al., *Application of piezoelectric technology in automotive systems.* Materials Today: Proceedings, 2018. **5**(10): p. 21299-21304.
8. Kim, D.-H., et al., *Epidermal Electronics.* Science, 2011. **333**(6044): p. 838.
9. Wang, P., et al., *The Evolution of Flexible Electronics: From Nature, Beyond Nature, and To Nature.* Adv Sci (Weinh), 2020. **7**(20): p. 2001116.
10. Kenry, J.C. Yeo, and C.T. Lim, *Emerging flexible and wearable physical sensing platforms for healthcare and biomedical applications.* Microsyst Nanoeng, 2016. **2**: p. 16043.
11. Wang, H., Y. Yang, and L. Guo, *Nature-Inspired Electrochemical Energy-Storage Materials and Devices.* Advanced Energy Materials, 2017. **7**(5).
12. Rogers, J.A., T. Someya, and Y. Huang, *Materials and Mechanics for Stretchable Electronics.* Science, 2010. **327**(5973): p. 1603.
13. Bertolazzi, S., J. Brivio, and A. Kis, *Stretching and Breaking of Ultrathin* MoS_2. ACS Nano, 2011. **5**(12): p. 9703-9709.
14. Cui, C., et al., *Two-dimensional materials with piezoelectric and ferroelectric functionalities.* npj 2D Materials and Applications, 2018. **2**(1): p. 18.
15. Novoselov, K.S., et al., *Electric Field Effect in Atomically Thin Carbon Films.* Science, 2004. **306**(5696): p. 666.
16. Zhang, J. and S.A. Meguid, *Piezoelectricity of 2D nanomaterials: characterization, properties, and applications.* Semiconductor Science and Technology, 2017. **32**(4): p. 043006.
17. Hinchet, R., et al., *Piezoelectric properties in two-dimensional materials: Simulations and experiments.* Materials Today, 2018. **21**(6): p. 611-630.
18. Cheon, G., et al., *Data Mining for New Two- and One-Dimensional Weakly Bonded Solids and Lattice-Commensurate Heterostructures.* Nano Letters, 2017. **17**(3): p. 1915-1923.

19. Wu, W.Z., et al., *Piezoelectricity of single-atomic-layer MoS2 for energy conversion and piezotronics.* Nature, 2014. **514**(7523): p. 470-+.
20. c
21. Zhou, Y., et al., *Out-of-Plane Piezoelectricity and Ferroelectricity in Layered α-In $_2$ Se $_3$ Nanoflakes.* Nano Letters, 2017. **17**(9): p. 5508-5513.
22. Konabe, S. and T. Yamamoto, *Piezoelectric coefficients of bulk 3R transition metal dichalcogenides.* Japanese Journal of Applied Physics, 2017. **56**(9): p. 098002.
23. Curie, J. and P. Curie, *Développement par compression de l'électricité polaire dans les cristaux hémièdres à faces inclinées.* Bulletin de la Société minéralogique de France, 1880. **3**(4): p. 90-93.
24. Lippmann, G., *Principe de la conservation de l'électricité, ou second principe de la théorie des phénomènes électriques.* Journal de Physique Théorique et Appliquée, 1881. **10**(1): p. 381-394.
25. Ahmed, R., F. Mir, and S. Banerjee, *A review on energy harvesting approaches for renewable energies from ambient vibrations and acoustic waves using piezoelectricity.* Smart Materials and Structures, 2017. **26**(8).
26. Bowen, C.R., et al., *Piezoelectric and ferroelectric materials and structures for energy harvesting applications.* Energy Environ. Sci., 2014. **7**(1): p. 25-44.
27. Liu, H., et al., *A comprehensive review on piezoelectric energy harvesting technology: Materials, mechanisms, and applications.* Applied Physics Reviews, 2018. **5**(4): p. 041306.
28. contributors, W. *List of piezoelectric materials*. 3 January 2021 05:33 UTC]; Available from: https://en.wikipedia.org/w/index.php?title=List_of_piezoelectric_materials&oldid=997834470.
29. Zhang, Y., et al., *Ferroelectric and Piezoelectric Effects on the Optical Process in Advanced Materials and Devices.* Advanced Materials, 2018. **30**(34): p. 1707007.
30. Dahiya, R.S. and M. Valle, *Robotic Tactile Sensing*. 2013.
31. Tiersten, H.F., *Linear Piezoelectric Plate Vibrations*. 1969: Springer US.
32. *IEEE Standard on Piezoelectricity.* ANSI/IEEE Std 176-1987, 1988: p. 0_1.
33. Mason, W.P., *Electromechanical transducers and wave filters*. 1948, New York: D. Van Nostrand Co.
34. Dobson, P., *Physical Properties of Crystals – Their Representation by Tensors and Matrices.* Physics Bulletin, 1985. **36**: p. 506-506.
35. Li, F., et al., *Recent Advances in Strain-Induced Piezoelectric and Piezoresistive Effect-Engineered 2D Semiconductors for Adaptive Electronics and Optoelectronics.* Nano-Micro Letters, 2020. **12**(1): p. 106.
36. Barlian, A.A., et al., *Review: Semiconductor Piezoresistance for Microsystems.* Proceedings of the IEEE, 2009. **97**(3): p. 513-552.
37. Bao, M.-H., *Chapter 1 - Introduction to micro mechanical transducers*, in *Handbook of Sensors and Actuators*, M.-H. Bao, Editor. 2000, Elsevier Science B.V. p. 1-21.
38. Smith, C.S., *Piezoresistance Effect in Germanium and Silicon.* Physical Review, 1954. **94**(1): p. 42-49.
39. Fiorillo, A.S., C.D. Critello, and S.A. Pullano, *Theory, technology and applications of piezoresistive sensors: A review.* Sensors and Actuators A: Physical, 2018. **281**: p. 156-175.

40. Pierret, R.F., *Semiconductor device fundamentals*. 2006, Massachusetts: Addison-Wesley Longman.
41. Sun, Y., S.E. Thompson, and T. Nishida, *Physics of strain effects in semiconductors and metal-oxide-semiconductor field-effect transistors.* Journal of Applied Physics, 2007. **101**(10).
42. He, J.H., et al., *Piezoelectric Gated Diode of a Single ZnO Nanowire.* Advanced Materials, 2007. **19**(6): p. 781-784.
43. Yang, Q., et al., *Enhancing Sensitivity of a Single ZnO Micro-/Nanowire Photodetector by Piezo-phototronic Effect.* Acs Nano, 2010. **4**(10): p. 6285-6291.
44. Yu, R.M., et al., *Piezotronic effect enhanced performance of Schottky-contacted optical, gas, chemical and biological nanosensors.* Nano Energy, 2015. **14**: p. 312-339.
45. Wang, Z.L., *Piezopotential gated nanowire devices: Piezotronics and piezo-phototronics.* Nano Today, 2010. **5**(6): p. 540-552.
46. Wang, C.F., et al., *Enhanced emission intensity of vertical aligned flexible ZnO nanowire/p-polymer hybridized LED array by piezo-phototronic effect.* Nano Energy, 2015. **14**: p. 364-371.
47. Zhu, L.P., et al., *Piezo-Phototronic Effect Enhanced Flexible Solar Cells Based on n-ZnO/p-SnS Core-Shell Nanowire Array.* Advanced Science, 2017. **4**(1).
48. Han, X., et al., *Progress in piezo-phototronic effect enhanced photodetectors.* Journal of Materials Chemistry C, 2016. **4**(48): p. 11341-11354.
49. Peng, Y.Y., et al., *Progress in piezotronic and piezo-phototronic effect of 2D materials.* 2d Materials, 2018. **5**(4).
50. Wu, W.Z., Y.G. Wei, and Z.L. Wang, *Strain-Gated Piezotronic Logic Nanodevices.* Advanced Materials, 2010. **22**(42): p. 4711-+.
51. Wang, Z.L. and W.Z. Wu, *Piezotronics and piezo-phototronics: fundamentals and applications.* National Science Review, 2014. **1**(1): p. 62-90.
52. Wang, Z.L., *Piezoelectric Nanogenerators Based on Zinc Oxide Nanowire Arrays.* Science, 2006. **312**(5771): p. 242-246.
53. Xue, F., et al., *Piezotronic Effect on ZnO Nanowire Film Based Temperature Sensor.* Acs Applied Materials & Interfaces, 2014. **6**(8): p. 5955-5961.
54. Zhu, H., et al., *Observation of piezoelectricity in free-standing monolayer MoS2.* Nature Nanotechnology, 2015. **10**(2): p. 151-155.
55. Ghasemian, M.B., et al., *Peculiar piezoelectricity of atomically thin planar structures.* Nanoscale, 2020. **12**(5): p. 2875-2901.
56. Lin, P., C. Pan, and Z.L. Wang, *Two-dimensional nanomaterials for novel piezotronics and piezophototronics.* Materials Today Nano, 2018. **4**: p. 17-31.
57. Mele, E.J. and P. Kral, *Electric polarization of heteropolar nanotubes as a geometric phase.* Phys Rev Lett, 2002. **88**(5): p. 056803.
58. Michel, K.H. and B. Verberck, *Theory of elastic and piezoelectric effects in two-dimensional hexagonal boron nitride.* Physical Review B, 2009. **80**(22).
59. Duerloo, K.-A.N., M.T. Ong, and E.J. Reed, *Intrinsic Piezoelectricity in Two-Dimensional Materials.* The Journal of Physical Chemistry Letters, 2012. **3**(19): p. 2871-2876.
60. Li, Y., et al., *Probing symmetry properties of few-layer MoS2 and h-BN by optical second-harmonic generation.* Nano Lett, 2013. **13**(7): p. 3329-33.
61. Fei, Z., et al., *Ferroelectric switching of a two-dimensional metal.* Nature, 2018. **560**(7718): p. 336-339.
62. Blonsky, M.N., et al., *Ab Initio Prediction of Piezoelectricity in Two-Dimensional Materials.* Acs Nano, 2015. **9**(10): p. 9885-9891.

63. Manzeli, S., et al., *2D transition metal dichalcogenides.* Nature Reviews Materials, 2017. **2**(8).
64. Blonsky, M.N., et al., *Ab Initio Prediction of Piezoelectricity in Two-Dimensional Materials.* ACS Nano, 2015. **9**(10): p. 9885-9891.
65. Alyörük, M.M., et al., *Promising Piezoelectric Performance of Single Layer Transition-Metal Dichalcogenides and Dioxides.* The Journal of Physical Chemistry C, 2015. **119**(40): p. 23231-23237.
66. Li, W. and J. Li, *Piezoelectricity in two-dimensional group-III monochalcogenides.* Nano Research, 2015. **8**(12): p. 3796-3802.
67. Fei, R.X., et al., *Giant piezoelectricity of monolayer group IV monochalcogenides: SnSe, SnS, GeSe, and GeS.* Applied Physics Letters, 2015. **107**(17).
68. Gomes, L.C., A. Carvalho, and A.H. Castro Neto, *Enhanced piezoelectricity and modified dielectric screening of two-dimensional group-IV monochalcogenides.* Physical Review B, 2015. **92**(21).
69. Khan, H., et al., *Liquid metal-based synthesis of high performance monolayer SnS piezoelectric nanogenerators.* Nat Commun, 2020. **11**(1): p. 3449.
70. Şahin, H., et al., *Monolayer honeycomb structures of group-IV elements and III-V binary compounds: First-principles calculations.* Physical Review B, 2009. **80**(15).
71. Gao, R. and Y. Gao, *Piezoelectricity in two-dimensional group III-V buckled honeycomb monolayers.* physica status solidi (RRL) - Rapid Research Letters, 2017. **11**(3): p. 1600412.
72. Xia, F., H. Wang, and Y. Jia, *Rediscovering black phosphorus as an anisotropic layered material for optoelectronics and electronics.* Nat Commun, 2014. **5**: p. 4458.
73. Tao, J., et al., *Mechanical and Electrical Anisotropy of Few-Layer Black Phosphorus.* ACS Nano, 2015. **9**(11): p. 11362-11370.
74. Drissi, L.B., S. Sadki, and K. Sadki, *Phosphorene under strain:electronic, mechanical and piezoelectric responses.* Journal of Physics and Chemistry of Solids, 2018. **112**: p. 137-142.
75. Dong, L., J. Lou, and V.B. Shenoy, *Large In-Plane and Vertical Piezoelectricity in Janus Transition Metal Dichalchogenides.* ACS Nano, 2017. **11**(8): p. 8242-8248.
76. Ding, W.J., et al., *Prediction of intrinsic two-dimensional ferroelectrics in In2Se3 and other III2-VI3 van der Waals materials.* Nature Communications, 2017. **8**.
77. Xue, F., et al., *Multidirection Piezoelectricity in Mono- and Multilayered Hexagonal alpha-In2Se3.* ACS Nano, 2018. **12**(5): p. 4976-4983.
78. Zheng, C., et al., *Room temperature in-plane ferroelectricity in van der Waals In2Se3.* Sci Adv, 2018. **4**(7): p. eaar7720.
79. Zhou, Y., et al., *Out-of-Plane Piezoelectricity and Ferroelectricity in Layered alpha-In2Se3 Nanoflakes.* Nano Lett, 2017. **17**(9): p. 5508-5513.
80. Geim, A.K. and K.S. Novoselov, *The rise of graphene.* Nature Materials, 2007. **6**(3): p. 183-191.
81. Chandratre, S. and P. Sharma, *Coaxing graphene to be piezoelectric.* Applied Physics Letters, 2012. **100**(2).
82. Ong, M.T. and E.J. Reed, *Engineered Piezoelectricity in Graphene.* ACS Nano, 2012. **6**(2): p. 1387-1394.

83. Zelisko, M., et al., *Anomalous piezoelectricity in two-dimensional graphene nitride nanosheets.* Nature Communications, 2014. **5**(1): p. 4284.
84. Ong, M.T., K.-A.N. Duerloo, and E.J. Reed, *The Effect of Hydrogen and Fluorine Coadsorption on the Piezoelectric Properties of Graphene.* The Journal of Physical Chemistry C, 2013. **117**(7): p. 3615-3620.
85. El-Kelany, K.E., et al., *Piezoelectricity of Functionalized Graphene: A Quantum-Mechanical Rationalization.* The Journal of Physical Chemistry C, 2016. **120**(14): p. 7795-7803.
86. Kim, H.J., M. Noor-A-Alam, and Y.-H. Shin, *Piezoelectric enhancement by surface effect in hydrofluorinated graphene bilayer.* Journal of Applied Physics, 2015. **117**(14).
87. Chang, Z., et al., *Piezoelectric properties of graphene oxide: A first-principles computational study.* Applied Physics Letters, 2014. **105**(2).
88. Noor, A.A.M. and Y.H. Shin, *Switchable polarization in an unzipped graphene oxide monolayer.* Phys Chem Chem Phys, 2016. **18**(30): p. 20443-9.
89. da Cunha Rodrigues, G., et al., *Strong piezoelectricity in single-layer graphene deposited on SiO2 grating substrates.* Nat Commun, 2015. **6**: p. 7572.
90. Hu, T. and J. Dong, *Two new phases of monolayer group-IV monochalcogenides and their piezoelectric properties.* Phys Chem Chem Phys, 2016. **18**(47): p. 32514-32520.
91. Nye, J.F. and P.P.L.J.F. Nye, *Physical Properties of Crystals: Their Representation by Tensors and Matrices*. 1985: Clarendon Press.
92. Sai, N. and E.J. Mele, *Microscopic theory for nanotube piezoelectricity.* Physical Review B, 2003. **68**(24).
93. Chowdhury, R., S. Adhikari, and F. Scarpa, *Elasticity and piezoelectricity of zinc oxide nanostructure.* Physica E: Low-dimensional Systems and Nanostructures, 2010. **42**(8): p. 2036-2040.
94. Nakhmanson, S.M., et al., *Spontaneous polarization and piezoelectricity in boron nitride nanotubes.* Physical Review B, 2003. **67**(23).
95. Michel, K.H. and B. Verberck, *Phonon dispersions and piezoelectricity in bulk and multilayers of hexagonal boron nitride.* Physical Review B, 2011. **83**(11).
96. Tan, C., et al., *Recent Advances in Ultrathin Two-Dimensional Nanomaterials.* Chemical Reviews, 2017. **117**(9): p. 6225-6331.
97. Varrla, E., et al., *Large-Scale Production of Size-Controlled MoS2 Nanosheets by Shear Exfoliation.* Chemistry of Materials, 2015. **27**(3): p. 1129-1139.
98. Ahmed, H., et al., *Ultrafast Acoustofluidic Exfoliation of Stratified Crystals.* Adv Mater, 2018. **30**(20): p. e1704756.
99. Mohiuddin, M., et al., *Liquid Phase Acoustic Wave Exfoliation of Layered MoS2: Critical Impact of Electric Field in Efficiency.* Chemistry of Materials, 2018. **30**(16): p. 5593-5601.
100. Liu, K.K., et al., *Growth of large-area and highly crystalline MoS2 thin layers on insulating substrates.* Nano Lett, 2012. **12**(3): p. 1538-44.
101. Lin, M., et al., *Controlled Growth of Atomically Thin In2Se3 Flakes by van der Waals Epitaxy.* Journal of the American Chemical Society, 2013. **135**(36): p. 13274-13277.
102. Zhou, J., et al., *Controlled Synthesis of High-Quality Monolayered alpha-In2Se3 via Physical Vapor Deposition.* Nano Lett, 2015. **15**(10): p. 6400-5.
103. Higashitarumizu, N., et al., *Self-passivated ultra-thin SnS layers via mechanical exfoliation and post-oxidation.* Nanoscale, 2018. **10**(47): p. 22474-22483.

104. Syed, N., et al., *Printing two-dimensional gallium phosphate out of liquid metal.* Nature Communications, 2018. **9**(1): p. 3618.
105. Gruverman, A., M. Alexe, and D. Meier, *Piezoresponse force microscopy and nanoferroic phenomena.* Nat Commun, 2019. **10**(1): p. 1661.
106. Ursic, H. and U. Prah, *Investigations of ferroelectric polycrystalline bulks and thick films using piezoresponse force microscopy.* Proc Math Phys Eng Sci, 2019. **475**(2223): p. 20180782.
107. Eliseev, E.A., et al., *Electromechanical detection in scanning probe microscopy: Tip models and materials contrast.* Journal of Applied Physics, 2007. **102**(1).
108. Eng, L.M., et al., *Nanoscale reconstruction of surface crystallography from three-dimensional polarization distribution in ferroelectric barium–titanate ceramics.* Applied Physics Letters, 1999. **74**(2): p. 233-235.
109. Seol, D., B. Kim, and Y. Kim, *Non-piezoelectric effects in piezoresponse force microscopy.* Current Applied Physics, 2017. **17**(5): p. 661-674.
110. Harnagea, C., et al., *Contact resonances in voltage-modulated force microscopy.* Applied Physics Letters, 2003. **83**(2): p. 338-340.
111. Jesse, S., A.P. Baddorf, and S.V. Kalinin, *Switching spectroscopy piezoresponse force microscopy of ferroelectric materials.* Applied Physics Letters, 2006. **88**(6).
112. Jesse, S., et al., *The band excitation method in scanning probe microscopy for rapid mapping of energy dissipation on the nanoscale.* Nanotechnology, 2007. **18**(43).
113. Rodriguez, B.J., et al., *Dual-frequency resonance-tracking atomic force microscopy.* Nanotechnology, 2007. **18**(47).
114. Brennan, C.J., et al., *Out-of-Plane Electromechanical Response of Monolayer Molybdenum Disulfide Measured by Piezoresponse Force Microscopy.* Nano Letters, 2017. **17**(9): p. 5464-5471.
115. Lu, A.-Y., et al., *Janus monolayers of transition metal dichalcogenides.* Nature Nanotechnology, 2017. **12**(8): p. 744-749.
116. Nasr Esfahani, E., et al., *Piezoelectricity of atomically thin WSe2 via laterally excited scanning probe microscopy.* Nano Energy, 2018. **52**: p. 117-122.
117. Wang, X., et al., *Subatomic deformation driven by vertical piezoelectricity from CdS ultrathin films.* Science Advances, 2016. **2**(7): p. e1600209.
118. Zhang, J., et al., *Second harmonic generation in 2D layered materials.* 2D Materials, 2020. **7**(4).
119. Malard, L.M., et al., *Observation of intense second harmonic generation from MoS2atomic crystals.* Physical Review B, 2013. **87**(20).
120. Shi, J., et al., *3R MoS_2 with Broken Inversion Symmetry: A Promising Ultrathin Nonlinear Optical Device.* Advanced Materials, 2017. **29**(30): p. 1701486.
121. Qi, J., et al., *Piezoelectric effect in chemical vapour deposition-grown atomic-monolayer triangular molybdenum disulfide piezotronics.* Nat Commun, 2015. **6**: p. 7430.
122. Balandin, A.A., *Thermal properties of graphene and nanostructured carbon materials.* Nat Mater, 2011. **10**(8): p. 569-81.
123. Song, H., et al., *Two-Dimensional Materials for Thermal Management Applications.* Joule, 2018. **2**(3): p. 442-463.
124. Jiang, P., X. Qian, and R. Yang, *Tutorial: Time-domain thermoreflectance (TDTR) for thermal property characterization of bulk and thin film materials.* Journal of Applied Physics, 2018. **124**(16): p. 161103.

125. Zhang, Y., et al., *A Review on Principles and Applications of Scanning Thermal Microscopy (SThM).* Advanced Functional Materials, 2019. **30**(18).
126. Balandin, A.A., et al., *Superior Thermal Conductivity of Single-Layer Graphene.* Nano Letters, 2008. **8**(3): p. 902-907.
127. Sahoo, S., et al., *Temperature-Dependent Raman Studies and Thermal Conductivity of Few-Layer MoS2.* The Journal of Physical Chemistry C, 2013. **117**(17): p. 9042-9047.
128. Zhang, X., et al., *Measurement of Lateral and Interfacial Thermal Conductivity of Single- and Bilayer MoS2 and MoSe2 Using Refined Optothermal Raman Technique.* ACS Appl Mater Interfaces, 2015. **7**(46): p. 25923-9.
129. Kim, P., et al., *Thermal transport measurements of individual multiwalled nanotubes.* Phys Rev Lett, 2001. **87**(21): p. 215502.
130. Aiyiti, A., et al., *Measuring the thermal conductivity and interfacial thermal resistance of suspended MoS 2 using electron beam self-heating technique.* Science Bulletin, 2018. **63**(7): p. 452-458.
131. Lee, M.J., et al., *Thermoelectric materials by using two-dimensional materials with negative correlation between electrical and thermal conductivity.* Nat Commun, 2016. **7**: p. 12011.
132. Luo, Z., et al., *Anisotropic in-plane thermal conductivity observed in few-layer black phosphorus.* Nat Commun, 2015. **6**: p. 8572.
133. Sood, A., et al., *Quasi-Ballistic Thermal Transport Across MoS2 Thin Films.* Nano Lett, 2019. **19**(4): p. 2434-2442.
134. Bodzenta, J., A. Kaźmierczak-Bałata, and K. Harris, *Quantitative thermal measurement by the use of scanning thermal microscope and resistive thermal probes.* Journal of Applied Physics, 2020. **127**(3).
135. Vaziri, S., et al., *Ultrahigh thermal isolation across heterogeneously layered two-dimensional materials.* Science Advances, 2019. **5**(8): p. eaax1325.
136. Zhang, X., et al., *Phonon and Raman scattering of two-dimensional transition metal dichalcogenides from monolayer, multilayer to bulk material.* Chemical Society Reviews, 2015. **44**(9): p. 2757-2785.
137. Ganta, D., S. Sinha, and R.T. Haasch, *2-D Material Molybdenum Disulfide Analyzed by XPS.* Surface Science Spectra, 2014. **21**(1): p. 19-27.
138. Luo, C., et al., *In Situ Transmission Electron Microscopy Characterization and Manipulation of Two-Dimensional Layered Materials beyond Graphene.* Small, 2017. **13**(35).
139. Kou, J., et al., *Progress in piezotronics of transition-metal dichalcogenides.* Journal of Physics D: Applied Physics, 2018. **51**(49): p. 493002.
140. Kim, S.K., et al., *Directional dependent piezoelectric effect in CVD grown monolayer MoS 2 for flexible piezoelectric nanogenerators.* Nano Energy, 2016. **22**: p. 483-489.
141. Han, S.A., et al., *Point-Defect-Passivated MoS $_2$ Nanosheet-Based High Performance Piezoelectric Nanogenerator.* Advanced Materials, 2018. **30**(21): p. 1800342.
142. Dai, M., et al., *Enhanced Piezoelectric Effect Derived from Grain Boundary in MoS2 Monolayers.* Nano Lett, 2020. **20**(1): p. 201-207.
143. Dai, M., et al., *Two-Dimensional van der Waals Materials with Aligned In-Plane Polarization and Large Piezoelectric Effect for Self-Powered Piezoelectric Sensors.* Nano Letters, 2019. **19**(8): p. 5410-5416.
144. Song, H., et al., *Lead iodide nanosheets for piezoelectric energy conversion and strain sensing.* Nano Energy, 2018. **49**: p. 7-13.

145. Lu, S.N., et al., *Size effect in a cantilevered ZnO micro/nanowire and its potential as a performance tunable force sensor.* Rsc Advances, 2013. **3**(42): p. 19375-19379.
146. Wu, J.M., et al., *A self-powered piezotronic strain sensor based on single ZnSnO3 microbelts.* Rsc Advances, 2013. **3**(47): p. 25184-25189.
147. Zhu, D., et al., *Piezo/active humidity sensing of CeO2/ZnO and SnO2/ZnO nanoarray nanogenerators with high response and large detecting range.* Sensors and Actuators B-Chemical, 2014. **205**: p. 12-19.
148. Yu, R.M., et al., *Enhanced Performance of a ZnO Nanowire-Based Self-Powered Glucose Sensor by Piezotronic Effect.* Advanced Functional Materials, 2013. **23**(47): p. 5868-5874.
149. Yu, R.M., C.F. Pan, and Z.L. Wang, *High performance of ZnO nanowire protein sensors enhanced by the piezotronic effect.* Energy & Environmental Science, 2013. **6**(2): p. 494-499.
150. Jenkins, K., et al., *Piezotronic Effect: An Emerging Mechanism for Sensing Applications.* Sensors, 2015. **15**(9): p. 22914-22940.
151. Guo, J., et al., *Piezotronic Effect Enhanced Flexible Humidity Sensing of Monolayer MoS2.* ACS Appl Mater Interfaces, 2018. **10**(9): p. 8110-8116.
152. Wang, F., et al., *Piezopotential gated two-dimensional InSe field-effect transistor for designing a pressure sensor based on piezotronic effect.* Nano Energy, 2020. **70**.
153. Wu, W., et al., *Piezophototronic Effect in Single-Atomic-Layer MoS2 for Strain-Gated Flexible Optoelectronics.* Adv Mater, 2016. **28**(38): p. 8463-8468.
154. Lin, P., et al., *Piezo-Phototronic Effect for Enhanced Flexible MoS_2/WSe_2 van der Waals Photodiodes.* Advanced Functional Materials, 2018. **28**(35): p. 1802849.
155. Zheng, D.Q., et al., *High-performance piezo-phototronic solar cell based on two-dimensional materials.* Nano Energy, 2017. **32**: p. 448-453.
156. Michael, G., et al., *High-performance piezo-phototronic multijunction solar cells based on single-type two-dimensional materials.* Nano Energy, 2020. **76**.
157. Kingon, A.I. and S. Srinivasan, *Lead zirconate titanate thin films directly on copper electrodes for ferroelectric, dielectric and piezoelectric applications.* Nature Materials, 2005. **4**(3): p. 233-237.
158. Funakubo, T., et al., *Ultrasonic Linear Motor Using Multilayer Piezoelectric Actuators.* Japanese Journal of Applied Physics, 1995. **34**(Part 1, No. 5B): p. 2756-2759.
159. Scott, J.F., *Applications of modern ferroelectrics.* Science, 2007. **315**(5814): p. 954-959.
160. Wang, Z.L., *Nanogenerators and nanopiezotronics.* 2007 Ieee International Electron Devices Meeting, Vols 1 and 2, 2007: p. 371-374.
161. McMeeking, R.M., *Towards a fracture mechanics for brittle piezoelectric and dielectric materials.* International Journal of Fracture, 2001. **108**(1): p. 25-41.
162. Tan, D., *Prediction of strong piezoelectricity in 3R-MoS2 multilayer structures.* Nano Energy, 2019: p. 4.
163. Liu, F., et al., *Room-temperature ferroelectricity in CuInP2S6 ultrathin flakes.* Nature Communications, 2016. **7**(1): p. 12357.
164. Jesse, S., A.P. Baddorf, and S.V. Kalinin, *Dynamic behaviour in piezoresponse force microscopy.* Nanotechnology, 2006. **17**(6): p. 1615-28.
165. Eda, G., et al., *Photoluminescence from Chemically Exfoliated MoS2.* Nano Letters, 2011. **11**(12): p. 5111-5116.

166. Ganatra, R. and Q. Zhang, *Few-Layer MoS2: A Promising Layered Semiconductor.* ACS Nano, 2014. **8**(5): p. 4074-4099.
167. Suzuki, R., et al., *Valley-dependent spin polarization in bulk MoS2 with broken inversion symmetry.* Nature Nanotechnology, 2014. **9**(8): p. 611-617.
168. Samad, L., et al., *Layer-Controlled Chemical Vapor Deposition Growth of MoS2 Vertical Heterostructures via van der Waals Epitaxy.* ACS Nano, 2016. **10**(7): p. 7039-7046.
169. Zhu, D., et al., *Capture the growth kinetics of CVD growth of two-dimensional MoS2.* npj 2D Materials and Applications, 2017. **1**(1).
170. Kumar, N., et al., *Second harmonic microscopy of monolayer MoS2.* Physical Review B, 2013. **87**(16).
171. Lee, J.-U. and H. Cheong, *Resonance Raman effects in transition metal dichalcogenides.* Journal of Raman Spectroscopy, 2018. **49**(1): p. 66-75.
172. He, K., et al., *Experimental demonstration of continuous electronic structure tuning via strain in atomically thin MoS2.* Nano Lett, 2013. **13**(6): p. 2931-6.
173. Zou, W.N., C.X. Tang, and E. Pan, *Symmetry types of the piezoelectric tensor and their identification.* Proceedings of the Royal Society A: Mathematical, Physical and Engineering Sciences, 2013. **469**(2155).
174. Liu, K., et al., *Elastic Properties of Chemical-Vapor-Deposited Monolayer MoS2, WS2, and Their Bilayer Heterostructures.* Nano Letters, 2014. **14**(9): p. 5097-5103.
175. Pang, Y., et al., *Wearable Electronics Based on 2D Materials for Human Physiological Information Detection.* Small, 2020. **16**(15): p. e1901124.
176. Rohaizad, N., et al., *Two-dimensional materials in biomedical, biosensing and sensing applications.* Chem Soc Rev, 2020.
177. Yi, F., et al., *Wearable energy sources based on 2D materials.* Chem Soc Rev, 2018. **47**(9): p. 3152-3188.
178. Miller, N.C., et al., *Accurate electromechanical characterization of soft molecular monolayers using piezo force microscopy.* Nanoscale Advances, 2019. **1**(12): p. 4834-4843.
179. Kalinin, S.V. and D.A. Bonnell, *Imaging mechanism of piezoresponse force microscopy of ferroelectric surfaces.* Physical Review B, 2002. **65**(12): p. 125408.
180. Wu, F., et al., *Energy scavenging based on a single-crystal PMN-PT nanobelt.* Sci Rep, 2016. **6**: p. 22513.
181. Labuda, A. and R. Proksch, *Quantitative measurements of electromechanical response with a combined optical beam and interferometric atomic force microscope.* Applied Physics Letters, 2015. **106**(25): p. 253103.
182. Wang, Z.L., W.Z. Wu, and C. Falconi, *Piezotronics and piezo-phototronics with third-generation semiconductors.* Mrs Bulletin, 2018. **43**(12): p. 922-927.
183. Zhao, Y., et al., *Thermal Transport in 2D Semiconductors—Considerations for Device Applications.* Advanced Functional Materials, 2019. **30**(8).
184. Zhang, G. and Y.-W. Zhang, *Thermal properties of two-dimensional materials.* Chinese Physics B, 2017. **26**(3).
185. Jiang, J.W., X. Zhuang, and T. Rabczuk, *Orientation dependent thermal conductance in single-layer MoS2.* Sci Rep, 2013. **3**: p. 2209.
186. Bae, J.J., et al., *Thickness-dependent in-plane thermal conductivity of suspended MoS2 grown by chemical vapor deposition.* Nanoscale, 2017. **9**(7): p. 2541-2547.
187. Li, X., et al., *Isotope-Engineering the Thermal Conductivity of Two-Dimensional MoS2.* ACS Nano, 2019. **13**(2): p. 2481-2489.

188. Aiyiti, A., et al., *Thermal conductivity of suspended few-layer MoS2.* Nanoscale, 2018. **10**(6): p. 2727-2734.
189. Sledzinska, M., et al., *Record Low Thermal Conductivity of Polycrystalline MoS2 Films: Tuning the Thermal Conductivity by Grain Orientation.* ACS Appl Mater Interfaces, 2017. **9**(43): p. 37905-37911.
190. Meng, X., et al., *Thermal Conductivity Enhancement in MoS_{2} under Extreme Strain.* Phys Rev Lett, 2019. **122**(15): p. 155901.
191. Ding, Z., et al., *Manipulating the Thermal Conductivity of Monolayer MoS2via Lattice Defect and Strain Engineering.* The Journal of Physical Chemistry C, 2015. **119**(28): p. 16358-16365.
192. Zhu, L., et al., *Thermal conductivity of biaxial-strained MoS2: sensitive strain dependence and size dependent reduction rate.* Nanotechnology, 2015. **26**(46): p. 465707.
193. Zhang, J., *Piezoelectric effect on the thermal conductivity of monolayer gallium nitride.* Journal of Applied Physics, 2018. **123**(3).
194. Yuan, P., et al., *Interfacial thermal conductance between few to tens of layered-MoS2 and c-Si: Effect of MoS2 thickness.* Acta Materialia, 2017. **122**: p. 152-165.
195. Yalon, E., et al., *Temperature-Dependent Thermal Boundary Conductance of Monolayer MoS2 by Raman Thermometry.* ACS Appl Mater Interfaces, 2017. **9**(49): p. 43013-43020.
196. Yasaei, P., et al., *Interfacial Thermal Transport in Monolayer MoS2*

- and Graphene-Based Devices. Advanced Materials Interfaces, 2017. **4**(17).
197. Ding, Z., et al., *Interfacial thermal conductance in graphene/MoS2 heterostructures.* Carbon, 2016. **96**: p. 888-896.
198. Wang, Y., X. Ruan, and A.K. Roy, *Two-temperature nonequilibrium molecular dynamics simulation of thermal transport across metal-nonmetal interfaces.* Physical Review B, 2012. **85**(20).
199. Mao, R., B.D. Kong, and K.W. Kim, *Thermal transport properties of metal/MoS2 interfaces from first principles.* Journal of Applied Physics, 2014. **116**(3).
200. Liu, X., G. Zhang, and Y.-W. Zhang, *Thermal conduction across the one-dimensional interface between a MoS2 monolayer and metal electrode.* Nano Research, 2016. **9**(8): p. 2372-2383.
201. Yan, R., et al., *Thermal Conductivity of Monolayer Molybdenum Disulfide Obtained from Temperature-Dependent Raman Spectroscopy.* ACS Nano, 2014. **8**(1): p. 986-993.
202. Li, X., et al., *Layer-number dependent reflection spectra of MoS2 flakes on SiO2/Si substrate.* Optical Materials Express, 2018. **8**(10).
203. contributors, W. *Absorbance*. 4 January 2021 17:28 UTC 16 January 2021 11:31 UTC]; Available from: https://en.wikipedia.org/w/index.php?title=Absorbance&oldid=998282000.
204. Castellanos-Gomez, A., et al., *Spatially resolved optical absorption spectroscopy of single- and few-layer MoS(2) by hyperspectral imaging.* Nanotechnology, 2016. **27**(11): p. 115705.
205. Dhakal, K.P., et al., *Confocal absorption spectral imaging of MoS2: optical transitions depending on the atomic thickness of intrinsic and chemically doped MoS2.* Nanoscale, 2014. **6**(21): p. 13028-35.

206. Klots, A.R., et al., *Probing excitonic states in suspended two-dimensional semiconductors by photocurrent spectroscopy.* Sci Rep, 2014. **4**: p. 6608.
207. Splendiani, A., et al., *Emerging Photoluminescence in Monolayer MoS2.* Nano Letters, 2010. **10**(4): p. 1271-1275.
208. *Spectrophotometry and spectrofluorimetry : a practical approach*, M.G. Gore, Editor. 2000, Oxford University Press: Oxford ;.
209. Duo, S., et al., *Resistance of polyimide/silica hybrid films to atomic oxygen attack.* Surface and Coatings Technology, 2006. **200**(24): p. 6671-6677.
210. Peercy, P.S. and B. Morosin, *Pressure and Temperature Dependences of the Raman-Active Phonons in SnO2.* Physical Review B, 1973. **7**(6): p. 2779-2786.
211. Rice, C., et al., *Raman-scattering measurements and first-principles calculations of strain-induced phonon shifts in monolayer MoS2.* Physical Review B, 2013. **87**(8).
212. Wang, Y., et al., *Raman Spectroscopy Study of Lattice Vibration and Crystallographic Orientation of Monolayer MoS $_2$ under Uniaxial Strain.* Small, 2013. **9**(17): p. 2857-2861.
213. Taube, A., et al., *Temperature-dependent thermal properties of supported MoS2 monolayers.* ACS Appl Mater Interfaces, 2015. **7**(9): p. 5061-5.
214. Cai, W., et al., *Thermal transport in suspended and supported monolayer graphene grown by chemical vapor deposition.* Nano Lett, 2010. **10**(5): p. 1645-51.
215. Moghadasi, A., *Electronic and phononic modulation of MoS2 under biaxial strain.* Physica B, 2017: p. 6.
216. Suryavanshi, S.V., et al., *Thermal boundary conductance of two-dimensional MoS2 interfaces.* Journal of Applied Physics, 2019. **126**(5).
217. Ong, Z.-Y., *Thickness-dependent Kapitza resistance in multilayered graphene and other two-dimensional crystals.* Physical Review B, 2017. **95**(15).
218. Kang, J., et al., *Computational Study of Metal Contacts to Monolayer Transition-Metal Dichalcogenide Semiconductors.* Physical Review X, 2014. **4**(3).
219. Hamaoui, G., et al., *Electronic contribution in heat transfer at metal-semiconductor and metal silicide-semiconductor interfaces.* Sci Rep, 2018. **8**(1): p. 11352.
220. Kwon, J., et al., *Thickness-dependent Schottky barrier height of MoS2 field-effect transistors.* Nanoscale, 2017. **9**(18): p. 6151-6157.
221. Kaushik, N., et al., *Schottky barrier heights for Au and Pd contacts to MoS2.* Applied Physics Letters, 2014. **105**(11).
222. Manzeli, S., et al., *Piezoresistivity and Strain-induced Band Gap Tuning in Atomically Thin MoS $_2$.* Nano Letters, 2015. **15**(8): p. 5330-5335.
223. Geim, A.K. and I.V. Grigorieva, *Van der Waals heterostructures.* Nature, 2013. **499**(7459): p. 419-25.
224. Xia, W.S., et al., *Recent progress in van der Waals heterojunctions.* Nanoscale, 2017. **9**(13): p. 4324-4365.
225. Wu, J., et al., *Perspectives on Thermoelectricity in Layered and 2D Materials.* Advanced Electronic Materials, 2018. **4**(12).
226. Dryfe, R.A.W., *2D transition metal chalcogenides and van der Waals heterostructures: Fundamental aspects of their electrochemistry.* Current Opinion in Electrochemistry, 2019. **13**: p. 119-124.
227. Wu, W.Z., X.N. Wen, and Z.L. Wang, *Taxel-Addressable Matrix of Vertical-Nanowire Piezotronic Transistors for Active and Adaptive Tactile Imaging.* Science, 2013. **340**(6135): p. 952-957.

228. Zhang, K., J. Zhai, and Z.L. Wang, *A monolayer MoS2 p-n homogenous photodiode with enhanced photoresponse by piezo-phototronic effect.* 2D Materials, 2018. **5**(3).
229. Zhang, K., et al., *A flexible p-CuO/n-MoS2 heterojunction photodetector with enhanced photoresponse by the piezo-phototronic effect.* Materials Horizons, 2017. **4**(2): p. 274-280.
230. Han, G., et al., *Indium selenides: structural characteristics, synthesis and their thermoelectric performances.* Small, 2014. **10**(14): p. 2747-65.
231. Jacobs-Gedrim, R.B., et al., *Extraordinary Photoresponse in Two-Dimensional In2Se3 Nanosheets.* Acs Nano, 2014. **8**(1): p. 514-521.
232. Zheng, Z.Q., J.D. Yao, and G.W. Yang, *Growth of centimeter-scale high-quality In2Se3 films for transparent, flexible and high performance photodetectors.* Journal of Materials Chemistry C, 2016. **4**(34): p. 8094-8103.
233. Mech, R.K., et al., *In2Se3 Visible/Near-IR Photodetector With Observation of Band-Edge in Spectral Response.* Ieee Photonics Technology Letters, 2019. **31**(11): p. 905-908.
234. Jiang, Y., et al., *Construction of In2Se3/MoS2 heterojunction as photoanode toward efficient photoelectrochemical water splitting.* Chemical Engineering Journal, 2019. **358**: p. 752-758.
235. Ding, W., et al., *Prediction of intrinsic two-dimensional ferroelectrics in In2Se3 and other III2-VI3 van der Waals materials.* Nat Commun, 2017. **8**: p. 14956.
236. Xue, F., et al., *Room-Temperature Ferroelectricity in Hexagonally Layered α-In2Se3 Nanoflakes down to the Monolayer Limit.* Advanced Functional Materials, 2018. **28**(50).
237. Xue, F., et al., *Room-Temperature Ferroelectricity in Hexagonally Layered α-In2Se3 Nanoflakes down to the Monolayer Limit.* Adv. Funct. Mater., 2018: p. 7.
238. Zhou, B., *Enhanced carrier separation in ferroelectric In2Se3/MoS2 van der Waals heterostructure.* J. Mater. Chem. C, 2020: p. 8.
239. Shuoguo, Y., *2D ferroelectricity and piezoelectricity for electronic devices*. 2020, THE HONG KONG POLYTECHNIC UNIVERSITY.
240. Poh, S.M., et al., *Molecular-Beam Epitaxy of Two-Dimensional In2Se3 and Its Giant Electroresistance Switching in Ferroresistive Memory Junction.* Nano Letters, 2018. **18**(10): p. 6340-6346.
241. Zhang, Z.D., et al., *Longitudinal twinning -In2Se3 nanowires for UV-visible-NIR photodetectors with high sensitivity.* Frontiers of Optoelectronics, 2018. **11**(3): p. 245-255.
242. Wi, S., et al., *Enhancement of Photovoltaic Response in Multilayer MoS_2 Induced by Plasma Doping.* ACS Nano, 2014. **8**(5): p. 5270-5281.
243. Tang, W., et al., *MoS_2 nanosheet photodetectors with ultrafast response.* Applied Physics Letters, 2017. **111**(15): p. 153502.
244. Chen, M., et al., *Stable few-layer MoS_2 rectifying diodes formed by plasma-assisted doping.* Applied Physics Letters, 2013. **103**(14): p. 142110.
245. Sze, S.M. and K.K. Ng, *Physics of semiconductor devices*. 3rd ed ed. 2007, Hoboken, N.J: Wiley-Interscience. 815.
246. Tao, X. and Y. Gu, *Crystalline–Crystalline Phase Transformation in Two-Dimensional In_2Se_3 Thin Layers.* Nano Letters, 2013. **13**(8): p. 3501-3505.

247. Yang, C., et al., *Planar Direction - Dependent Interfacial Properties in Monolayer In $_2$ Se $_3$ –Metal Contacts.* physica status solidi (b), 2020. **257**(1): p. 1900198.
248. Lin, P., et al., *Tunable WSe2-CdS mixed-dimensional van der Waals heterojunction with a piezo-phototronic effect for an enhanced flexible photodetector.* Nanoscale, 2018. **10**(30): p. 14472-14479.
249. Zou, Z., et al., *Epitaxial synthesis of ultrathin β-In $_2$ Se $_3$ /MoS $_2$ heterostructures with high visible/near-infrared photoresponse.* Nanoscale, 2020. **12**(11): p. 6480-6488.
250. Solanke, S., et al., *Integration of multi-layered materials with wide bandgap semiconductors for multi-spectral photodetectors: case for MoS2/GaN and β-In2Se3/GaN.* Semiconductor Science and Technology, 2019.
251. Liu, B., et al., *Photodetector based on heterostructure of two-dimensional WSe $_2$ /In $_2$ Se $_3$.* Nanotechnology, 2020. **31**(6): p. 065203.
252. Solanke, S.V., et al., *UV/Near-IR dual band photodetector based on p-GaN/{\alpha}-In2Se3 heterojunction.* arXiv:2008.13770 [cond-mat, physics:physics], 2020.
253. Zhang, J.-R., et al., *Theoretical study on the intrinsic properties of In $_2$ Se $_3$ /MoS $_2$ as a photocatalyst driven by near-infrared, visible and ultraviolet light.* Catalysis Science & Technology, 2019. **9**(17): p. 4659-4667.
254. Mak, K.F., et al., *Atomically Thin MoS 2 : A New Direct-Gap Semiconductor.* Physical Review Letters, 2010. **105**(13): p. 136805.
255. Hao, L., et al., *Electrical and photovoltaic characteristics of MoS $_2$ /Si p-n junctions.* Journal of Applied Physics, 2015. **117**(11): p. 114502.
256. Balakrishnan, N., et al., *Epitaxial growth of γ-InSe and α, β, and γ-In2Se3 on ε-GaSe.* 2D Materials, 2018. **5**(3).
257. Drapak, S.I., et al., *On the mechanisms of current transfer in n-In2Se3-p-GaSe heterostructures.* Technical Physics Letters, 2002. **28**(9): p. 707-710.
258. Anderson, R.L., *EXPERIMENTS ON Ge-GaAs HETEROJUNCTIONS.* p. 15.
259. Doan, M.-H., et al., *Charge Transport in MoS $_2$ /WSe $_2$ van der Waals Heterostructure with Tunable Inversion Layer.* ACS Nano, 2017. **11**(4): p. 3832-3840.
260. Zhou, X., et al., *Tunneling Diode Based on WSe $_2$ /SnS $_2$ Heterostructure Incorporating High Detectivity and Responsivity.* Advanced Materials, 2018. **30**(7): p. 1703286.
261. Hou, P., et al., *In-Plane Strain-Modulated Photoresponsivity of the α-In $_2$ Se $_3$ -Based Flexible Transistor.* ACS Applied Electronic Materials, 2020. **2**(1): p. 140-146.
262. Nipane, A., et al., *Few-Layer MoS $_2$ p -Type Devices Enabled by Selective Doping Using Low Energy Phosphorus Implantation.* ACS Nano, 2016. **10**(2): p. 2128-2137.
263. Wu, D., et al., *Thickness-Dependent Dielectric Constant of Few-Layer In2Se3 Nanoflakes.* Nano Letters, 2015. **15**(12): p. 8136-8140.
264. Laturia, A., M.L. Van de Put, and W.G. Vandenberghe, *Dielectric properties of hexagonal boron nitride and transition metal dichalcogenides: from monolayer to bulk.* npj 2D Materials and Applications, 2018. **2**(1): p. 6.